UNIVERSITY OF OKLAHOMA

GRADUATE COLLEGE

A SYNOPTIC AND DYNAMIC CLIMATOLOGY OF HEAVY MIDLATITUDE RAINFALL: TRENDS ACROSS THE UNITED STATES FROM 1950–2009

A DISSERTATION

SUBMITTED TO THE GRADUATE FACULTY

in partial fulfillment of the requirements for the

Degree of

DOCTOR OF PHILOSOPHY

By

ELAINE SAVAGEAU GODFREY
Norman, Oklahoma
2010

A SYNOPTIC AND DYNAMIC CLIMATOLOGY OF HEAVY MIDLATITUDE RAINFALL: TRENDS ACROSS THE UNITED STATES FROM 1950–2009

A DISSERTATION APPROVED FOR THE
SCHOOL OF METEOROLOGY

BY

Dr. Michael B. Richman (Co-Chair)

Dr. Kenneth C. Crawford (Co-Chair)

Dr. Peter J. Lamb

Dr. Lance M. Leslie

Dr. David Easterling

Dr. Aondover Tarhule

Dedication

To my husband, Christopher, a fantastic support and my best friend–thank you for your enduring patience, support, and being there for me “in all kinds of weather”.

To my daughter, Kathleen–may you always be inspired to pursue your dreams and always do your best in your endeavors serving the Lord.

To “Skyler”–I can hardly wait to meet you and encourage your growth.

To God, with whom all things are possible–may this work bring you honor.

Acknowledgments

"If I have seen further, it is by standing on the shoulders of giants."
—Sir Isaac Newton

With my pursuit of higher education, it has become increasingly apparent that I have only traveled thus far by the support, encouragement, and training afforded me by numerous scientists, institutions, friends, and family over my lifetime. Beginning in the hallowed halls of the Finneytown Local School District outside Cincinnati, Ohio with the encouragement of numerous teachers, the GATEWAYS program, and especially my enthusiastic physics teacher, Mr. Barney, my studies continued at The Ohio State University, where the professors in the Department of Physics challenged me beyond my wildest dreams. Dr. Jay Hobgood and Dr. Jeff Rogers provided great encouragement to me when I switched my major to atmospheric sciences during my senior year and helped make it a smooth transition. The excellent education that I received at The Ohio State University solidified my interest in the field of meteorology and prepared me for graduate studies at the University of Oklahoma.

I wish to express my appreciation to Dr. William Beasley for accepting my application out-of-season and to Celia Jones for her great assistance at this time and throughout my graduate career. I am very grateful to all of the professors at the University of Oklahoma who facilitated my higher education through outstanding teaching without burdensome expenses and provided teaching and research assistantships. Consequently, I would like to express my great appreciation to the taxpayers of Ohio, Oklahoma, and the United States of America, who provide the necessary support for scientists to push the boundaries of the frontier of human knowledge and understanding.

I would like to thank Dr. Kenneth Crawford, Dr. Peter Lamb, and Dr. Lance Leslie for believing in me three years ago and giving me a second chance at obtaining a Ph.D. in meteorology at the University of Oklahoma. I am especially indebted to Dr. Crawford for his unwavering confidence in my ability to complete the requirements for this very challenging degree, the seemingly endless hours communicating long-distance with me via email, tele-

phone, and Skype, and for his extremely helpful and thorough critiques and additions to the content and text of this dissertation. Dr. Crawford has gone to great lengths to work with me first across the continent, and later, across the globe. I am honored to be the recipient of his wisdom and one of his final Ph.D. students at OU. I greatly appreciate Dr. Michael Richman's insight into the statistical methods used in this project, assistance with the S-Plus program, and for stepping in as committee chair upon Dr. Crawford's retirement. I am grateful for the support provided by Dr. David Easterling, Dr. John Bates, the National Science Foundation, and the National Climatic Data Center (NCDC) for funding my research project and providing work space, computer access, climatological data, and library resources. I greatly appreciate Mara Sprain's efforts to obtain numerous obscure publications in my literature search and to Dr. Matthew Menne, Claude Williams, and Karsten Shein for their assistance with and provision of NCDC data. I also appreciate Robin Evans for her kindness, her continued administrative assistance, and for introducing me to NCDC three years ago. I would like to thank the University of North Carolina at Asheville for the use of computing resources for my NCEP Reanalysis data plotter.

Completing a doctorate while caring for a young child turned out to be much more difficult than I had ever imagined. I am so thankful for the encouragement and support of my fellow mommy friends Jamie, Lauren, Kristen, Lisa, and Brenda, who have listened patiently, expressed their great faith and confidence in me, provided public-speaking advice and lots of laughs, watched my plants for weeks at a time, and looked after Kathleen so I was able to work on my seemingly never-ending dissertation. I look forward to watching our children continue to grow together.

I am thankful for my parents, Dr. Cheryl W. Savageau and Charles B. Savageau, for always believing in me, stressing the value of an excellent education, and encouraging me to pursue my dreams. You have always inspired me to reach for the stars, and instilled faith and confidence in me when I lacked it. I appreciate the friendship offered by my brother, Dr. Andrew C. Savageau, who has always had confidence in his big sister even when times were tough. I wish my grandparents, Dr. Willard W. Winter and Mardell K. Winter, were

here to celebrate with me today–I owe much of who I am to their love, support, faith, and modeling. I would especially like to thank my best friend and husband, Dr. Christopher Godfrey, for his unwavering support of my extended pursuit of a Ph.D., caring for Kathleen extensively in these difficult last few months, providing lots of assistance with all kinds of computer code, sharing his NCEP Reanalysis data and plotter, and offering helpful editorial suggestions. Christopher understands better than anyone the commitment and challenges faced while completing such a challenging degree program, and I could not have completed this project without his constant support and encouragement.

Most importantly, I would like to thank God for continually hearing my prayers, providing for all my needs (Philippians 4:19), granting me the opportunity to pursue my dream, and the intellect to achieve it. Through the ups and downs of this long and sometimes painful and uncertain journey, I have taken great encouragement from the Lord's words to Joshua, as written in Joshua 1:9:

> "Have I not commanded you? Be strong and courageous. Do not be terrified; do not be discouraged, for the LORD your God will be with you wherever you go."

May everyone who reads this take great encouragement from these words and look to the one true God, who is the creator of all good things and who alone holds the keys to true wisdom and understanding (Isaiah 29:14; 1 Corinthians 1:25). Finally, do not quit, for *"at the proper time we will reap a harvest if we do not give up"* (Galatians 6:9)!

Contents

List of Tables

List of Figures

Abstract

The increasing regularity and intensity of heavy precipitation events across the United States during the latter part of the 20th century is widely recognized. Many climate models predict continued growth in the proportion of precipitation from extreme rainfall events concurrent with the projected increase in average global temperatures.

To evaluate heavy precipitation events on a regional scale, the principal component analysis (PCA) technique is applied using the expanded version of the evenly-distributed Richman–Lamb precipitation dataset. The PCA technique identifies climatologically similar regions with respect to rainfall in the United States east of the Rocky Mountains over a 52-year period. Results revealed 13 regions of coherent precipitation patterns across the eastern two-thirds of the Continental U.S.

A subset of observations from the Global Historical Climatology Network-Daily dataset for the same domain was used to identify heavy and significant rainfall events between 1950–2009. The heavy event definition is based on the 90th or higher percentile of total precipitation events with at least 1 inch (25 mm) of rainfall. Similarly, significant events were the top twenty unique heavy events in each region. Furthermore, when the heavy and significant events were stratified by decade, region, and/or season, meaningful spatial and temporal trends were revealed.

The NCEP–NCAR 40-Year Reanalysis data were used to create composite synoptic maps from the significant events in each region. A region-by-region analysis revealed strong similarities but unique differences in the synoptic-scale environment associated with non-tropical significant events across different regions. A national composite of non-tropical events from inland regions enabled the identification of common patterns in the synoptic environments associated with significant events. A comparison of national composites from the first half and second half of the study period enabled the assessment of potential temporal trends in the synoptic-scale environment. Of all variables, precipitable water had a noticeable increase in the post-1980 significant events over those prior to 1980.

The final work on this research focused on the dynamical forcings (as calculated using terms in the Q-G Omega equation) and assessed possible temporal trends that occurred in the troposphere during the course of the significant precipitation events. This study discovered that, during episodes of significant rainfall, vorticity advection plays little role in initiating or modulating the rainfall event. Instead, thickness advection is by far the most dominant synoptic-scale forcing mechanism to initiate an outbreak of heavy to significant rainfall.

Chapter 1

Introduction

With each passing decade during the 20th century, floods caused more property damage and loss of life in the United States than did any other natural disaster (Perry 2000). Climate extremes, population growth, development and public policy were factors in establishing trends in flood damage across the United States (Pielke and Downton 2000). Underlying these episodic events, major flood damages occur as a result of heavy precipitation concentrated in a small region (i.e., basin). Typically, a second or a third in a series of convective cells creates the flooding when these new cells 'train' over previously saturated soil (e.g., Austin, Texas in May 1981 and Minneapolis-St. Paul in July 1987 are older examples while 14 June 2010 in Oklahoma City is a recent example). Figure 1.1 shows a plot of flood fatalities and fatality events from 1959 through 2005, excluding Hurricane Katrina but including Hurricanes Camille and Agnes. For city managers and state officials to develop plans to mitigate extreme events of high impact weather, meteorologists must quickly and accurately identify the likelihood of potentially devastating precipitation episodes in an ever-changing climate (National Research Council 2010).

The evidence is compelling that the global average temperature is warming and the climate is changing. Although the frequency of all types of precipitation is increasing in a few regions (Groisman et al. 2001, 2004), the increasing regularity and intensity of heavy precipitation events across the United States during the latter part of the 20th century is widely recognized (Kunkel et al. 1993, 1999b; Changnon and Kunkel 1995; Karl et al.

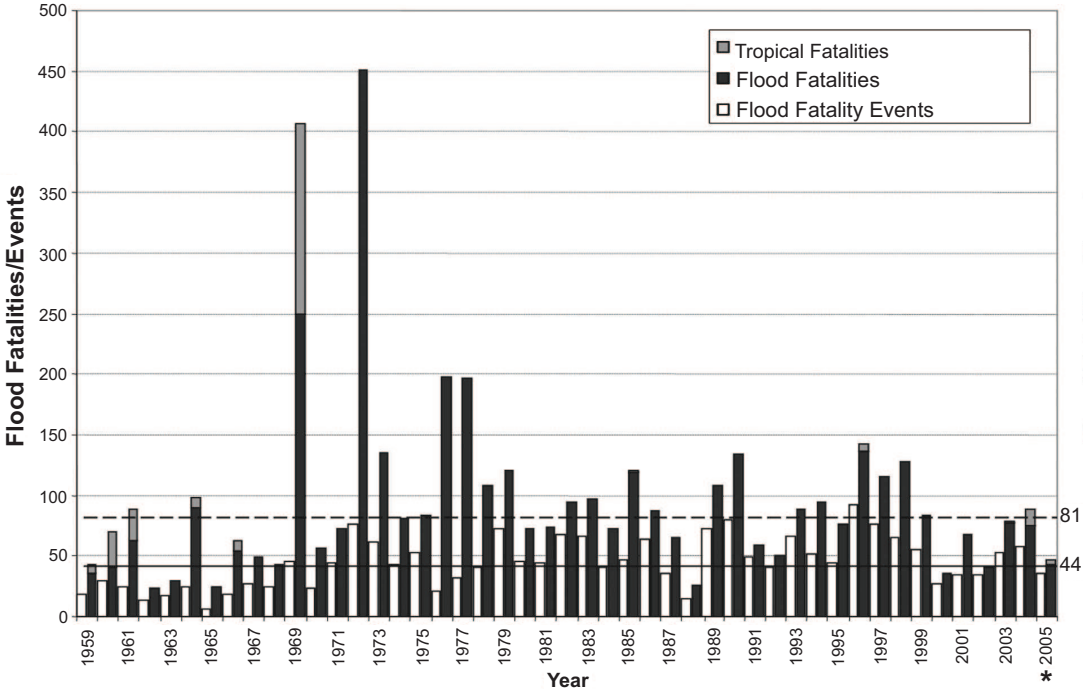

FIG. 1.1: The frequency of flood fatalities and fatality events (excluding indirect) from 1959 to 2005. Black bars represent deaths due strictly to flooding for all event types in the study. Gray bars represent deaths due to tropical systems but not to flooding alone. Light gray bars represent deadly events. The dashed horizontal line represents the yearly fatality median, and the non-dashed horizontal line represents the yearly fatality event median. The asterisk indicates that 2005 data are preliminary and do not include Hurricane Katrina fatalities from Louisiana (adapted from Ashley and Ashley 2008).

1995a,b; Karl and Knight 1998; Easterling et al. 2000; Groisman et al. 2001, 2004, 2005; Madsen and Figdor 2007). Many climate models predict continued growth in the proportion of precipitation from extreme rainfall events concurrent with the projected increase in average global temperatures (Hennessy et al. 1997; Wilby and Wigley 2002; Kharin and Zwiers 2005; Meehl et al. 2005; Barnett et al. 2006). The increasing frequency and intensity of heavy precipitation events will create greater runoff, less ground water recharge, and more opportunities for floods. The more frequent and intense heavy rainfall events are expected to impact urbanized areas to a greater extent, exacerbated by the rise of populations in flood-prone areas such as the coastal United States, mountainous regions and recently converted wetlands. The importance of assessing and projecting risk from these events has grown ever more important (Western Governors' Association 2010).

The observed increase in heavy precipitation in the United States and in other locations across the world (e.g., Groisman et al. 1999) during the latter part of the 20th century raises questions about whether these changes in precipitation were due to the general warming of the environment documented during the same period. Alternatively, perhaps changes in the atmospheric forcing mechanisms have occurred to create additional heavy precipitation events. The first issue (i.e., general warming leading to increases in heavy precipitation) is beyond the scope of this study. However, it may be addressed indirectly by focusing on the latter issue (i.e., changes in atmospheric forcing) in Chapters Five and Six, which culminates a search for detectable trends in rainfall distributions and the transition toward more favorable synoptic environments. Thus, the focus of this research was facilitated by data mining efforts to quantify the frequency and extent of favorable atmospheric dynamics associated with observed heavy precipitation events.

This dissertation is based on the null hypothesis that *the observed increased frequency and intensity of extreme rainfall events from 1950–2009 was not accompanied by changes in the dynamical forcings in the atmosphere on the national scale*.

To evaluate this hypothesis, the principal component analysis (PCA) technique was applied using the expanded version of the Richman–Lamb (Richman and Lamb 1985, 1987) precipitation dataset. The PCA technique was used to identify regions of climatologically similar precipitation across the United States east of the Rocky Mountains. In addition, a subset of observations from the Global Historical Climatology Network (GHCN) was acquired for the same domain along with a complete history of each station. The resulting subset of observations, containing a reasonably high degree of quality in the data, was used to identify 'heavy' and 'significant' rainfall events during a 24-hour period. The heavy event definition was based on the percentile ranking of all 24-hour precipitation events that exceeded a threshold of at least 1 inch (25 mm) of rainfall. On the other hand, the significant event definition depended upon the ranking of events in each PCA-defined region. These heavy and significant precipitation events were stratified by season, decade, and region to assist in uncovering meaningful temporal trends in the event classifications and the

synoptic-scale environment.

The identification of climatologically coherent areas of heavy precipitation and the development of a heavy precipitation climatology spanning each of the PCA-determined regions will provide the foundation for new insights into the mechanisms for heavy precipitation and spatial/temporal trends (i.e., seasonal, decadal and regional) across much of the continental United States. This work will define the synoptic environment and the relevant dynamical forcing associated with many regional events. Thus, an overarching goal of this work is to provide forecasters with quantitative tools to improve their forecasts of excessive precipitation. For example, by comparing the regional and national composite patterns with extended synoptic-scale guidance maps (1–7 days in advance) produced by state-of-the-science numerical weather prediction models, forecasters can be alerted to high impact weather during a given period. More specifically, when the extended guidance maps resemble composite maps from a given region, operational meteorologists will be able to recognize dangerous events several days in advance and provide more accurate quantitative precipitation forecasts (QPFs), heavy precipitation outlooks, and flood watches with a substantial lead time.

Three intermediate goals must be met to achieve the overarching goal of improving human forecasts of excessive rainfall. They are:

1. Use the PCA technique to define spatially coherent regions of heavy precipitation across the eastern half of the United States so that a climatology can be developed to reveal potential spatial/temporal trends of heavy precipitation across seasons, decades and regions.

2. Create composite maps of the synoptic-scale environment associated with significant rainfall events on a regional level and national level and identify any trends in the regions over the period from 1950–2009.

3. Assess the accuracy of a qualitative statement made 30 years ago when Maddox and Doswell (1982) said: “It is felt that by shifting the emphasis away from mid-

tropospheric vorticity advection, the operational meteorologist might be better able to anticipate one of the most difficult forecast problems: organized, intense convective storms occurring within relatively benign synoptic settings." By quantifying this statement through the development of region-specific composite maps, this work will meet its overarching goal and have an immediate impact on forecast operations in the study domain.

To provide a contextual background for the proposed research, the second chapter describes previous scientific work and the development of analytical tools used to form the foundation of this study. The climatological data, the datasets, and their characteristics are described in the third chapter. Chapter Four introduces the methods used to identify climatologically similar regions with respect to rainfall, while the fifth chapter describes the classification of heavy and significant precipitation events. Seasonal and decadal trends also are discussed in this chapter. The sixth chapter of this dissertation describes the synoptic environment and the dynamical forcing in the troposphere during significant non-tropical precipitation events and any spatial/temporal trends in the associated dynamical forcings. These 'cause and effect' relationships uncovered and discussed in Chapter Six will use the three-dimensional reanalysis data set developed by Kalnay et al. (1996). The same concepts listed within the paragraph above and how they are interrelated are illustrated on the flow chart of Figure 1.2.

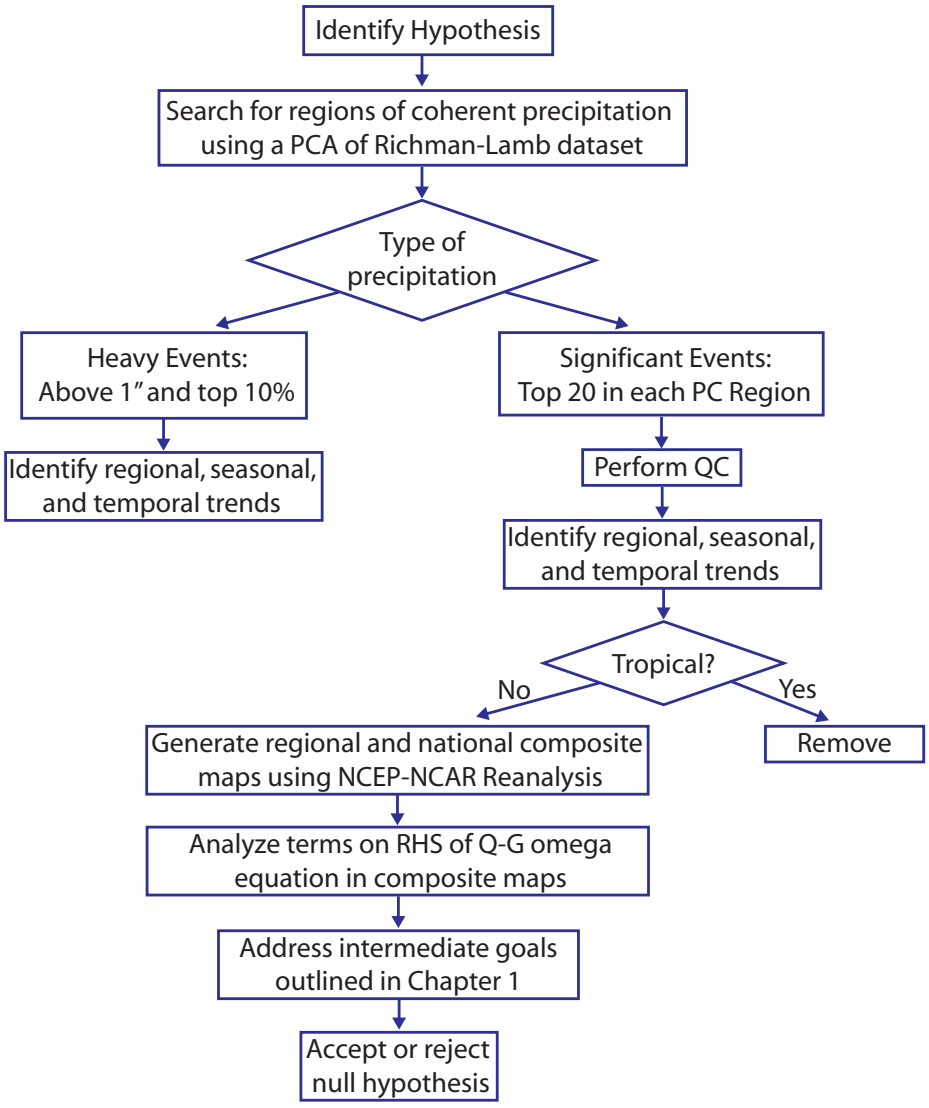

FIG. 1.2: Flow chart outlining the work described in this dissertation.

Chapter 2

Literature Review

2.1 20th Century Heavy Precipitation–The Continental United States

Groisman et al. (2001) noted an increase of mean seasonal precipitation totals over the contiguous United States during all seasons except winter. In a similar study, Groisman et al. (2004) documented an increase of ∼7% in the nationwide mean precipitation between 1908–2002 with results statistically significant at the 5% level. Many scientific manuscripts in recent years focused on detecting trends in the occurrence of heavy precipitation by studying observations of daily precipitation; it is the heavy to extreme precipitation events that are most likely to have the greatest societal and economic impact (e.g., Kunkel et al. 1993, 1999b; Karl et al. 1995a,b; Karl and Knight 1998; Easterling et al. 2000; Groisman et al. 2001, 2004, 2005; Madsen and Figdor 2007).

Numerous studies established that heavy precipitation events escalated in both frequency and intensity across the United States during the latter part of the 20th century at rates greater than observed with lighter precipitation amounts. Kunkel et al. (1993) studied daily heavy precipitation events in the Midwest from 1921–1990 by developing one-year return periods and comparing them with concurrent streamgage observations to uncover heavy precipitation events which were followed closely by episodic floods. The number of heavy precipitation events were aggregated into 5-year periods (pentads) and compared with the total pentad precipitation. Their work revealed an increased trend in both the

pentad precipitation amounts and the number of extreme precipitation events. Karl et al. (1995a) also documented an increase in precipitation across the lower 48 states (CONUS) from 1970–1995 and concluded that precipitation amounts increased to be, on average, about 5% higher than observed during the previous 70 years. Thus, average rainfall across the CONUS during the latter part of the 20th century has been documented to be higher versus the century mean. They also determined that rainfall increased in magnitude primarily due to an increase in regional precipitation during autumn. Karl et al. (1995b) detected an increase in the proportion of annual precipitation derived from a category of extreme precipitation (> 50.8 mm day^{-1}) across the continental United States between 1911–1994. Most of the increase in precipitation across the CONUS resulted from increases in extreme precipitation events during the convective season (March–August). However, the authors noticed little systematic change in precipitation variability over the former Soviet Union between 1935–1989 or across China between 1952–1989.

Karl and Knight (1998) documented an 8% increase in precipitation across the United States at USHCN stations since 1910. Most of the increase in this historical dataset was attributed to increases in the top 10% of rainfall amounts for daily events. Kunkel et al. (1999a) detected an upward trend in the 7-day precipitation events with a one-year return period of about 3% per decade between 1931–1996; their results were significant at the 0.5% level. They detected the largest increase in precipitation across the East North Central region/Great Lakes states. Easterling et al. (2000) also studied changes in daily precipitation for numerous countries around the world; they concluded that changes in the magnitude of heavy precipitation on a daily basis were significantly larger than magnitude changes in seasonal precipitation (i.e., while extreme events became more frequent, less rain fell during a given season). Although precipitation changes across the 20th century were not linear, Groisman et al. (2001) determined that "when a linear approximation is used, precipitation totals during the twentieth century have increased significantly over most of the contiguous United States in all seasons except winter." The authors also noted that, during the 20th century, the frequency of very heavy precipitation events increased

after 1910 while the return periods shortened across much of the eastern United States (e.g. from 10 to 7 years in the Midwest, from 4 to 2.7 years in the South and from 26 to 11 years in the Northeast. Groisman et al. (2004) noted an average increase in annual U.S. precipitation of 7% during the preceding hundred years (1900–2002). Throughout the same period, the magnitude of heavy precipitation events (the top 1% of all precipitation event totals) increased by an average of 20% and were greatest across the eastern two-thirds of the country, primarily during the warm season. A similar study reported that the frequency of very heavy precipitation events from 1893–2002 in the Central United States increased by 20%, with all of the increase occurring during the last 33 years of that period (Groisman et al. 2005). Most recently, Madsen and Figdor (2007) documented that extreme precipitation events (historical 1-year return period) increased in frequency by 24% across the contiguous United States, and even more in New England and the Mid-Atlantic States (61% and 42%, respectively).

Studies from other regions of the world detailed similar results (Iwashima and Yamamoto 1993; Osborn et al. 1999; Groisman et al. 1999; Brunetti et al. 2001a; Brunetti et al. 2001b). For example, Groisman et al. (1999) determined that summer precipitation increased by at least 5% in Canada, the United States, Mexico, the former Soviet Union, Australia, Norway, and Poland during the second half of the 20th century. A mean statistical model revealed a 20% increase in daily summer precipitation totals in excess of 25.4 mm across Canada, Norway, Russia, and Poland coincident with the 5% rise in mean summer rainfall. The same model also revealed a 20% increase in daily amounts in excess of 50.8 mm across the USA, Mexico, China, and Australia as part of the overall 5% increase in mean summer precipitation. Brunetti et al. (2001a) noted an increase in the mean precipitation on wet days across northern Italy between 1951–1996 due to an increasing trend in heavy precipitation events. Using seven stations in northeastern Italy and observations between 1920–1998, Brunetti et al. (2001b) detected an increase in the contribution of extreme rainfall events (upper 0.1%) to total precipitation. Karl et al. (1995b) also reported an increase in the proportion of total annual precipitation derived from the extreme

precipitation category (> 50.8 mm day^{-1}) across the United States between 1911–1994. Unfortunately, high-quality historic climate records in many countries are not available and much reliance instead is placed on numerical models, which simulate climatic changes with time (e.g., Duffy et al. 2001).

The heaviest precipitation events, often convective in nature, usually occur over very small areas and often may be unreported at nearby stations[1] (Groisman et al. 2001, 2004). The Hourly Precipitation Dataset (HPD), archived at the National Climatic Data Center (NCDC), may be the most complete and accurate set of precipitation measurements across the contiguous United States presently available at the time of the current research. The HPD, which contains observations deployed with an average of 50-km spacing, remains inadequate for capturing these extreme events due to the very large spatial gradients that characterize convective precipitation (Brooks and Stensrud 2000). Konrad (2001) noted that relatively few of the small-scale events—those with a one-year return period in a small spatial area—were characterized by the same return period frequency on the larger spatial scale. Nevertheless, it may be possible to distinguish trends in heavy precipitation based on the less extreme events, which occur more frequently and are more likely to be recorded by a surface-based observing network.

What could cause the escalating frequency and/or intensity of the very heavy events? Some scientists hypothesized (Ross and Elliot 1996; Trenberth 1998, 1999) that an increase in globally-averaged surface temperatures creates an increase in the saturation vapor pressure of the atmosphere and consequently, precipitation–even though the atmosphere can be supersaturated on occasions. According to Wentz et al. (2007), the Clausius-Clapeyron equation implies that the total amount of water in the saturated atmosphere will increase at a rate of approximately 7% per degree Kelvin of surface warming (at the standard surface

[1]Based upon personal observations of maps of radar estimated rainfall during the 1980s in central Oklahoma, excessive rainfall was recorded by weather radars somewhere in the area of surveillance at a frequency that was ~ 3 times greater than the frequency of excessive rainfall captured by a surface-based rain gauge network. (Personal communication from Ken Crawford, 2010).

temperature of 288.15 K). This equation:

$$e_s(T) = e_{s_0} \exp\left(\frac{17.67T}{T + 243.5}\right) \tag{2.1}$$

where T is temperature (°C), e_{s_0} is the saturation water vapor pressure at 0°C (6.112 hPa), and e_s is saturation water vapor pressure (hPa; Bolton 1980), suggests that saturation water vapor pressure increases exponentially with an increase in temperature[2]. Numerical simulations with global climate models (GCMs) also reveal that atmospheric moisture in the troposphere will increase and will be accompanied by an increase in tropospheric warming across the globe (Del Genio et al. 1991; Bony et al. 1995). Observational studies also support this concept. For example, rawinsonde data between 1973–1990 revealed a positive correlation between surface air temperature and precipitable water (surface to 500 hPa) in the middle and high latitudes (Gaffen et al. 1992). In addition, Ross and Elliot (1996) discerned a statistically significant increase in the annual mean precipitable water from the surface to 500 hPa across the United States, Hawaii, and the Caribbean by 3–7% per decade between 1973–1995. During the same period, the average annual temperature across the contiguous United States increased at the rate of 0.41°F per decade (available from NCDC). Ross and Elliott (2001) examined 850 hPa specific humidity from 1958–1995 and surface–500 hPa precipitable water from 1973–1995 using rawinsonde data in the Northern Hemisphere. The authors noted an increase in these variables occurred at most stations across the study period; larger and more uniform increases occurred across North America (namely the eastern United States), while a decrease was observed over Europe. Although specific humidity increased throughout the study period, the greatest increase occurred in the post-1973 period. Cao and Ma (2009) observed an increase in the

[2]Bolton's formula is empirically derived and is accurate to 0.3% for −35°C to +35°C. The fundamental version of the Clausius-Clapeyron equation is

$$\frac{de_s}{dT} = \frac{L}{T(\alpha_2 - \alpha_1}} \tag{2.2}$$

(Petty 2008, p. 180), where L is the latent heat of vaporization, α_1 is the specific volume of liquid water and α_2 is the specific volume of water vapor.

number of summertime severe precipitation events over Ontario, Canada between 1979–2002 and associated this with an observed increase in available precipitable water across the same area during this period. Gaffen et al. (1991) also noted an increase in the specific humidity across North America in the late 1970s; this occurred several years after the 1972 change in U.S. radiosonde instruments that measured humidity. Zangvil et al. (2010) noted an increase in moisture flux convergence associated with increased precipitation over the southern Great Plains during May and June in 2006 and 2007 and also across the Midwest during the summers of 1975, 1976, 1979 and 1988; different sources of data were used in each region. A comprehensive review of changes in atmospheric precipitable water during the 20th century is beyond the scope of this research.

With more abundant precipitable water available in the atmosphere, the magnitude of resultant rainfall events also may increase. The work of Allen and Ingram (2002), who used the Hadley Centre model, estimated a precipitation increase of 3.4% for every degree Celsius increase in the average surface temperature. The authors expected an even greater increase (6.5% per degree Celsius) in the uppermost quantiles of rainfall distribution across the middle latitudes and still greater increases across the tropics.

Frei et al. (1998) suggested that modeled increases in precipitation intensity and frequency are closely guided by the relationship expressed in the Clausius-Clapeyron equation (Eq. 2.1). However, an increase of atmospheric water vapor by itself may not offer a complete explanation for the significant increases in the amount and frequency of heavy precipitation versus the slight-to-no increase in non-extreme precipitation observed during the last half of the 20th century. While increased temperature and moisture in the lower troposphere are favorable conditions for the development of convective clouds (Groisman et al. 2004), global climate models indicate that an increase in heavy precipitation also is an anticipated result (Ross and Elliot 1996; Trenberth 1998, 1999). This scenario assumes, of course, that the tropospheric warming is not concentrated in the upper troposphere, which in turn would create more stable conditions inside the modeled atmosphere. Thus, Trenberth (1998, 1999) indicated that increases in atmospheric moisture content likely would

enhance local precipitation by strengthening convective storms through more available moisture and subsequent latent heat release. Changnon (2001) related the average annual number of thunderstorm days with the average number of rain days when more than one inch or two inches of precipitation occurred (depending on the region of the U.S), suggesting that thunderstorms were the primary cause of most heavy rain events. Additionally, Changnon (2001) detected significant increases in thunderstorm rainfall across most of the United States, except across the upper Midwest and a small portion of the Southeast between 1950 and 1994; those results are consistent with other studies of non-thunderstorm heavy precipitation events. It should be noted that, despite the results of Changnon (2001) and Groisman et al. (2004), an earlier study by Changnon (1985) detailed an 8% decrease in the number of days reporting thunder in North America between 1945-1980, primarily because airport observations of thunderstorms no longer are located in rural settings (where thunder can be heard by a human observer) but have been overtaken by automation and urban sprawl. Perhaps those thunderstorms that do form are more intense and produce heavier amounts of rainfall due to increased available potential energy and moisture than their counterparts of past decades.

Several studies used GCMs and other climate models to estimate the effects of increased globally-averaged surface temperature and moisture on the distribution of precipitation events in a simulated atmosphere. Hennessy et al. (1997) used a GCM to demonstrate that with an equilibrium doubling of carbon dioxide (392 parts per million observed in June 2010), precipitation in the middle latitudes will shift toward more intense convective events with fewer moderate non-convective events. While the Hennesy et al. (1997) study used an early GCM, more recent work by Wilby and Wigley (2002) used the HadCM2 and CSM climate models over North America to determine that heavy and extreme precipitation events likely will constitute an increasingly greater proportion of the total precipitation (at the expense of lighter rainfall events that will occur less frequently). Kharin and Zwiers (2005) demonstrated, using a GCM, that increases in extreme global daily precipitation rates (those with 10-, 20-, and 50-year return values) were greater than the modeled

changes in the annual mean precipitation. Their results suggested the probability of extreme precipitation events will nearly double by the end of the 21st century. Based on GCM forecasts of increased water vapor, Meehl et al. (2005) predicted an increase in both mean and extreme precipitation intensity across northwest and northeast North America, northern Europe, northern Asia, the east coast of Asia, southeast Australia, and south-central South America. Their results suggested that precipitation intensity would increase over most continental areas in the tropics. Recently, Barnett et al. (2006) estimated that the relative frequency of the top 1% of precipitation events in 2006 would increase to approximately 20–30% of future events under doubled CO_2 conditions (not expected until well into the 22nd century). Frei et al. (1998) used a regional climate model over Europe to simulate the effects of a warmer and more humid atmosphere on heavy precipitation patterns. Their numerical experiments indicated a substantial shift towards more intense and more frequent heavy precipitation events during the autumn (and, consequently, a shift away from light and moderate events). These results imply that an increase in atmospheric moisture content associated with higher temperatures could be sufficient to create significant increases in the intensity and frequency of heavy precipitation events.

Despite similar results by numerous researchers who used multiple models, it should be noted that GCMs and other climate models have a limited ability to capture both the diurnal precipitation cycle and convective precipitation (Trenberth et al. 2003). Thus, the modeling results should be interpreted with caution. The full complexity of the atmosphere cannot be represented by a simple equation or even a low-resolution climate model.

2.2 Principal Component Analysis

The principal component analysis (PCA) technique, first developed by Hotelling (1933), is a widely used multivariate statistical data reduction technique in the atmospheric sciences. The usefulness of PCA lies in its ability to explain much of the variance in an original data set by reducing the number of variables needed to explain that variance. The new

variables, or principal components, are uncorrelated linear combinations of the initial correlated variables; each principal component represents the maximum amount of variance possible from the original data (Haan 1977; Wilks 2006). New orthogonal components, called principal components (PCs), explain a certain amount of the system variance, with the first components explaining the most variance. An advantage of using PCA on meteorological data is the potential to gain insight into the spatial and temporal variations of meteorological fields (Wilks 2006). For example, PC loadings (the individual elements of the scaled eigenvectors) can be used to identify regions of similar coherent rainfall patterns (e.g., Boone 2010). A coherent rainfall pattern is a region where the anomalies of rainfall tend to occur over the observational time unit being studied (e.g., 24 hours). In this research, the coherent areas are defined by the spatial correlation structure of the rainfall. Because the correlation structure of rainfall is localized in space, rotated PC loadings are a useful tool to summarize the set of coherent rainfall patterns across a large domain, such as the United States. Alternately, one might define 'coherent rainfall patterns' as those areas where the spatial autocorrelation function of the precipitation events has a very slow spatial decay. Chapter 4 of this work will describe and apply the PCA technique in greater detail.

An eigentechnique was first applied to meteorological data for forecasting purposes by Fukuoka (1951). Later, Lorenz (1956) developed the terminology further and gave it the name *empirical orthogonal function* (EOF) analysis. More recently, Richman (1986) demonstrated the benefits of rotating the PCs for meteorological analysis. Although unrotated PCs retain temporal orthogonality and are insensitive to the number of retained PCs, rotated solutions offer significant advantages, because they are unaffected by a dependence on the domain shape, sampling errors, or modal pattern instability (Richman 1986). The rotated results are as physically meaningful as the correlation patterns from which they are derived, unlike the results of unrotated EOFs or PCs. Wilks (2006) also added that rotated PCs are not limited by the orthogonality constraint of unrotated components. This allows multiple PCs to reflect multiple physical processes. However, rotated PCs lack the economy, pattern insensitivity to the number of PCs retained, and ability to extract the

maximum variance on a PC-by-PC basis from a data set when compared to the unrotated method (Richman 1986). It is the eigenvalue truncation process that separates noise from the signal, a fact that is not implicit in the unrotated solutions. If the full set of unrotated PCs are retained, most represent noise.

Richman and Lamb (1985; hereafter RL85) examined individual daily rainfall amounts across the Central United States over 3- and 7-day intervals during the May–August periods of 1949–1980 to demonstrate the advantage of using PCs over EOFs with meteorological data. This important study, as evidenced by its frequent use in numerous studies (96 citations in the literature), established that the primary advantage of using PCs over EOFs stemmed from the ability to rotate the PCs and derive meaningful patterns (EOFs can be rotated, but rotated EOFs have great uncertainty in their meaning). The Varimax-rotated PCs (Kaiser 1958) portrayed spatial patterns in 3- and 7-day summer rainfall events in the Central United States. The unrotated PC loading patterns closely resembled the domain-dependent results described by Buell (1975, 1979). Unlike the unrotated PCs, the Varimax-rotated PCs were of uniform strength (i.e., they explain similar amounts of variance) and uniform size and were not influenced by the shape of the domain. The ten orthogonally rotated PCs that explained the most variance each reflected a different coherent region of precipitation. Richman and Lamb (1987; hereafter RL87) obtained similar results, which supported the use of Varimax-rotated PCs in a precipitation study using data from stations in southern Canada.

Cluster analysis (CA) is another statistical method that has been used in the atmospheric sciences to regionalize precipitation patterns (e.g., Gadgil and Iyengar 1980; Winkler 1985; Easterling 1989; White and Perry 1989; White et al. 1991; Fovell and Fovell 1993; Gong and Richman 1995). CA is an exploratory data analysis tool that separates (clusters) data into groups based on distance or the degree of similarity between individual observations (Wilks 2006). Although the technique can regionalize precipitation data, similar to the capabilities of PCA, CA possesses several weaknesses. For example, certain types of CA are susceptible to the chaining phenomenon (e.g., single-linkage clusters) when additional

observations are close to a point at the edge of the group, even though the observations may be quite far from other points in the same group (Wilks 2006). Gong and Richman (1995) pointed out that CA is susceptible to aggregation error, which is the clustering of two or more geographically diverse areas. This clustering results in an unrealistic and disjointed regionalization of the data where the algorithm did not fit the problem or identify the coherent cluster patterns. The regionalized spatial pattern boundaries produced by a CA vary from method to method and can vary based upon slightly different amounts of input variance (Gong and Richman 1995). Similar to PCA, the morphology of the cluster results can vary depending on the number of clusters retained. However, Gong and Richman (1995) asserted that further research is needed on the appropriate cutoff for cluster retention, whereas several methods for PC retention have already been established. Unlike the smooth overlapping regions produced by PCA, CA regions are irregularly shaped due to the hard boundary constraint (required for the majority of algorithms) that each observation can be assigned to only one cluster at most (Gong and Richman 1995). Finally, the authors noted a decrease in accuracy of nearly 24% variance in nonoverlapping methods. The results of Gong and Richman (1995) suggested that the PCA method produced regions that were as accurate as or more accurate than those produced by the best CA methods, given a sufficient sample size. The authors suggested that statistical methods be chosen based on the data characteristics and goals of the research project. That statement, when applied to this study, must accommodate the underlying meteorological conditions of heavy precipitation events. Because the atmosphere has no hard boundaries in the horizontal, a clustering methodology with overlapping boundaries is required. The PCA technique produces PCs with overlapping loadings (when a loading threshold is isoplethed based on the suggested probability of a station belonging to a given PC). Thus, the PCA technique best preserves the underlying physical processes associated with heavy precipitation events.

PCA is an important tool when used in a meteorological context. Frequently, climatologically similar regions can be identified with respect to a particular atmospheric variable. For example, Changnon (1985) performed a PCA on the number of days reporting thunder

across the United States during most of the 20th century and identified nine similar regions in North America. PCA also has been used to identify teleconnection relationships, such as between sea surface temperature anomalies in the Pacific Ocean and precipitation in Central America or North America (e.g., Montroy 1997; Montroy et al. 1998).

Historically, the results of rotated PCs have often been used to reveal insights with regard to the spatial distribution of precipitation patterns, which can be associated with synoptic features in the atmosphere. For example, Walsh et al. (1982) performed a PCA of monthly precipitation data across the United States and related the PC patterns to surface pressure. Molteni et al. (1983) used PCA to examine rainfall distributions over northern Italy during the cold season and associated each of the first four PCs with a synoptic pressure pattern. The results of the PCA performed in the seminal work of RL85 regionalized the study domain into ten areas of spatially-coherent summer patterns associated with 3- and 7-day rainfall. Similarly, RL87 performed a PCA with a spatially-expanded version of the original RL85 daily precipitation dataset to identify spatial patterns in three- and seven-day summer precipitation totals in southern Canada, east of the Rockies. Easterling (1990) used the PCA technique to identify climatologically persistent synoptic-scale patterns associated with warm-season thunderstorm activity in the Central United States for the period 1948–1977. The regions identified by Easterling (1990) for the primary four rotated components were tied to synoptic-scale features such as the low level jet, northwest flow outbreaks, and mesoscale convective complexes. More recently, Boone (2010) identified and characterized recurring precipitation patterns in Oklahoma using the PCA technique.

The capability of the PCA technique to identify climatologically meaningful patterns in rainfall makes it a powerful tool for the current study, which seeks to regionalize daily precipitation patterns based on data from 1949–2000. Subsequently, decadal trends in heavy rainfall events will be an important focus of this work. A primary focus of this study is to develop conceptual models of the synoptic environment and the associated atmospheric dynamics that create intense episodes of precipitation for each of the PCA regions identi-

fied.

2.3 Synoptic Environment of Heavy Rainfall–The Continental United States

As described in Section 2.1, many authors have investigated the increasing frequency and intensity of heavy precipitation events during the second half of the 20th century in the United States and other parts of the world. In addition, accurate forecasts of such events have become more critical. Based on the work of Rockwood and Maddox (1988) and Schwartz et al. (1990), two distinct phases exist in the forecasting process for convective weather events. The first step involves an examination of the synoptic-scale environment for large areas favorable for developing and sustaining convective storms. The second step identifies smaller areas within the broad favorable environment where convective storms are most likely to initiate, grow, and mature. The current work focuses on the first step in this process.

Because a single mesoscale convective complex (MCC; Maddox 1980a) has been shown by Fritsch et al. (1981) to produce "about half of an average summer month's rainfall across an area the size of the state of Missouri", accurate forecasts of MCCs are one of the most critical forecasts the NWS is charged with issuing.

Numerous studies already have examined the synoptic environments associated with many types of heavy precipitation events on both a regional and national scale, establishing groundwork upon which this project will build (e.g., Maddox et al. 1979; Uccellini and Kocin 1987; Junker et al. 1999). Fundamentally, a moist parcel must rise to its lifting condensation level and continue upward until the condensates are large enough to fall to the surface. Considering the most basic ingredients, heavy precipitation requires atmospheric moisture, condensation nuclei, an unstable atmosphere, and a lifting mechanism. Not surprisingly, heavy precipitation events tend to occur within areas with copious amounts of deep-layer moisture (i.e., Maddox et al. 1979; Bradley and Smith 1994); precipitable water

values are close to 200% of seasonal normals at the location of major floods. The environment supplies this moisture partially in the form of soil moisture (Mo et al. 1997), evapotranspiration (Raddatz 2000, 2005) and, to some extent, through horizontal advection. Regions of high-θ_e (equivalent potential temperature) air have been shown to contain the necessary moisture (e.g., Pontrelli et al. 1999).

The low level jet (LLJ), synoptically evident east of the Rocky Mountains, has been associated with numerous heavy precipitation events (e.g., Maddox et al. 1979; Maddox and Doswell 1982; Mo et al. 1997; Moore et al. 2003). Primarily during the warm season, moisture flux made available by the LLJ and moisture convergence downwind from the LLJ provide the essential water vapor ingredients needed to create heavy precipitation events (Mo et al. 1997; Moore et al. 2003). An unusually strong LLJ may contribute large volumes of moisture convergence, which often facilitates the 'training' of convective cells (also known as 'backbuilding' cells that develop when propagation overpowers translation). The results are sometimes catastrophic due to the excessive rainfall produced (Junker et al. 1999). In addition to providing moisture, the LLJ plays an important role in strengthening the warm air advection and θ_e advection, two valuable indicators for identifying locations of heavy precipitation events (Junket et al. 1999). Bonner (1968) examined LLJs and discovered that the majority of jets were nocturnal, occurred most often with southerly flow, and were located over the southern Great Plains centered over western Oklahoma. However, low level jets occur in multiple locations across the United States east of the Rocky Mountains; this fact will be demonstrated in Chapter 6.

Multiple mechanisms play a role in lifting the moist parcel. In the absence of strong dynamic forcing, the flow of moist air over surface boundaries, such as quasi-stationary fronts and residual outflow boundaries produced by earlier mesoscale systems, can lift moist parcels sufficiently to generate heavy precipitation events (Bradley and Smith 1994). Strong frontal systems can force air parcels to rise along sloped isentropic surfaces. Terrain, in the appropriate atmospheric environment, can also play an important role as a lifting mechanism for convective events near the Rocky and Appalachian Mountains (e.g.,

Petersen et al. 1999; Pontrelli et al. 1999; Carbone et al. 2002; Maddox et al. 1978). In addition, diurnal surface heating plays an important role in lifting parcels on a smaller scale and in the generation of land, vegetation, and sea breezes (i.e., Yan and Anthes 1988). Surface convergence from these breezes can force lifting and generate precipitation under the right stability conditions.

Moisture and surface lifting alone are insufficient to generate storms capable of producing heavy precipitation; the atmosphere must be sufficiently unstable to allow a rising parcel to continue its ascent to the point of condensation and to its level of free convection. Zawadzki and Ro (1978) noted the connection between heavy precipitation events and available convective energy for a surface parcel. Lifting in the lowest several kilometers can release conditional instability, which supports and enhances convective development (Maddox and Doswell 1982). Diffluence and divergence in the upper troposphere, when combined with an approaching shortwave trough aloft, also assists in destabilizing the atmosphere (Pontrelli et al. 1999).

Large-scale ascent also can result from divergence of the ageostrophic wind at upper levels. In the vicinity of an upper-level trough, cold air advection at low levels causes geopotential height falls aloft, which in turn intensifies the horizontal pressure (height) gradient high in the troposphere. At the entrance to this region of stronger height gradients, the real wind develops an ageostrophic component towards the area of lower pressure (or lower heights). This progression causes the surface pressure to decrease beneath the ageostrophic divergence, which in turn creates weak surface convergence, and that begets weak ascending vertical motion. In addition, concentrated areas of warm and cold air advection at lower levels in the troposphere both act to increase the strength of the thermal wind (because horizontal gradients of temperature are strengthened), which reveals itself as an intensifying upper level jet. This scenario leads to an increase in the ageostrophic divergence at upper levels, creating transverse ageostrophic circulations, strengthening the cycle and leading to increasingly stronger vertical motion.

Appendix A describes several methods for assessing synoptic-scale vertical motion in

the atmosphere using established mathematical relationships. The quasi-geostrophic omega equation, as thoroughly explained in Appendix A, expresses the relationship between differential vorticity advection and thickness advection to force vertical motion. At times, differential advection of geostrophic absolute vorticity and thickness advection oppose one another (Hoskins et al. 1978). In many situations, differential advection of geostrophic absolute vorticity (the first term on the right-hand side of the quasi-geostrophic omega equation) is the primary mechanism that causes vertical motion. However, low-level thermal advection (part of the second term on the right-hand side) has been shown to dominate mid-level differential vorticity advection by forcing vertical motion during synoptically benign situations (Maddox and Doswell 1982), such as when areas of intense low-level warm air advection occur in a region of strong conditional instability. Warm thickness advection in the lower troposphere is often the key ingredient responsible for the intensity and persistence of several widespread and persistent intense convective storms when the synoptic environment is weak (i.e., during the middle of the warm season; Maddox and Doswell 1982). Moore et al. (2003) supported these results and theorized that warm air advection/isentropic lift in the lower atmosphere assisted in the production of meso-α-scale vertical motion.

A few studies used the quasi-geostrophic omega equation to identify regions of vertical motion associated with synoptic storms (e.g., Lupo et al. 1992; Mercer and Richman 2007). Mercer and Richman (2007) used this equation to conduct a more thorough review of three types of cyclones in North America: Alberta Clippers, Colorado Cyclones, and East Coast storms. The authors noticed that low-level warm air advection was present east or northeast of the surface low for all three types of storms. Using the quasi-geostrophic omega equation, the differential advection of geostrophic absolute vorticity was determined to reach its maximum value south of the 500 hPa low near the northern extreme of the warm sector.

Convective systems often produce heavy rainfall and are frequently responsible for flash floods (e.g., Maddox et al. 1979; 1980; Petersen et al. 1999; Pontrelli et al. 1999). Flash floods are created when intense rainfall repeatedly traverses the same region. Doswell et

al. (1996) described the necessary atmospheric ingredients for rainfall events that produce flash-floods. The authors asserted that atmospheric moisture content associated with flash flood events was well above seasonable normals (frequently 200% of normal). These narrow corridors of rich low-level moisture sometimes are forced to rapidly ascend to the point of condensation (i.e., its lifting condensation level). A high precipitation rate occurs when low-level moisture is copious (i.e., collision and coalescence become effective), storms slowly translate, and propagation or backbuilding comes into play. Environmental factors such as the entrainment rate, environmental relative humidity, and wind shear also can affect the precipitation efficiency, as do mesoscale factors and microphysical processes (topics beyond the scope of this research). Doswell et al. (1996) noted that convective systems tend to produce higher rainfall rates than other rain-producing systems due to their favorable moist and unstable environment. Slow-moving precipitation systems often are responsible for flash flood events (e.g., Chappell 1985; Moore et al. 1995; Doswell et al. 1996; Pontrelli et al. 1999; Pettet and Johnson 2003), especially when the prevailing flow aloft is toward the cold side of a low-level boundary (e.g. the MSP flood of July 1987 and the OKC flood of June 2010). Weak tropospheric winds (Pontrelli et al. 1999; Doswell et al. 1996) or strong moisture convergence on the rear flank of a mesoscale convective system (MCS; Chappell 1985) may slow the system movement due to the added factor of propagation.

Meteorological processes on multiple scales contribute important factors necessary for flash flood events (Doswell et al. 1996). On the microscale, condensation nuclei, ice microphysics (such as condensation/deposition, accretion, rime splintering, aggregation, collision and coalescence), temperature, and liquid water content influence the formation of rain drops which produce heavy precipitation (Rogers and Yau 1989). On the storm-scale, numerous processes, such as the environmental evaporation potential, the perturbation of synoptic-scale flow by the release of latent heat (Fritsch and Maddox 1981), location of the precipitation cascade, and environmental shear, can influence whether or not copious rainfall might occur (Doswell et al. 1996). Mesoscale processes such as latent heat re-

lease, mid-level entrainment of cooler environmental air and subsequent mid-tropospheric inflow help strengthen the developing convection. These mesoscale processes associated with MCSs can influence system propagation, create new outflow boundaries, and provide copious amounts of precipitation within the embedded convective and stratiform segments (Doswell et al. 1996). In turn, MCSs alter their environment by inducing a large region of anticyclonic difluence aloft, a warm moist region at 30 kPa (300 mb), relatively colder air at the tropopause, and a deep layer of moist ascent on the mesoscale in response to convection (Fritsch and Maddox 1981; Maddox et al. 1981). These upper-level mesohighs are produced *in response to* the low-level convergence of mass, which helps force ascent and the release of latent heat, and the geostrophic adjustment of the pressure field to the anticyclonic flow over several hours (Fritsch and Maddox 1981). Maddox et al. (1981) noticed the development of a large mesoscale anticyclone embedded in the upper-level wind that had been created by mesoscale processes associated with a persistent MCS. On the planetary scale, the underlying causes of extreme rainfall events within the United States likely have global teleconnections (e.g., the El Niño Southern Oscillation, North Atlantic Oscillation, and the Pacific-North American teleconnection pattern [PNA] indirectly impact weather across the United States). Henderson and Robinson (1994) and Yin (1994) associated the PNA teleconnection pattern with the number of precipitation events and moisture conditions in the southeastern United States. Although such teleconnection patterns may influence the number of rainfall events, Henderson and Robinson (1994) surmised that the actual precipitation amount and event duration are predominantly determined by more localized conditions. Furthermore, oceanic currents affect general circulation patterns evident in the atmosphere. Thus, for example, periods of cool surface temperatures in the eastern Pacific Ocean (La Niña) have been associated with areas of increased precipitation across the central United States (CPC 2010). However, such teleconnections are beyond the scope of this study, which examined the synoptic-scale environment in the atmosphere directly above the continental United States.

Synoptic-scale weather systems also have an important connection with deep, moist

convection (e.g., Maddox et al. 1980; Doswell et al. 1996). This connection is evident ahead of shortwave troughs (Maddox et al. 1980; Doswell 1987), near a synoptic-scale 500-hPa ridge axis (Maddox et al. 1979; Glass and Ferry 1995; Konrad 2001), and in association with tropical cyclones (Konrad 2001). Konrad (2001) observed that the center of most 500 hPa cyclones were located northwest of the center of heavy precipitation events. Mo et al. (1997) noted that low pressure was predominant across the western half of North America during summertime heavy precipitation events, while high pressure was typically located in the east.

Several studies examined the types of systems responsible for heavy precipitation events across the United States (e.g., Heideman and Fritsch 1988; Houze et al. 1990; Doswell et al. 1996; Schumacher and Johnson 2005, 2006). For example, Schumacher and Johnson (2005; hereafter SJ05) studied heavy rainfall events (those which exceeded the 50-year recurrence interval for 24-hour accumulated precipitation) between 1999–2001 east of the Rocky Mountains, excluding Florida. The authors classified the cause of each event as an MCS, a synoptic system, or a tropical system based on radar reflectivity data at the time of heaviest precipitation. Of the 116 extreme rain events examined, 65% were caused by MCSs, 27% were associated with synoptic weather systems, and the remaining 8% were the result of tropical systems. SJ05 discovered that 90% of extreme rainfall events associated with synoptic weather systems were convective in nature. Most convective events occurred in the warm sector of an extratropical cyclone ahead of a synoptic-scale cold front. Schumacher and Johnson (2006; hereafter SJ06) added to the results of SJ05 by including two additional years of data (2002–2003) and examining the distribution of events by definition and region. Similar to SJ05, SJ06 noted that nearly two-thirds of all extreme rainfall events (using the same definition as SJ05) were associated with MCSs, 25% were associated with synoptic systems, and tropical systems were responsible for the remainder of events. When synoptic events were stratified, the authors determined that convectively-dominated synoptic events produced a greater proportion of the extreme rainfall events than did non-convective events. Heideman and Fritsch (1988) noticed that precipitation

associated with extratropical cyclones and associated frontal systems accounted for approximately half of the summertime significant events in the United States in 1982–1983; the rest were a result of mesoscale forcing mechanisms such as short waves and convective feedback events. These studies provide convincing evidence that synoptic systems, tropical storms, MCSs and other mesoscale forcing mechanisms, such as mesoscale convective complexes (MCCs), are predominantly responsible for heavy precipitation events in the conterminous United States east of the Rocky Mountains.

Elsewhere across North America, Raddatz and Hanesiak (2008) summarized mesoscale processes that initiated summertime convective events and produce significant precipitation across the Canadian prairies. Most were convective, but some were non-convective in nature. Both types of storms were created by surface low pressure centers, surface troughs, and both warm and cold fronts.

Flash flood events occur generally with multiple types of storms such as multicell and supercell convective systems, squall lines, MCSs, nonconvective systems, and orographically-forced events (Moore et al. 1995; Doswell et al. 1996; Smith et al. 2001). SJ06 noted that, although infrequent, the most widespread and destructive floods during the period of their study were associated with tropical systems. Gallus et al. (2008) examined nine types of convective storms and determined that squall lines with line-parallel stratiform rain or with trailing stratiform rain and broken lines created the greatest number of flood reports.

Numerous studies (e.g., Chappell 1985; Fritsch et al. 1986; Glass and Ferry 1995; Parker and Johnson 2000; Moore et al. 2003; Pettet and Johnson 2003; SJ05; SJ06) have indicated that MCSs are responsible for many heavy precipitation events in certain regions of the United States. Of the 116 extreme rain events examined by SJ05 in the eastern part of the nation (excluding Florida), nearly two-thirds were caused by MCSs. Parker and Johnson (2000, 2004) separated MCSs into sub-classifications of trailing stratiform (TS), parallel stratiform (PS), and leading stratiform (LS); they noticed that LS systems moved slower than PS or TS systems, and consequently, produced heavy rainfall in some instances. SJ05 used the MCS classifications of Parker and Johnson (2000), and added two more

classes: training line/adjoining stratiform (TL/AS) and backbuilding/quasi-stationary. Of these five, the TL/AS and backbuilding/quasi-stationary were most commonly associated with extreme rainfall events, followed by TS. SJ06 also noted that the TL/AS type produced more extreme rainfall events than did any other MCS classification. Pettet and Johnson (2003) studied LS precipitation modes and documented their potential association with flash flood events with slow system motion.

Although many heavy precipitation events are associated with MCSs, these events are not distributed evenly by season, time of occurrence or by geography. SJ06, in their study of heavy rainfall east of the Rocky Mountains (excluding Florida) observed that 74% of summer extreme precipitation events east of the Rocky Mountains were associated with MCSs, but the cool-season events were primarily caused by synoptic weather systems. Their results are supported by most MCSs are limited to the warm season, when moisture content in the atmosphere is greatest whereas synoptic systems tend to be driven by the strong baroclinic conditions present during the cool season. Heideman and Fritsch (1988) observed that nearly three-quarters of significant summertime precipitation events between the Rockies and the Mississippi River occurred at night, comparable to the observations of SJ05 and SJ06.

Heavy precipitation from MCSs have been associated with high K indexes (Maddox et al. 1979; Glass and Ferry 1995; hereafter GF95), cool mid-tropospheric temperatures (below 10°C; GF95; Junker et al. 1999), anticyclonic and diffluent upper-level flow (GF95; Moore et al. 2003) or weak upper-level flow (Moore et al. 1995). GF95 and Moore et al. (2003) documented the presence of low-level warm air advection with MCSs that produced heavy amounts of rainfall, while other authors noted the importance of the LLJ in such systems (i.e., Maddox et al. 1979; Houze et al. 1990; GF95; Moore et al. 2003; Tuttle and Davis 2006). Strong θ_e gradients or positive θ_e advection (Shi and Scofield 1987; Juying and Scofield 1989; GF95; Junker et al. 1999; Moore et al. 2003), a moist lower troposphere (Junker et al. 1999) and echo training (Fristch et al. 1986; GF95; Moore et al. 1995; Junker et al. 1999) are ingredient that also contributed to the production of heavy precipitation in

MCSs.

Typically, MCS-induced heavy rainfall is located west of an upper-level ridge axis (Maddox et al. 1979; GF95) and east of an upstream short-wave trough (GF95; Moore et al. 2003). Moore et al. (2003) observed a 500-hPa jet axis was regularly located west of an elevated MCS. Often, heavy rain-producing MCSs are associated with anticyclonic and diffluent upper-level flow on the west or southwest edge of and sometimes underneath the area of maximum divergence (GF95; Moore et al. 2003). The LLJ has been shown to be the most important forcing mechanism for heavy rain-producing MCSs (GF95) and other heavy rainfall events (Maddox et al. 1979) due to its transport of the necessary warm moist air (Means 1952, 1954). Tuttle and Davis (2006) observed that MCS rainfall intensity is typically proportional to the strength of the nocturnal LLJ. These authors noted that 'corridors' of MCS precipitation are strongly associated with the northern edge of the nocturnal LLJ. Despite the important role of the LLJ in organized convection (such as MCSs), the LLJ does not play a role in unorganized areas of convection that do not possess a linear structure (Houze et al. 1990).

When mesoscale convective weather systems occur in series, the total accumulated precipitation can rival or surpass that of hurricanes or tropical systems (Fritsch et al. 1986). Some MCSs produced more than 10 inches (254 mm) of rainfall in twenty-four hours (GF95). Precipitation amounts from mesoscale convective weather systems can be modulated by changes and trends in the large-scale circulation patterns, although the frequency of MCSs have not changed significantly (Fritsch et al. 1986). Tuttle and Davis (2006) observed that 68% of MCSs occurred as part of a series of events that took place over a 2–13 day period.

Although few studies examined all regions across the United States, several investigated the synoptic features associated with heavy precipitation events in specific regions. For example, Bradley and Smith (1994) used proximity soundings to study the meteorological environments associated with convective storms that produced more than 25 mm of rainfall in 24 hours across the southern plains. The authors discovered that extreme rainfall

events occurred in an environment of convectively unstable air with abundant moisture, where low-level winds advected additional warm moist air, and winds veered with height. More specifically, extreme precipitation events, characterized by strong dynamic forcing, tended to be associated with the approach of an upper-level disturbance, often a cutoff low or a short-wave trough at the 500-mb level (Maddox et al. 1980; Bradley and Smith 1994). The heaviest precipitation amounts across the southern plains tended to occur in the warm sector ahead of a quasi-stationary front as the low or an embedded short-wave approached the region. Events which were characterized by weak dynamic forcing tended to be associated with a quasi-stationary front or residual gust front in the presence of low-level southerly winds transporting warm moist air. The storms that developed moved as a system along the frontal boundary (a result of translation toward the cold side of the boundary and propagation back toward the tongue of high θ_e values); the result was a training of multiple storms over the same area that created large totals of precipitation (Bradley and Smith 1994; Moore et al. 1995). Aylward and Dyer (2010) studied training convective storms across the east-central United States from 2004–2006 and observed that these events tended to be associated with either a closed upper-level trough (CULL), an upper-level trough (ULT), or an 850-hPa trough–low (850TL). The CULL and ULT events tended to occur in strongly forced synoptic environments, while the 850TL tended to have weak upper-level forcing.

On the large synoptic-scale, involving areas as large as most of the conterminous United States, Carbone et al. (2002) examined clusters of heavy precipitation during the warm seasons of 1997–2000 and noticed that these episodes were primarily initiated by diurnal forcing (thermal and topographical) near the Appalachian and Rocky Mountains and by semidiurnal forcing between these mountain ranges. Maddox et al. (1980) observed similar patterns in the western United States, even though the heavy rainfall events in the west tended to be lesser in magnitude than their eastern counterparts. Carbone et al. (2002) suggested that convection near the Rockies created upper tropospheric potential vorticity anomalies that were advected east and thus linked with subsequent convective systems. They also asserted that trapped gravity waves in the boundary layer or inertial gravity waves

in the free troposphere could connect successive convective events of a longer duration and zonal extent than can be explained by a single MCS.

Two recent studies (SJ05 and SJ06) examined heavy precipitation events in the eastern two-thirds of the United States by region and classified them by parent storm type (MCS, synoptic event, tropical cyclone). SJ05 noted that extreme rainfall events in the eastern part of the country were primarily caused by synoptic or tropical systems. MCSs tended to produce a greater proportion of the extreme rainfall events (SJ05) across every region except the Southeast, where tropical systems created extreme events (SJ06). In the plains and north regions, nearly all extreme rain events resulted from MCSs during the warm season, when the most moisture was available (SJ06). Fritsch et al. (1986) also reported that mesoscale convective weather systems are the primary producers of warm-season rainfall across much of the Midwest. Although MCSs dominate, synoptic systems played a larger role than the national average role in the Northeast, Ohio-Mississippi River Valleys, and South regions (SJ06). SJ06 observed that MCSs also dominated the extreme precipitation events in the Ohio-Mississippi River Valley, although cool season synoptic systems played a more significant role in this area than in other areas. Extreme events in the South were primarily associated with late-spring MCSs and with multiple sources during the fall. Relatively few extreme events occurred in the Northeast during their five year period of study, although all three types of systems contributed to the 16 observed extreme events (SJ06).

Heavy precipitation events in the winter also are driven by large synoptic-scale forcing mechanisms. Uccellini and Kocin (1987) studied 8 snowstorms along the eastern coast of the United States. The authors noticed that the heaviest snow totals tended to occur in an area where two upper-level jets produce overlapping areas of rising vertical motion (Figure 2.1). These transverse circulations are associated with the diffluent exit region of a more southern subtropical jet and the confluent entrance region of the more northern polar jet. Upper-level divergence near the region of favorable interaction by these two circulations facilitates surface cyclonic development. The advection of warm moist air northward along sloped isentropes supported this development and supplied copious moisture sufficient for

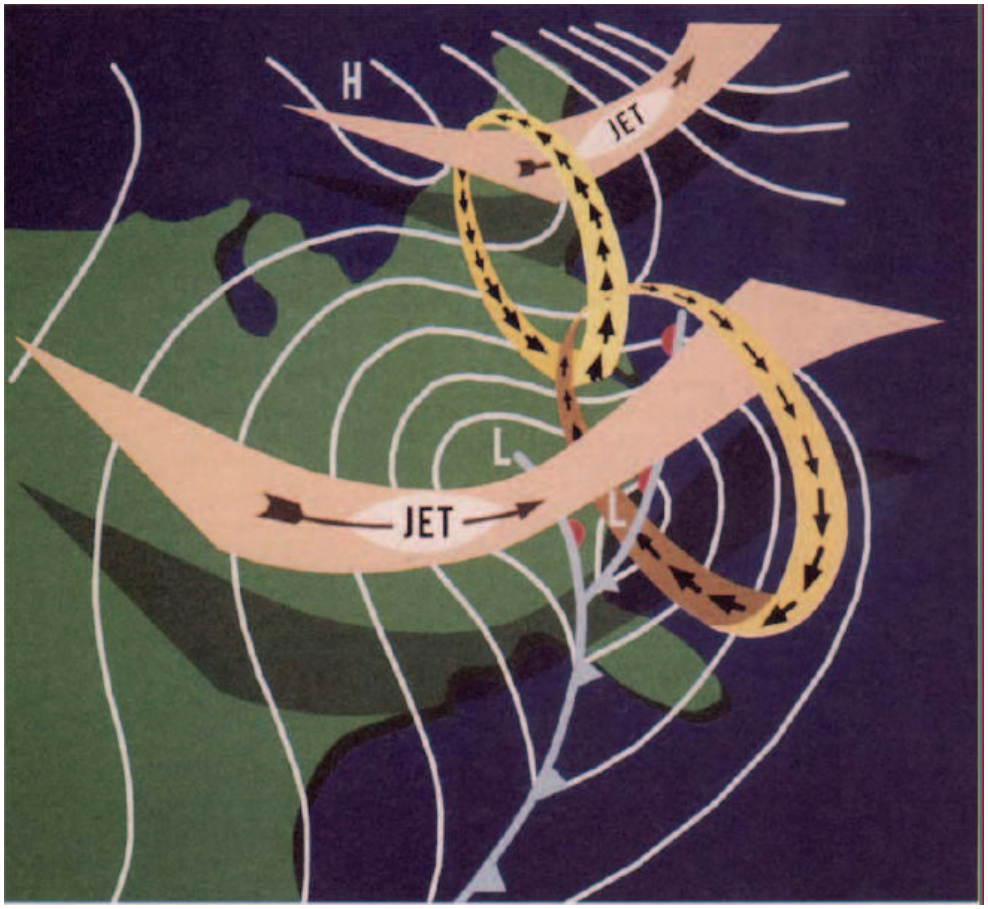

FIG. 2.1: Three-dimensional schematic of jet-related circulation patterns during East Coast snowstorms. The transverse circulations are associated with the diffluent exit region of a southern jet streak and the confluent entrance regions of northeastern jet streak. Surface low and high pressure systems, isobars, and frontal positions are also indicated (from Uccellini and Kocin 1987).

producing heavy snowfall totals.

2.4 Early applications of composite maps in operational forecasting

The development of composite maps for use as a decision-support tool in operational weather forecast offices is not a new concept. Theoretical models of the atmosphere (better termed as a 'conceptual model'), such as the Norwegian Cyclone Model, have been around since early in the 20th century. Because rawinsonde data were hard to access and NWP files from the old "National Meteorological Center" were impossible to access by those outside of the national center, the development of three-dimensional sets of composite images from

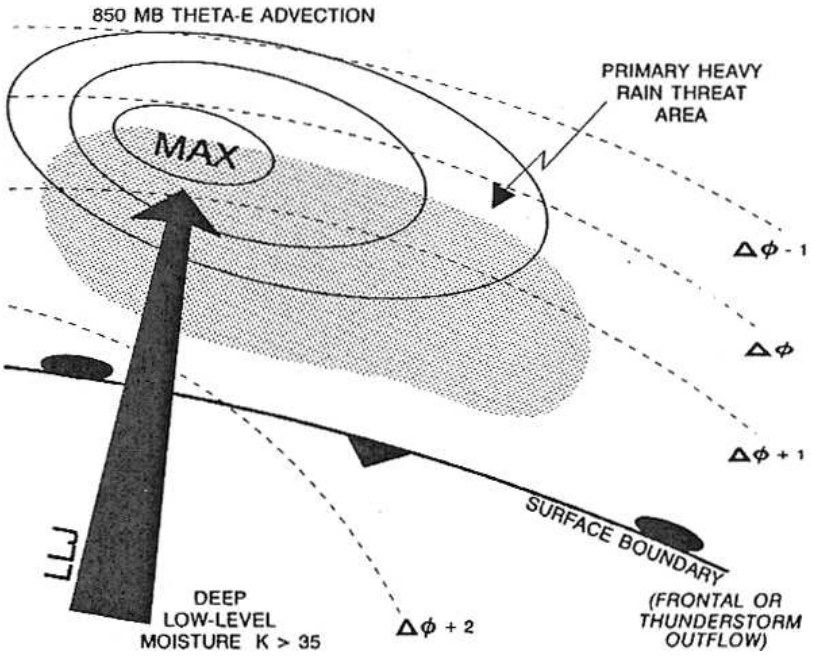

FIG. 2.2: Conceptual model of favorable area for heavy convective rainfall (shaded) from MCSs. Dashed lines represent 850–300 mb thickness contours (from Glass and Ferry 1995).

selected case-study maps did not really begin until the early 1970s. The work of Smith and Younkin (1972) led to the creation of a regionally-focused set of composite images used to improve forecasts of heavy snowfall in the northeast United States. Based on the study of 151 significant rain events (mostly MCSs that occurred between May and October), the development work by Maddox et al. (1979; 1980) became the first comprehensive set of tools to help forecasters with difficult decisions prior to flood-producing rain events. Though the early composite modeling work of Maddox et al. (1979) was subjectively derived, their composite models remain in widespread use today, primarily because their models became 'proxies for experience' in a forecast environment.

During the late 1980s, Uccellini and Kocin (1987) studied eight East Coast snowstorms and created a composite map of the ageostrophic circulation patterns associated with two high-level jet streams that were interacting favorably (Figure 2.1). A few years later, Glass and Ferry (1995) examined warm season heavy convective rainfall events in the mid-Mississippi Valley during 1993–94 and generated a composite model of the area

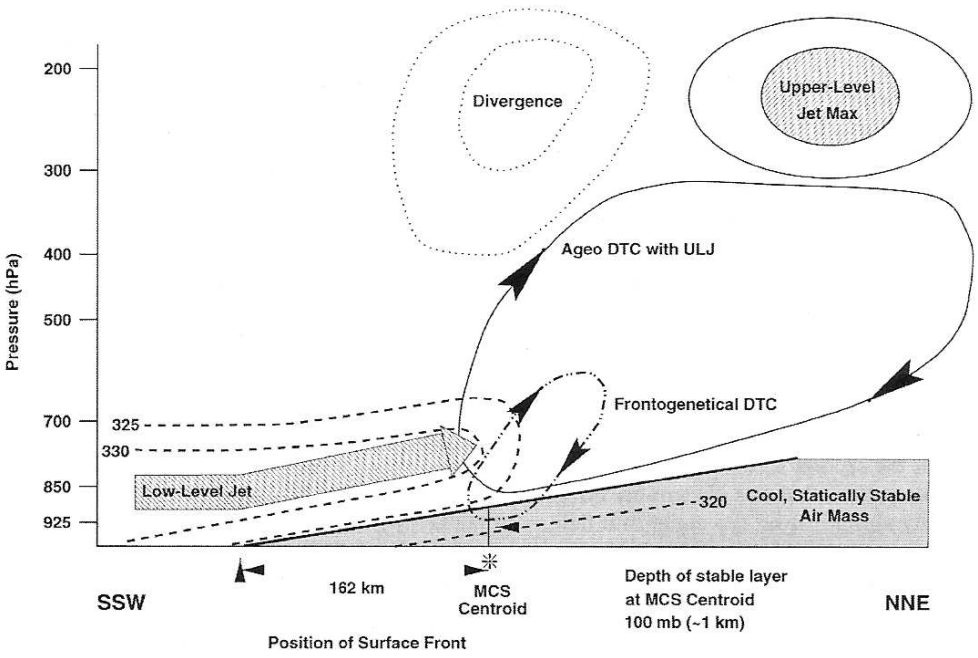

FIG. 2.3: Cross-sectional view of MCS centroid, parallel to the LLJ and across the surface frontal zone. Dashed lines represent typical θ_e values, thin oval with arrows represents the ageostrophic direct thermal circulation (DTC) associated with the upper-level jet (ULJ) streak, and the dashed-dotted oval represents the DTC associated with the low-level frontogenetical forcing (from Moore et al. 2003).

favorable for the development of heavy rainfall (Figure 2.2). Based on their studies of 12 heavy rain events in the vicinity of Iowa and Missouri during the summer of 1993, the compositing work of Junker et al. (1999; not shown) is considered to be a polished edition of the compositing technique. The most recent composite models of heavy rain events were developed by Moore et al. (2003), who examined 21 MCS events with heavy rainfall. Their maps (Figures 2.3 and 2.4) illustrate a composite view of an MCS centroid relative to important synoptic-scale features.

The template proposed to generate a three-dimensional set of objectively-derived composite maps is a moveable Cartesian grid centered on the location of heaviest precipitation. During the application of the technique, the appropriate weather maps for the cases under investigation are digitized onto the moveable grid. However, when only a small region is considered, it may not be necessary to use a moveable grid (i.e., Winkler 1988). Once all cases have been digitized, the average value of each variable is calculated. The re-

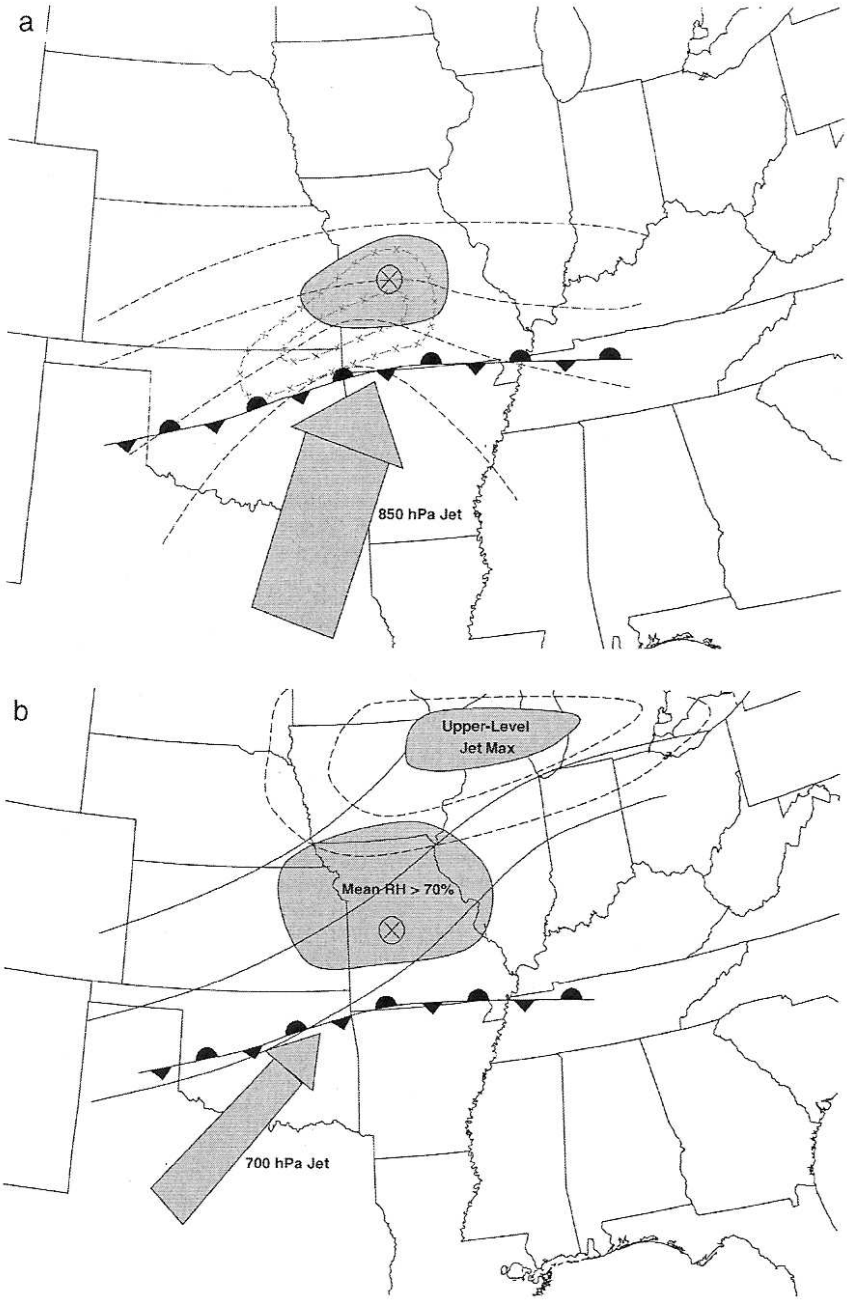

FIG. 2.4: Plan view of the typical synoptic environment of warm-season heavy precipitation events from elevated thunderstorms in a) lower troposphere and b) middle troposphere. In both figures, the encircled X represents the MCS centroid location. In a), dashed lines represent typical θ_e values decreasing to the north, dashed-cross lines represent 925–850 mb moisture convergence maxima, the shaded area is a region of maximum θ_e advection, and the broad arrow represents the LLJ. In b), the dashed lines are isotachs associated with the upper-level jet, the 500 hPa height lines are represented by the solid lines, the shaded area indicates a region of mean surface-to-500-hPa relative humidity above 70%, and the arrow represents the 700-hPa jet (from Moore et al. 2003).

sult is a series of composite maps. This established technique conveys information about synoptic-scale features relative to the epicenters of heavy precipitation. Knowledge about the synoptic environment continues to assist operational forecasters in the assimilation of information from real-time atmospheric conditions.

While the previous composite studies are noteworthy and were considered state-of-the-art in the late 20th century, all previous composite maps of heavy rain events were subjectively derived through the eyes and minds of the research scientits who developed them. Three-dimensional sets of objectively-derived composite maps associated with heavy precipitation events does not exist in the current literature.

This dissertation will access objectively-analyzed atmospheric data using the 40-Year Reanalysis (Kalnay et al. 1996) produced by the National Centers for Environmental Prediction/National Center for Atmospheric Research (NCEP/NCAR).[3] This unique dataset provides a detailed, hydrostatically consistent analysis in space and time of numerous upper-air parameters for a multitude of uses, including the development of conceptual models and for quantifying the magnitude of dynamic forcing parameters. Although the NCEP North American Regional Reanalysis (NARR; Mesinger et al. 2006) offers a higher resolution than does the 40-Year Reanalysis, the NARR data are available only from 1971 through the first half of 2009, which excludes nearly half of the dataset used in this study.

2.5 This Study

Although the trends of heavy precipitation events and their synoptic environments have been studied extensively, two issues raised in Chapter 1 remain unanswered. First: Are the increases in heavy precipitation simply a result of increasing global temperature and moisture? The literature suggests this scenario is happening, but this scientific issue is beyond the scope of this research. Second: Have changes occurred in the forcing mechanisms that drive heavy precipitation events? In other words, has the synoptic environment or atmo-

[3]The NCEP/NCAR Reanalysis has been expanded and currently includes data from 1950–2008.

spheric dynamics associated with heavy precipitation events changed during the past half century? The lack of research on this topic provides a unique opportunity for the topic to become a prime focus in this study.

While a number of studies examined synoptic environments conducive for heavy precipitation, almost all prior work did little to provide decision-support tools for operational forecasters during tense moments when high impact weather is unfolding and life saving decisions must be made. In other words, objectively-derived decision support tools remain as a void in the forecasters' arsenal. Thus, this work will develop composite maps for small but spatially coherent regions of precipitation across the United States east of the Rocky Mountains. These tools will be used to describe regional-scale environments in three dimensions that are favorable for the production of significant precipitation. In addition, the forcing mechanisms for synoptic-scale vertical motions will be evaluated qualitatively within each of the spatially coherent regions of precipitation.

The study of synoptic features related to heavy precipitation events across small regions can reveal meteorological features not captured in studies that developed national composites (Winkler 1988). Thus, a classification of the synoptic environment and atmospheric dynamics associated with observed heavy precipitation events for spatially coherent regions of the United States will benefit operational forecasters at local offices of the National Weather Service.

This study will seek to uncover the relevant features and long-term trends in the synoptic environments and atmospheric dynamics associated with the heaviest precipitation events during the past 60 years on both the national and regional scale. A prime motivation for this climatological study of significant weather events lies in the immediate applicability and practical implementation of the study results at NWS Forecast Offices across the United States.

Results from the research portion of this work will be reported in Chapters 4, 5, and 6 and include:

1. Use of the PCA technique to identify spatially coherent regions of precipitation us-

ing the expanded Richman–Lamb precipitation dataset. Based on the PCA analysis and the associated frequency distributions of precipitation (seasonal, decadal and regional), a set of climatologically similar regions for precipitation will be determined.

2. The dissertation work also will develop composite images of map features considered important to operational meteorologists (e.g., surface isobars, corridors of precipitable water, zones of low-level convergence, 850 hPa winds and thermal advection, 500 hPa vertical motion and vorticity advection, 200 hPa isotachs and divergence, etc.).

3. The study ends with a quantitative evaluation of the atmospheric variables that force vertical motion. These latter results will be developed in the smaller PCA-determined regions, on a national scale, and across the 60-year study period during which the key events occurred.

Chapter 3

Data and Methodological Framework

While high-quality rainfall data are available worldwide, most of the available rainfall data falls below desirable standards. However, in the United States, automated and manually acquired gauge observations have been archived from relatively dense networks; these data are reasonably high in quality and extend back in time to the 19th century. This historically long record of precipitation observations across the United States provides an excellent dataset to enable a wide range of precipitation analyses.

To conduct a principal component analysis that reflects the unbiased correlation structure within the data, variables must be evenly distributed in space to equalize the spatial variance (Karl et al. 1982). However, the gauge networks across the Rocky Mountains are irregularly spaced, and that fact could negatively impact the results of a PCA for these regions by underestimating the covariance structure of the precipitation. In addition, precipitation systems are discontinuous in mountainous terrain. Thus, the results from studies of precipitation data across the Rocky Mountains will differ from study results that used data from the rest of the United States. Thus, only precipitation data east of the Rocky Mountains will be used in this study.

The Global Historical Climatology Network (GHCN; Vose et al. 1992), compiled by the NCDC in Asheville, North Carolina, provides a dense set of high-quality precipitation observations whose periods-of-record exceed 75 years. More than 43,000 locations around the globe are involved. Approximately 8500 of these stations still provide data on a regular

basis (Menne et al. 2009). The GHCN-Daily data (GHCN-D) comprise a subset of the monthly GHCN data and include observations of maximum and minimum temperature, temperature at the time of observation, precipitation amount, snowfall amount, and snow depth (Menne et al. 2009). Within the contiguous U.S., over 22,000 GHCN-D stations exist with varying periods-of-record. The majority of U.S. measurements are acquired from the U.S. Cooperative Summary of the Day, which includes the National Weather Service's (NWS) Cooperative Observer Network as well as automated measurements from some "first order" stations. Other GHCN-D data are acquired from the following sources: Global Climate Observing System Surface Network, U.S. Fort data, High Plains Regional Climate Center Cooperative Summary of the Day, CDMP U.S. Cooperative Summary of the Day, U.S. First Order Summary of the Day, ASOS Summary of the Day, Global Summary of the Day, International collection, Governmental Exchange Data, as well as the U.S. Climate Reference Network. The high density of the GHCN-D data provides much more data than does the more sparsely deployed USHCN or is available in the Richman–Lamb datasets. Thus, use of the GHCN-D data will contain the observations of more extreme precipitation events, thereby partially addressing the concerns of Brooks and Stensrud (2000).

The daily precipitation data in the GHCN-D record underwent rigorous quality control procedures at the NCDC to ensure data reliability. Specifically, the results from each day reporting more than five inches (127 mm) of precipitation were compared with the original manuscript forms of data, volumes of climatological data, climate record books, Monthly Weather Review, and occasionally Weekly Weather and Crop Bulletins and the Bulletin of the American Meteorological Society (Claude Williams, NCDC, 2009, personal communication). The NCDC methodology reduced the likelihood of including erroneous reports or omitting actual extreme precipitation events. More thorough descriptions of the GHCN-D dataset appear in Vose et al. (1992) and Menne et al. (2009).

Despite the many advantages of using GHCN-D data, the stations are somewhat irregularly spaced and could therefore create an artificial bias in the PCA results. Regions of high station concentrations tend to dominate a PCA, while data-sparse regions receive less

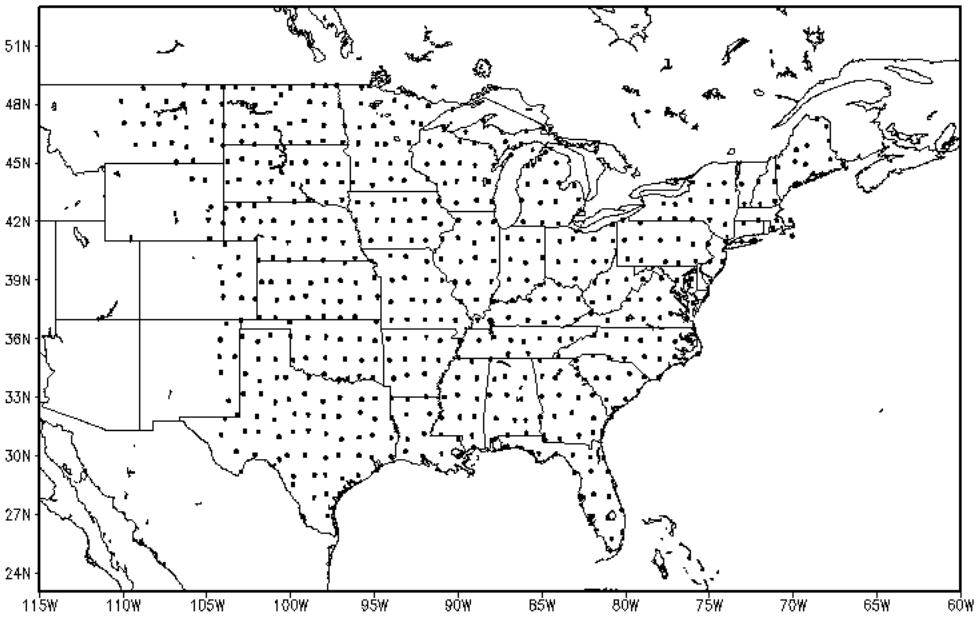

FIG. 3.1: Locations of the 576 U.S. stations from the expanded Richman–Lamb precipitation dataset.

weight (Wilks 2006). The PCA technique also requires the continuous availability of data in time, which is nearly impossible to secure in datasets from typical station observations that span a 52-year record. Most sites report some missing data due to instrument failure, human error, or other reasons at some point in the station's history.

To conduct a principal component analysis on precipitation data across the eastern two-thirds of the United States and to minimize bias in that analysis, the research in this manuscript required an evenly-spaced set of observations with no missing data during the 52-year span (1949–2000). While objective analysis techniques can be used to interpolate the observations from the GHCN dataset onto a grid (e.g., Barnes 1964, 1973; Maddox et al. 1979), this strategy would harm efforts to examine the most extreme rainfall events by reducing their intensity after the objective analysis routines 'smoothed' the extremes (Daley 1991). Fortunately, a nearly uniform grid of observed precipitation data over the time period in question already existed. RL85 developed such a dataset by selecting those U.S. Cooperative Observer Network stations and NWS first-order stations with the most complete record and located closest to a prescribed $1^\circ \times 1^\circ$ grid mesh. In so doing, the

authors created a nearly uniform array of precipitation observations (Figure 3.1). The average distance between the primary observation location and a given grid in RL85 point is 10.4 km. On days when observations at the primary site were missing, the observation from the next-closest station to the grid point was substituted for the missing observation. This approach prevented temporal gaps in the dataset. About 15% of the daily precipitation values come from secondary or tertiary station locations when data from the primary site were unavailable (Timmer and Lamb 2007).

The expanded Richman–Lamb dataset (Timmer and Lamb 2007) includes U.S. temperature and precipitation observations east of the Rockies from 1 January 1949 through 31 December 2000, and represents 52 years of evenly spaced, nearly gridded observations. The large temporal extent of the Timmer–Lamb dataset will enable a search for trends and meet the requirements for an unbiased PCA component in this manuscript. A complete description of this unique dataset appears in RL85, RL87, Gong and Richman (1995), Montroy et al. (1998), and Timmer and Lamb (2007).

The stations composing the updated Richman–Lamb dataset have an average station spacing between 80–110 km. This spatial resolution does not adequately capture many of the heaviest precipitation events that occurred during the study period–events which tended to be convective in nature and occurred on spatial scales of a few kilometers (as outlined by Brooks and Stensrud 2000). These events are better captured by the higher-resolution GHCN. However, the large timeframe of precipitation records in the Richman–Lamb data allow for a sufficient sampling of extreme precipitation events as well as heavy events that covered an extensive spatial area. Most importantly, the RL85 data can be used in a PCA to identify regions of coherent daily precipitation that can be used to study extreme rainfall events as documented in Chapters Five and Six.

An examination of the synoptic environment and dynamical forcing associated with heavy rainfall events requires a high-quality upper-air dataset. Because changes in numerical assimilation systems can affect atmospheric analyses (Kalnay et al. 1996), the National Centers for Environmental Prediction (NCEP) and National Center for Atmospheric Re-

Class	Field type
A	Zonal wind
A	Meridional wind
A	Geopotential height
A	Virtual temperature
A	Absolute vorticity
B	Vertical velocity (1000–100 hPa only)
B	Specific humidity (1000–300 hPa only)

FIG. 3.2: Data fields on standard pressure levels saved on a 2.5° latitude × 2.5° longitude grid (144 × 73; from Kalnay et al. 1996).

search (NCAR) jointly developed the NCEP–NCAR 40-Year Reanalysis (Kalnay et al. 1996) dataset. The Reanalysis Data provides atmospheric scientists and climatologists with a high-quality record of assimilated atmospheric data. The reanalysis contains an analysis and forecast of atmospheric variables from sources such as surface observations, radiosondes, ships, pibal, and satellites for the period 1948 through 2006. These data were incorporated into the NCEP global spectral model, which has a horizontal resolution of approximately 210 km and 28 vertical levels across the globe. The reanalysis contains three classes of gridded variables: *Type A variables*, such as upper air temperature, wind, and geopotential height, which were considered the most reliable variable because they were strongly influenced by observations. *Type B variables*, such as surface parameters, divergent wind, and moisture variables, were influenced by both the model itself and by the observations. On the other hand, *Type C variables*, such as precipitation and surface fluxes, were solely determined by the model and are the least reliable of the variables in the Reanalysis Data (Kistler et al., 2001). The research reported in this manuscript primarily used the first two classes of variables (Figures 3.2 and 3.3).

Fewer upper-air observations were acquired between 1948 and 1957 than during more recent periods. During the early days of NWP, upper air observations were acquired three hours before the now-standard observation times of 0000, 0600, 1200, and 1800 UTC observation times. To facilitate a comparison with upper air observations from the later years, three-hour forecasts were calculated to match the primary synoptic times of the later years

Class	Field type
B	Surface temperature
C	Skin temperature
B	2-m temperature
B	Surface pressure
D	Albedo
C	Surface sensitivity and latent fluxes
C	Top-of-the-atmosphere fluxes
B	Zonal wind at 10 m
B	Meridional wind at 10 m
C	Surface wind stress
A	Mean sea level pressure
B	Precipitable water
C	Snow depth
B	Snow cover
C	Precipitation (total and convective)
B	Mean relative humidity (multiple layers)
C	Soil wetness and temperature
C	Surface runoff
C	Cloud fraction (high, middle, low)
C	Cloud forcing, clear-sky fluxes
C	Gravity wave drag
B	Max and min temperature

FIG. 3.3: Surface flux data saved on the T62 Gaussian grid (192×94; from Kalnay et al. 1996).

(Kistler et al., 2001). Thus, the reanalysis data prior to 1958 may be of lesser quality than that available during later years, and the reanalysis data after 1979, which incorporated satellite data, may be of higher quality than its predecessors (Kistler et al., 2001). Kistler et al. (2001) also cautioned that trends estimated using the reanalysis data would be unreliable due to changes in the observing systems over the course of time. The authors suggested that it may be possible to calculate trends if the periods before and after 1979 were examined separately and if the observational rawinsonde coverage available to the reanalysis prior to 1979 was taken into account. Considering the dense rawinsonde coverage over the study domain in the eastern continental United States and areas west of the study domain, personal communication with Eugenia Kalnay, and the results of Portis et al. (2006), the reanalysis data may be useful for examining trends. The version of the reanalysis dataset used in this study made use of observations at 0000Z and 1200 UTC. Despite a few unavoidable changes in the reanalysis techniques, the reanalysis dataset provides unique analyses of the

tropospheric features. Thus, the current study of the synoptic environment and dynamic parameters associated with heavy precipitation events is uniquely enabled.

To calculate the terms on the right hand side of the quasi-geostrophic (Q-G) omega equation in terms of the geopotential field (see Appendix A), the gradient and Laplacian operators were calculated using a centered-difference finite differencing scheme between adjacent horizontal grid points. Vertical derivatives (i.e., $\frac{\partial}{\partial p}$) at the 850 hPa level used a centered differencing scheme between the 1000 and 500 hPa levels. Similarly, vertical derivatives at the 500 hPa level used a centered differencing scheme between the 850 and 200 hPa levels. The accuracy of the centered differencing scheme results is limited by the wide spacing of the observations (i.e., the reanalysis data, which may not best represent the data); this scheme will not be accurate in situations where the variable has a sharp gradient. However, the data provided in the reanalysis is limited in its spatial and vertical resolution. Thus, this differencing scheme is the best possible method of computing variables that require a spatial derivative (such as vorticity, divergence, advection, and the terms of the Q-G omega equation).

The average rainfall across the eastern two-thirds of the United States ranges from less than ten inches (254 mm) annually in arid regions of the plains to over 65 inches (1651 mm) per year near the Gulf of Mexico. The average annual precipitation during the period from 1949–2000 for the study domain (Figure 3.4) is based on the data from the expanded Richman–Lamb dataset. This map of average precipitation, though like many others published elsewhere, represent the characteristics of a dataset that was critical to the current investigation. This annual rainfall map was included to help the reader better understand the data used in this study. Across the eastern two-thirds of the United States, 35.6 inches (904 mm) of precipitation typically falls each year at the Richman–Lamb stations. The maximum average annual precipitation of 67.4 inches (1710 mm) occurred at the Sheridan Firetower in southeast Louisiana. In contrast, the minimum average precipitation of 9.83 inches (250 mm) occurred at Boquillas Ranger Station in southwest Texas during the same period.

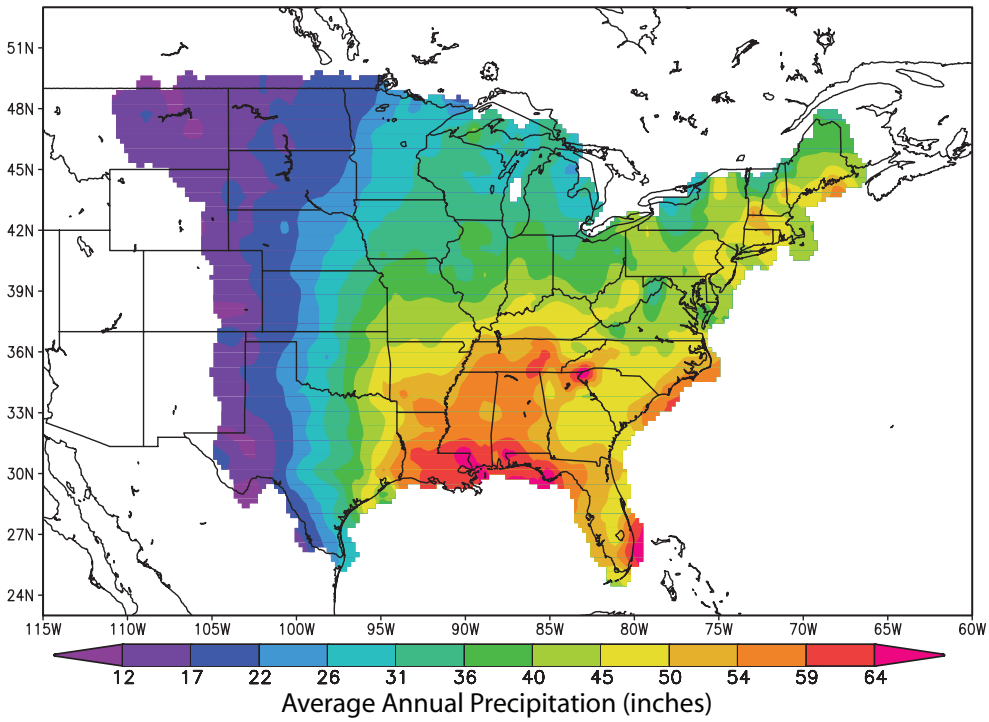

FIG. 3.4: Average total annual precipitation (inches) at the stations in the Richman–Lamb dataset shown in Fig. 3.1 from 1949–2000.

The variance of precipitation for the period 1949–2000 across the eastern two-thirds of the United States is shown in Figure 3.5. The average variance over the Richman–Lamb dataset is 0.0988 $inches^2$, which corresponds to an average standard deviation of 0.314 inches. Lower variance values occurred in the western plains, northern plains, and northern edges of the domain–areas characterized by lower average annual precipitation. The station in Rock Spring, Montana had the lowest precipitation variance (0.0157 in^2). Precipitation events that occur in regions of low variance likely have similar magnitude; fewer exceptionally large precipitation events occur in these areas than regions with higher variance. Larger variance amounts occurred along the northern coastline of the Gulf of Mexico in an area that also has some of the highest average annual precipitation totals. The largest precipitation variance ($0.3139 in^2$) occurred in Fort Morgan, Alabama, which is located on the tip of a narrow peninsula in the Gulf of Mexico. It is possible that some of the larger variance along the Gulf Coast stemmed from the irregular patterns of tropical systems, which tended to drop extremely large amounts of rainfall. Irregular but intense

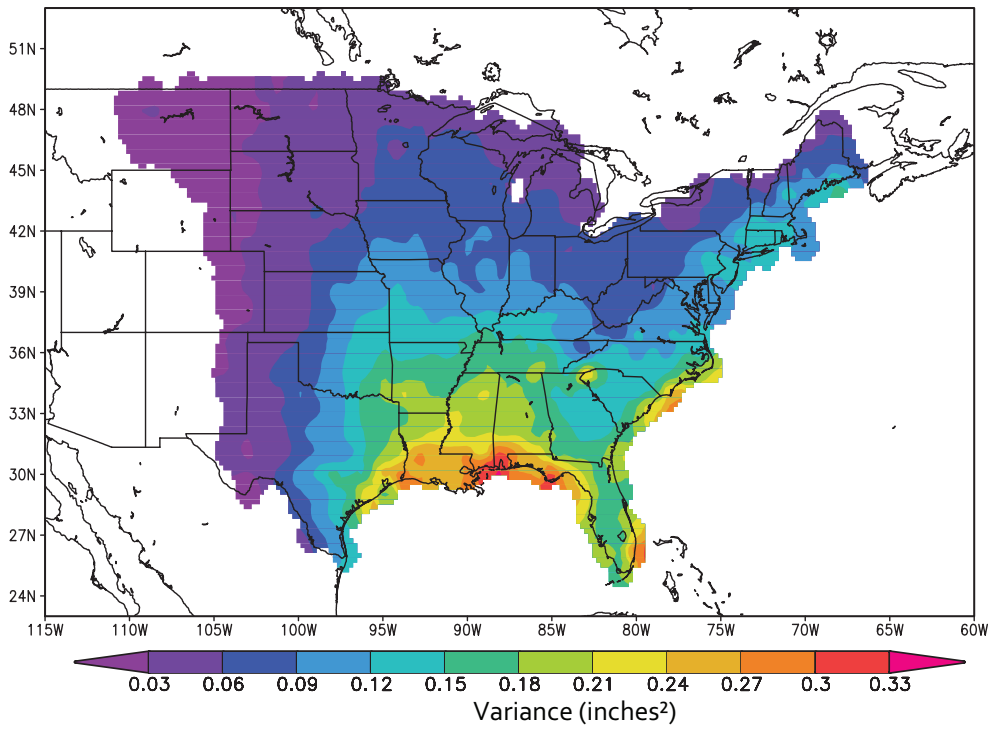

FIG. 3.5: Precipitation variance (σ^2) for the period 1949–2000 at the stations in the Richman–Lamb dataset shown in Fig. 3.1.

orographically-induced rainfall likely led to higher variance along the escarpment in the western Carolinas.

Based on an inspection of Figure 3.4, regional similarities in mean precipitation become evident. For example, an area which encompasses the central Gulf Coast states and which extends from Louisiana and parts of eastern Arkansas eastward to Georgia, the Carolinas and the Florida Panhandle received the most precipitation each year. The far western portions of the domain, in contrast, received very little precipitation. As is well known among those familiar with high impact weather across the south, strong gradients of precipitation are very evident across the southern plains and southern Ohio River Valley. They are caused partially by abrupt changes in terrain features and by the availability or non-availability of moisture. Along the Appalachian Mountains from Georgia to Maine, the topography impacts the amount of precipitation because the mountains provide enhanced precipitation via orographic lift of unstable, surface-based moist air. The terrain also limits the east-west transport of moisture. The Northeast received moderate amounts of annual

precipitation and is also influenced by terrain and proximity to the Atlantic Ocean.

Regions of similar rainfall means become apparent when one inspects Figure 3.4. For example, the southern Gulf Coast states, the northeast, the far northwest, the upper Mississippi Valley, the southeast, and the west Central Plains have similar precipitation patterns. A PCA of the daily precipitation observations will quantify the features in these general patterns; the results of the PCA are described in Chapter 4.

Chapter 4

Principal Component Analysis

4.1 PCA Technique

Principal component analysis (PCA) reduces a large number of variables in a data set to a smaller number of uncorrelated variables with the significant advantage that the variance in the original data set is retained. Some of the applications of the PCA technique to meteorological data and its usefulness for precipitation studies were discussed in Section 2.2. Longer descriptions of the PCA technique can be found in Haan (1977), Wilks (2006), and Richman (1986). A brief review of this analysis technique appears below.

A principal component analysis is represented best using a geographically uniform distribution of data to avoid a misrepresentation of data features wherein certain regions are over-sampled with numerous stations (i.e., overweighted) while other regions are under-sampled with only a paucity of data stations available (i.e., underweighted). In general, the covariance structure of the observing locations of meteorological fields has higher values in data-rich areas (i.e., stations are not evenly spaced and tends to cluster in areas of higher population density). In many analysis techniques, the data are interpolated to an equal-area grid (i.e., a Fibonacci grid or a Cartesian grid over the middle latitudes; Mercer 2008). On the other hand, the interpolation of precipitation data to any grid and by any interpolation method lessens the impact of extreme events. Because extreme precipitation events are the focus of this study, an alternative is to use observation sites near grid points to approximate

a gridded dataset without modifying the original rainfall data. The Richman–Lamb dataset, described in Chapter 3, provides a set of near-gridded rainfall observations that is of sufficient spatial homogeneity to minimize this bias. The Richman–Lamb data also contains no missing observations, a second requirement for PCA.

Most often, PCA is applied to either the correlation (**R**) or covariance (**S**) matrix of the original data. A PCA on the covariance matrix removes the mean of the data and accentuates the anomalies with the largest variance, those areas with high spatial variability in the observations. In contrast, a PCA on the correlation matrix analyzes the standardized anomalies of equally weighted data to examine the joint variance structure of the precipitation data. For example, if every variable had a variance equal to 1.0 in a correlation matrix, the joint variance structure would be represented by the off-diagonal similarities that are decomposed. This method identifies patterns of data similarity and is appropriate for the detection of spatial precipitation patterns. A PCA of the correlation matrix also is the preferred analyses tool when the data set contains variables from a wide range of sensors, each using different units (e.g., temperature data with precipitation observations) because the data are first standardized (Wilks 2006).

The PCA is conducted in an S-mode analysis to associate the stations with time periods for a single parameter, such as precipitation (RL85; Compagnucci and Richman 2007). In the current analysis, the eigenvectors represent spatial patterns of a single field (i.e., precipitation). Following the notation of Wilks (2006), let **X** represent the data matrix of dimensions $n \times k$, where n denotes time and k the variable index (i.e., the number of stations). The standardized data vectors z, are given by

$$z = \frac{x - \overline{x}}{\sigma}, \tag{4.1}$$

where $\overline{x}$ represents the mean of the variable (the mean value of each station's precipitation averaged across the entire dataset) and σ the standard deviation of data from each station.

The standardized data vectors z are used in the correlation matrix **R**, such that

$$\mathbf{R} = \frac{1}{n-1}(\mathbf{Z}^T\mathbf{Z}) \tag{4.2}$$

and represents the variance-covariance matrix of the standardized data matrix, **Z**. The eigenvalues (λ) of the correlation matrix are used in the following equation to calculate the eigenvectors e_k:

$$(\mathbf{R} - \lambda\mathbf{I})e_k = 0, \tag{4.3}$$

where **I** is the identity matrix. The full matrix of eigenvectors **E**, when weighted by the diagonal matrix of the square roots of the corresponding eigenvalues ($\mathbf{D^{0.5}}$, sorted in descending order) generates the PC loadings, **A**:

$$\mathbf{A} = \mathbf{E}\mathbf{D^{0.5}}. \tag{4.4}$$

The $k \times k$ principal component score matrix **U** is given by

$$\mathbf{U} = \mathbf{Z}\mathbf{A}(\mathbf{A^T}\mathbf{A})^{-1}. \tag{4.5}$$

The first PC points in the direction of maximum variance of all the variables, the second toward the second-highest variance, and so forth while each is orthogonal to all of the others. Typically, data reduction is a goal of PCA and the matrix of PC loadings has a certain number of columns discarded. Those columns are associated with the smallest eigenvalues, thought to represent noise. The orthogonality property of the eigenvectors tends to result in a set of predictable spatial patterns. If such orthogonality in space is deemed undesirable or if there is theory to explain why subsets of variables should cluster together, then a transformation can be applied to the PC loadings to rotate them into a new reference frame that explains such localizations in the variance field. As described in Section 2.2, rotated PC loading vectors are unaffected by the domain shape and reproduce

the clusters of data from the correlation matrix when such clusters are present. Spatial studies of atmospheric data may benefit from rotation by enabling the identification of subsets (subregions) of the data. Although rotations complicate the analysis somewhat, the benefits from improved pattern recognition and the release from dependence on the domain's shape outweigh the increased computational complexity.

The retained PCs are rotated using a Varimax rotation (Kaiser 1958; Boone 2010), the most widely used orthogonal rotation (Richman 1986). The Varimax rotation iteratively seeks to maximize the sum of the variances of the squared rotated eigenvector elements (Wilks 2006) to simplify each PC loading vector so that it isolates a highly correlated subset of the variables. This iteration causes the rotated PCs to differ depending on the number of PCs retained. Consequently, care must be taken with proper selection for component truncation prior to rotation.

The rotated PC loading vectors $\widetilde{\mathbf{A}}$ can be represented by the linear transformation of m of the original k PCs:

$$\widetilde{\mathbf{A}} = \mathbf{A}\mathbf{T}^{-\mathbf{1}}, \tag{4.6}$$

where $\mathbf{A}$ and $\widetilde{\mathbf{A}}$ are $k \times m$ matrices, but the orthogonal transformation matrix $\mathbf{T}$ is an $m \times m$ matrix. The new rotated PC loadings, $\widetilde{\mathbf{A}}$, are used to calculate the new rotated principal component scores ($\widetilde{\mathbf{U}}$; e.g., Eq. 4.5). Both $\widetilde{\mathbf{A}}$ and $\widetilde{\mathbf{U}}$ will be shown.

4.2 PCA Results

S-PLUS, a statistical software package (Insightful Corporation 2007), was used to perform the calculations necessary to complete a PCA of the Richman–Lamb dataset. Prior to rotating the PCs, a decision must be made on the number of components to retain. Although retaining all PCs would recreate the original dataset, it is neither necessary nor beneficial to retain all 576 components to describe rainfall patterns at 576 stations as the higher-order PCs (those associated with the smallest eigenvalues) are thought to be associated with random and meteorological noise. The first goal of the current research is to identify coherent

regions within the rainfall signal. Due to the geographical locations and synoptic environments of the regions, the heaviest rainfall events in each region will vary in magnitude and by season of occurrence. Successfully identifying these coherent regions will be used to help meet the second goal of this research, which is to examine the atmospheric environment associated with major precipitation events from each region and search for large-scale trends in the 60-year dataset. Consequently, relatively few PCs need remain.

Several methods provide general guidance for estimating the truncation point for PC retention. The scree test (Cattell 1966) narrows down potential cutoff values to 12 or 15 retained components (Figure 4.1), while the LEV test suggests retaining 10, 14 or 18 components (not shown). The estimated sample errors on the eigenvalues, employing North's test (North et al. 1982), also are shown in Figure 4.1. Because the sample size in North's test assumes independent samples, the effective sample size was determined by examining the autocorrelation function. At lag 8, the correlation was no larger than white noise. Despite their nomenclature, these screened LEV tests are really rules of thumb. They do not provide quantitative statistical guidance; instead, they involve subjectivity. Nevertheless, these tools can be used for some clarification of the otherwise ambiguous PC results. The scree and LEV plots suggest a starting approximation of about 12 PCs to experiment with different rotation methods. As described in Section 4.1, the Varimax rotation is appropriate for use with time series of spatial precipitation data measured within a network of stations. Accordingly, the Varimax rotation provides rotated PC loadings with the highest (absolute) magnitude in locations where the greatest correlations between the stations exist.

Calculating PC loading congruence coefficients (RL85) provides guidance about potential cutoff points for PC retention. Using the Varimax rotated PCs with the correlation matrix, Figure 4.2 shows a box-plot of the congruence coefficients (i.e., RL85) between the rotated PC loadings and the correlation match vectors. The green bar represents the upper and lower quartiles, the upper and lower whiskers show the highest and lowest coefficients, respectively, the white line shows the median value, and the red line shows the median of 13 PCs. Based on this plot alone, the results suggest retaining 9 PCs due to the highest co-

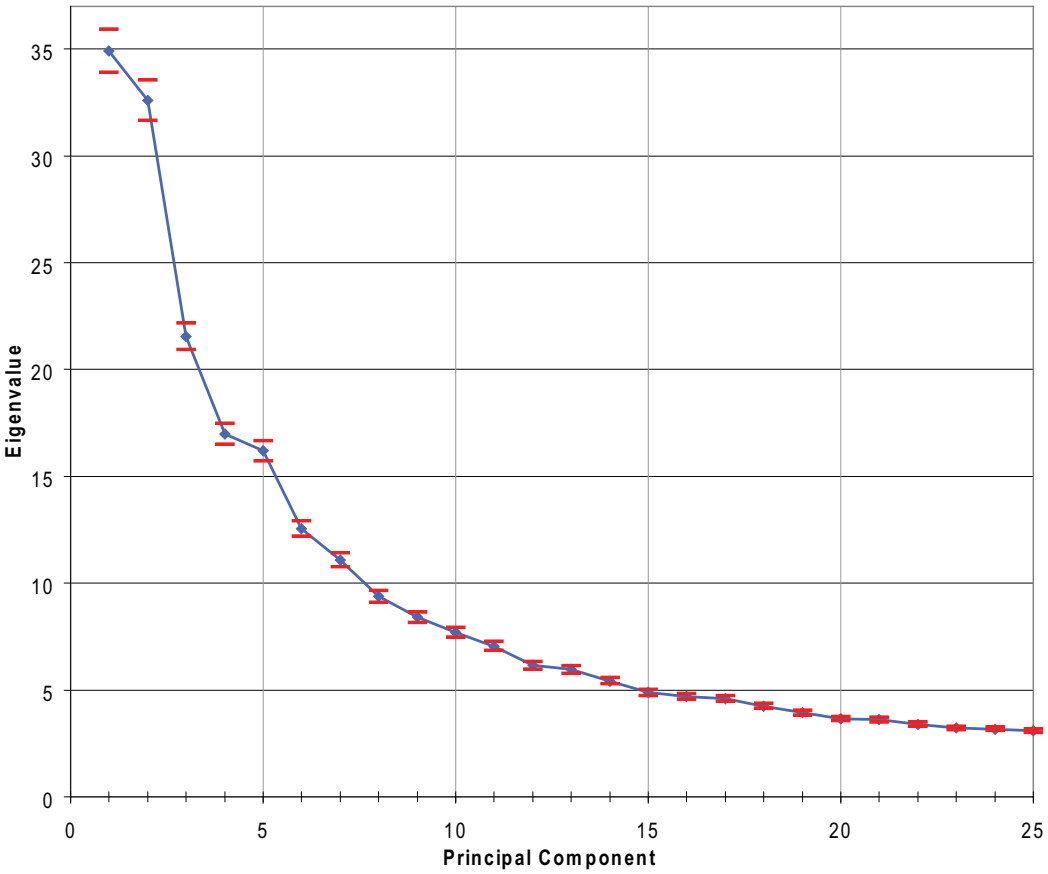

FIG. 4.1: Scree Test of the correlation matrix eigenvalues for the first 25 principal components shown with the corresponding sampling error markers (red; North et al. 1982).

efficient values (all congruence coefficients > 0.89), while 13 PCs has a higher coefficient median.

The retention of only six, nine, ten or eleven components does not sufficiently capture the variability of precipitation across the eastern two-thirds of the Continental U.S. (see RL85). With only six components retained, over 40% of the stations have a maximum loading value below 0.4. This value drops to nearly 30% for nine retained PCs, 28% for 11 PCs, and 14% for 18 retained components. Although 21% of stations have a maximum loading value below 0.4 when 13 components are retained (Figure 4.3), less than 10% of all stations have a maximum loading below 0.35 (Figure 4.4). The percent variance explained by the retention of 6, 9, 10, 11 and 13 PCs is shown in Table 4.1. Thirteen retained PCs

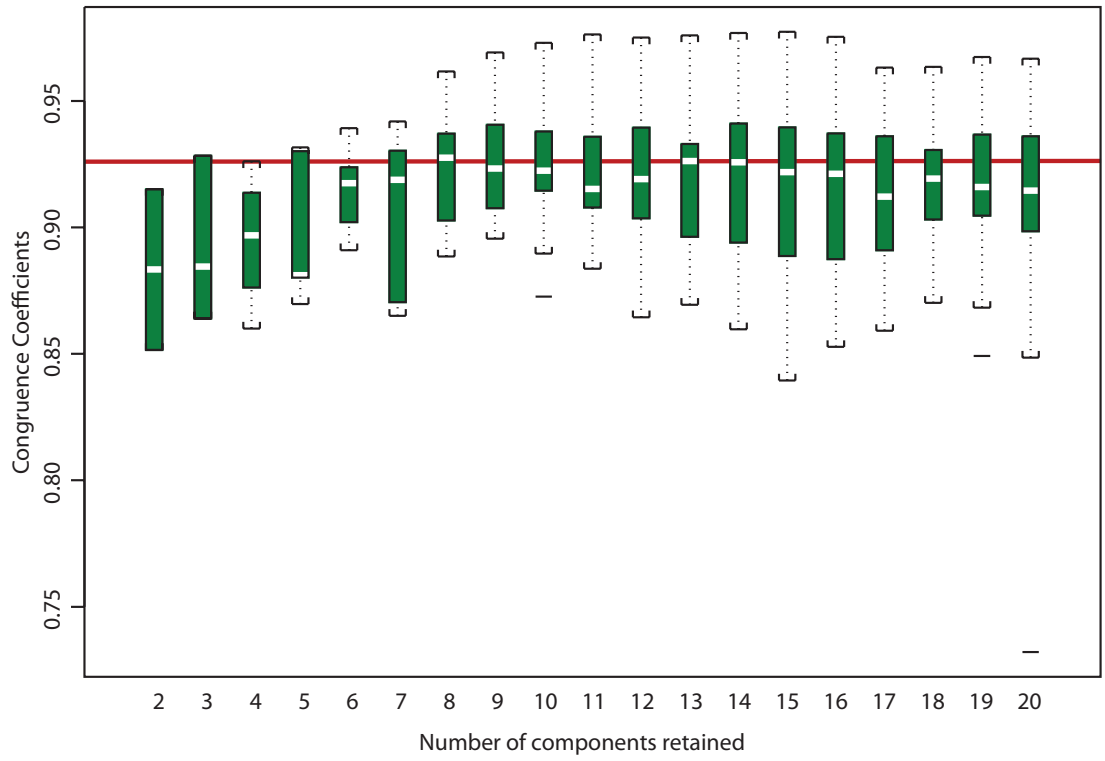

FIG. 4.2: Boxplot of the congruence coefficients between the retained PCs and the correlation matrix values at the stations with the maximum loading for that PC. The short white lines indicate the median value of the retained PCs and the long horizontal red line (at 0.925) indicates the median value of 13 retained PCs.

explain more variance than did fewer principal components; this percentage increases with additional retained PCs. However, the retention of more than 13 components appears simply to subdivide existing areas (Figures 4.4 and 4.5), yields diminishing return, and does not contribute improvements to the congruence values. The noise level of the higher order PCs with very small eigenvalues is thought to represent white noise. Consequently, the selection of thirteen components is most logical from both a physical and statistical point of view.

Interestingly, the 0.35 loading isopleths of the 13 retained PCs (Figure 4.4) bear a strong resemblance to those shown in RL85 (Figure 4.6). The primary differences are the more irregular boundaries of the current results and the smaller size of the components centered over the west Texas panhandle and southern Texas. These differences likely result from a disparity between the study periods (summer versus annual and 3-day versus 1-day rainfall

TABLE 4.1: Percent variance explained from each Varimax-rotated principal component for different numbers of retained components using the daily Richman–Lamb precipitation data from 1949–2000.

PC Number	6 PCs	9 PCs	10 PCs	11 PCs	12 PCs	13 PCs
1	3.93	3.03	2.86	2.75	2.57	2.37
2	4.17	3.03	3.04	3.12	3.07	3.03
3	3.37	3.51	3.26	2.36	2.24	1.72
4	3.68	2.79	2.84	2.80	2.02	2.03
5	3.96	3.07	2.83	2.57	2.44	2.69
6	4.28	2.65	2.33	2.04	1.94	2.11
7		3.52	3.07	3.04	2.97	2.85
8		3.14	3.01	2.97	2.76	2.61
9		3.67	3.73	3.67	3.19	3.07
10			2.79	2.68	2.48	2.57
11				2.98	3.41	3.34
12					2.94	2.35
13						2.33
Total Variance	23.40	28.41	29.75	30.97	32.04	33.07

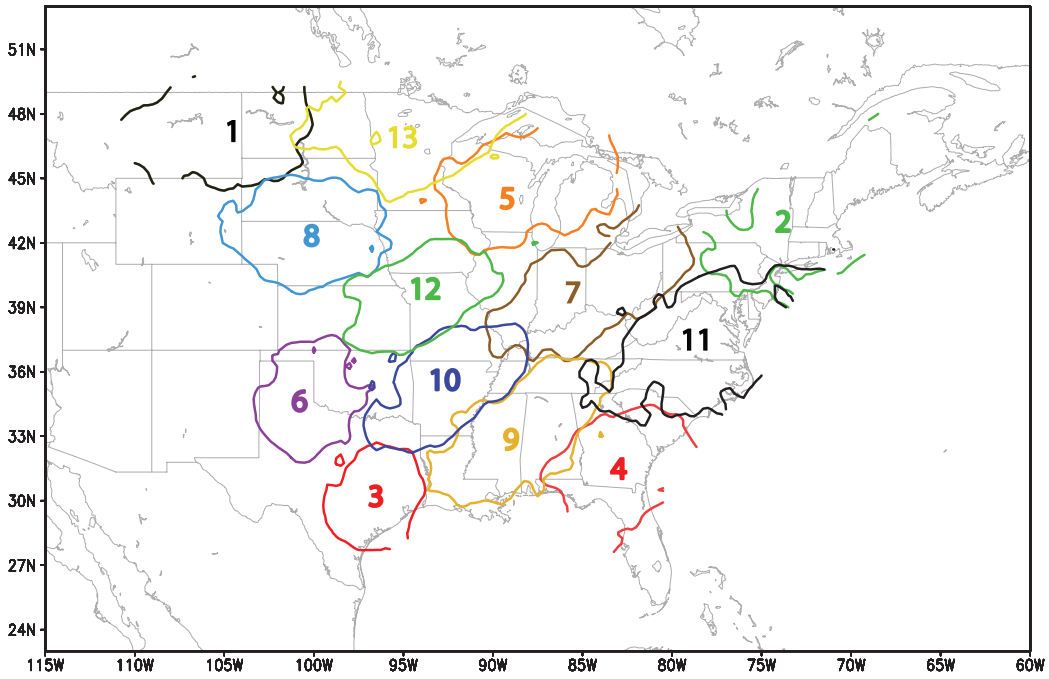

FIG. 4.3: Regionalization of the eastern and central United States for one-day annual rainfall on the basis of the Varimax-rotated PC patterns along 0.4 loading isopleths. Thirteen PCs were retained.

totals, respectively). The similarities suggest that short-term rainfall events less than 24 hours in duration may play a significant role in summer rainfall over much of the central United States, excluding Texas. Summer rainfall, in turn, may influence substantially the annual precipitation patterns in these regions. Alternatively, perhaps precipitation patterns do not shift notably from season to season. The distribution of precipitation by season is

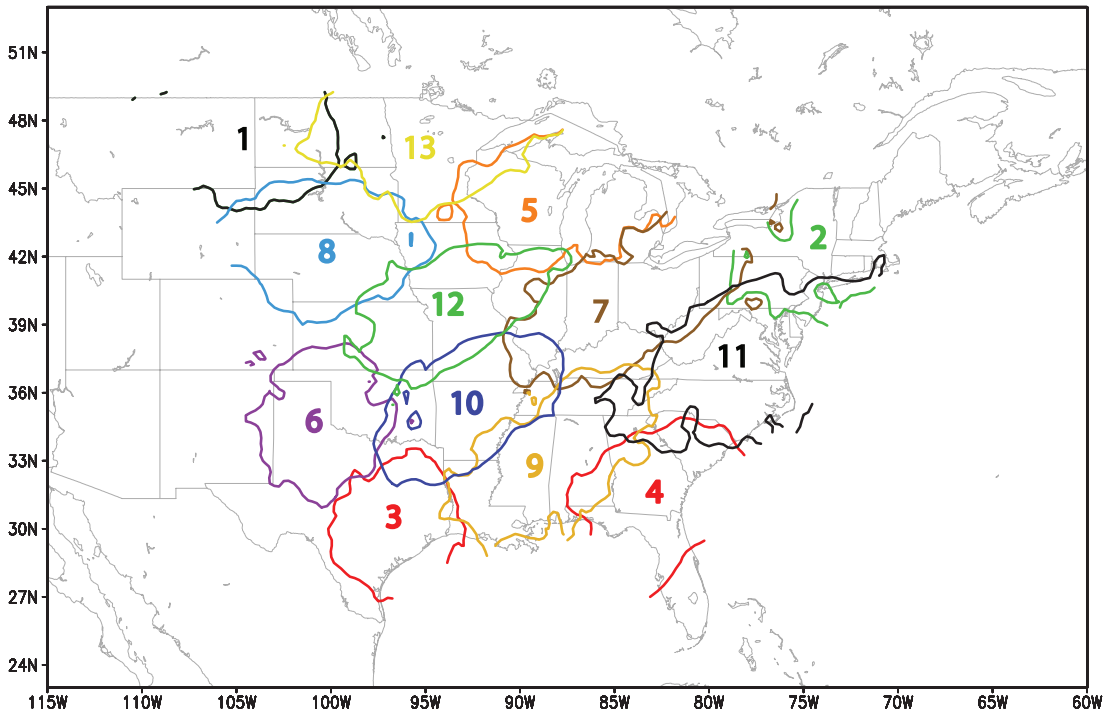

FIG. 4.4: As in Fig. 4.3, but with components numbered and identified along 0.35 loading isopleths. Thirteen PCs were retained.

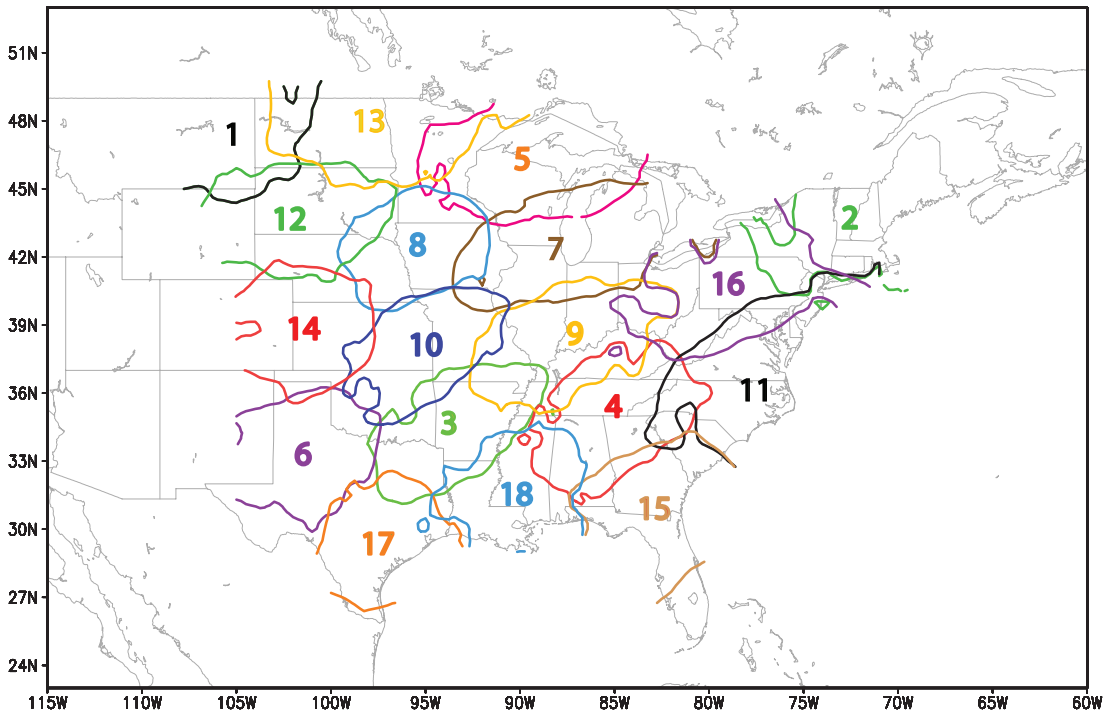

FIG. 4.5: As in Fig. 4.3, but with 18 retained PCs identified along 0.35 isopleths.

described in Chapter Five.

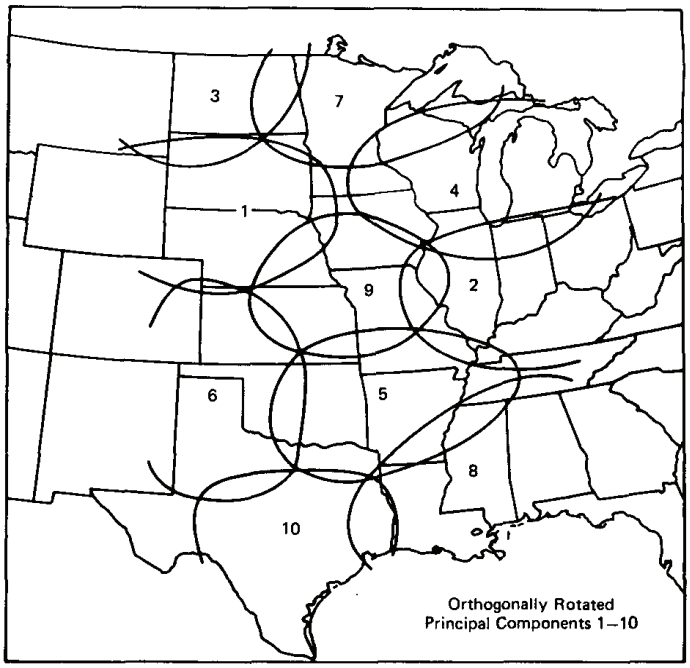

FIG. 4.6: Regionalization of the central United States for three-day 1949–1980 summer rainfall on the basis of the Varimax-rotated PC patterns along 0.4 loading isopleths (from RL85).

To determine the efficacy of the Varimax PC rotation, pairwise plots of select principal components were examined (Figure 4.7). These plots compare the magnitude of the loadings for each station against two PCs simultaneously by plotting the loadings of one PC on the horizontal axis and the other on the vertical axis. Such plots show clusters of stations and the degree of local maximization of the precipitation variation, known as simple structure (Thurstone 1947; Richman 1986). Strong simple structure shows clusters of stations appearing along the axes of each PC and near the origin, whereas data with weak simple structure appear scattered and have moderate loading values for both PCs (e.g., Richman 1986). Whereas the results with strong simple structure identify subsets (or subregions) in the data, results with weak simple structure may indicate poorly defined subregions and the failure of the Varimax rotation to capture a simple structure for the dataset studied. In the latter instance, a different and non-simple-structure rotation, such as Procrustes target rotation, may produce more meaningful results (Richman 1986).

For the present study, the simple structure plots of two non-neighboring PC regions,

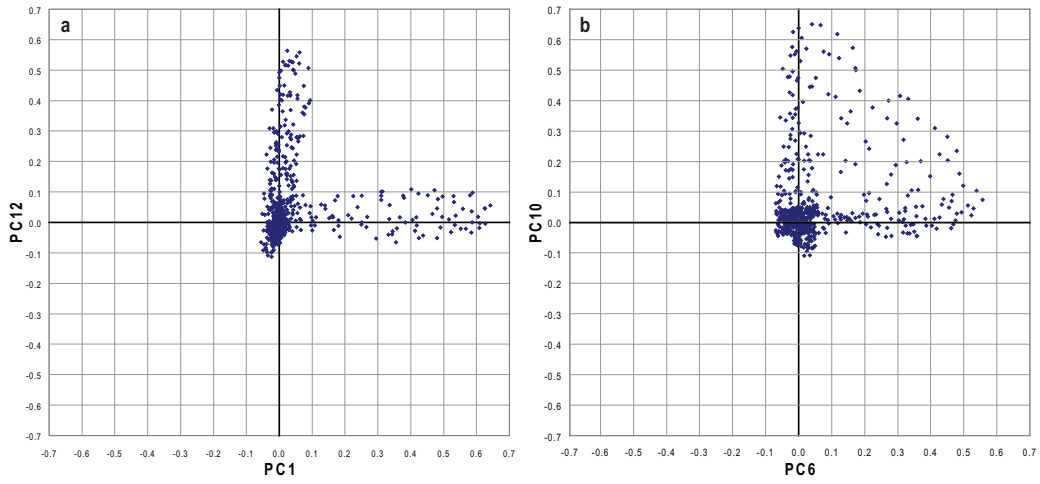

FIG. 4.7: Plots of rotated principal component loadings from a) PCs 1 and 12 and b) PCs 6 and 10 based on the regions shown in Fig. 4.4. Fig. a) shows strong simple structure from two non-adjacent regions and Figure b) shows moderate simple structure results from two adjacent regions in the southern Great Plains.

such as PC 1 in the northwest portion of the domain and PC 12 in the central U.S. (see Figure 4.4), the loadings generally follow the axes that have secondary PC loading values less than 0.1 (Figure 4.7a). These strong simple structure results make physical sense due to the significant geographic separation between the components. However, somewhat more complex results appear in the comparison of neighboring components such as PC 6 and PC 10 (Figure 4.7b). Some loadings (representing individual stations) are more complex and contribute to both PCs. These moderate simple structure results are expected in that the components have a geographical overlap (Figure 4.4). Because precipitation systems do not follow firm geographic boundaries, neither do patterns derived from the variance structure of that precipitation. Results with weak structure do not appear in this study, even when comparing overlapping PCs that were isoplethed at 0.35.

Inspection of Table 4.2 reveals that the combination of the first 13 of the 576 total unrotated PCs accounts for 33.1% of the total station variance. Although the contributions from the individual components vary substantially, the exact same amount of variance is explained by the first thirteen rotated Varimax PCs. This is due to the orthogonal transformation matrix of the Varimax rotation that preserves the uncorrelated properties of the PC scores. Given the large number of data points and the short time scale of the rainfall

TABLE 4.2: Results from the unrotated and Varimax-rotated principal components for 24-hour precipitation observations for all stations in Figure 3.1 from 1949–2000. The PC numbers in Figure 4.4 correspond with the numbered components given here.

PC Number	Unrotated % variance	Cumulative unrot. variance (%)	Varimax % variance	Cum. Var. variance (%)
1	6.06	6.06	2.37	2.37
2	5.66	11.72	3.03	5.40
3	3.74	15.46	1.72	7.12
4	2.95	18.41	2.03	9.16
5	2.81	21.22	2.69	11.84
6	2.18	23.40	2.11	13.95
7	1.92	25.33	2.85	16.81
8	1.63	26.95	2.61	19.41
9	1.46	28.41	3.07	22.48
10	1.34	29.75	2.57	25.05
11	1.22	30.97	3.34	28.39
12	1.07	32.04	2.35	30.74
13	1.03	33.07	2.33	33.07

observations, these results are expected. The results for the variance explained across the total domain compare well with those of RL85, who explained 35–44% of the joint variance in 3-day rainfall (a less noisy dataset than 1-day rainfall) with 10 components (out of 402 PCs). The relatively even distribution of the variance explained by each of the 13 Varimax PCs (Table 4.2) confirms the method's ability to identify independent and coherent precipitation patterns.

Choosing an appropriate cutoff value of the PC loadings (i.e., 0.3, 0.35, or 0.4) significantly impacts the quality of the analysis results. If the cutoff value is set too high, important precipitation signal information may be lost. However, including those loadings with a very weak signal may result in using information from those PCs that are not optimally aligned with data clusters, relationships or sampling variability (Richman and Gong 1999). Thus, it is important to select a loading cutoff value that extracts the maximum amount of useful information from the precipitation correlation matrix (Richman and Gong 1999). The number of stations excluded from the cutoff provides insight into the amount of potentially relevant data ignored or those stations at which the precipitation patterns are different from those of the surrounding classified regions. The latter is often due to a large distance from the region's center.

The PC scores provide insight into the influence of individual precipitation events on the PC region categorization. Those dates with a high PC score represent precipitation

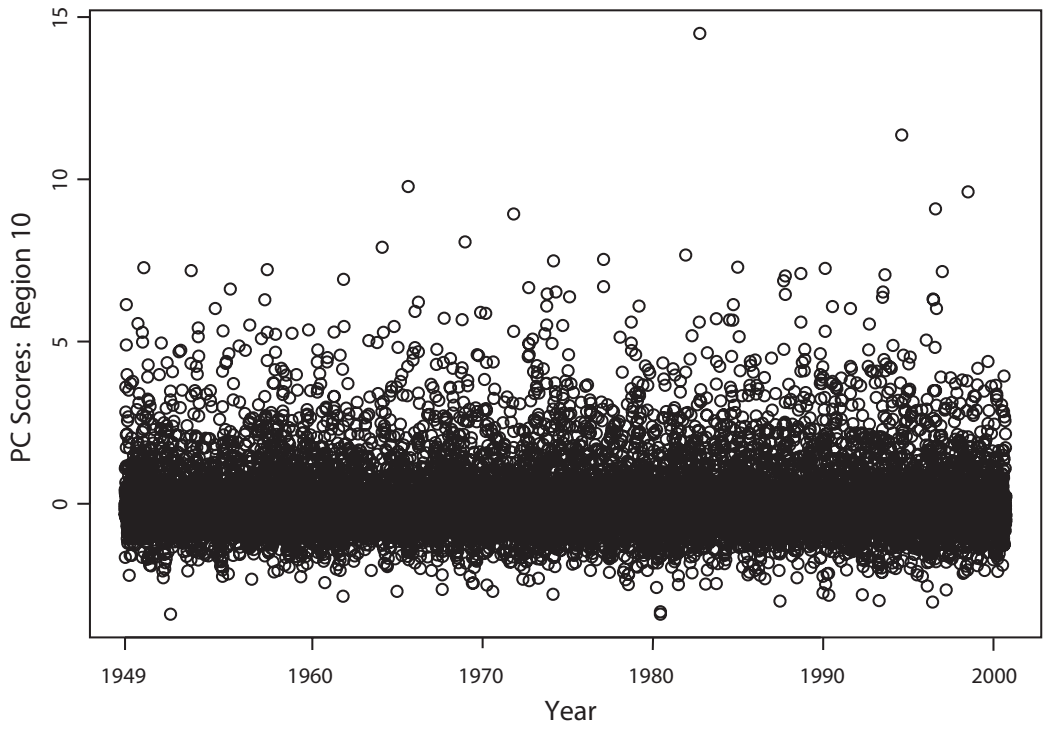

FIG. 4.8: Principal component scores from region 10 shown in Fig. 4.4 from 1949–2000.

events that significantly influenced the definition of the associated PC region. A set of PC scores from region 10 (eastern OK, AR, and southern MO) from 1949 through 2000 is shown in Figure 4.8. In this figure, the event with the highest PC score (14.49) occurred on 3 December 1982. A plot of precipitation from 3 December 1982 is shown in Figure 4.9. Precipitation was measured at nearly every station in Region 10, giving it a high PC score for this region. On this day, 357.1 mm (14.06 inches) of precipitation was measured at Big Fork, Arkansas, which was one of the largest 20 unique 24-hour events (significant events) described in Section 5.1.2.

Because the PCA used data through 2000, those events from 2001 through 2009 are not included. Thus, the PC scores would not reflect the biggest and most meaningful events between 1949 and 2009. Additionally, fewer than half of the 13 events with the highest PC score in each region appeared in the top 20 unique heavy precipitation events (260 significant events) in each region. This is because precipitation events with a high PC score typically affected much of the region and are not necessarily extremely large events (which

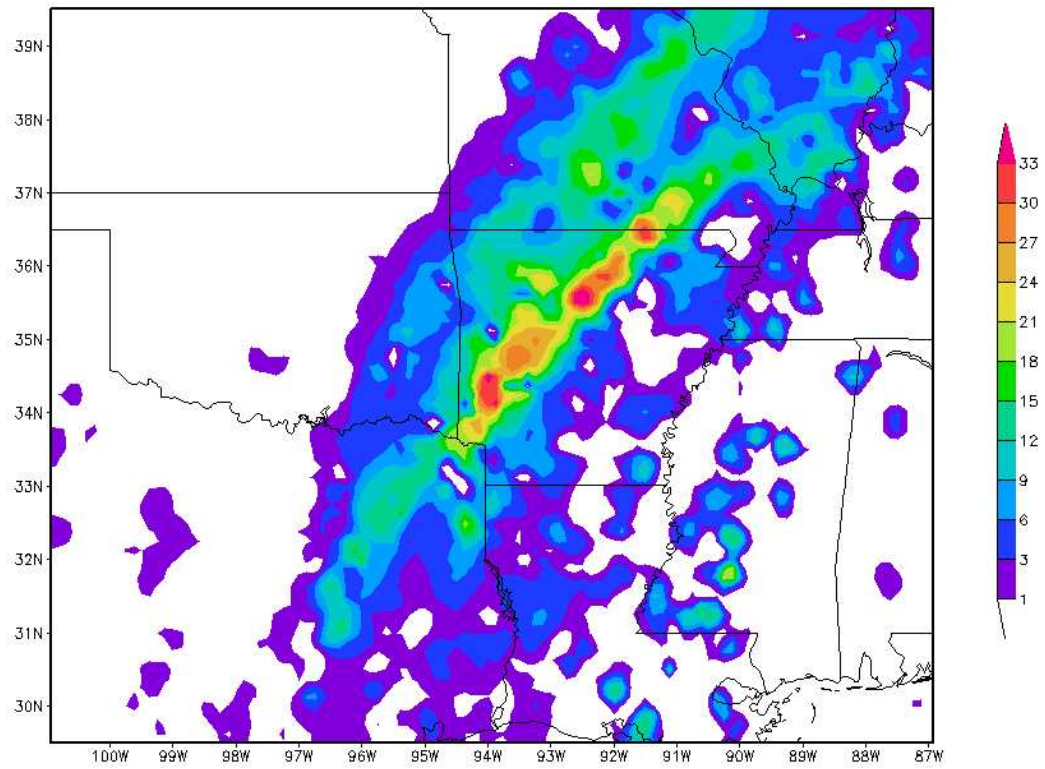

FIG. 4.9: Precipitation (centimeters) on 3 December 1982 in PC Region 10.

usually occur over a very small area). Events occurring across the border of neighboring PC regions likely would have weak PC scores if the event did not affect most of one region. Due to these issues, the current study did not use PC scores to identify extraordinarily large precipitation events.

The 13 orthogonally rotated components encompass most of the study domain and each PC identified a distinct area of spatially coherent precipitation (Figure 4.4). The regions were relatively similar to one another in area and in the magnitude of the loading coefficients. The simple structure, as illustrated in the data cloud by the Varimax criterion (e.g., Figure 4.7), represents very little station variance outside the area that is contoured. Because relatively little overlap existed between PC regions, only 15 stations have a loading > 0.4 in more than one region and none had loadings above 0.4 in more than two regions. Fifty-six stations possessed a maximum loading below 0.35, while only six stations were below 0.2 for all 13 PC regions. These six stations were located in southern Florida, a peninsula that contained relatively few observations and which were far removed from the

nearest coherent rainfall pattern centered over southern Georgia. Each station was classified into the principal component for which it possessed the highest loading. Overall, the Varimax rotation of 13 principal components subdivided the eastern two-thirds of the Continental U.S. into regions of coherent rainfall patterns. These 13 unique regions will be used in the following chapters of this dissertation to analyze heavy and significant precipitation events based on event definitions.

4.3 Seasonal Reanalysis Results

To see if the PCA results revealed a seasonal dependency, a PCA was conducted on all precipitation data in the Richman–Lamb dataset by warm season (April through September) and by cool season (October through March). The cool season PCA had very similar patterns to the PCA of annual precipitation data, although the cutoff for the number of the number of PCs to retain was somewhat ambiguous. The highest congruence coefficient mean occurred when 9 PC regions were retained (13 retained PCs had the second-highest mean; Figure 4.10), but the number of unclassified stations (those with a maximum loading under 0.4) was 2.5 times larger for 9 PC regions than for 13 PC regions. Consequently, 13 PC regions–from the cool season events–could be justifiably retained; these results were similar to those determined from the annual PCA.

The warm season results were not clear-cut. The congruence coefficient values, which ideally would decrease after the optimal number of retained PCs, formed a wide plateau between 12 and 19 retained PCs, then progressively decreased beyond 19 (Figure 4.11). The number of unclassified stations increased sharply when the number of PC regions exceeded 17, ruling out a cut-off point greater than 17. The retention of 13 PC regions provides the highest median congruence coefficients and moderate variability. A map of the loadings for 13 retained PCs (Figure 4.12) shows very similar results to the annual results (Figure 4.4). However, due to the plateau in the congruence coefficient values, it was difficult to determine a definitive cutoff point for the number of PCs to retain for warm-

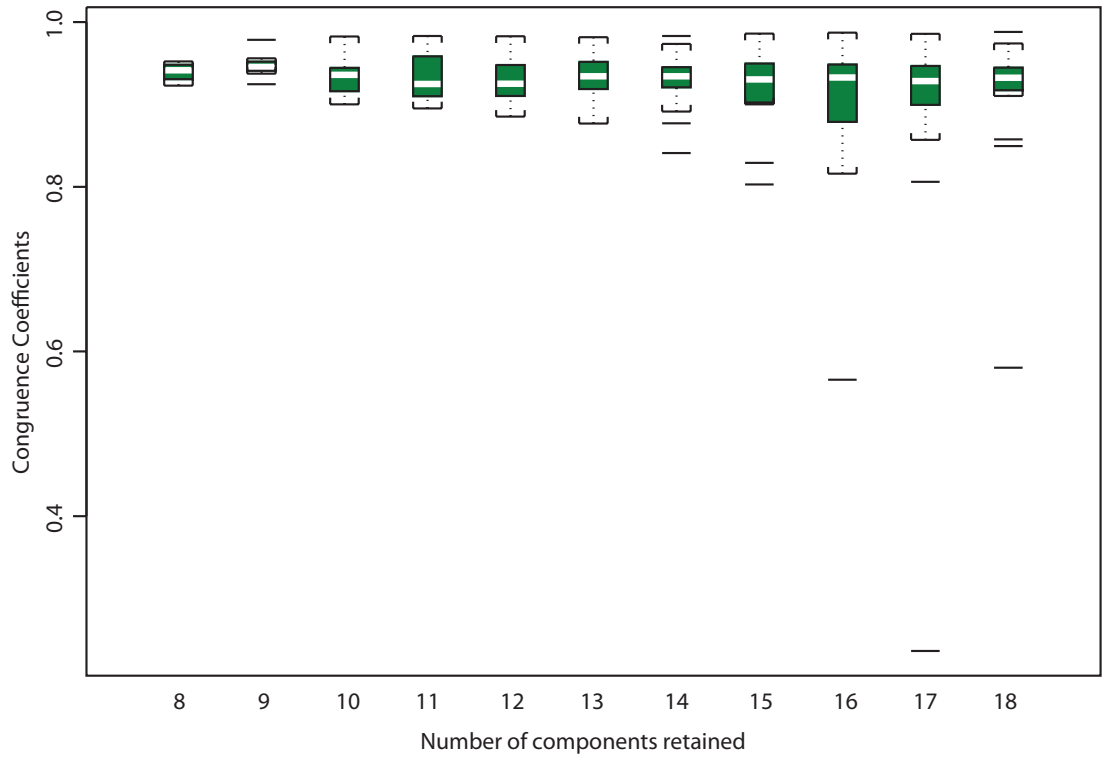

FIG. 4.10: As in Figure 4.2, but boxplots of cool-season congruence coefficients. Boxplots of 19 and 20 components are not shown due to their low values.

season precipitation events. Therefore, 13 is deemed to be a convenient number of PCs to retain; these 13 regions will be used to develop the synoptic climatologies and evaluate the dynamical forces to be reported in Chapters Five and Six.

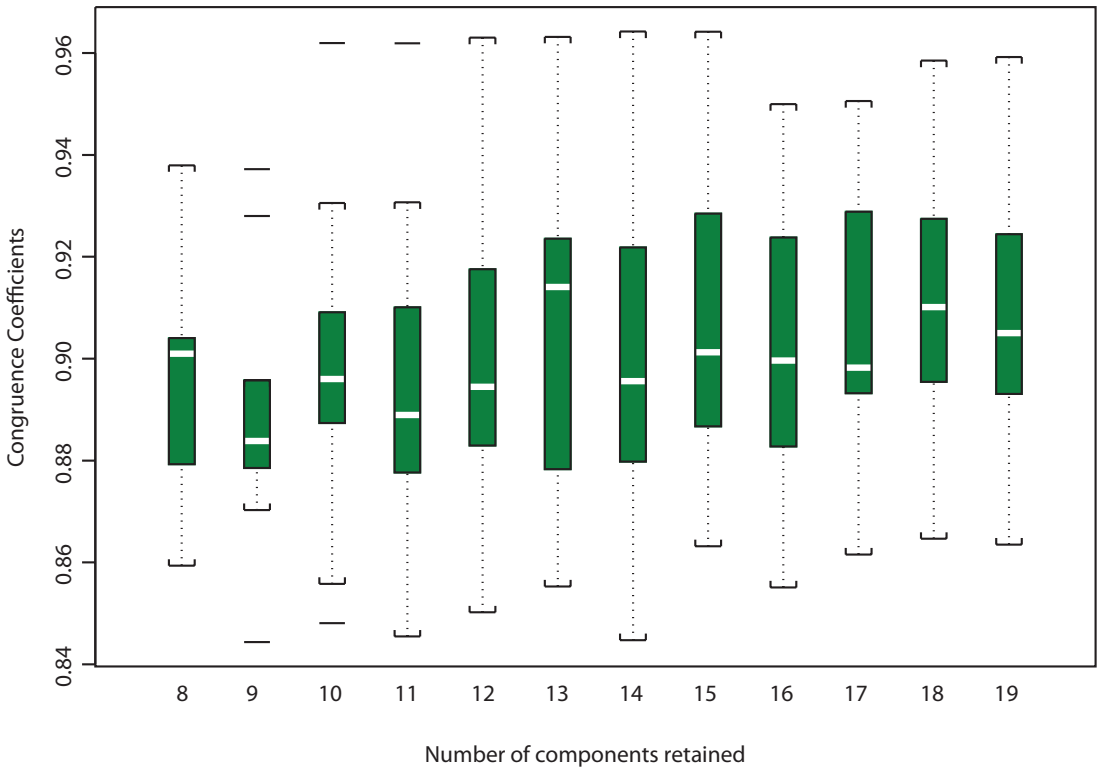

FIG. 4.11: As in Figure 4.2 but for warm-season congruence coefficients. The boxplot of 20 components is not shown due to low values.

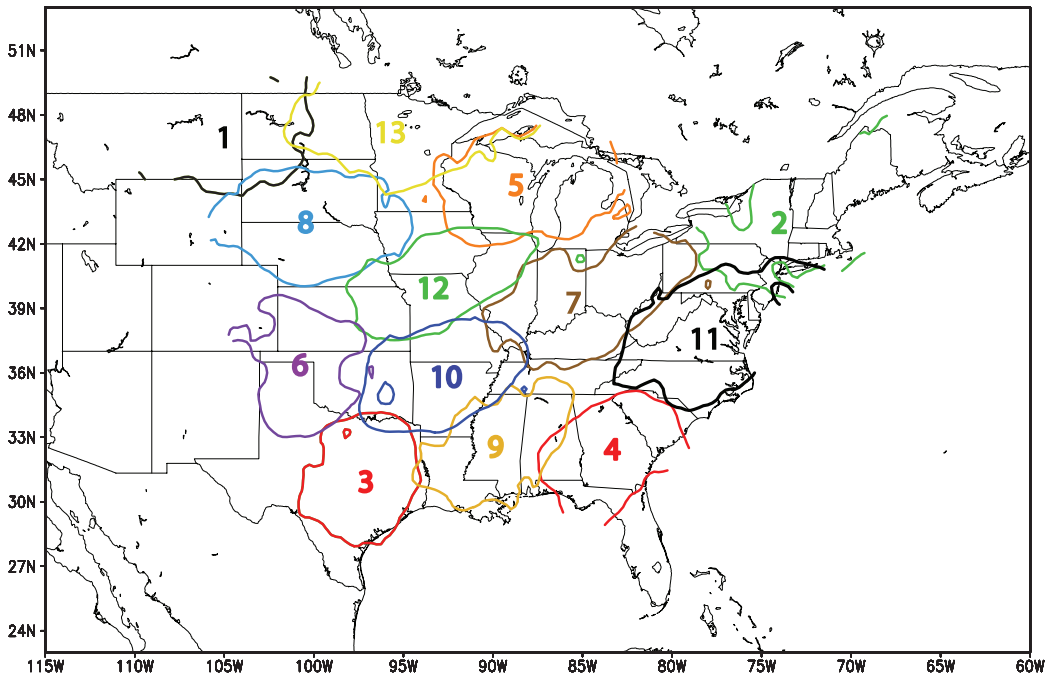

FIG. 4.12: As in Fig. 4.4, but for 13 retained PCs from warm-season precipitation data.

Chapter 5

Precipitation Events

5.1 Precipitation Data

As described in Chapter 3, the GHCN-D precipitation dataset provides daily observations from thousands of stations across the Continental U.S. However, only those GHCN-D stations within the same domain as the Richman–Lamb data were of interest in this study. Thus, only those GHCN-D stations located within 85 km (52.8 miles) of the primary stations used in the Richman–Lamb dataset were selected. The cutoff length of 85 km is slightly larger than half the average diagonal distance [157 km (105.6 miles)] between Richman–Lamb grid points (Figure 5.1). While the GHCN-D stations within the Richman-Lamb domain were selected, those stations more than 85 km west of the domain were elminated.

Of the remaining 15,100 GHCN-D stations coinciding with the Richman–Lamb domain, not all provided sufficient temporal coverage to detect trends in the precipitation data. In addition, those stations missing 10% or more of the possible daily observations during the period January 1950 to December 2009 were discarded from the current study (cf. Kunkel et al. 2003). The remaining stations (i.e., those not discarded or were missing more than 10% of their station observations) were associated with a principal component region (Figure 4.4) based on the region identification of the closest Richman–Lamb station. Although it is likely that many extreme precipitation events were excluded by removing sta-

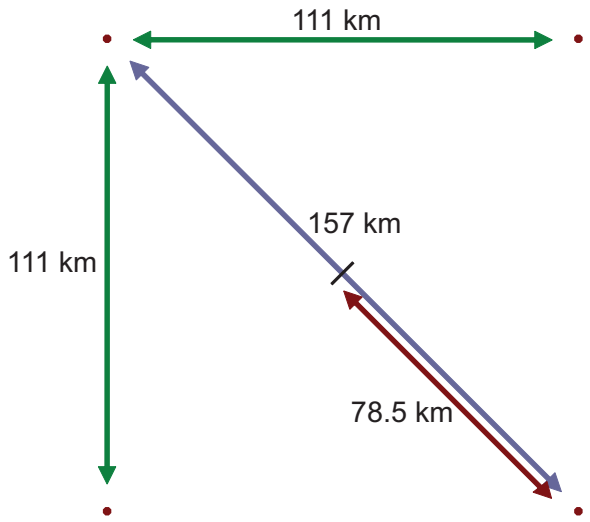

FIG. 5.1: Average station spacing of the Richman–Lamb primary stations. The average distance from one grid point to the center of their grid is 78.5 km (48.8 miles), slightly less than the 85 km (52.8 miles) distance cutoff used for GHCN-D stations located near Richman–Lamb primary sites.

tions, selecting stations with long-term data records permitted the identification of trends in the data. These quality control measures reduced the study data set to 2978 GHCN-D stations with $\geq$ 90% of the precipitation observations archived for the study period. The location of the remaining GHCN-D stations (Figure 5.2) are colored by the associated PC region as shown in Figure 4.4. These stations are relatively densely spaced. Only a few regions have relatively sparse data coverage; these regions include northern Maine, southwest Texas, northwest Nebraska, northern Minnesota, south Florida, and a few others.

5.1.1 Heavy Rainfall Events: Top 10% and Above 1 inch (25 mm)

Of the 2978 GHCN-D stations with $\geq$ 90% of the data available between January 1950 and December 2009, the daily non-zero precipitation values were ranked from lowest to highest in magnitude. At each station, the top 10% of all measured precipitation events (those above a trace), which also had an observation greater than one inch (25 mm), were categorized as heavy rainfall events. Approximately 1.63 million events at 2978 sites in the eastern two-thirds of the Continental U.S. were stratified into this category. Despite quality control measures at several points along the collection/archiving path, erroneous measure-

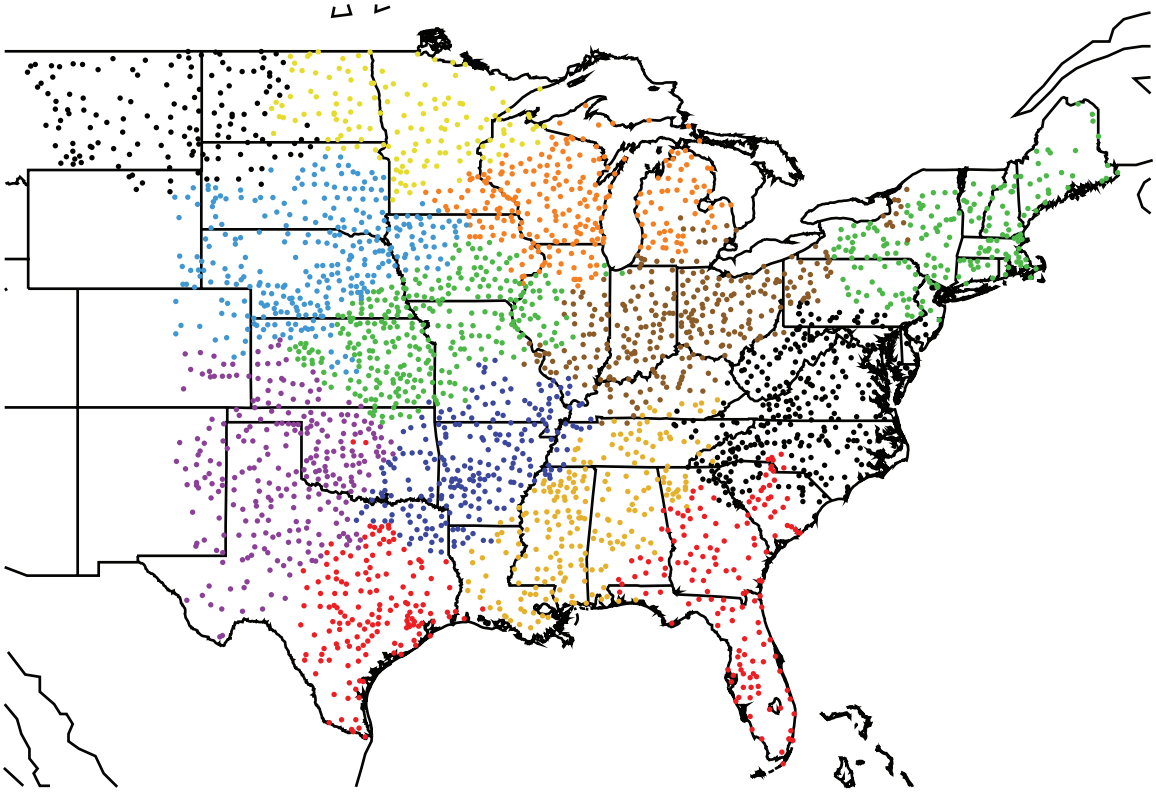

FIG. 5.2: Map of the 2978 GHCN-D stations within 85 km of the Richman–Lamb stations and with less than 10% missing data between 1950–2009. Colors correspond to the colors of the associated PC regions shown in Fig. 4.4.

ments occasionally slipped into the database. To ensure that the heavy event observations did not exceed verified observations, a list of the largest 24-hour rainfall events in each state was obtained from NCDC (Karsten Shein, personal communication). Heavy precipitation events at each station were compared with the largest verified 24-hour event in its home state; events larger than the state record were discarded and not used in this work. Thus, the dataset of heavy precipitation does not include erroneously large precipitation events. All flagged GHCN-D data were discarded with the exception of flags for climatologically unusual daily rainfall totals. The most extreme events may stand out as climatological outliers and could have had erroneous flags; 15 observations in the retained dataset had such a flag. These 15 observations were compared with NCDC's form records, but only 7 were verified as being correct and were retained. It is possible that the remaining data may still contain unchecked errors, but time and the effort required prevented a manual check of

TABLE 5.1: Number and percentage of the heavy precipitation events by region, average of the heavy precipitation amounts (cm) by region, approximate size of each PC region (thousands of km^2), and precipitation thresholds (cm).

Region	1	2	3	4	5	6	7	8	9	10	11	12	13
Number	16646	109353	97766	130901	96659	91283	153260	84031	227734	199634	224322	162742	37406
Percentage	1.02	6.70	5.99	8.02	5.92	5.59	9.39	5.15	13.96	12.23	13.75	9.97	2.29
Average	3.7	3.9	4.7	4.4	3.9	4.2	3.9	3.9	4.4	4.4	4.1	4.2	3.9
Est. Area	322	479	221	282	282	347	422	479	487	394	468	379	406
90%	1.27	2.11	3.30	3.18	1.88	2.54	2.11	1.96	3.43	3.38	2.51	2.59	1.70
95%	1.91	2.97	4.70	4.45	2.69	3.63	2.95	2.82	4.72	4.67	3.51	3.68	2.54
99%	3.66	5.21	8.59	7.72	4.88	6.48	5.13	5.08	8.18	7.92	6.10	6.50	4.72
99.9%	6.73	9.47	16.76	14.22	8.94	11.68	9.09	9.27	14.73	13.54	11.40	11.58	8.79

every observation in the top 10%, or even top 1%, of all records during the study period. Thus, it is presumed that the remaining events are correct.

As expected, the distribution of heavy events varied from region to region. The number and percentage of all heavy events tabulated in each of the 13 PC regions are shown in Table 5.1. Region 1, located in the northwest corner of the domain, had the lowest average amount and the smallest percentage of heavy precipitation events. Regions 2, 5, 7, 8, and 13 all had an average between 3.8 and 4.0 cm. Region 3, in southeast Texas, had the largest average of 4.7 cm. Regions 9, 10 and 11 in the Deep South and Mid-Atlantic states had the largest percentage of heavy precipitation events. Regions 2, 8, 9 and 11 were the largest areas, which may explain why Regions 9 and 11 had such a large number of heavy events. In contrast, Regions 3, 4, and 5 were the smallest regions.

The frequency distribution of the heavy precipitation events across the study domain is shown in Figure 5.3. As expected, the plot is skewed toward the smaller magnitudes of heavy events; in addition, the number of events decayed at a nearly log-linear rate (based on a 'best fit line'–not shown) with increasing magnitudes of precipitation. The events at the extremely large end of the rainfall spectrum were so infrequent that the semi-log line no longer approximated the data (in fact, between 18 inches and 26 inches, no single distribution fit the plot).

The intensity of precipitation by region will vary due to the availability of moisture (notably in the planetary boundary layer), the scale of precipitation-producing weather systems, and the underlying forcing mechanisms. To no one's surprise, the distribution

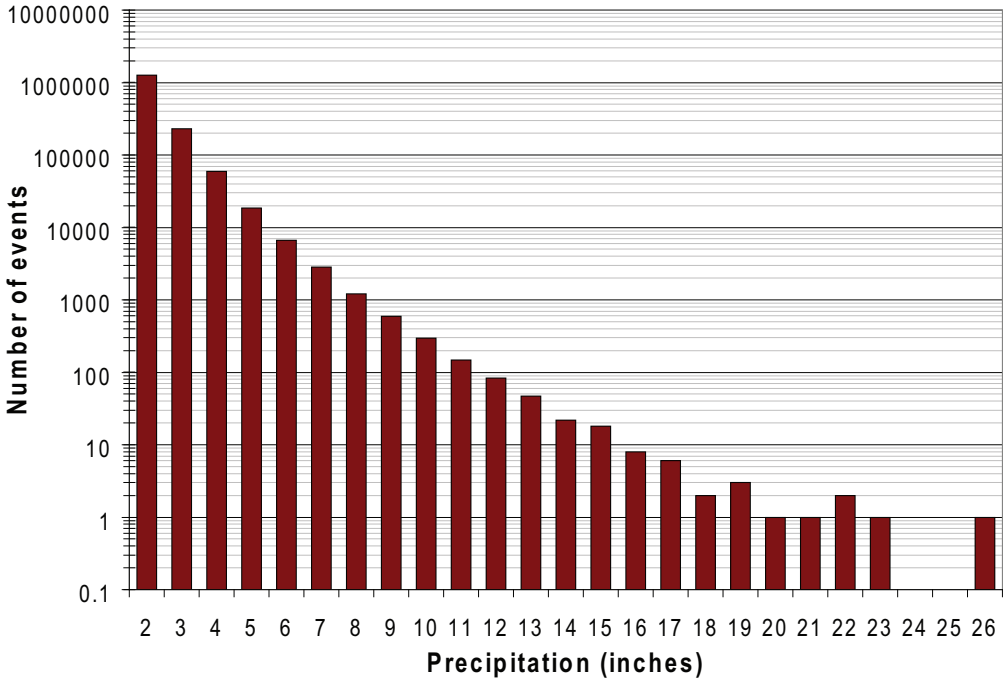

FIG. 5.3: Frequency distribution of heavy precipitation events in one-inch increments plotted on a logarithmic scale. The first bin includes precipitation observations greater than one but less than two inches (25–51 mm), the second includes observations greater than two but less than three inches (51–76 mm), and so forth. The largest event in the study dataset was 25.8 inches (654 mm).

of heavy precipitation events separated by region and magnitude revealed major differences between the moisture-laden Gulf Coast and the dry High Plains (Figure 5.4). The far northwestern PC regions (1 and 13) had many fewer heavy events of all magnitudes. In the northwest, precipitation events with more than ten inches (254 mm) did not occur or were not captured in the study dataset. Region 1, in eastern Montana and western North Dakota, had only one event above 7 inches (178 mm) and fewer than 14,000 events between 1-2 inches (25-51 mm). In contrast, regions along the Gulf of Mexico and Atlantic Ocean (with the exception of Region 2 in the northeast) had the greatest number of events across the spectrum of precipitation. Along the mid-Atlantic coast, Region 11 had approximately 180,000 events in the 1-2 inch category but only 135 events in the 7-8 inch category (Region 9 had 286 events in this latter category). The intensity distribution of PC Region 10 (eastern Oklahoma, northeastern Texas, Arkansas, and southern Missouri) closely resembled those regions along the Gulf of Mexico, the Southeast, and Mid-Atlantic

rather than surrounding regions to the west, north, and northeast (Figure 5.4a-b), likely due to the ready ability of moisture and the nocturnal LLJ. Similarly, Region 8 and Region 5 (Nebraska/South Dakota and Wisconsin/Michigan, respectively) more closely resembled neighboring regions in the Central United States in most categories except the category of most extreme events (Figure 5.4b-c).

The 90%, 95%, 99% and 99.9% precipitation thresholds in each of the 13 PC regions varied from region to region (Figure 5.5 and Table 5.1). For example, the threshold for the top 1% of observations in Region 5 (Great Lakes) is lower (2.5 inches versus 3.2 inches) than that of Region 4 (southeast). Regions 3, 4, and 9 along the Gulf Coast have the biggest spread between the 99% and 99.9% event thresholds. The 99% threshold is plotted in Figure 5.6 along with the total number of non-zero precipitation observations in each region. Interestingly, the regions with the largest number of observations (Regions 11, 7, 5, and 2) do not have the highest thresholds for events. Conversely, the regions with the highest event thresholds (Regions 3, 4, 6, 9, and 10) tended to have fewer measurable precipitation events. These previously unknown parings indicated that the southern regions (3, 4, 6, 9 and 10) tended to have fewer days with measured precipitation than regions farther north and east (Great Lakes and Ohio Valley eastward). However, the southern regions tended to have more extreme events than those regions farther north.

To investigate the existence of temporal trends in this large dataset, heavy events were separated by decade (i.e., 1950–1959, 1960–1969, and so forth). Figure 5.7 shows the distribution of heavy precipitation events between January 1950 and August 2009. Considerably fewer heavy precipitation events occurred in the higher categories during the 1950s and 1960s than in during subsequent decades. Data from the 1970s and 1980s revealed a long transition period into the extreme events that characterized the 1990s. The decade of the 1990s witnessed more heavy events than occurred during other decades as revealed by the number of events in rainfall categories in all precipitation measurement categories above 9 inches (228.6 mm). A timeline of heavy events with the five- and ten-year running means is shown in Figure 5.8. The ten-year running mean reveals a strong increasing trend

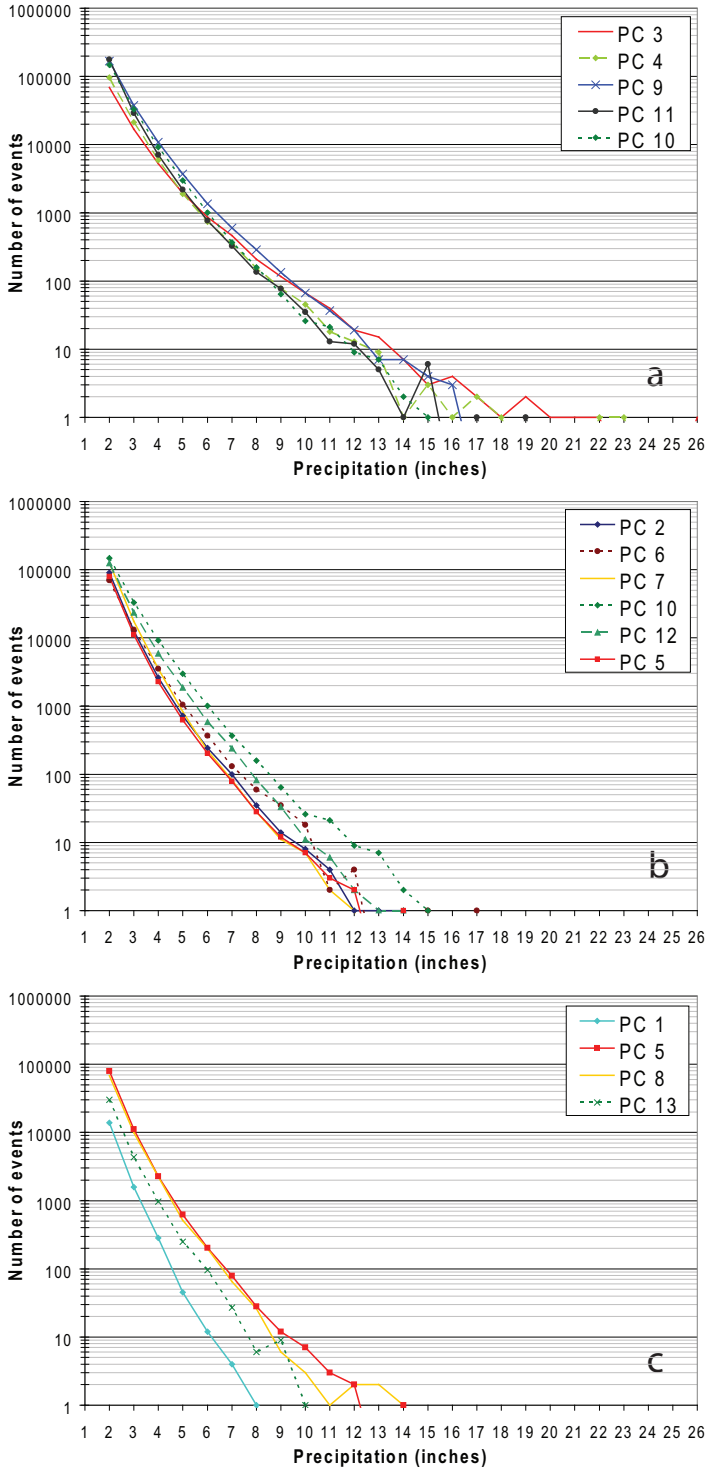

FIG. 5.4: As in Fig. 5.3 but for each of the 13 PC regions shown in Fig. 4.4. The plots display the distribution for those regions a) along the Gulf Coast and Mid-Atlantic, b) in the Central through Northeast U.S., and c) in the northwestern part of the domain and High Plains regions. PC Region 10 is depicted in both a) and b) and Region 5 is depicted in both b) and c) for ease of a visual comparison across the plots.

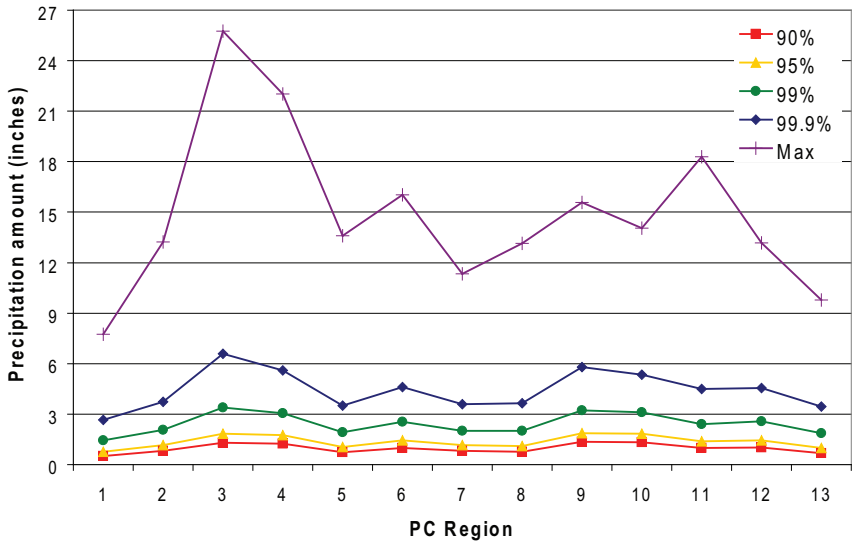

FIG. 5.5: The largest observation and the 90%, 95%, 99% and 99.9% precipitation thresholds of each of the 13 PC regions shown in Fig. 4.4.

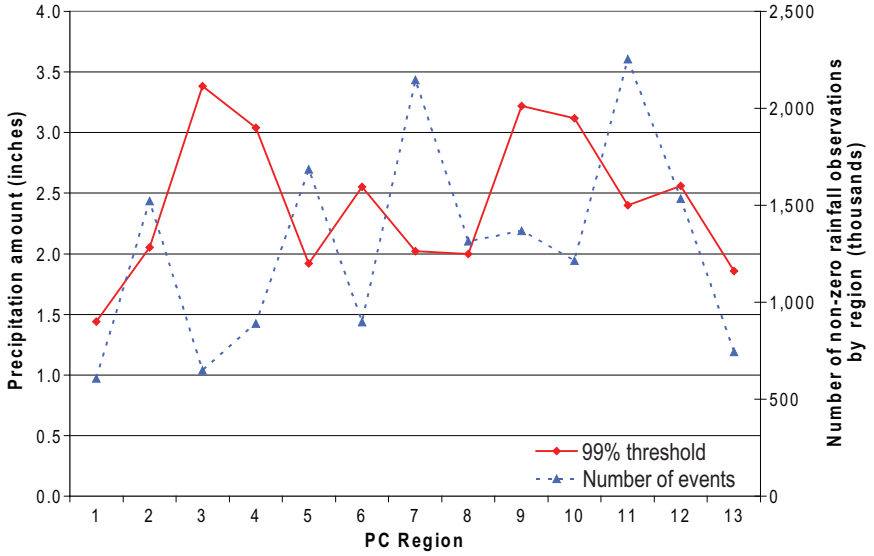

FIG. 5.6: The 99% precipitation threshold of each of the 13 PC regions shown in Fig. 4.4 (left axis). The blue dashed line (right axis) denotes the total number of non-zero precipitation observations in each region (thousands).

in the number of heavy events from the beginning of the study period through the 1970s, a gradual increase through the mid-1990s and a slight decrease in the number of heavy events through the 2000s. The variance in the number of heavy precipitation events during the 1990s and 2000s was considerably lower (by approximately 20%) than the amount of variance during the 1950s and 1970s (meaning that the heavy events had less variability

late in the study period when compared to the beginning of the study period).

When the data of the frequency distribution plotted in Figure 5.3 are stratified by decade, Figure 5.7 is the result. The resulting frequency distributions revealed:

- Heavy events of between 5–8 inches (127–208 mm) during a 24-hour period increased in frequency with each passing decade through the period of record (i.e., 1950–2009).
- Very heavy events that exceeded 10 inches (254 mm) increased in frequency during each passing decade through the end of the 20^{th} century.
- Between 1950–2009, the top 1% of all rainfall observations (not shown) occurred with increasing frequency in all regions.
- Fewer heavy events –those that produced $<$ 12 inches (305 mm)–occurred during the 1950s and 1960s than occurred during subsequent decades.
- The most extreme events (i.e., those with $>$ 15 inches/381 mm) were so infrequent that they represent the truly rare event (the top 0.0001% of events across all PC Regions).
- The decade of the 1990s stands out as the 'wettest' decade during the period of record for events above 1 inch while the 1950s stand out as the 'driest' decade in this study.
- The 1990s had the largest number of events in 15 of the 22 precipitation bins from 1–23 inches (25–548 mm).

When the data of the frequency distribution plotted in Figure 5.3 were stratified by PC region, the resulting frequency distributions (not shown) revealed:

- The decadal variation of heavy rainfall events across most of the 13 PC regions revealed an increasing trend from the 1950s through the 1990s (Figure 5.8).

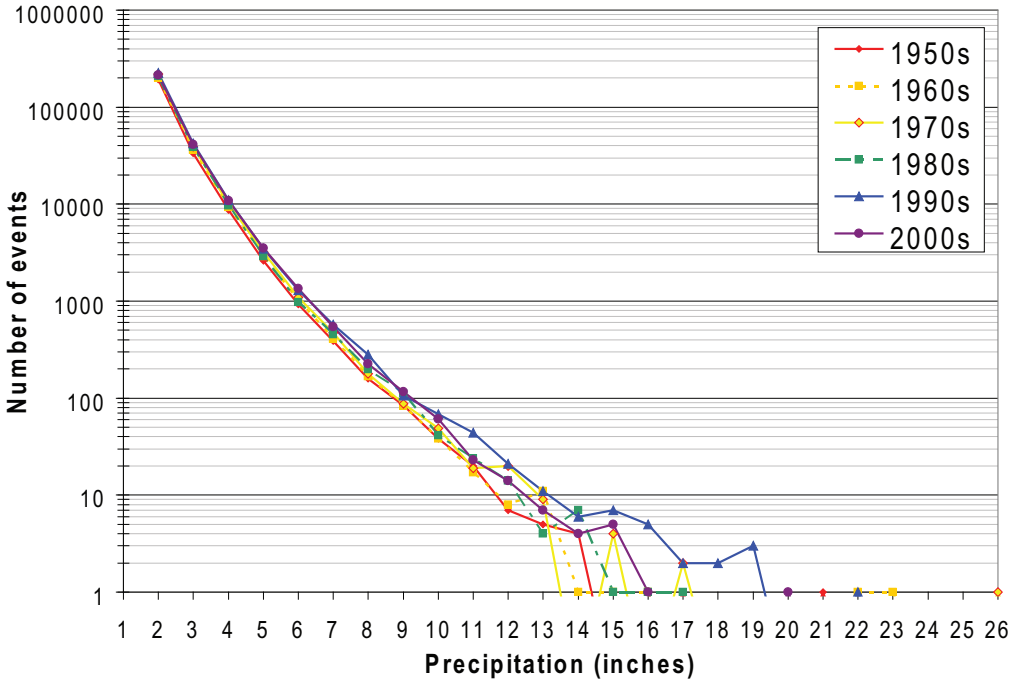

FIG. 5.7: As in Fig. 5.3 but stratified by decade from 1950–2009.

- Region 7 (the Ohio River Valley) and Region 8 (Nebraska and South Dakota) showed a tendency for the increased occurrence of heavy rainfall $<$ 6 inches (152 mm) over the study period.

- Across PC Region 4, more heavy rainfall events occurred during the 1990s than during other decades, a result similar to those revealed by plots of the frequency distributions from the national database (Figure 5.4).

- Across PC Region 9 (south-central Gulf Coast states), a larger number of heavy precipitation events between 6–8 inches (152–203 mm) were recorded during the 1990s and the early part of the 21st century than were recorded during previous decades.

- Across PC Regions 4 and 11 during the 1950s, fewer heavy events were recorded than occurred during later decades; on the other hand, these same two regions recorded more events between 6–8 inches (152–203 mm) than all other regions did in this specific rainfall category.

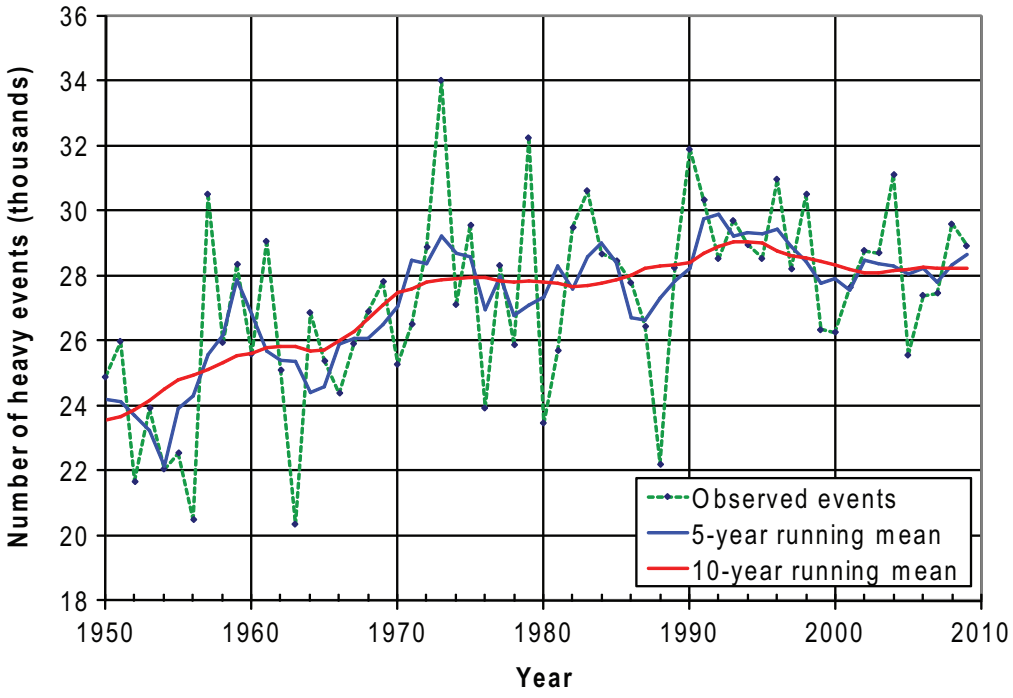

FIG. 5.8: Timeline of the number of heavy events (in thousands) from 1950–2009. The green dashed line is the observed number of heavy events, the blue line is the five-year running mean of heavy events, and the red line is the ten-year running mean of heavy events.

5.1.2 Significant Rainfall Events: The Twenty Largest Unique Events per PC Region

Given that the PCA has served its purpose (to identify the coherent precipitation regions across the United States east of the Rocky Mountains), from this point forward in the narrative, the emphasis will shift to an examination of the twenty largest events in each of the 13 PC-defined Regions. Three reasons exist for this shift in emphasis:

1. These twenty largest rainfall events (i.e., the extreme events in each region) are the type that most concern operational forecasters and the public-at-large, because they are extremely rare events by any standard of measure.

2. These type of events, now being termed “very high impact weather” (VHIW) received a call for increased research and development into phenomena known as VHIW (National Research Council 2010). The NRC noted that predictions of very high impact weather are ”not recognized or emphasized in previous studies (ibid,

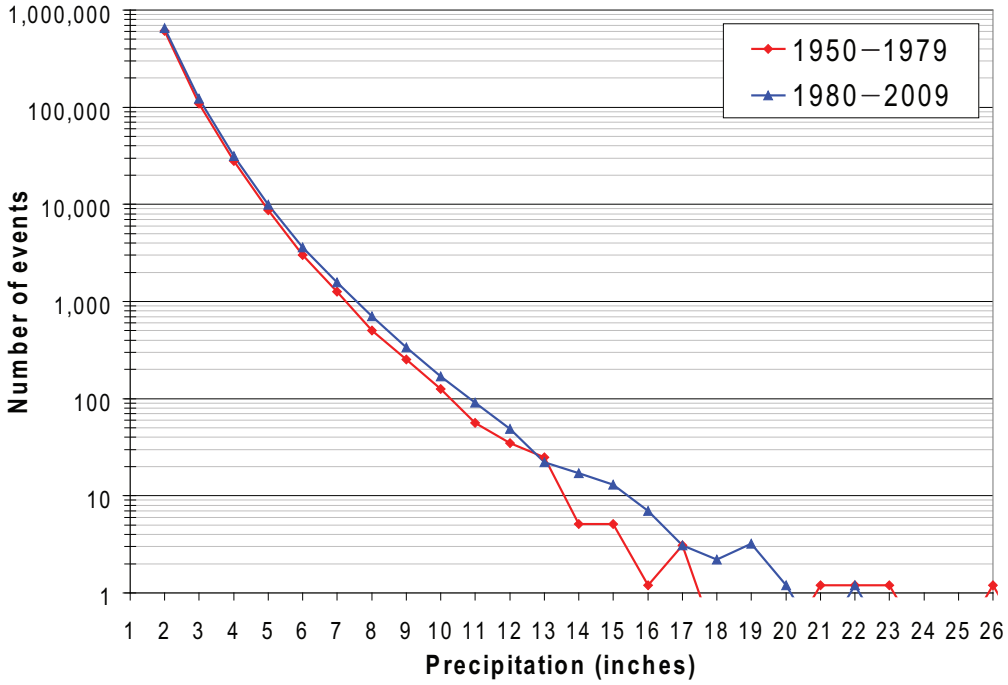

FIG. 5.9: As in Fig. 5.3 but separated by pre-1980 events and post-1980 events.

Page 1).

3. Synoptic-scale, decision-support tools are needed by operational forecasters that are quantitative and regionally focused in nature. On average, the new tools–in reality, three-dimensional composite models of the atmosphere and discussed in Chapter 6–were based on approximately twice as many case events as were used in all previous subjective studies of synoptic-scale composites.

To examine the largest rainfall events on a region-by-region basis, the top twenty unique extreme rainfall events in each region were identified; they were defined to be 'significant' events in this study (i.e., those in the top 0.0009% of all measured precipitation events in Region 11 and the top 0.003% of all events in Region 1). When extreme rainfall occurred at multiple observing stations during a 24-hour observation period in the same region, only the largest significant event was identified for further investigation.

Although it was not possible to quality-check the thousands of heavy precipitation events observed during the temporal domain of the study time data set (e.g., most were

tabulated on original paper archives preserved by the National Climatic Data Center), the much smaller subset of significant events made this task practical. The most extreme observations were the most prone to errors during the manual digitization process (e.g., a misplaced decimal point by a human observer, a key-entry mistake, or a possible human override of the quality control results). These extreme observations, if verified to be accurate, contain the most interesting data for study (as noted by Brooks and Stensrud 2000). To verify the accuracy of these events, the precipitation observations from *all* GHCN-D stations in the study area were plotted for each of the 260 event days (i.e., using more than the 2978 stations by including those stations with more than 10% missing data during the 60 year period). An examination of these plots revealed many potentially erroneous observations. Questionable observations were individually checked by a direct comparison of the archived rainfall amounts with scanned copies of the original cooperative observer forms (NCDC) or the historic monthly climate reports issued by each state (NCDC). From these manual inspections, numerous errors were detected in the significant events dataset. These errors often were caused by multi-day reports totaled by the human observer as a one-day total, by sloppy recordkeeping or handwriting on the observer's forms, or simply data that differed significantly from NCDC's historical records. All suspicious observations were removed from the study dataset and replaced with the next-largest unique event in each PC region. All substituted events also were hand-verified with the observation forms or climate reports. The precipitation plots also revealed several events on a given day with rainfall totals greater than the significant event reported in the data archives; these events occurred at stations not used in this study because these stations had more than 10% missing data between 1950–2009.

The precipitation plots from the verified 260 significant events revealed some patterns that appeared tropical in nature. Every potentially tropical event was checked against historical tropical storm and hurricane tracks. Those events caused by a tropical storm or hurricane (or a formerly tropical system) were flagged in the significant events database. Region 11 had the most tropical significant events with 12 out of the 20 significant events

TABLE 5.2: Number of significant events caused by tropical systems by region.

Region	1	2	3	4	5	6	7	8	9	10	11	12	13
Tropical	0	8	8	5	0	1	0	0	9	0	13	0	0

caused by tropical systems (Table 5.2).

In many instances, two very large rainfall events occurred in the same region on neighboring days. Sometimes the 'apparent' extended rainfall event was due to different recording times by the human observer (i.e., 7 p.m. at one site and 7 a.m. the next day at another); sometimes the two large rainfall events were caused by a slow-moving synoptic system that produced significant precipitation events on neighboring days. See Fiebrich (2007) for a discussion of the accuracy of "time of day flags." In either case, the synoptic environments from these multi-day events do not represent multiple unique environments; they show the evolution of a single event environment. To identify 20 unique environments, only one day from each of these multi-day events was used (16 events were discarded). The chosen date was selected based on the amount of rain that fell each day, the spatial extent of the event and, in some cases, a subjective decision based on the synoptic environment thought to be more representative. The next-largest unique single-day event in each region replaced the duplicate event to retain 20 unique significant events in each region. All replacement events were subjected to the quality-control measures described above. In total, 34 of the 260 significant events were replaced due to data archiving/recording errors or multi-day events. Appendix B contains a list of the 260 significant events used in this study.

As expected, the significant rainfall events varied in magnitude from region to region. The maximum, minimum, and average precipitation totals from each region are displayed in Table 5.3 to help the reader better understand characteristics of the dissertation dataset:

- The northwest PC Regions 1 and 13 had the smallest significant events, while the largest events were found in Region 3 (SE Texas), Region 4 (SE U.S.), Region 9 (Southern Gulf states), and Region 11 (Mid-Atlantic).

- The smallest significant events in the moisture-rich PC Regions 3, 4, and 9 surpass

TABLE 5.3: Statistics of the significant precipitation events by region. Precipitation measurements are in centimeters.

Region	1	2	3	4	5	6	7	8	9	10	11	12	13
Maximum	19.69	33.63	65.41	53.59	34.54	40.69	28.80	31.83	39.57	35.71	46.48	33.48	24.84
Average	14.34	21.58	39.70	34.19	23.98	26.52	22.66	21.88	33.57	29.68	29.97	25.55	18.91
Minimum	12.07	17.96	30.99	29.08	19.76	22.35	19.96	18.29	29.39	25.91	25.12	22.23	16.13

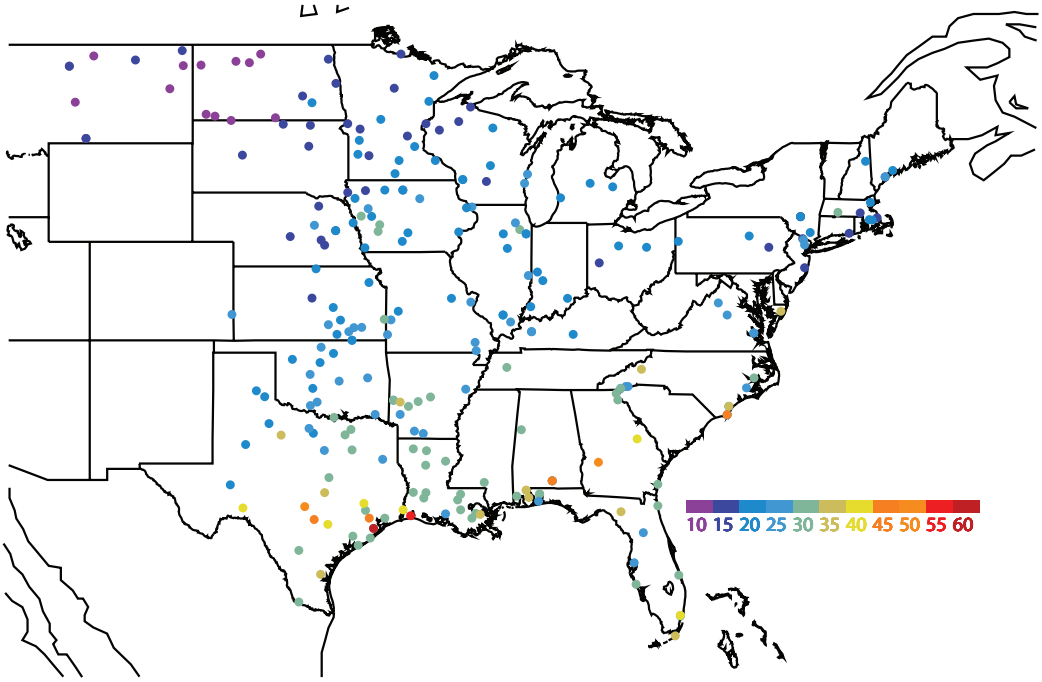

FIG. 5.10: Locations of significant events. Color indicates the magnitude of the precipitation event at each station (inches). In instances where more than one significant event occurred at the same point, the color represents the magnitude of the largest event at that station.

even the largest events in the much drier northwest PC Regions 1 and 13 and PC Region 7 across the Ohio Valley.

The location and magnitude of the top twenty significant events detected in the study 13 PCA-determined regions are plotted in Figure 5.10. A visual inspection of this figure reveals that most of the significant events with the smallest intensity occurred across the northern Great Plains, while significant events with the largest magnitude of rainfall occurred in the regions bordering the Gulf of Mexico and Atlantic Ocean.

The total number of significant events varied considerably from decade to decade (Table 5.4). The 1990s captured many more significant events than all other decades (by more

TABLE 5.4: Percentages of heavy and significant events with respect to event type and organized by decade.

	1950s	1960s	1970s	1980s	1990s	2000s
Heavy events	15.1	15.8	17.3	16.6	18.0	17.2
Significant events	14.2	16.5	15.8	13.5	20.4	19.6

than 20%) during the study period while the 1950s and 1980s recorded the fewest. These numbers indicate an increasing trend in the number of significant events in recent decades. Similarly, the heavy event totals reflected a gradual tendency to increase in magnitude with time. The locations of the significant events by decade are shown in Figure 5.11. The spatial distribution of these events does not reveal an underlying pattern, but an increasing number of heavy rainfall events were classified as significant during recent decades.

5.1.3 Seasonal distribution

To determine if the forcing mechanisms which produced heavy and significant precipitation events differed based on the time of year, an examination of the seasonal distribution

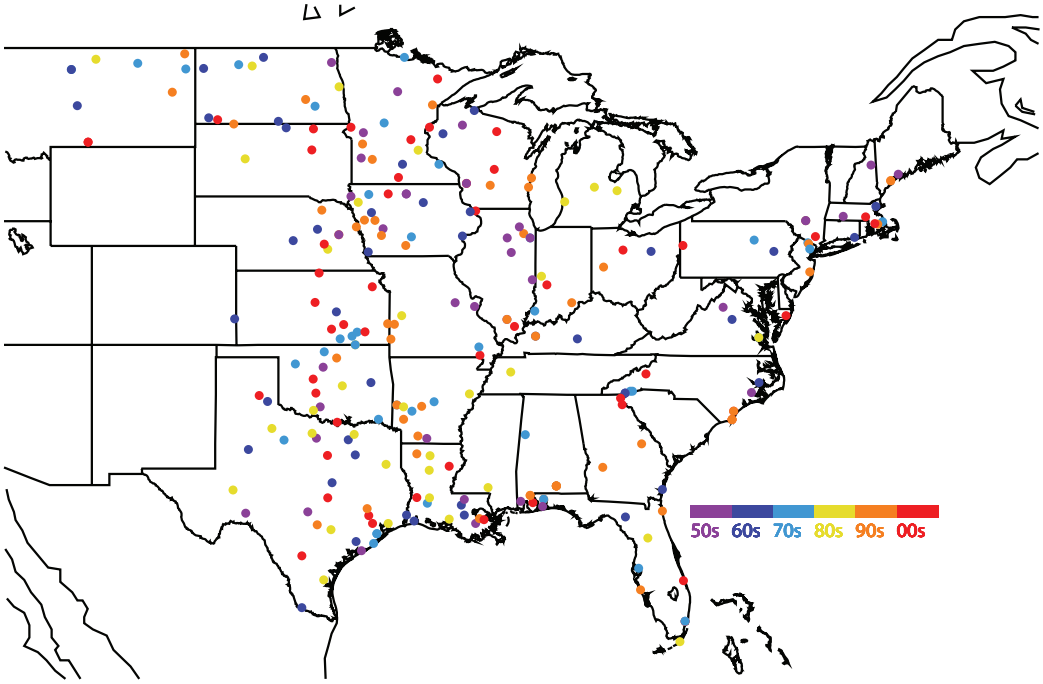

FIG. 5.11: As in Fig. 5.10; except color coding indicates the decade during which the significant event occurred. In instances where more than one significant event occurred at the same point, the color represents the decade during which the event with the largest magnitude occurred.

of precipitation was performed to provide additional insights. The percentages of heavy and significant events by climatological seasons(Table 5.5) exhibited a marked difference between the high percentages of events which fell during the summer and autumn and low percentages of events, which were uncommon in the spring and winter. In fact, nearly 80% of the significant events occurred during the two seasons of summer and autumn. A less substantial difference arose with the occurrence of heavy events, which tended to have a larger presence (over 40%) during the winter and spring. More heavy events occurred during the spring than during autumn, while significant events were more common during the autumn than during spring.

When the data of Table 5.5 are stratified by PC regions, Figure 5.12 results. Across PC Regions 1, 5, 8 and 13, fewer than 5% of the annual heavy events occurred during winter but $\sim 50\%$ of the heavy events were summer events. The drier areas contrasted sharply with the substantially warmer and more moist PC Regions 9 and 10, which recorded over half of their heavy precipitation events during the winter and spring and less than a quarter during the summer. Those regions near the Gulf of Mexico and Atlantic Ocean (PC Regions 2, 3, 9, 10, and 11) received less than one-third of their heavy precipitation events during the summer. The exception is Region 4, where disorganized afternoon thunderstorms during the summer can create considerable rainfall.

The distribution of the extreme precipitation events (i.e., the top 1% in each region) were plotted by region and season in Figure 5.13. When this plot of the extreme events is compared with the plot of heavy events (Figure 5.12), the top 1% of events in each region occurred more frequently during the summer across most areas except PC Regions 4, 9 and 10. Notably, fewer of the top 1% events than the heavy events occurred during the winter

TABLE 5.5: Percentages of heavy and significant events organized by climatological season, defined as March–May, June–August, September–November and December–February for spring, summer, autumn and winter, respectively.

	Spring	Summer	Autumn	Winter
Heavy events	26.3	32.9	24.6	16.3
Significant events	20.0	47.7	31.5	0.8

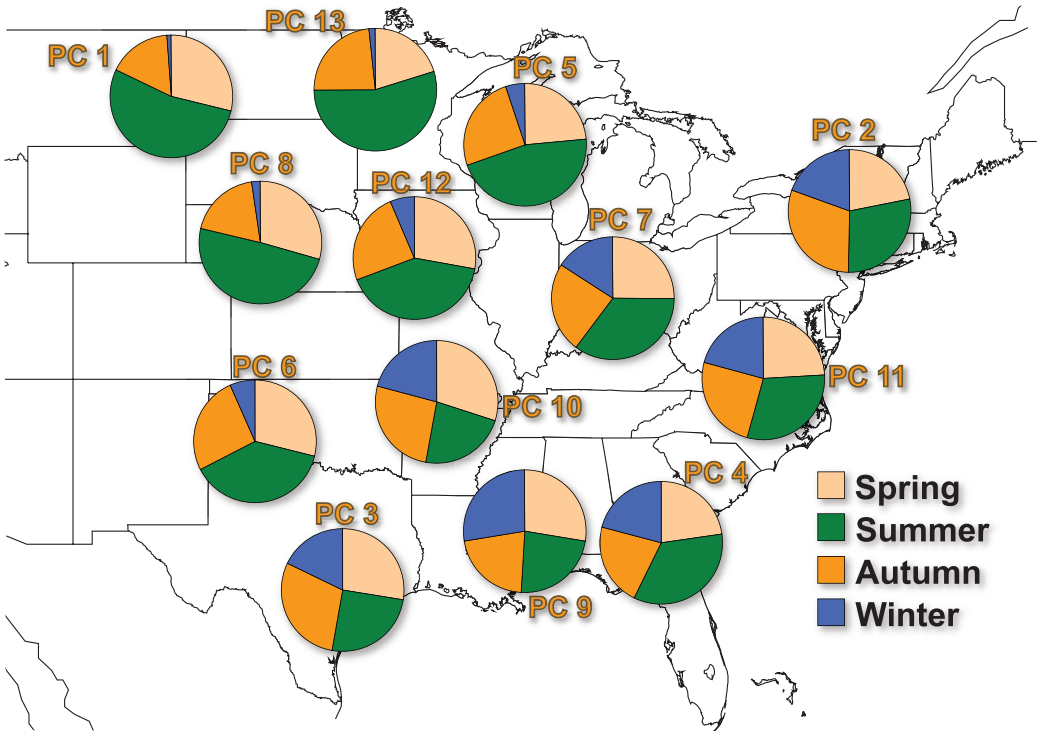

FIG. 5.12: The seasonal distribution of heavy precipitation events for each PC region shown in Fig. 4.4.

months in every region.

The significant events, similar to the heavy events, displayed a wide range of variability when stratified by region and by season. At least half of the significant events in PC Regions across the northwest, Midwest and Great Lakes occurred during the summer months. Of the 20 significant events across PC Region 8 (NE and SD) and Region 5 (Great Lakes), 17 and 16 events, respectively, occurred during the summer. At the other extreme, the Atlantic PC Regions 2 (Northeast) and 11 (Mid-Atlantic) witnessed 11 and 14 significant events, respectively, during the autumn months. The vast majority (84%) of significant events in this study occurred during the warm season (April–September). Region 2 (Northeast) had the most cool season events (8) while Region 1 (MT and ND) and Region 8 (NE and SD) had no significant events during the cool season. Other facts may be gleaned by a visual inspection of Table 5.6.

The seasonal distribution of heavy precipitation events by season and decade (Figure 5.14a) revealed two well known facts:

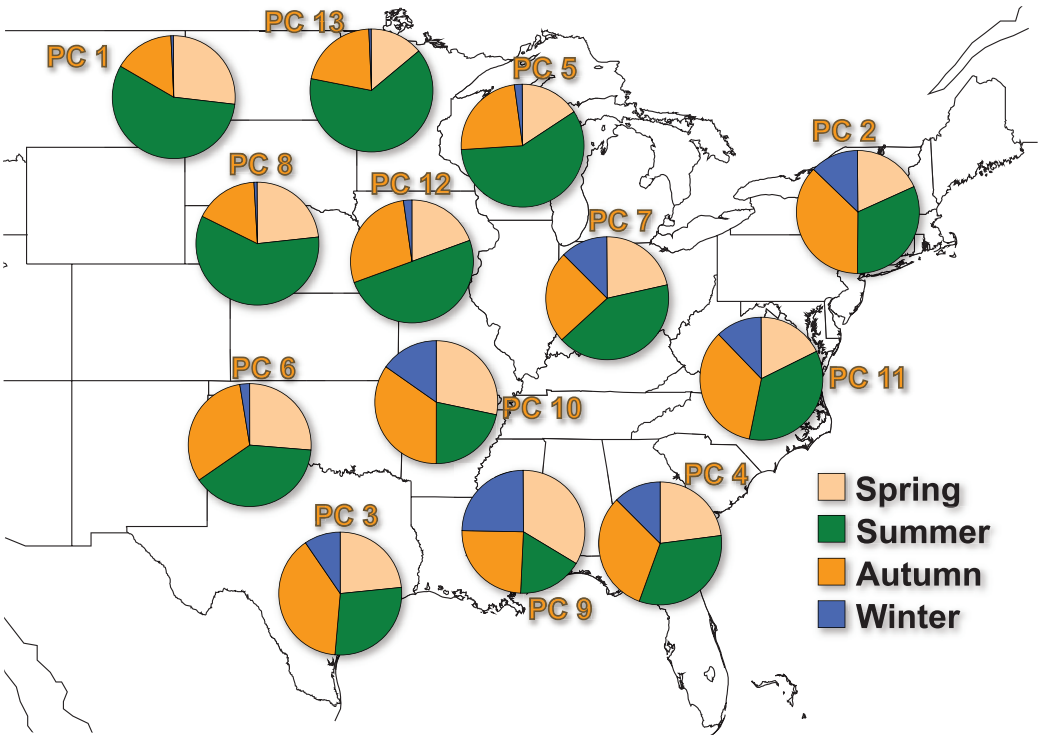

FIG. 5.13: The seasonal distribution of the top 1% of precipitation events in each of the PC regions shown in Fig. 4.4.

TABLE 5.6: Statistics of the significant precipitation events by climatological season. The warm season includes events which occurred in April–September while the cool season includes events in October–March.

Region	1	2	3	4	5	6	7	8	9	10	11	12	13
Spring	6	2	1	7	0	6	4	3	8	10	1	1	3
Summer	12	7	10	7	16	8	14	17	3	2	5	10	13
Autumn	2	11	9	6	4	6	2	0	9	6	14	9	4
Winter	0	0	0	0	0	0	0	0	0	2	0	0	0
Warm Season	20	12	18	15	19	14	18	20	18	14	16	15	19
Cool Season	0	8	2	5	1	6	2	0	2	6	4	5	1

1. Most heavy precipitation events occurred during the summer while relatively few happened during the winter.

2. Temporal trends in the seasonal distribution of precipitation events are hard to discern and were not evident. A greater occurrence of autumn heavy events were recorded during the 1980s and the early part of the 21st century, but during the 1950s–1960s, the greatest number were summertime events. By decade, a greater number of events occurred during the 1990s than during other decades across all seasons except au-

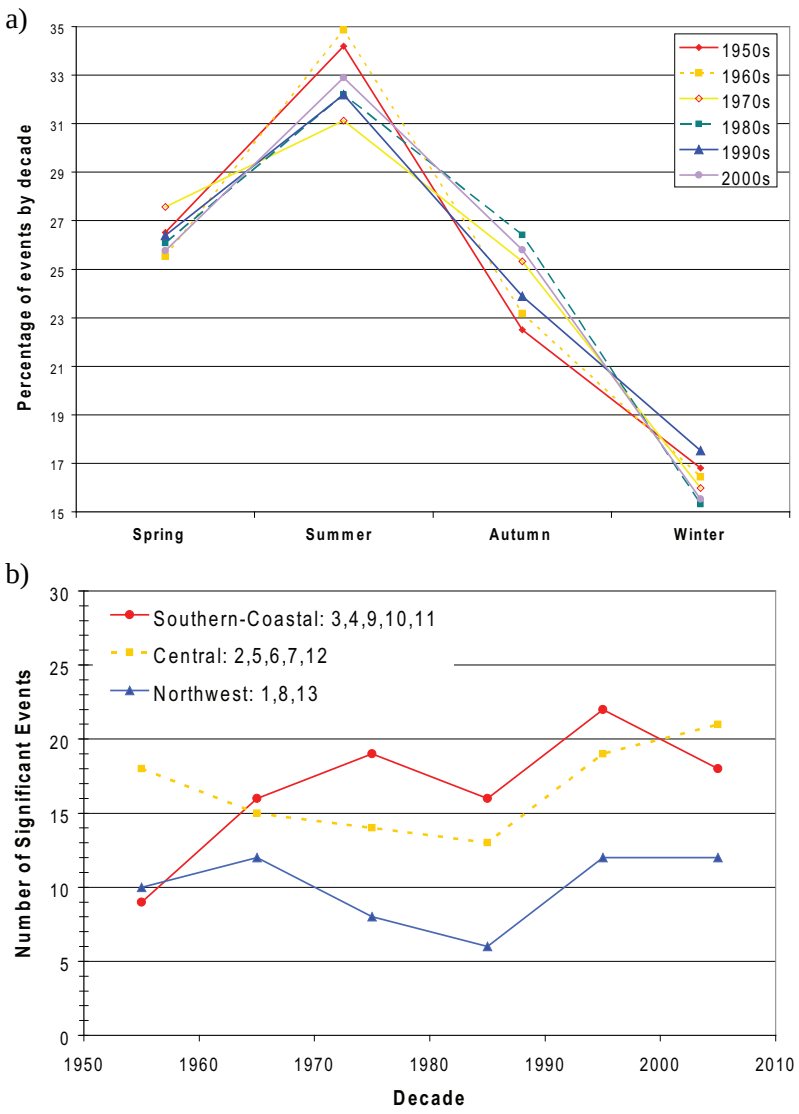

FIG. 5.14: The a) percentage of seasonal heavy precipitation events, separated by decade, and b) the percentage of significant precipitation events, separated by decade from 1950–2009.

tumn. Relatively few heavy events were recorded during the 1950s and 1960s.

When the significant events from several regions were grouped together into a larger dataset based on their precipitation distributions (Figure 5.4), an increasing trend in the number of significant events clearly is evident throughout the period of record across all coastal and southern regions (Figure 5.14b). Across the remainder of the United States, the number of significant events reached their peak during the wet decade of the 1990s, thus ending the upward trend of significant events in those regions.

Chapter 6

Composite Maps of the Synoptic-Scale Atmosphere

6.1 The Genesis of Composite Maps

The work of Maddox et al. (1979), Junker et al. (1999), and Moore et al. (2003) began a series of independent investigations, each designed to assist operational forecasters with recognizing favorable weather patterns prior to the occurrence of very high impact weather events (in their cases, flood-producing rainfall). The driving force behind the work of Maddox et al. (1979) was their unrelenting desire to develop elementary decision support tools as a step toward eliminating the possibility of catastrophic flood events occurring when the official NWS forecast called for 'fair weather.' Three catastrophic floods–Rapid City (SD) of June 1972, Big Thompson (CO) of August 1976, and Johnstown (PA) of July 1977–all "struck without warning." At the end of each event, hundreds of fatalities were the grim results. While the work of Maddox et al. (1979) should be considered successful, their composite maps were subjectively derived through their mind's eye after a thorough study of 151 flood events drawn from a 5-year period during the 1970s. Unfortunately, almost all of their events were Mesoscale Convective Systems.

While the work of Junker et al. (1999) and Moore et al. (2003) was a more modern approach to the work of Maddox et al. (1979), they nevertheless were subjective in nature. In addition, the work of these latter two teams produced results that had the following characteristics:

- If the work of all three teams were combined (i.e., Maddox, Junker, and Moore), the number of cases investigated still will be less than the 260 events investigated in this dissertation.

- Junker et al. (1999) used only 12 cases of heavy rainfall drawn from the concentrated area of Iowa and Missouri during 1993, the year of the Great Flood along the Mississippi and Missouri Rivers.

- To their great credit, Junker et al (1999) were the first to use data from an initial analysis of gridded fields produced by NCEP (versus interpolated data from rawinsondes).

- However, the composites by Junker et al. (1999) were valid only between the ground surface and 850 hPa; only a minimal effort at 200 hPa is reported in their work.

- Finally, the last of the role model examples was produced by Moore et al. (2003), who investigated only 21 MCS systems that occurred across the middle Mississippi River Valley. Their results, while composite in nature, actually were vertical cross-sections that displayed the thermally-driven circulations associated with a mature MCS.

With the retirement of Wes Junker and the death of Professor Jim Moore, the early leaders who valued composite models are no longer available to the scientific community. Fortunately, a just-released report from the NRC (2010) clearly stated that predictions of very high impact weather was "not recognized or emphasized in previous studies." Suddenly, three external events created a broad audience for the work in this dissertation, even going beyond the overarching goal stated in Chapter 1. As a result, Chapter 6 begins the final transition to evaluate the previously-stated null hypothesis. Regardless of whether the null hypothesis is accepted or rejected, the path forward will lead to the creation of regionalized composite maps of synoptic features for use as decision support tools. At the end of this process, the three intermediate goals stated in Chapter 1 should have been met as well.

To help the reader better understand the flow of this research, Figure 1.2 provides an overview that links the theoretical foundation of this dissertation (Chapters 1–2) with the

data available for data mining purposes (Chapter 3). The data analysis tools are linked with the quality controlled data to identify 13 coherent regions of precipitation across the United States east of the Rocky Mountains (Chapter 4). Using these 13 PCA-determined regions, a synoptic climatology of heavy and significant heavy rainfall was conducted and reported on in Chapter 5. Finally, in Chapter 6, the dissertation will use the PCA-determined regions to develop a new generation of objectively-determined decision support tools. The work described in Chapter 6 will build off the results reported in previous chapters and will use the scientific literature as guidance to conclude with an evaluation of the null hypothesis.

6.2 Significant Rainfall–A New Generation of Decision Support Tools

The twenty largest rainfall events (i.e., the extreme events in each of the 13 PCA-determined regions) represent 260 extreme events from all regions of the United States east of the Rocky Mountains. It is these 260 events that will be used to develop regionally- and nationally-focused composite maps in a three-dimensional context to serve as quantitative decision support tools for operational forecasters. In so doing, the second intermediate goal and the overarching goal of Chapter 1 will be achieved by a successful completion of these composites.

Composite maps, if properly developed, can reveal important characteristics of the synoptic-scale environment associated with significant precipitation events across each region. To generate these maps, the grid point on the NCEP–NCAR Reanalysis closest to the significant event location was first identified. This grid point forms the center point of a 23×23 data grid for each significant event. The grid spacing in each direction follows the grid spacing of the Reanalysis (approximately 1.875° longitude $\times$ 1.905° latitude).

While other scientists have used the Reanalysis data for compositing work (primarily to calculate proximity soundings), this project was the first to use the NCEP–NCAR Reanalysis to examine the synoptic-scale environment associated with significant rainfall events across a large domain over a long period of time. Upon plotting each of the 260 significant

events using the Reanalysis, it became clear that the environments favorable for producing significant events across each inland region (i.e., those that do not border either the Gulf of Mexico or Atlantic Ocean) had synoptic-scale features that appeared similar and had ingredients supportive of strong convection (e.g., high level divergence over a zone of low-level convergence and a tongue of high precipitable water advected on the heels of a lower level jet into a well-defined zone of low-level warm thermal advection). On the other hand, synoptic-scale composites developed for the coastal regions (2, 3, 4, 9, and 11) failed to provide a convergence of favorable ingredients into a single area (i.e., the features were broad and diffuse). These important but seemingly anomalous events along the coastal regions were examined individually to garner clues as to why the significant rainfall events across these regions failed to provide a striking array of meteorological clues that would help explain each event. In the end, the coastal events were deemed to be driven by thermodynamic and/or mesoscale features (i.e., low-to-the-ground LCLs, mesoscale outflow boundaries, microscale features in the underlying terrain, etc.). Consequently, the coastal regions were excluded from the national composites described in Section 6.3. Even so, composite maps for each region, including the coastal PC-determined regions, were analyzed independently and individually in Sections 6.5 and C.

To create the composites, the value of each parameter of interest at each grid point surrounding a significant event was averaged with the corresponding point from each of the approximately 160 significant events digitized across the inland regions. This averaging process created a national composite map for each Reanalysis field used in this study. One significant event, caused by a tropical storm which moved inland (Erin in 2007), was excluded from the composite process. Reanalysis data for 2009 were not available at the time of this study, so the single non-coastal significant event during 2009 (in Region 10) was excluded. Computations and composite maps were produced using the Grid Analysis and Display System (GrADS; COLA 2010). [1]

[1]The GrADS code which generated the composite maps is available online at http://blizzard.atms.unca.edu/~cgodfrey/elaine/comp/.

All composite maps are overlaid on a map of the central United States to give the reader a feel for the scale of the events. The black square in the center of each map, which indicates the centroid of heaviest rainfall for each composite, was located at the average latitude/longitude coordinates of all non-tropical significant events in the non-coastal regions ($40.7^{\circ}N$, $-95.1^{\circ}W$). The following maps represent national composites and represent 60 years of data associated with the $\sim$ 160 significant rainfall events. As a convenience to the reader, all should note that any geographical descriptions of feature locations (i.e., a surface low along the Colorado-Kansas border) are features relative to the location of the heaviest rainfall. The geographic location of specific features will vary with the location of specific events.

6.3 Composite Map Results–A New Generation of Decision Support Tools

Across the non-coastal regions of the United States east of the Rocky Mountains, the preferred location for significant rainfall during a 24-hour period between the years of 1950–2009 occurred $\sim$ 800 km (500 miles) northeast of a 1008 hPa surface low (Figure 6.1). The centroid of significant rainfall center was located at the north end of a narrow tongue of maximum precipitable water (values near 0.35 kg m^{-2}; not shown), and along a surface dew point ridge that extended north-northwest from the central Gulf Coast states (Figure 6.1). This rainfall centroid also was in the middle of an axis of warm thermal advection (Figure 6.1) that stretched southwest-to-northeast. This location was at the nose of a θ_e ridge (equivalent potential temperature; not shown). A northeast/southwest zone of surface-based convergence began $\sim$ 300 km (200 miles) west-southwest of the significant event centroid (Figure 6.1); maximum convergence values (in excess of 5×10^{-6} s^{-1}) were west-southwest of the centroid of significant rainfall and along a baroclinic zone (Figure 6.1). The LCL height (Lawrence 2005) was only $\sim$ 150 m above the surface (not shown).

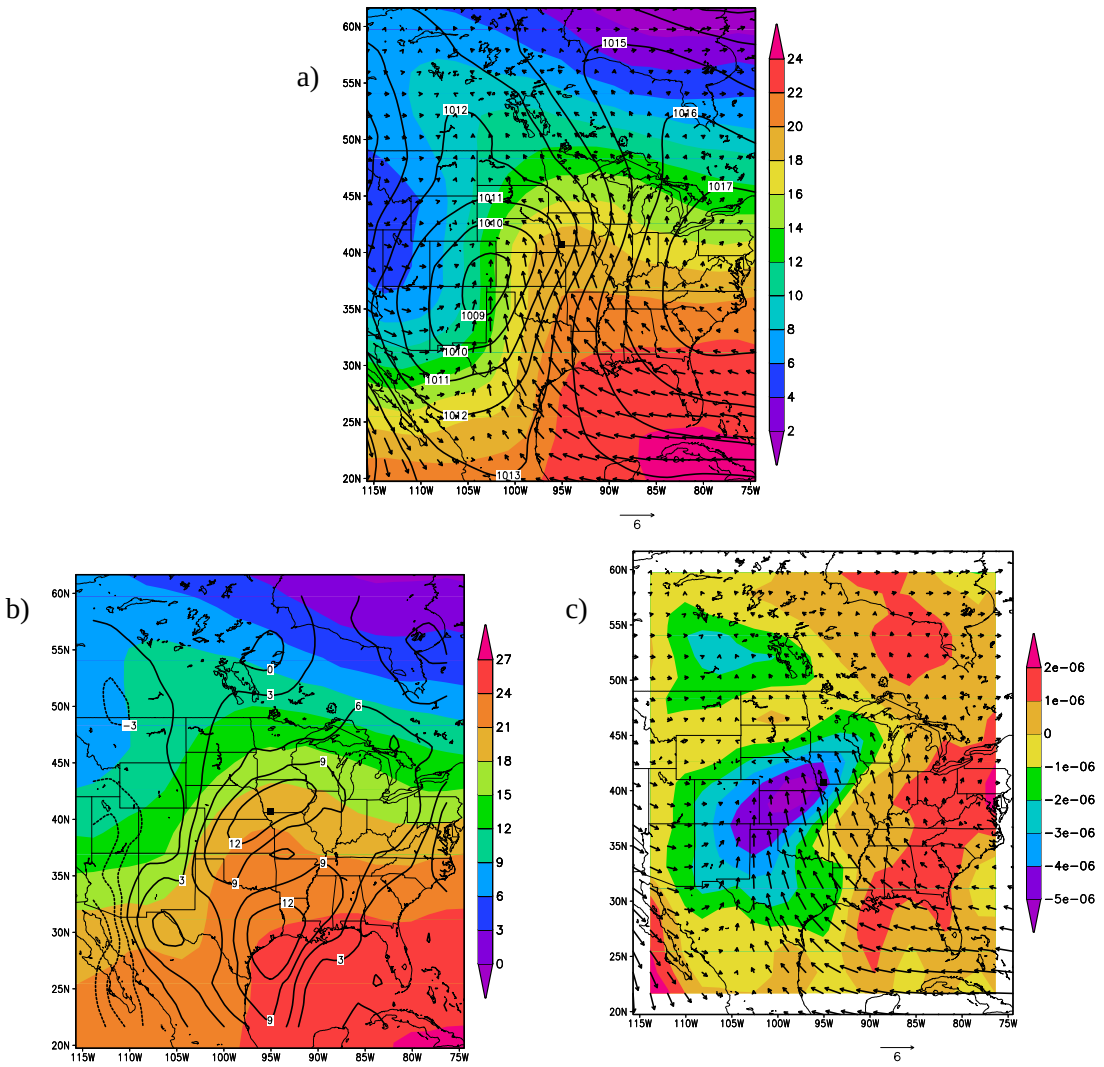

FIG. 6.1: Composite map of a) mean seal level pressure (MSLP, contours are hPa), 1000 hPa wind vectors (m s^{-1}) and T_d (shaded, °C), b) 1000 hPa thermal advection (contours, K s^{-1}) and temperature (shaded, K), and c) 1000 hPa divergence (shaded, s^{-1}) and wind vectors (m s^{-1}). The grid is centered on the calculated centroid location of significant rainfall contributed by each composite member. Thus, the national composite has been normalized to a centroid location along the western Iowa-Missouri border (the small black square).

At 850 hPa, the rainfall centroid occurred at the convergent end of a strong southerly jet at 850 hPa (loosely termed as the 'low level jet' or the LLJ), at the nose of a broad ridge of warm θ_e and was almost in the center of an elongated area of warm thermal advection (Figure 6.2). Although the significant precipitation events occurred in an area of convergence at 850 hPa, the strongest convergence was located $\sim$ 640 km (400 miles) west-southwest of the precipitation event center (Figure 6.2). However, this convergence zone was northwest

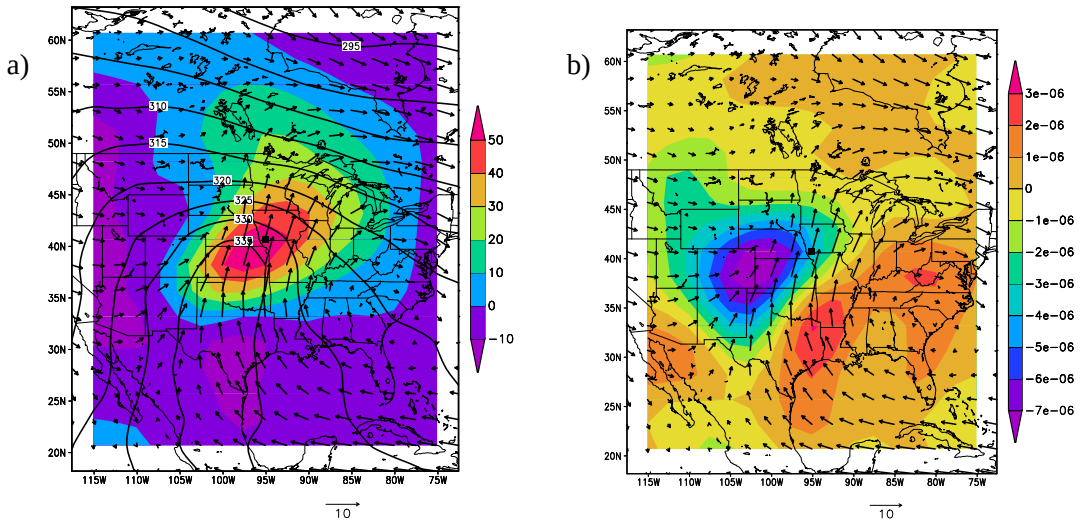

FIG. 6.2: As in Figure 6.1 but for 850 hPa. Map a) is a national composite of θ_e (contours, K) and thermal advection (shaded, K s^{-1}) while Map b) represents 850 hPa divergence (s^{-1}) and wind vectors (m s^{-1}).

of the warm thermal advection below and very nearly co-located with the axis of 1000 hPa convergence.

By 500 hPa, the most remarkable feature was the concentrated bulls-eye of ascent (-0.12 Pa sec^{-1}) located slightly west of the preferred location of significant rainfall (Figure 6.3). This location also was very near the inflexion point region where ageostrophic divergence (due to curvature; Figure 6.3) was created by a trough west of the significant event centroid and a well-defined ridge to the east. A polar jet was well northeast of the significant rainfall location; hence, the ageostrophic responses were weak in the vicinity of the heaviest precipitation (Figure 6.3). Instead, the preferred location of significant rainfall was downwind from a weak vorticity maximum (central values near 0.00025 sec^{-2}; Figure 6.3) and in an area of weak cold thermal advection at 500 hPa.

At 200 hPa, the significant rainfall events were classically located in the right entrance region of an anticyclonically curved jet and just downwind from the inflexion point of the trough/ridge pattern (Figure 6.4). A weak ageostrophic component in the wind field was evident at the entrance and exit regions of the Polar jet (Figure 6.4). As a result of these features, a concentrated bulls-eye of divergence (8×10^{-6} s^{-1}) was centered $\sim$ 300 km

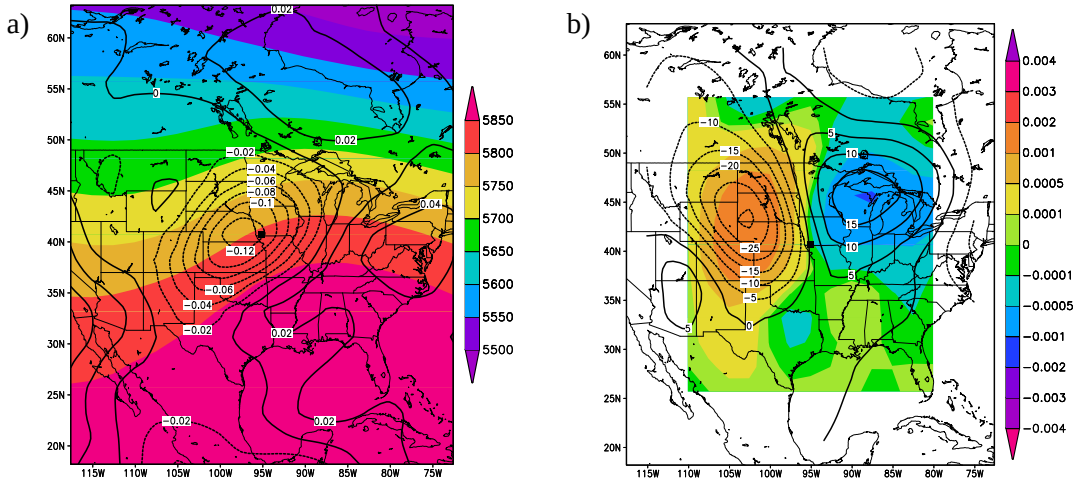

FIG. 6.3: As in Figure 6.1 but for 500 hPa. Map a) represents vertical velocity (contours, Pa s^{-1}) and geopotential heights (shaded, m) while Map b) represents 500 hPa thermal advection (contours, K s^{-1}) and vorticity advection (shaded, s^{-2}).

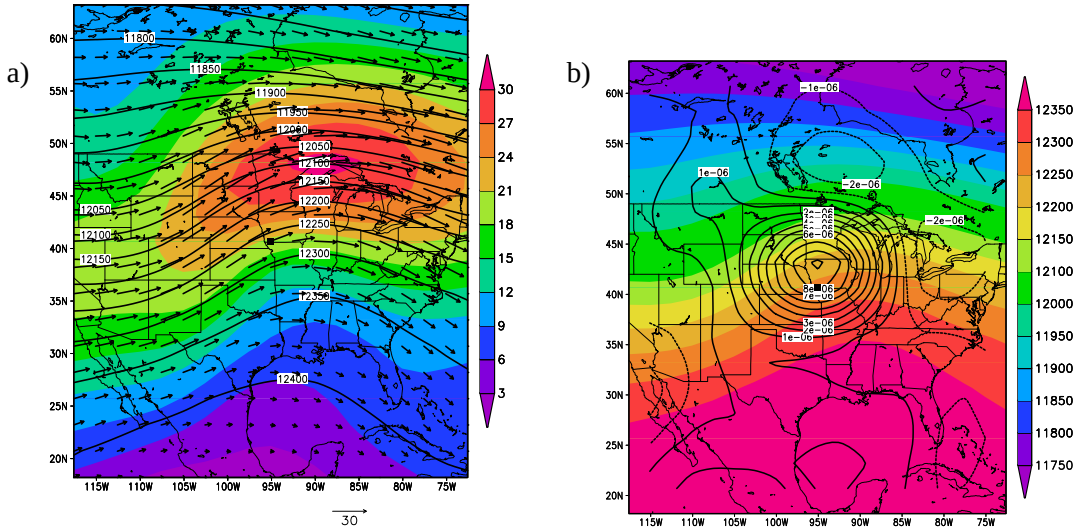

FIG. 6.4: As in Figure 6.1 but for 200 hPa. Map a) represents wind vectors, geopotential heights (contours, m) and isotachs (shaded, m s^{-1}) while Map b) represents hPa divergence (contours, s^{-1}) and geopotential heights (shaded, m).

(185 miles) north of the location of maximum rainfall (Figure 6.4) and west of the 200 hPa ridge apex. The veering of a relatively weak wind field between 850 hPa and 200 hPa supported the movement of storms along the baroclinic zone where the LLJ provided a steady supply of warm moist air.

The composite averages of $\sim$ 160 inland significant rainfall events revealed dynamically-consistent relationships between the preferred location of significant rainfall features that

led to synoptic-scale forcing. In the national composite, the synoptic scale forcing focused on an area slightly north of the centroid of maximum rainfall. These forcing features included the presence of strong moisture convergence into the area (Figure 6.1), low-level warm thermal advection (Figure 6.2), 500 hPa ascent due to inflexion point divergence (Figure 6.3) and weak cold thermal advection (Figure 6.3), a preferred location in the right entrance region of an anticyclonically-curved Polar jet (Fig 6.4), and the underneath the resulting bulls-eye of high-level divergence (Fig 6.4).

That these many synoptic-scale features were aligned spatially in a dynamically consistent relationship is a testimony to the correct use of three concepts of synoptic meteorology: (1) the compositing methodology was thoughtfully implemented (otherwise, the features would have been 'smeared' across the weather map), (2) the $\sim$ 160 members, when juxtaposed next to each other, were like mirror images of one another (discussions to follow will provide details of how closely related the various members were to their national or regional composite), and (3) significant precipitation events require the presence of key ingredients that are aligned–from a synoptician's perspective–in a classical manner (otherwise, significant rainfall would have failed to develop).

A common method for estimating vertical motion in the atmosphere utilizes the Q-G Omega equation (described extensively in Appendix A):

$$\underbrace{\left[\nabla_p^2 + \frac{f_0^2}{\sigma}\frac{\partial^2}{\partial p^2}\right]\omega}_{\mathbf{A}} = \underbrace{-\frac{f_0}{\sigma}\frac{\partial}{\partial p}\left[-\vec{v}_g \cdot \nabla_p(\zeta_g + f)\right]}_{\mathbf{B}} \underbrace{-\frac{R}{\sigma p}\nabla_p^2\left[-\vec{v}_g \cdot \nabla_p T\right]}_{\mathbf{C}}. \qquad (6.1)$$

Here, ω is vertical velocity in pressure coordinates, p is pressure, f_0 is the Coriolis parameter, σ is the static stability parameter, ζ_g is relative vorticity, f is planetary vorticity, R is the specific gas constant, T is temperature, and $\vec{v}_g$ is the geostrophic wind. Based on the national composite images just discussed, differential vorticity advection from the Q-G Omega equation ("Term B") played a minimal role at best in creating or sustaining the many significant rainfall events (Figure 6.5). Differential vorticity advection atop the centroid of

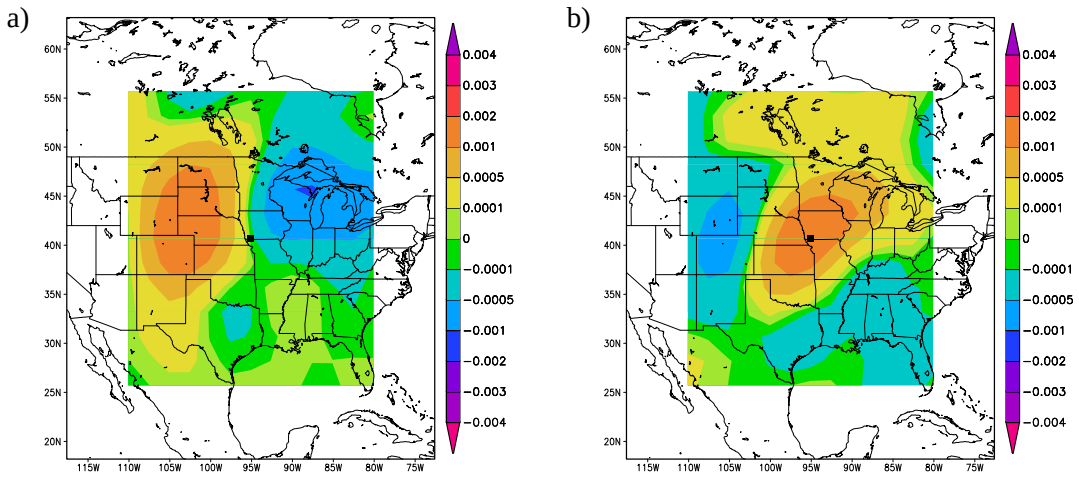

FIG. 6.5: As in Figure 6.1 but for the two terms on the right-hand side of the Q-G Omega equation. Map a) is the differential advection of absolute vorticity ("Term B", Pa km^{-2} hour^{-1}) through 500 hPa while Map b) is the 850 hPa thickness advection ("Term C", Pa km^{-2} hour^{-1}).

significant rainfall was ∼zero in value (even though a well defined vorticity maximum was ∼ 650 km (400 miles) west-northwest of the precipitation centroid; Figure 6.5). As Maddox and Doswell (1982) suggested, low-level warm thermal advection played a substantial role in initiating and sustaining the majority of significant rainfall events during their own investigations. In the national composite of the inland significant events, the maximum in warm thermal advection ("Term C") was centered on the centroid for significant rainfall (Figure 6.5); values ranged between 0.001 and 0.002 Pa km^{-2} hr^{-1}. The influx of warm air at lower levels strengthened the isentropic lift and released conditional instability, creating upward vertical motion conducive for heavy rainfall events (see Maddox and Doswell 1982). An in-depth explanation of how vertical motion in the atmosphere is created will rest on an understanding of terms in the Q-G Omega equation (Appendix A).

The national composite map images also have similarities with the results of Maddox et al. (1979), Junker et al. (1999) and Moore et al. (2003). However, there are fundamental differences between the work of the previous three teams and the work reported in this dissertation. First, all Chapter 6 results are quantitative in nature. Second, the results of this chapter are based on ∼ 160 unique events (compared to a fraction of that total by two of the three previous scientific teams). Third, the Chapter 6 results are dynamically

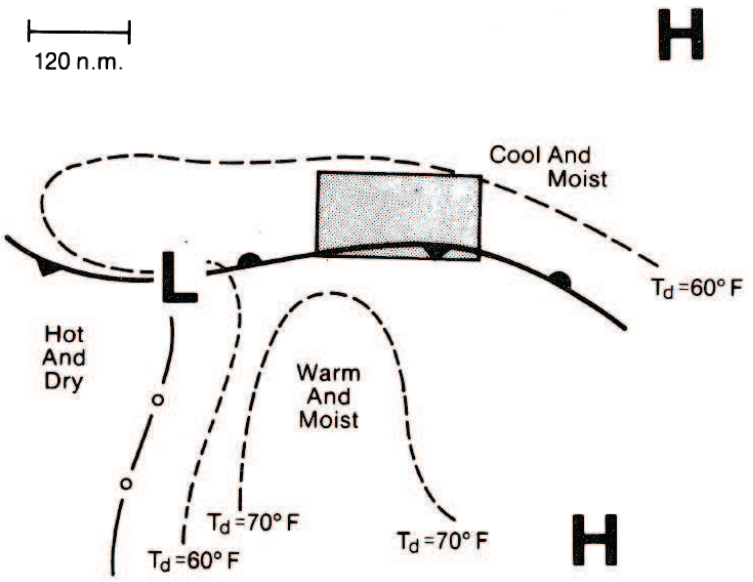

FIG. 6.6: Surface pattern for a typical Maddox frontal event. Potential for heavy rains and flash flooding exists in the shaded area. (From Maddox et al. 1979).

consistent through 200 hPa (other investigators either stopped at 850 hPa or drew schematic images of high-level features based on their understanding of the atmosphere). Fourth, the composites developed in this work used the hydrostatically consistent reanalysis data set and applied it to significant precipitation events (others interpolated between soundings or used limited model initialization data). Fifth, the results in this chapter quantitatively reveal that differential advection of vorticity played no role in sustaining significant rainfall events whereas thickness advection near the ground was a dominant force in creating ascending motion in a very focused area during the significant rainfall.

The national synoptic composite images documented in Figures 6.1– 6.4 are similar to the "frontal" pattern of flash flood events described by Maddox et al. (1979) and shown in Figure 6.6. Although Junker et al. (1999) examined only 12 heavy summertime events over a small portion of the Midwest during one summer, the fundamental ingredients in those events were present in the national composite maps composed of $\sim$ 160 events from eight inland regions across a 60-year period. At the end of their work, Moore et al. (2003) concisely summarized the work of Junker et al. (1999) by noting:

"Large-scale isentropic ascent, suggested by the lower-tropospheric warm-

> air advection and frontogenesis in the presence of the entrance region of the ULJ [upper-level jet], appears to be instrumental in lifting the layer to saturation. Moisture convergence within the left-exit region of the LLJ helps to initiate deep convection in the unstable layer along or above the frontal zone as parcels are lifted to their LFC [level of free convection]. The LLJ contributes to an axis of moisture convergence aligned nearly parallel to the surface boundary and cloud-layer winds, which promotes cell training and subsequent high rainfall totals."

Based on the work reported in Section 5.1.3, the vast majority (84%) of significant events occurred during the warm season. Consequently, one should not be surprised to learn that the current results have common characteristics with the work of Junker et al. (1999) and Moore et al. (2003). However, the inclusion of ~ 160 cases from many different inland regions demonstrates the applicability of the current composite models across a broad area of the United States. When composite maps were examined on a region-by-region basis (see Section 6.5 below), major differences with the work of Junker et al. (1999) become apparent. When the national composite images reported in Chapter 6 are compared with composites developed by Moore et al. (2003; studied 21 warm-season elevated MCSs over Missouri, Illinois, Iowa, eastern South Dakota and southwestern Minnesota from 1993–1998), several differences become apparent. Because the work of Maddox et al. (1979), Junker et al. (1999) and Moore et al. (2003) was based on a narrow dataset of rainfall events across a limited domain, the capability of the three subjective composites in representing significant rainfall events from other regions across the eastern United States has not been established.

6.4 National Composite Maps: Large-Scale Trends

To address the hypothesis of this dissertation, one must examine the synoptic environment and dynamical forcings associated with significant rainfall events for temporal trends. Due to the small sample size in each region, a national composite of non-tropical events from inland regions could reveal trends in the data, if the data are subdivided carefully. Data prior to 1980 constitute the first half of the dataset (74 events) and data from 1980

through 2008 constitute the second half (84 events).

Maps of Reanalysis data for the pre- and post-1980 events (similar to the Figures 6.1–6.5 shown above) revealed few differences. Both sets of composite images displayed a strong surface low to the west, a surface-temperature gradient indicating the presence of a baroclinic zone near the significant events, a strong LLJ conveying warm moist air from the south, an especially strong center of warm thermal advection at 850 hPa centered over the events, strong vertical velocities at 500 hPa, and very strong upper-level divergence at and slightly north of the event centroid.

To quantify variations between the pre- and post-1980 events, the differences between composite maps from the early and late event environments were examined (Figure 6.7). These difference maps between the late and early events revealed warmer surface temperatures well south and far to the northeast of the significant event locations during the latter decades. Cooler surface temperatures in latter decades were located far to the northwest when compared with the pre-1980 events. Surface pressure near and northwest of the significant event centroid was 2 hPa higher in the post-1980 events. Greater values of precipitable water occurred across much of the area south of the event centroid (Figure 6.7b) in the post-1980 events. An area of stronger downward vertical velocity at 500 hPa was present in the post-1980 events approximately 1000 km (620 miles) north-northwest of the significant event centroid (Figure 6.7c). The 200 hPa difference plot (Figure 6.7d) revealed the presence of a broad area of upper-level divergence in the post-1980 events southwest and east-northeast of the event centroid and the presence of weak convergence nearly coincident with the sinking motion at 500 hPa, northwest of the event centroid. Differences in the differential advection of vorticity (Term B) through 500 hPa were nearly an order of magnitude smaller than the features of positive vorticity advection at 500 hPa west of the event centroid. A plot of the differential thermal advection term from the Q-G omega equation (Term C) revealed no difference between the early and late events.

In order to evaluate the atmospheric moisture content across the domain, daily warm-season (April–September) precipitable water values were extracted from the reanalysis data

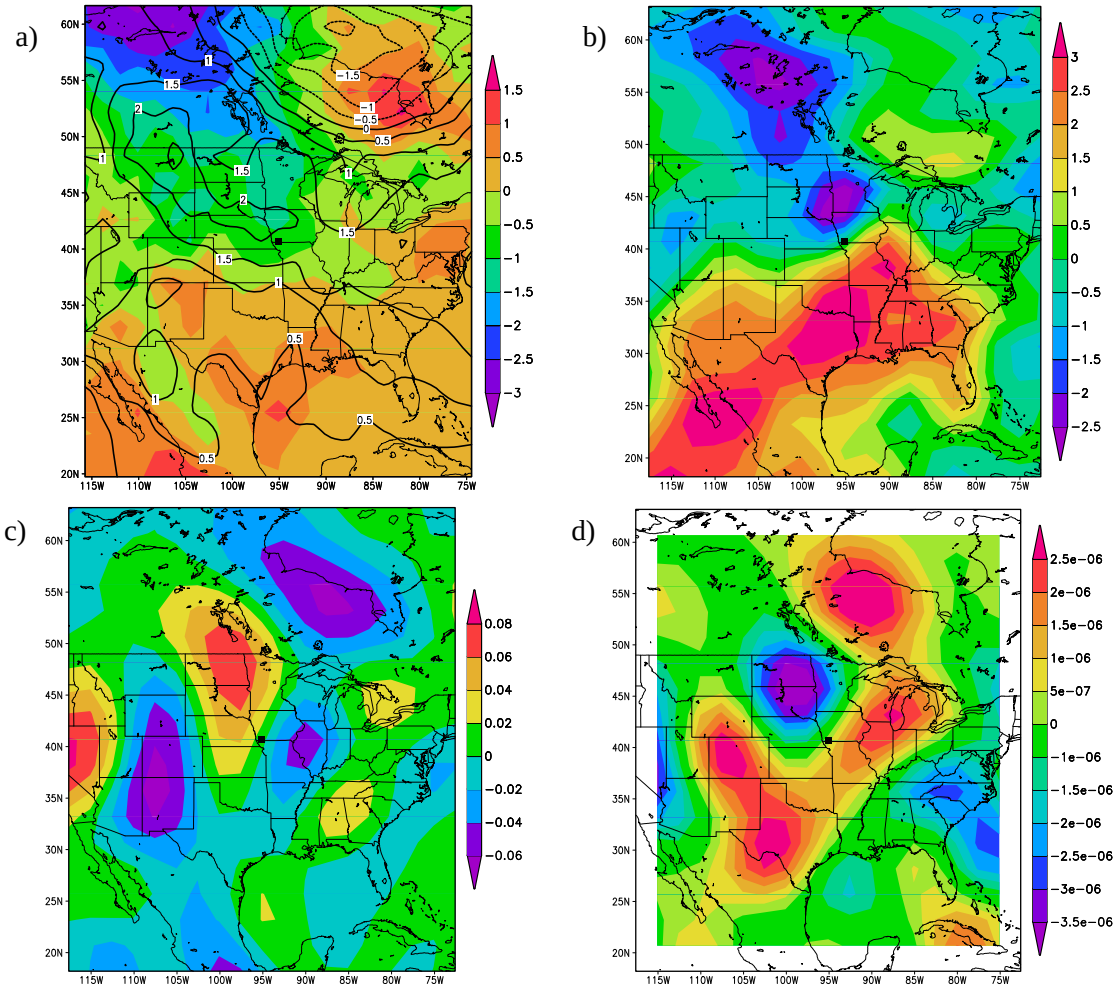

FIG. 6.7: As in Figure 6.1 but the difference between a) the MSLP (contours, hPa) and 1000 hPa temperature (shaded, K) composites of post-1980 significant events and pre-1980 significant events (more recent event composite minus older event composite b) precipitable water (mm), c) 500 hPa vertical velocity fields (Pa s^{-1}), and d) 200 hPa divergence fields (s^{-1}). Note that the scales on these plots differ from previous figures.

(Figure 6.8a). The average daily warm-season precipitable water value in the second half of the study period (1980–2008) was greater than that in the first half of the study period (1950–1979) across the Continental United States by up to 2 mm (Figure 6.8b). The observed increase in precipitable water represents a key ingredient in support of the observed increases in heavy and significant rainfall events documented in Chapter 5. The observed increase of seasonal precipitable water is consistent with the results shown in Figure 6.7b, which illustrates an increase in available precipitable water to the south of the significant event centroid on days with significant rainfall events. Regional precipitable water values

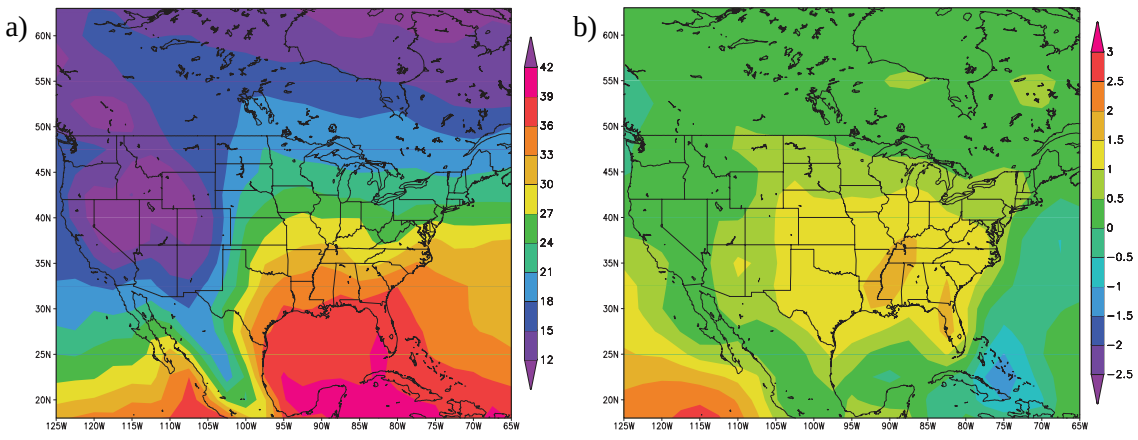

FIG. 6.8: a) Average warm-season (April–September) precipitable water values during the period 1950–2008 and b) the difference in precipitable water (mm) for all warm-season days during the period 1980–2008 versus the period 1950–1979 (most recent composite minus earlier composite).

associated with significant events averaged $\sim$ 20–50% higher than the daily averages for the 1950–2008 warm-season (April–September) calculated using the reanalysis data. Some individual events had much higher values than the seasonal average. The reasons behind the observed increases up to 5% above average seasonal precipitable water (in the lower Mississippi Valley) are beyond the scope of this dissertation; clearly further research on this topic is required.

Despite minor disparities between the early and late events, plots of most parameters revealed few large differences aside from the increase in precipitable water south of the centroid of post-1980 events. Consequently, one can conclude that no other appreciable changes in the synoptic environment or with the dynamical forcings associated with significant rainfall have occurred during the past 60 years.

6.5 Regional Composite Maps–Featured Results

Several significant rainfall events in each of the regions that bordered the Atlantic Ocean or the Gulf of Mexico (Regions 2, 3, 4, 9, and 11; Figure 4.4) originated from tropical systems (Table 5.2). The tropical events were flagged and not used. Consequently, some of the non-tropical composite maps in the coastal regions used fewer than 20 significant

events. Because reanalysis data for 2009 were not available at the time of this study, three significant events during 2009 (one from Regions 3, 10 and 11) were excluded and only 19 events were considered in these regions.

Table 6.1 lists the values of several key parameters at the significant event centroid for each PC region. The average precipitable water values were high (over 30 mm) for all but Region 1 in the northwest corner of the domain. The average precipitable water across all 13 regions was 36 mm; Region 3 (southeast Texas) had the highest regional value of 42 mm. Overall, the air was conditionally unstable with an average Total Totals[2] index value of 45; the highest value (52) occurred in Region 1 (MT/ND). The strongest composite value of the 850 hPa LLJ was found in Region 10 (near AR), with a speed of 23.5 knots. Region 13 (northern MS valley) had the strongest thermal advection at 850 hPa (96×10^{-6} K s^{-1}). The highest average θ_e value at the precipitation centroid was found in Region 8 (NE/SD) with a value of 337 K. The thickness advection (Term C of the Q-G Omega equation) had the strongest value in PC Region 12 (eastern KS through northern IL) of 0.0035 Pa km^{-2} hr^{-1}. However, the differential advection of vorticity (Term B) through 500 hPa had near-zero values at the event centroids for each region. The largest values of vorticity advection at 500 hPa were in Region 1 (0.001 Pa km^{-2} hr^{-1}) and Region 12 (0.0008 Pa km^{-2} hr^{-1}). At midlevels, Regions 7 (Ohio Valley) and 10 (near AR) had the strongest vertical velocity at 500 hPa (-0.26 Pa s^{-1}). At 200 hPa, the average upper-level divergence was 10×10^{-6} s^{-1} above the location of heaviest precipitation; Region 10 had the strongest regional value (15×10^{-6} s^{-1}).

A discussion of the meteorological features in the composite maps for each of the 13 PC Regions is either featured in this narrative (PC Regions 12, 2, 6, 13, and 11) or they were placed in Appendix C to serve as background information about the remaining PC Regions.

[2]Even though Peppler and Lamb (1989) nicely summarized the strengths and weaknesses of various stability indices, the reanalysis only provided the data for calculating one index–Total Totals. That index is not applicable for heavy rainfall environments, but severe weather environments.

TABLE 6.1: Statistics of the environments associated with the composite maps in each region and the average value across all regions. Individual values occur at the composite centroid. The LLJ, thermal advection, θ_e and thickness advection were from 850 hPa, the vertical velocity and vorticity advection were at 500 hPa and the divergence was at 200 hPa. Note to Reader: Seasonal biases have not been accounted for in the magnitudes reported for each variable.

Region	Pwat (mm)	TT (K)	LLJ (kts)	Thrm. Adv. ($\times 10^{-6}$ K s^{-1})	θ_e (K)	Thick. Adv. (Pa km^{-2} hr^{-1})	Vert. Vel. (Pa s^{-1})	Vort. Adv. (Pa km^{-2} hr^{-1})	Div. ($\times 10^{-6}$ s^{-1})
1	25	52	7.8	30	331	0.0025	-0.17	0.00100	11
2	34	42	17.5	35	319	0.0030	-0.19	-0.00070	9
3	42	42	14.2	10	333	-0.0004	-0.11	0.00010	10
4	34	39	8.5	15	325	0	-0.0500	-0.00020	5
5	39	45	17.5	55	333	0.0003	-0.11	0.00050	6
6	35	48	15.5	26	334	0.0020	-0.15	0	11
7	41	45	22.0	61	332	0.0010	-0.26	0.00010	10
8	37	49	15.5	67	337	0.0030	-0.12	-0.00010	9
9	40	46	17.9	40	330	0.0015	-0.17	-0.00050	10
10	41	47	23.5	55	331	0.0013	-0.26	0.00010	15
11	32	41	7.8	15	321	-0.0001	-0.09	0.00030	6
12	39	46	16.1	67	333	0.0035	-0.16	-0.00100	11
13	34	47	17.5	96	328	0.0025	-0.13	0.00080	12
Avg	36	45	15.5	54	330	0.0015	-0.15	0.00003	10
σ	4.7	3.6	4.9	25.4	5.2	0.0013	0.1	0.00056	2.7

6.5.1 Region 12: Eastern KS Through Northwestern IL

The majority of the 20 significant rainfall events in PC Region 12 occurred in one of two seasons: the usual season for early summer rains (8 events occurred during June–July) or the fall transition season (8 events occurred during September–October). The significant events in Region 12 occurred in the northeast quadrant of a surface low in the warm sector of a baroclinic zone (Figure 6.9). The composite maps revealed that the strongest atmospheric forcing was located over or upwind (i.e., back to the southwest) of the preferred location for significant rainfall. For example, the rainfall maximum was located at the nose of a low-level jet (also part of the warm conveyor belt) coincident with a narrow corridor of concentrated precipitable water (39 mm); the inferred isentropic ascent reached a maximum slightly to the southwest of the heaviest rainfall. Low-level convergence (magnitude $> 1 \times 10^{-5}$ sec^{-1}) was strongest 240 km (150 miles) to the southwest of the centroid. The center of significant rainfall was underneath the area of maximum thermal advection (67×10^{-6} K sec^{-1}) at 850 hPa and near the right edge of a ridge of high θ_e values (Figure 6.9).

In the middle of the troposphere, the maximum ascent (-0.16 Pa sec^{-1}) also was per-

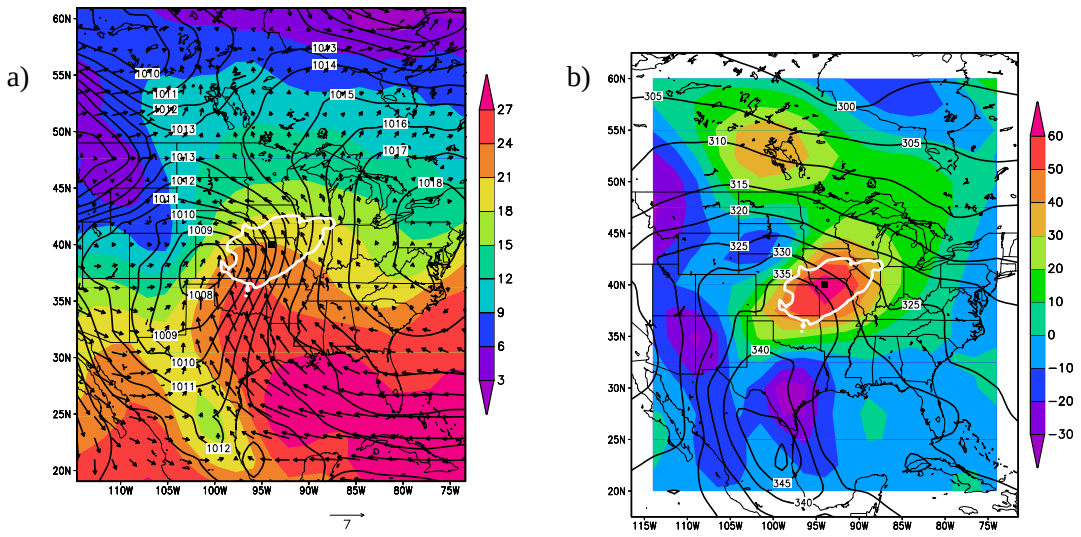

FIG. 6.9: As in Figure 6.1 but the a) MSLP (contours, hPa), 1000 hPa wind vectors (m s^{-1}) and 1000 hPa temperature (shaded, K) and b) 850 hPa θ_e (contours, K) and temperature advection (shaded, K s^{-1}) for Region 12. White line shows 0.35 isopleth for PC Region 12 (from Figure 4.4).

fectly aligned with the low-level thermal advection pattern at 850 hPa (located above the event centroid) and slightly northeast of the maxima of surface-based convergence (Figure 6.10). The location of significant rainfall occurred in the right entrance region of the anticyclonically curved polar jet located 725 km (450 miles) northeast of the significant rainfall (Figure 6.10). Tropopause-level divergence (1.2×10^{-5} sec^{-1}) was over and slightly north of the rainfall maximum; it was created by being in a 'textbook' location relative to all other meteorological features revealed in these composites.

Vorticity advection at 500 hPa was weakly positive over and approximately 450 km (250 miles) southwest of the centroid of significant rainfall. However, differential vorticity advection through 500 hPa was weakly negative (-0.001 Pa km^{-2} hr^{-1}) at the significant rainfall location (Figure 6.11). In contrast, the thickness advection at 850 hPa was very strong (0.0035 Pa km^{-2} $hour^{-1}$) and was centered directly over the precipitation centroid (Figure 6.11).

To illustrate an example of the internal consistency of the regional composites, the composite map of vertical velocities and geopotential heights at 500 hPa for Region 12 is shown with images for each of the 20 members in this region (Figure 6.12). A linear spatial corre-

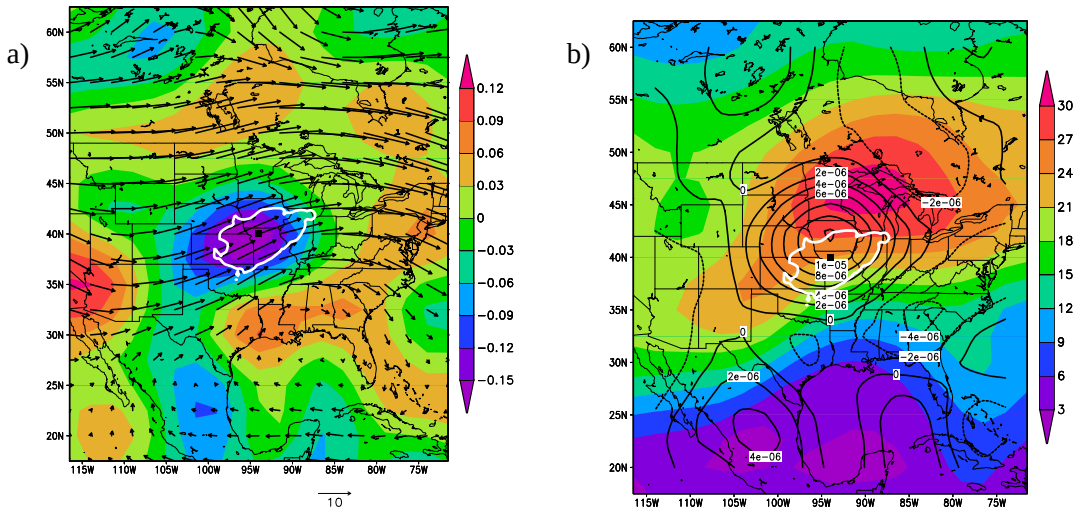

FIG. 6.10: As in Figure 6.9 but the a) 500 hPa vertical velocity (contours, Pa s^{-1}) and wind vectors (m s^{-1}) and b) 200 hPa divergence (contours, s^{-1}) and isotachs (shaded, m s^{-1}) for Region 12.

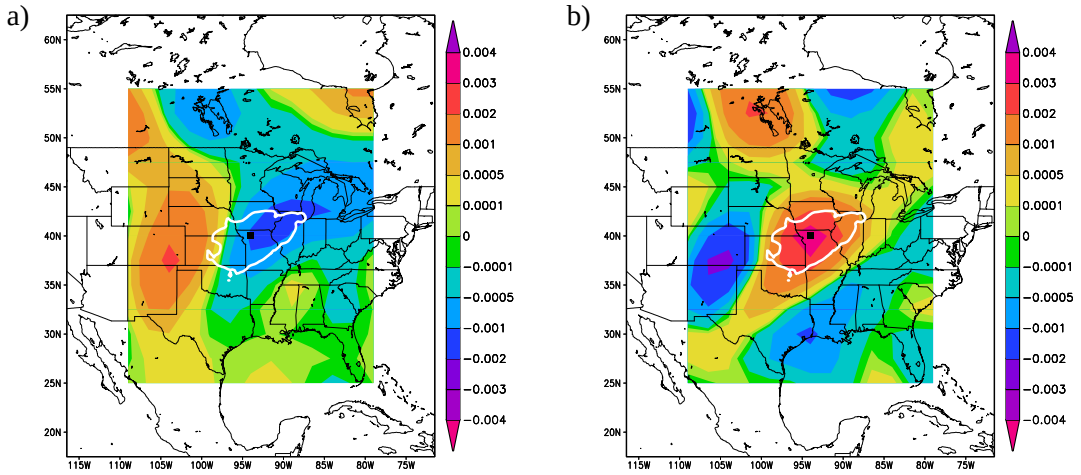

FIG. 6.11: As in Figure 6.9 but the a) 500 hPa differential absolute vorticity advection ("Term B", Pa km^{-2} $hour^{-1}$) and b) 850 hPa thickness advection ("Term C", Pa km^{-2} $hour^{-1}$) for Region 12.

lation coefficient between the 500 hPa geopotential height values for each individual case and the composite field quantified the robustness of the composite. A high correlation coefficient would indicate that there is agreement between the patterns of the composite field and the individual fields (e.g., Moore et al. 2003). In contrast, a low correlation coefficient may indicate that the patterns are shifted, there is little resemblance with the composite field, or the individual case may have a pattern opposite from that of the composite (Moore

et al. 2003). The median correlation value of 500 hPa geopotential heights for each of the 20 cases in this region was 0.89. The 200 hPa divergence field had a median correlation coefficient of 0.37. The high correlation values of the geopotential height and low correlation values of the derived 200 hPa divergence field were consistent with the results of Moore et al. (2003). These authors postulated that the horizontal derivatives involved in the calculation of divergence amplifies ‘noise’ in the data, which decreases the correlation values.

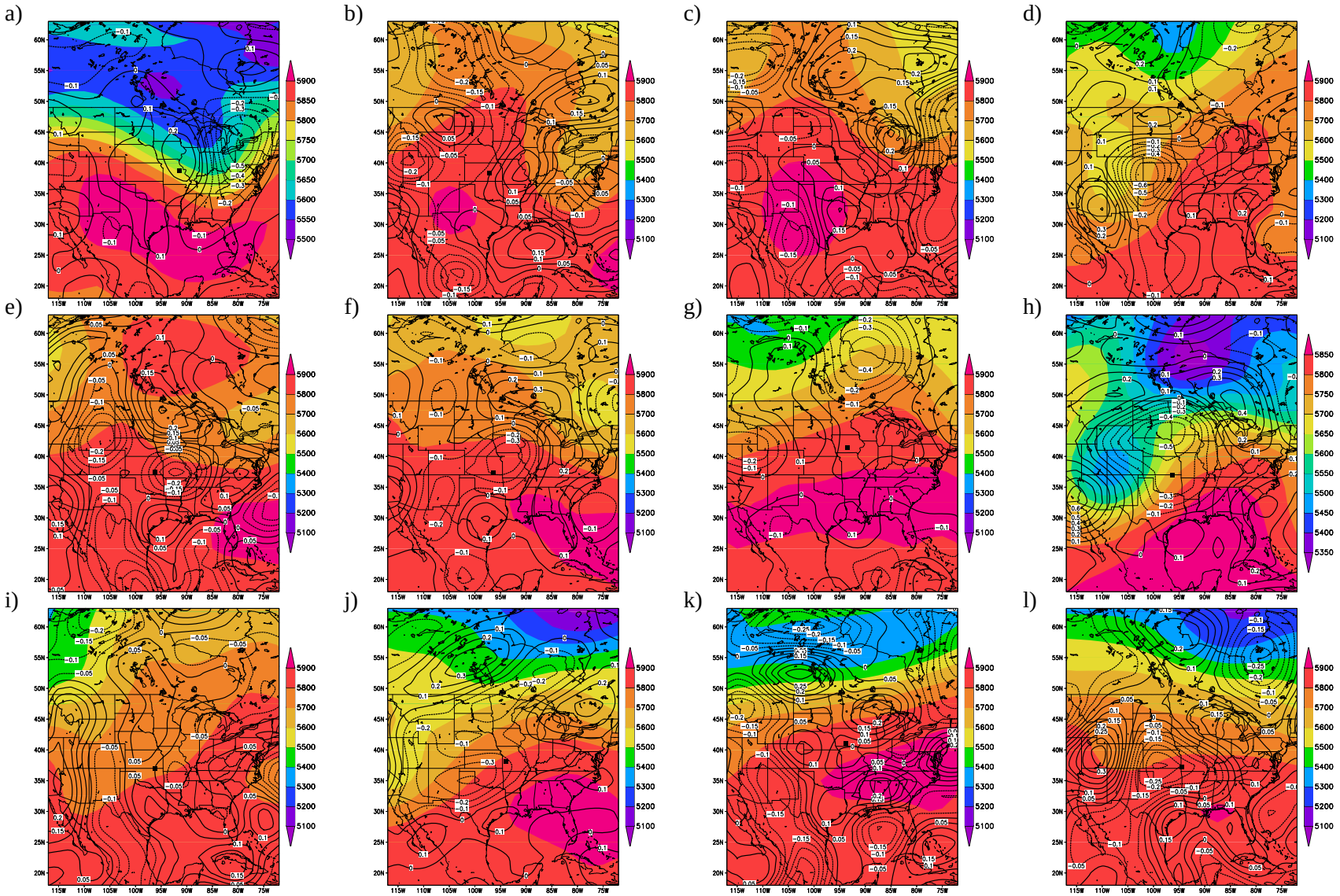

FIG. 6.12: Reanalysis plots of 500 hPa vertical velocity (contours, Pa s^{-1}) and geopotential heights (shaded, *m*) for each of the 20 members that compose PC Region 12 (a through t). Individual events, listed here chronologically, are detailed in Appendix B. The final plot, u, is the composite image of the 20 significant event plots (a through t).

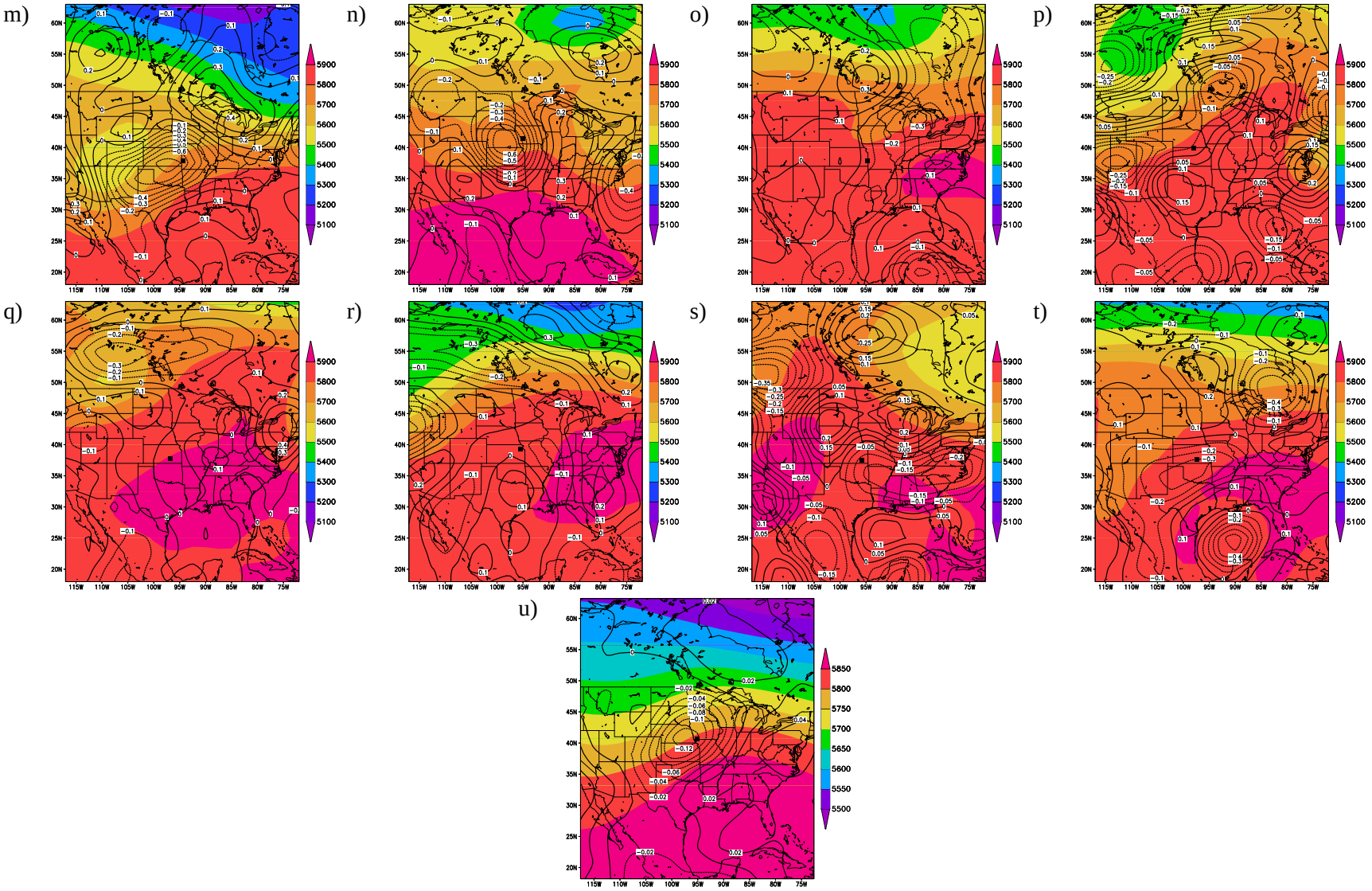

FIG. 6.12: (*Continued*).

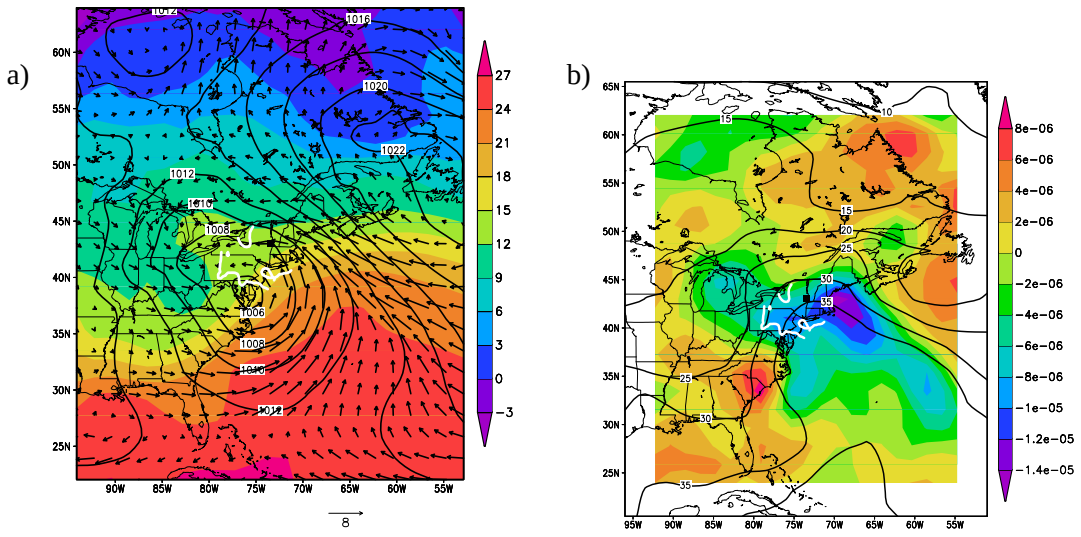

FIG. 6.13: As in Figure 6.1 but the a) MSLP (contours, hPa), 1000 hPa wind vectors (m s^{-1}) and 1000 hPa temperature (shaded, K) and b) 1000 hPa precipitable water (contours, mm) and divergence (shaded, s^{-1}) for Region 2. White line shows 0.35 isopleth for PC Region 2 (from Figure 4.4).

6.5.2 Region 2: Eastern PA Through ME

The average location of significant rainfall was positioned 450 km (280 miles) north-northeast of a closed low in the field of mean sea level pressure (i.e., maximum rainfall was in the northeast quadrant), on the cyclonic-shear side of a surface-based wind maxima, and slightly north of an inferred warm front (Figure 6.13; based on composite wind directions and the strong gradient of θ_e along coastal sections of PC Region 2). Due to the strong southeasterly winds and temperature gradient vector approximately perpendicular to the coast, implied isentropic ascent was located in the Atlantic just off the coast of New England. Once onshore, these winds also were forced to rise across higher topography; this further enhanced vertical motion. The significant rain area also was located at the nose of a precipitable water ridge (maximum values exceeded 3.6 cm) while a convergence bulls-eye was located 200 km (125 miles) east of the center of significant rainfall (Figure 6.13). The rainfall maximum appears unrelated to the ill defined 1000 hPa θ_e ridge (not shown).

At 850 hPa, the non-tropical significant events occurred on the eastern side of a deep trough, in the cyclonic-shear side of the low level jet, in the left exit region of the 850 hPa

wind maxima (Figure 6.14), and at the nose of a weak θ_e ridge (320 K; Figure 6.14). Strong warm thermal advection ($> 40 \times 10^{-6}$ K sec^{-1}) was aligned with the nose of the 850 hPa jet 300 km (190 miles) east of the significant rainfall location (Figure 6.14); the thermal advection also was co-located with the inferred isentropic lift at 1000 mb. The thickness advection through 850 hPa (Term C in the Q-G Omega equation) reached a maxima just upstream from the heaviest rainfall location; these magnitudes exceeded 0.004 Pa km^{-2} hour^{-1} (Figure 6.14). A strong convergence maxima at 850 hPa was located in between the areas of strong cold and warm air advection, and slightly north of the surface low pressure center (Figure 6.14).

Midway through the troposphere, a near-classic spatial relationship (Figure 6.15) existed between the left exit region of a cyclonically curved sub-tropical jet maxima (and a tight isotach gradient along the flow) and the inflexion point between the synoptic-scale ridge to the east and trough to the west. These short-wave-length features created a distinct region of weak ageostrophic divergence. In fact, a well-identified bulls-eye of synoptic-scale vertical velocities (magnitudes exceeded -0.18 Pa sec^{-1}) extended over the center of significant precipitation (Figure 6.15). Thermal advection at 500 hPa reached a maximum 300 km (190 miles) to the northeast of the significant rainfall centroid (Figure 6.15). At the rainfall centroid, vorticity advection at 500 hPa exceeded 0.0003 sec^{-2}, but differential vorticity advection through the 850–200 hPa layer (Term B in Equationřefqgomegaeq1) was weakly negative and an order of magnitude smaller than the second term evaluated at 850 hPa.

Although coupled jets were not evident at 500 hPa, two coupled jets were clearly apparent in the composite map at 200 hPa (Figure 6.16). Thus, a classic spatial relationship with two aligned transverse ageostrophic circulations was readily evident near the tropopause with a well-defined maximum of divergence (magnitudes exceeded 9×10^{-6} sec^{-1} centered slightly northeast of the significant rainfall centroid; Figure 6.16). Most importantly, the composite map of features at 200 hPa mirrored the work of Uccellini and Kocin (1987), who studied heavy snowfall events along the east coast of the United States.

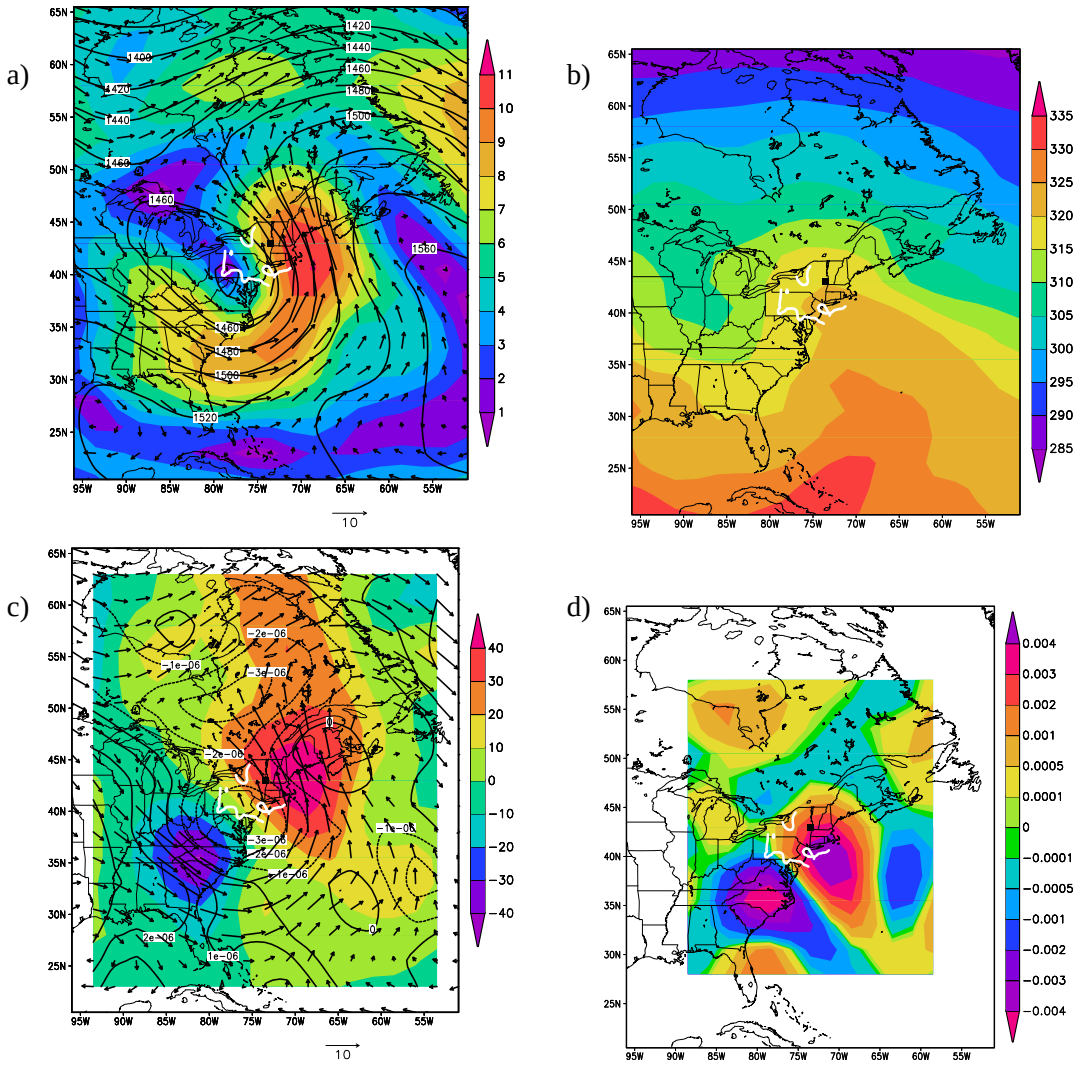

FIG. 6.14: As in Figure 6.13 but a) the 850 hPa wind vectors (m s^{-1}), geopotential heights (contours, m), and isotachs (shaded, m s^{-1}), b) 850 hPa θ_e (K), c) 850 hPa wind vectors (m s^{-1}), divergence (contours, s^{-1}), and temperature advection (shaded, K s^{-1}), and d) 850 hPa thickness advection ("Term C", Pa km^{-2} $hour^{-1}$) for Region 2.

When the composite images from PC Region 2 were compared with the work of others, they had the classic look of an Uccellini and Kocin (1987) east-coast snowstorm (Figure 6.17): coupled jets, inflection point divergence, strong on-shore flow of moist air at lower levels, and strong positive vertical velocities. These vertical velocities were spatially located about midway between the location of convergence at 850 hPa (approximately 200 km or 125 miles southwest of the mean location for significant rainfall) and upper level divergence (located just northeast of the centroid of significant rainfall). In addition, the

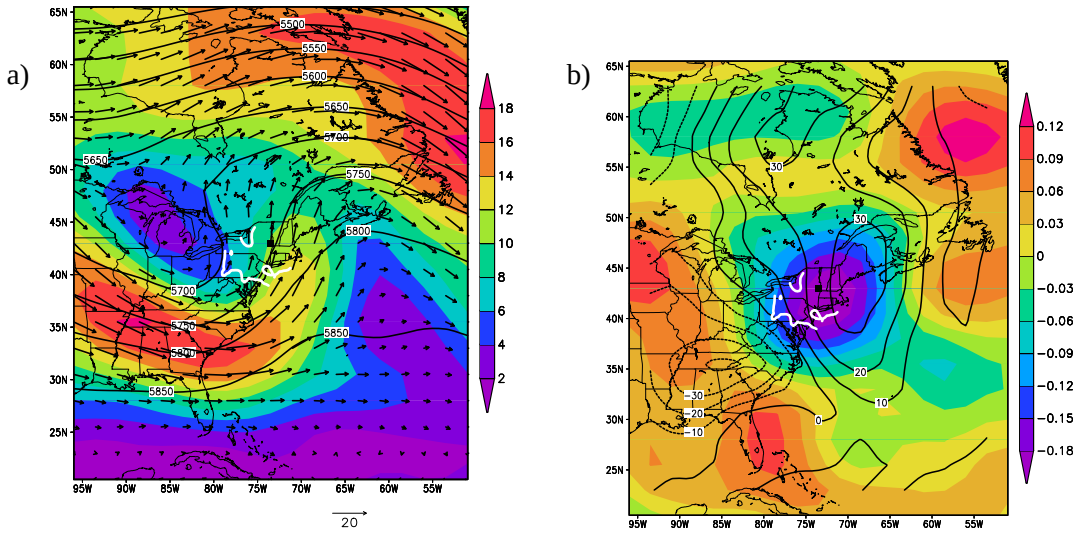

FIG. 6.15: As in Figure 6.13 but a) 500 hPa wind vectors (m s^{-1}), geopotential heights (contours, m), and isotachs (shaded, m s^{-1}) and b) 500 hPa thermal advection (contours, K s^{-1}) and vertical velocity (shaded, Pa s^{-1}) for Region 2.

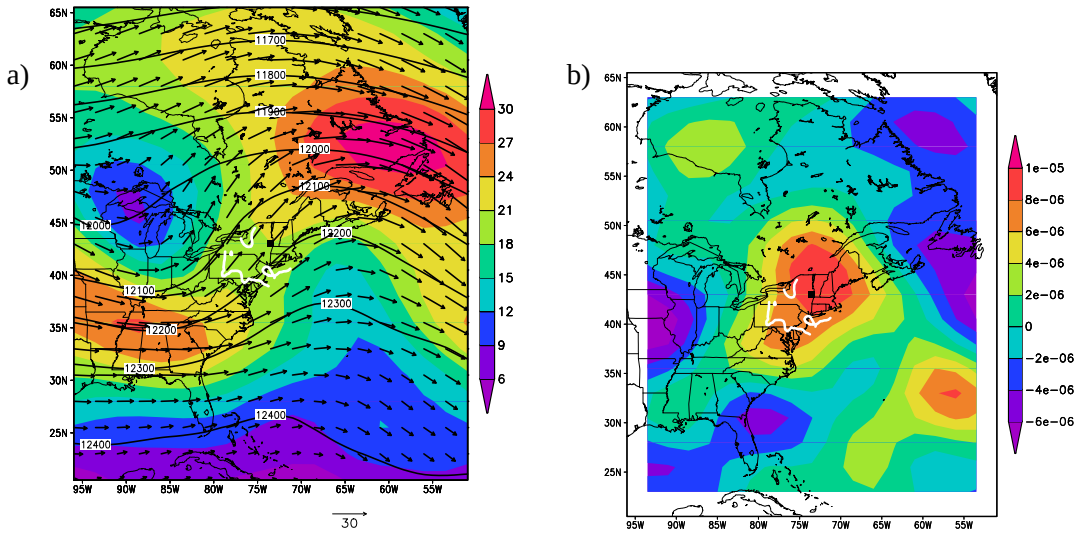

FIG. 6.16: As in Figure 6.13 but a) 200 hPa wind vectors, geopotential heights (contours, m) and isotachs (shaded, m s^{-1}) and b) 200 hPa divergence (contours, s^{-1}) for Region 2.

composite maps of Region 2 closely resembled the work of Junker et al. (1999) in that the rainfall events occurred on the cyclonic shear side of the low-level jet apex, in the northeast quadrant of a surface low with the preferred rainfall location west of the ageostrophic divergence aloft, and downwind from the thermal advection and isentropic ascent at low levels. This "sloped response" is consistent with the work of Uccellini and Kocin (1987) and the

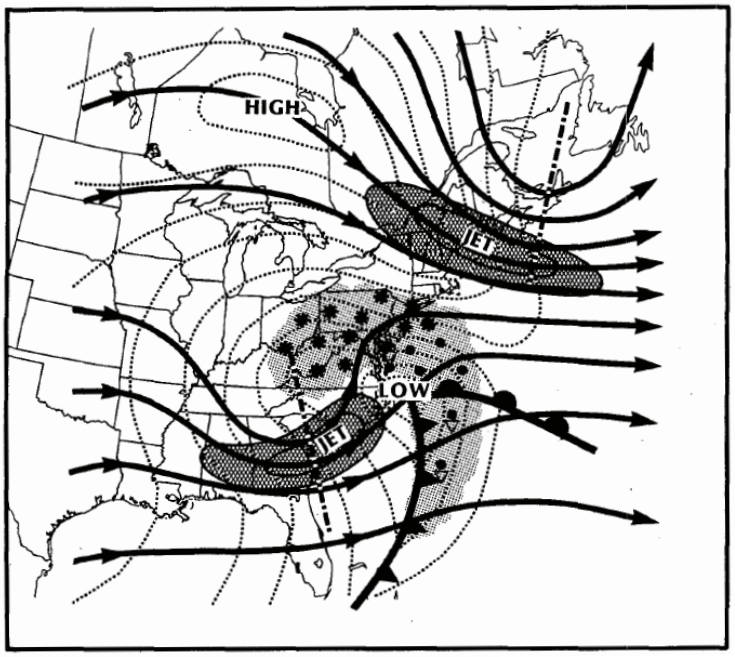

FIG. 6.17: Schematic of surface cold and warm fronts, high and low pressure centers, sea level isobars (dotted), precipitation (shading–asterisks represent snowfall; dots represent rain), upper-level flow (arrows), upper-level trough axes (dot-dashed), and jet streaks (cross-hatched shading) associated with a "typical" heavy snow event along the East Coast (from Uccellini and Kocin 1987).

experience of most operational forecasters–i.e., the atmosphere operates along sloped isentropic surfaces. The implication is that latent heat has been released in large quantities during the significant events that occurred in Region 2; however, an isentropic vertical cross section bisecting the location of significant rainfall would be needed to unambiguously reveal this fact (cf. Uccellini and Kocin 1987). Because thermal advection at 500 mb was weakly positive and lower-level features more strongly positive, the events in Region 2 were driven by synoptic-scale forces, though maybe not quite to the magnitude discovered in Region 12. Perhaps features in the significant rainfall composites from PC Region 2 resembled the work of Uccellini and Kocin (1987) so closely results from the fact that 7 of the 12 significant events occurred late in the warm season (August through October), and one during late November, when fall-like features can occur.

6.5.3 Region 6: Western TX, Western OK, and Southwestern KS

The average location of significant rainfall in PC Region 6 occurred at the nose of the low-level jet in a region of strong southeasterly flow from the Gulf of Mexico (Figure 6.18) that ascended along the terrain gradient. Due to the topography of the Southern Plains, southeasterly winds can cause terrain-induced lift. This region of significant rainfall was located 400 km (250 miles) east-northeast of the apex of a distinct θ_e ridge (values over 330 K). This thermal ridge was co-located with a strong gradient of dew point temperature, likely indicting a dry line (Figure 6.18). The strong cross-isodrosotherm flow of the surface winds was also conducive to lift. Of the 20 significant events in this region, nine occurred during the dry-line months of May-June; an additional six events occurred during the secondary rainy season of October. A closed surface low 225 km (140 miles) southwest of the rainfall maxima (not shown) no doubt contributed to the significant rainfall events occurring in the northeast quadrant of the developing low. The significant events occur on the western tip of a narrow moist tongue from the Gulf of Mexico (Figure 6.18) with over 3.5 cm of available precipitable water. Different from Region 12, thermal advection peaked 160 km (100 miles) west of the significant events. Maximum values of surface-based convergence also were co-located with the θ_e ridge and the strong gradient of dew point (Figure 6.18) even further west of the significant event center.

By 850 hPa, the average location of heavy rainfall was classically located at the nose of a very strong southerly jet and at the center of substantial warm air advection (Figure 6.19). The thermal advection also was evaluated using thickness advection and Term C of the Q-G Omega equation in Appendix A). These terms display a maximum directly over the significant event center (Figure 6.19; the magnitude of thermal/thickness advection was almost 30×10^{-6} K sec^{-1} and $0.002 - 0.003$ Pa km^{-2} hour^{-1}, respectively. The spatial relationships of these features perfectly mirrored the work of Junker et al. (1999). In addition, the convergence maximum was located well to the west of the preferred location of significant rainfall (Figure 6.19; this convergence feature seemed aligned with the location of the

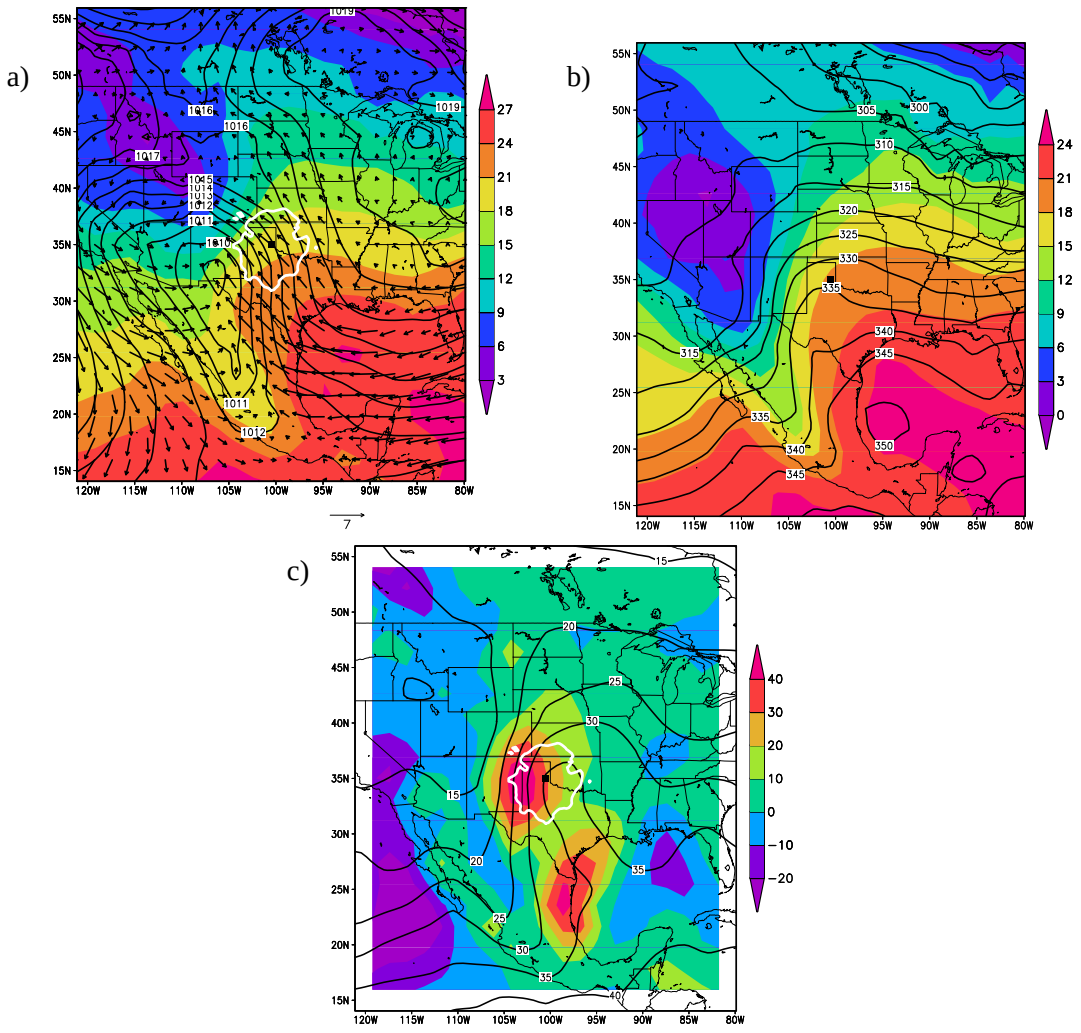

FIG. 6.18: As in Figure 6.13 but a) the MSLP (contours, hPa), 1000 hPa wind vectors (m s^{-1}) and 1000 hPa temperature (shaded, K), b) 1000 hPa θ_e (contours, K) and T_d (shaded, $^{\circ}C$), and c) 1000 hPa precipitable water (contours, mm) and temperature advection (shaded, K s^{-1}) for Region 6. White line shows 0.35 isopleth for PC Region 6 (from Figure 4.4).

dry line, its very strong gradient of dew point temperature, and the 850 hPa θ_e ridge (not shown).

Midway through the troposphere, the average location of significant rainfall was located in the right exit region of a weak upper level jet (Figure 6.20). For significant rainfall to have occurred in this average location relative to the jet at 500 hPa, transverse ageostrophic circulations and isentropic lift had to have initiated strong convection due–most likely–to a close-to-the-ground LCL. An inspection of individual proximity soundings from the PC Region revealed the LCL was less than 100 hPa above ground level and a simple calculation

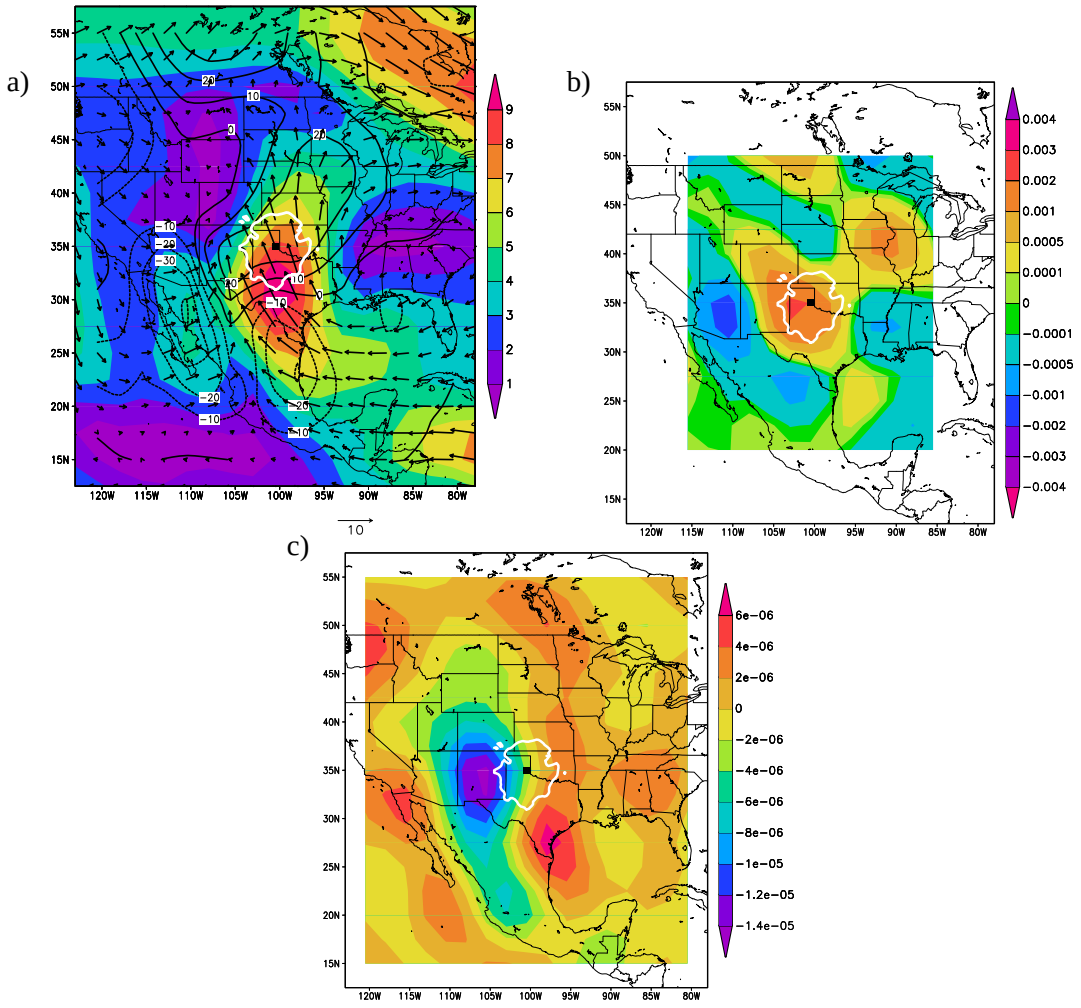

FIG. 6.19: As in Figure 6.18 but a) the 850 hPa temperature advection (shaded, K s^{-1}) and wind vectors (m s^{-1}), b) 850 hPa thickness advection ("Term C", Pa km^{-2} $hour^{-1}$), and c) 850 hPa divergence (s^{-1}) for Region 6.

places the LCL at 140 m above the surface (Lawrence 2005). Consequently, very little lifting was required to lift a parcel to its LCL at the center of significant rainfall. Vorticity advection at 500 hPa and differential vorticity advection through 500 hPa (i.e., Term B in the quasi-geostrophic omega equation) were both approximately zero at the centroid of significant rainfall, though a substantial vorticity maximum was located over 1120 km (700 miles) to the west-southwest (not shown).

Upward vertical velocities at 500 hPa (greater in magnitude than -0.21 Pa s^{-1}; (Figure 6.21) were present west-southwest of the significant precipitation events, not far from the classic location where curvature-induced ageostrophic divergence is typically found

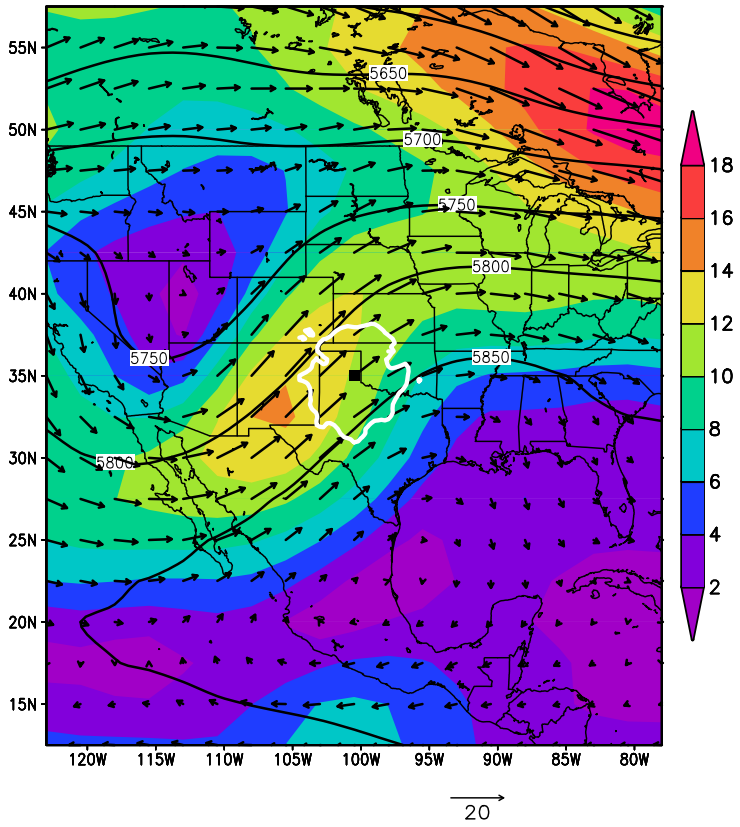

FIG. 6.20: As in Figure 6.18 but 500 hPa wind vectors (m s^{-1}), geopotential heights (contours, m), and isotachs (shaded, m s^{-1} for Region 6.

(Uccellini and Kocin 1987). A well identified temperature "no change line" was oriented north-to-south slightly west of the location of heavy rainfall (Figure 6.21), revealing weak cold thermal advection aloft in the composite mean that was west of the rainfall centroid but over the western half of the concentrated warm thermal/thickness advection noted at 850 hPa.

Near the tropopause, strong divergence was located above the significant rainfall events (Figure 6.22); it was above and slightly east of the warm thermal/thickness advection at 850 hPa and the cold thermal advection at 500 hPa (Figure 6.21), suggesting that the thermodynamical properties of the atmosphere at lower levels had a strong role in helping dynamical forcings create the preferred location of significant rainfall.

The meteorological features in this PC region resemble the work by Junker et al. (1999), but are rotated 45° to the northwest. The 200 mb jet is northwest of the significant event

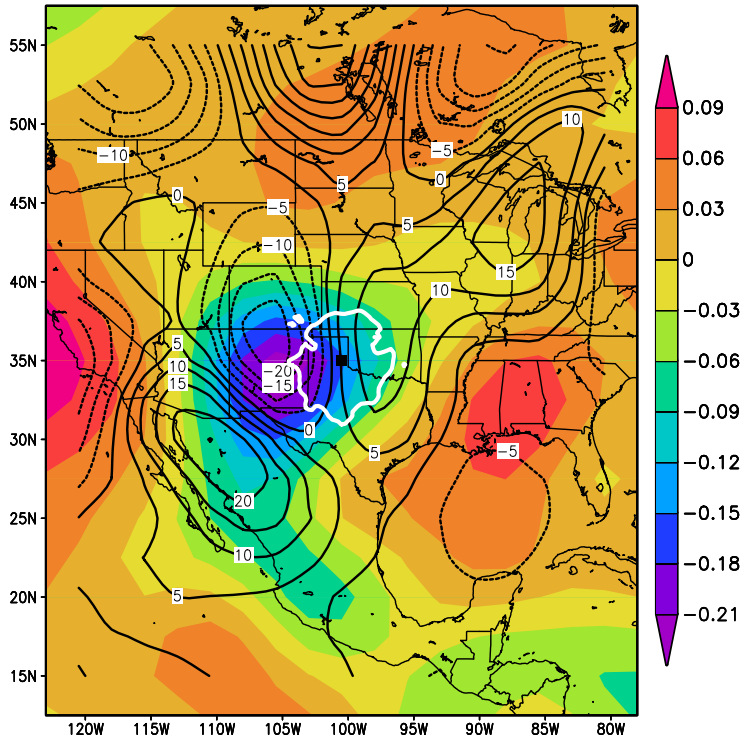

FIG. 6.21: As in Figure 6.18 but 500 hPa thermal advection (contours, K s^{-1}) and vertical velocity (shaded, Pa s^{-1}) for Region 6.

centroid, but still nearly perpendicular to the LLJ orientation (cf. Junker et al. 1999). These meteorological ingredients were aided by the low LCL (140 m above ground) and the associated isentropic lift in the right exit region of a 500-hPa jet.

6.5.4 Region 13: Eastern ND Through Western WI

The centroid of significant rainfall was in a text-book location of a composite cyclonic circulation (northeast quadrant, along a baroclinic zone, and at the termination of a long finger of precipitable water $>$ 33 mm extending northward from the Gulf of Mexico; Figure 6.23). A well-defined baroclinic zone, determined by inspecting the composite vector wind field across the Upper Mississippi River Valley, was located at the nose of a composite low-level jet, in a narrow corridor of mass convergence (1.2×10^{-5} K sec^{-1}), and co-located with an axis of warm thermal advection ($> 20 \times 10^{-6}$ K sec^{-1}), not shown. These features extended northeast from the cyclonic circulation toward the centroid of sig-

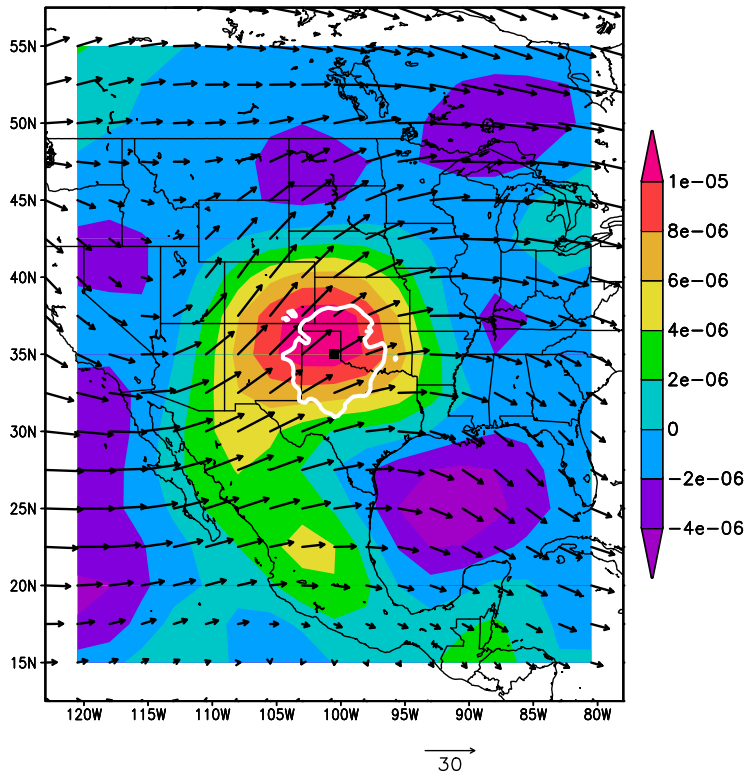

FIG. 6.22: As in Figure 6.18 but 200 hPa divergence (shaded, s^{-1}) and wind vectors (m s^{-1}) for Region 6.

nificant rainfall. Most were warm season events (16 of the 20 events occurred between June and September).

By 850 hPa, the warm thermal advection was even better defined ($> 80 \times 10^{-6}$ K sec^{-1}) and extended northeast/southwest through the centroid of significant rainfall (Figure 6.24). While the mass convergence (not shown) was weaker, it was displaced northwest of the surface-based convergence to lie along the expected synoptic-scale location for an 850-hPa front relative to its surface location (west of the surface low). A strong polar jet at 500 hPa was 1100 km (680 miles) northeast of the rainfall maximum (Figure 6.24), placing the preferred location for significant rainfall in the right entrance region of the weakly curved anticyclonic flow. As expected for a 'text book' set of events, strong vertical motion at 500 hPa (> -0.12 Pa sec^{-1}) was centered exactly over the location for significant rainfall (Figure 6.24). The center of maximum ascent was approximately co-located with the center of maximum tropopause-level divergence ($> 1.2 \times 10^{-5}$ K sec^{-1}).

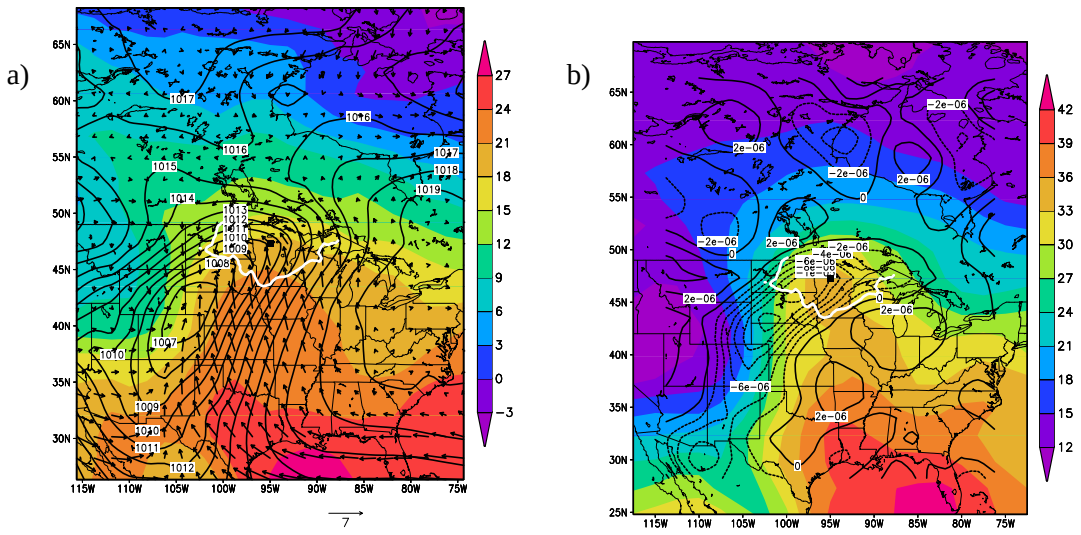

FIG. 6.23: As in Figure 6.13 but a) the MSLP (contours, hPa), 1000 hPa wind vectors (m s^{-1}) and 1000 hPa temperature (shaded, K) and b) the 1000 hPa divergence (contours, s^{-1}) and precipitable water (shaded, mm) for Region 13. White line shows 0.35 isopleth for PC Region 13 (from Figure 4.4).

The composite of 500 hPa vorticity advection was weakly positive upstream from the centroid of significant rainfall while differential vorticity advection through 500 hPa (Term B) was more supportive of tropospheric ascent (0.002 Pa km^{-2} $hour^{-1}$) and strong convection approximately 320 km (200 miles) to the southwest (Figure 6.25). On the other hand, thickness advection at 850 hPa (almost 0.003 Pa km^{-2} $hour^{-1}$) was strongly supportive of strong convection in a large oval-shaped area stretching southwest to northeast, centered on the centroid of significant rainfall.

It is difficult to discriminate any differences between the composites models of Regions 12 and 13; both sets of maps mirrored the lower-level composite models in the work of Junker et al. (1999) and the upper-level composite models of Uccellini and Kocin (1987). The composite models produced in Regions 12 and 13 also were internally consistent when the various forcing functions were inter-related.

6.5.5 Region 11: Mid-Atlantic States

Across the Mid-Atlantic States (PC Region 11), 18 of the 20 significant events occurred during August, September and October. Of the 20 significant rainfall events in Region 11,

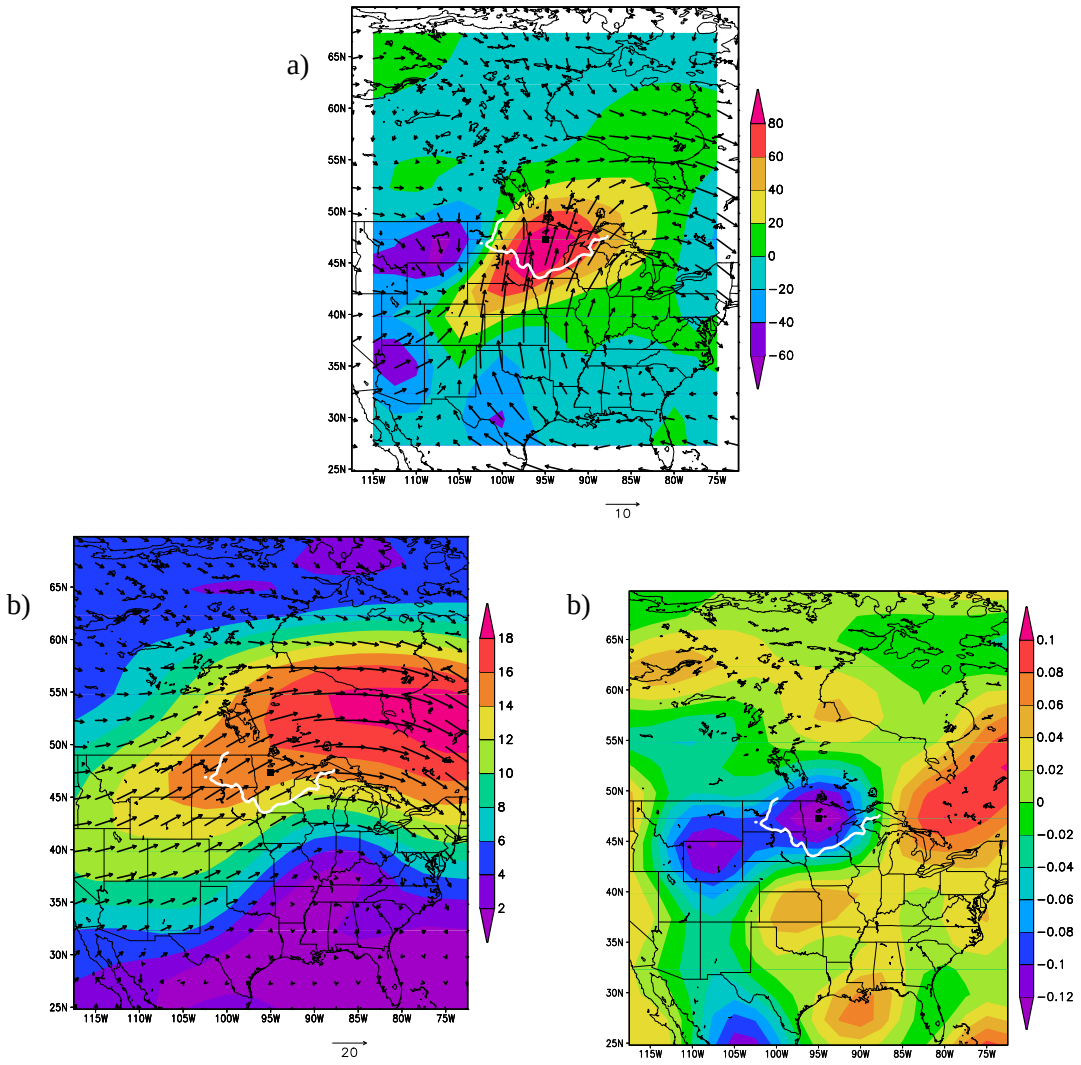

FIG. 6.24: As in Figure 6.23 but a) the 850 hPa temperature advection (shaded, K s^{-1} and wind vectors (m s^{-1}), b) the 500 hPa isotachs (shaded, m s^{-1}) and wind vectors (m s^{-1}), and c) the 500 hPa vertical velocity (contours, Pa s^{-1}) for Region 13.

12 were classified as tropical by NOAA's National Hurricane Center. Of the remaining 8 non-tropical events wherein Reanalysis data were available, one event appears to be a pre-satellite era tropical feature heretofore unrecognized by the National Hurricane Center. The 1000 mb surface MSLP, winds and temperature for 00Z on 30 June 1962 are shown in Figure 6.26 and a circular wind pattern and warm-core nature of this closed-low at 500 hPa are visible in Figure 6.26. Consequently, this manuscript determined that 13 of the 20 significant rainfall events in Region 11 were tropical in nature. Accordingly, these 13 tropical events were excluded from the composite images determined for each PC Region

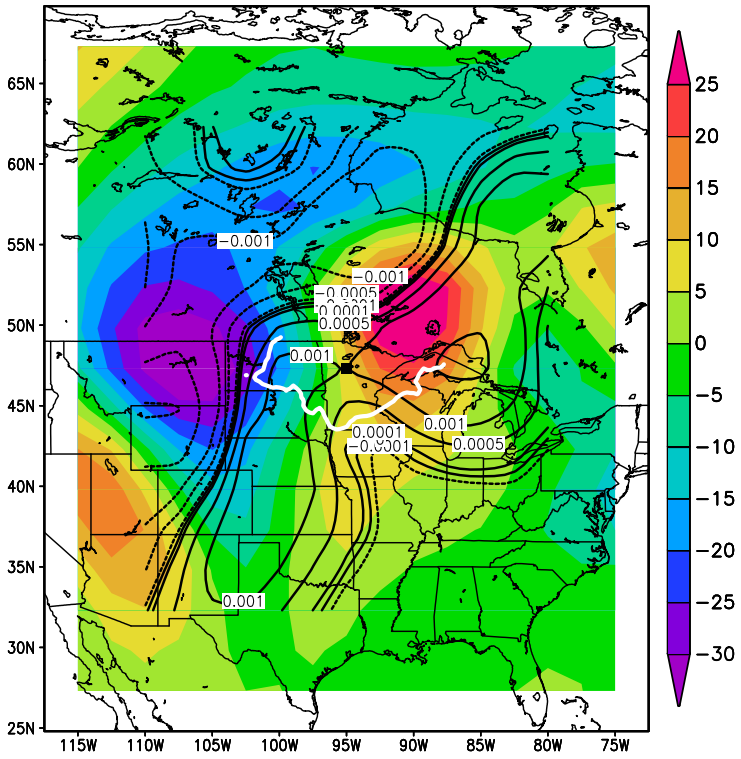

FIG. 6.25: As in Figure 6.23 but the 500 hPa thickness advection ("Term C", contours, Pa km^{-2} hour^{-1}) and thermal advection (shaded, K s^{-1}) for Region 13.

because their study was beyond the scope of this research. In addition, Reanalysis Data from one of the 7 remaining events also was missing.

As a result, a narrative to discuss the prevailing dynamical forces that created synoptic-scale heavy rainfall across this middle latitude region was based only on the meteorological patterns from the remaining 6 significant rainfall events. Because the remaining sample size was so small, it was impractical to calculate composite images of meteorological features from this region. Thus, the following summary is a subjective assessment of the antecedent synoptic conditions associated with some heavy rainfall events across the Mid-Atlantic States; the narrative was composed after visually inspecting numerous synoptic maps from individual events made possible by the Reanalysis Data.

Of the remaining 6 non-tropical events in Region 11, 4 occurred along an east-west escarpment between North and South Carolina in an environment of southerly low-level wind flow (e.g., Figure 6.27). Although not in an area of maximum warm air advection,

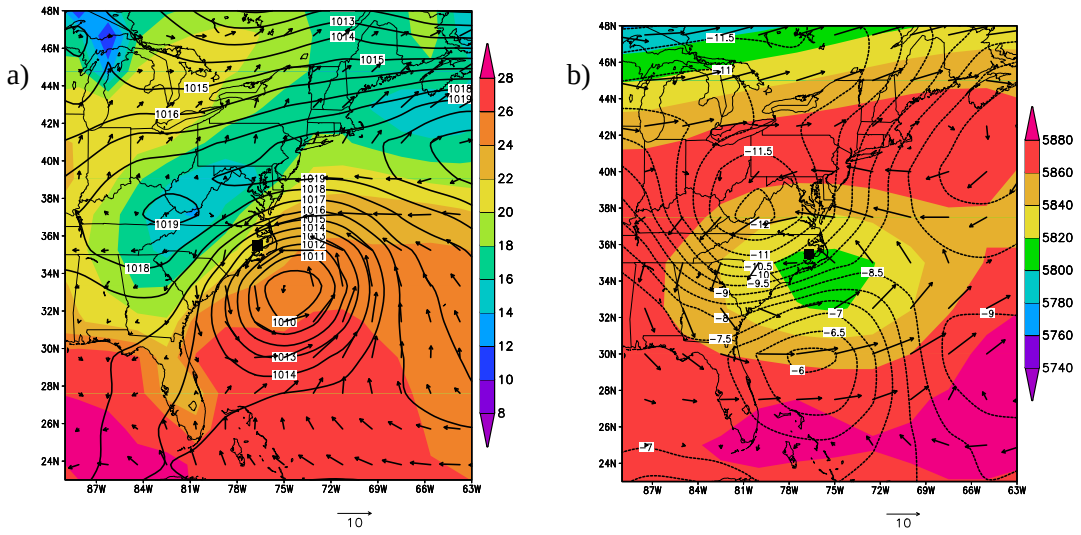

FIG. 6.26: The a) MSLP (contours, hPa), 1000 hPa wind vectors (m s^{-1}) and 1000 hPa temperature (shaded, K) and b) 500 hPa temperature (contours, K), geopotential height (shaded, m) and wind vectors (m s^{-1}) for the significant event on 30 June 1962 in Region 11.

these orographically-induced events had sufficient thermal advection and moisture to produce significant rainfall totals. These 4 terrain-driven events were located in an area of high 850 hPa heights to the southeast, east or northeast and low heights to the west or northwest. At 500 hPa, the four orographically-induced events occurred near the inflexion point of a trough-ridge pattern in an area of nonexistent to moderate vertical motion (0.03 to -0.25 Pa s^{-1}).

The remaining two events (1 September 1975 and 1 September 2002) both occurred southwest of a strong surface high in an area of onshore flow near the Atlantic Ocean. The significant events were in an area of moderate to strong vertical motion (-0.25 and -0.7 Pa s^{-1} at 500 hPa, respectively) and strong to moderate warm air advection at 850 hPa (40 and 25×10^{-6} K sec^{-1}). Both of these non-tropical and non-orographic events occurred in an area of strong upper-level divergence (17×10^{-6} and 8×10^{-6} sec^{-1}) in the right entrance region of a weak 200 hPa jet (one jet was cyclonically curved and the other was anticyclonically curved).

Side-by-side comparisons of composite maps from each of the 13 PC regions are shown in Figures 6.28, 6.29, and 6.30. A brief overview of the remaining eight regions not de-

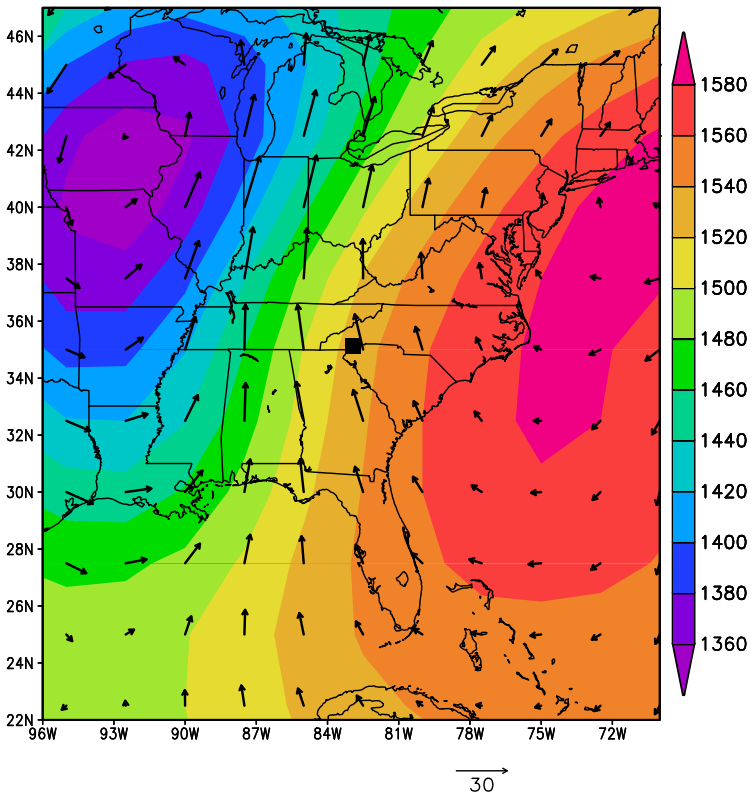

FIG. 6.27: The 850 hPa geopotential height (shaded, m) and wind vectors (m s^{-1}) for the significant event on 4 March 1979 in Region 11.

scribed above is provided in Appendix C.

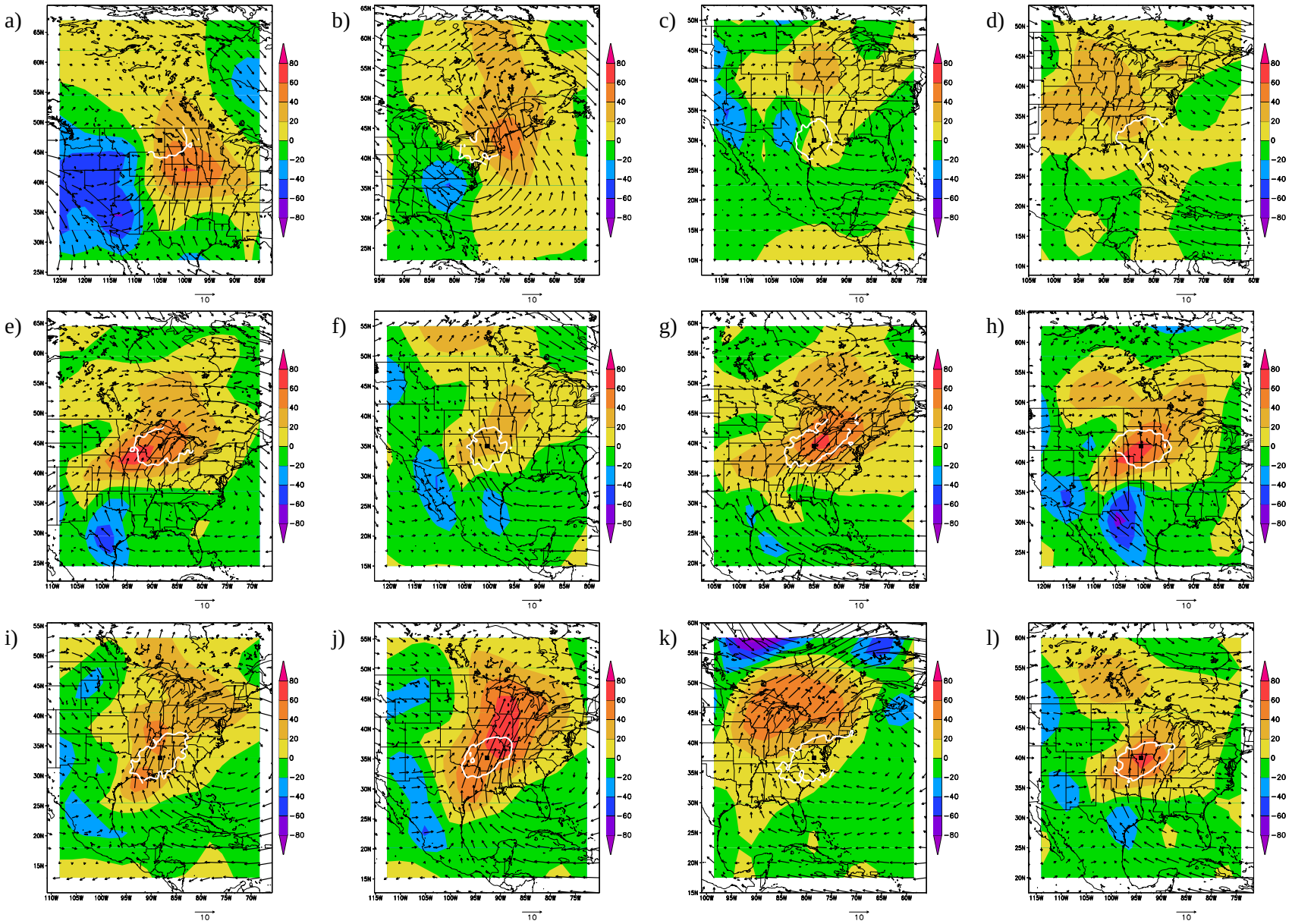

FIG. 6.28: Composite images of 850 hPa wind vectors (m s^{-1}) and thermal advection (K s^{-1}) for non-tropical events in PC Regions a) 1, b) 2, c) 3, d) 4, e) 5, f) 6, g) 7, h) 8, i) 9, j) 10, k) 11, l) 12, and m) 13 and n) the average of all inland PC Regions.

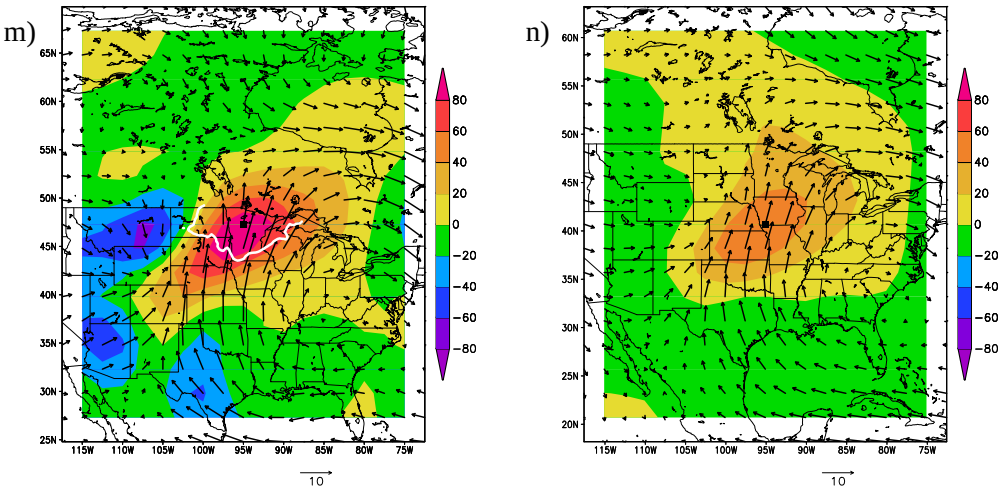

FIG. 6.28: (*Continued*).

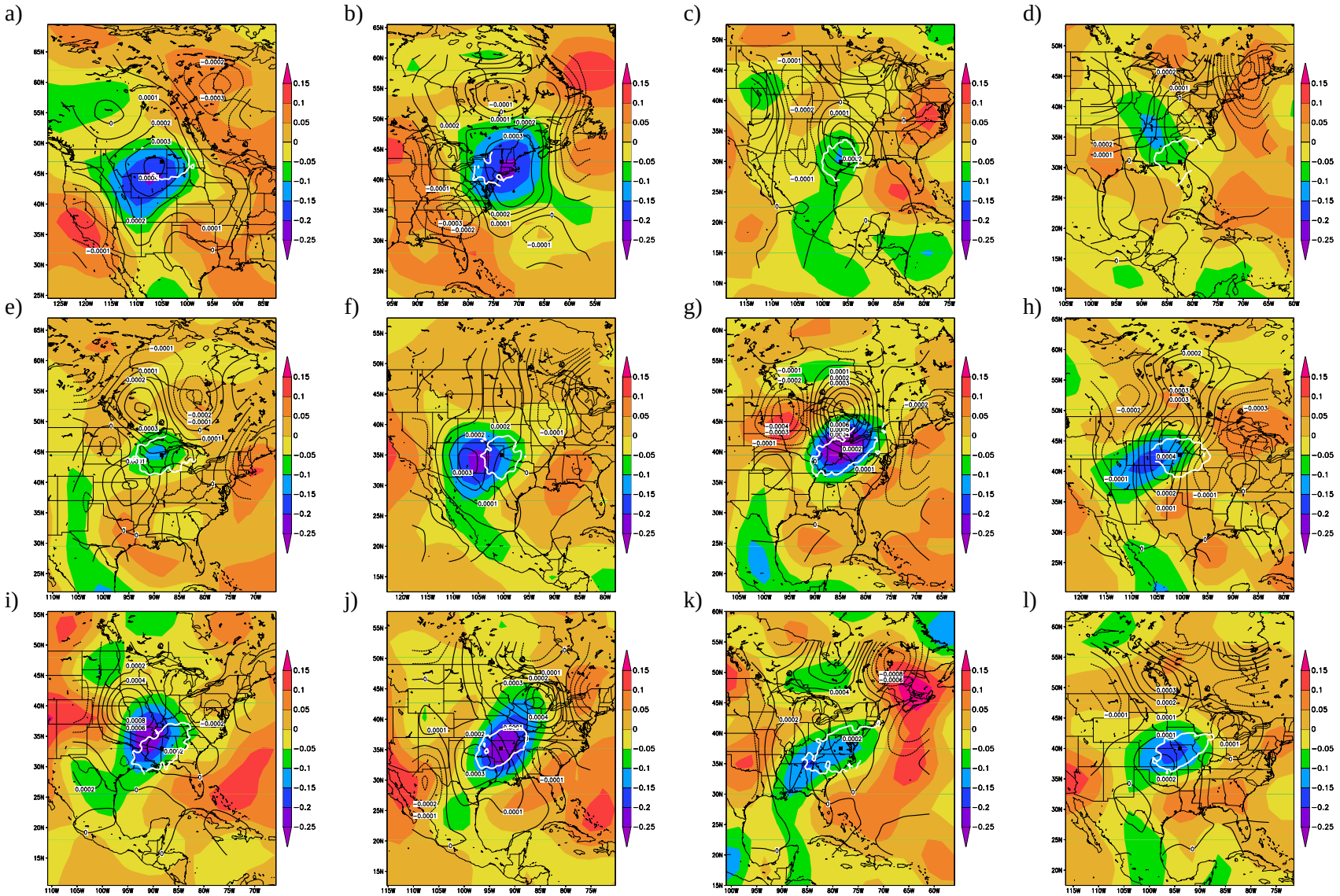

FIG. 6.29: Composite images of 500 hPa vorticity advection (contours, s^{-2}) and vertical velocity (shaded, Pa s^{-1}) for non-tropical events in PC Regions a) 1, b) 2, c) 3, d) 4, e) 5, f) 6, g) 7, h) 8, i) 9, j) 10, k) 11, l) 12, and m) 13 and n) the average of all inland PC Regions.

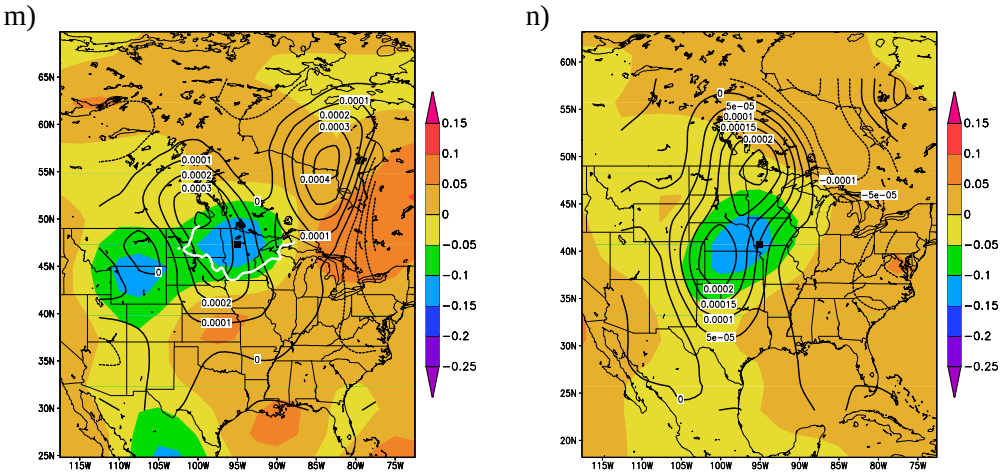

FIG. 6.29: (*Continued*).

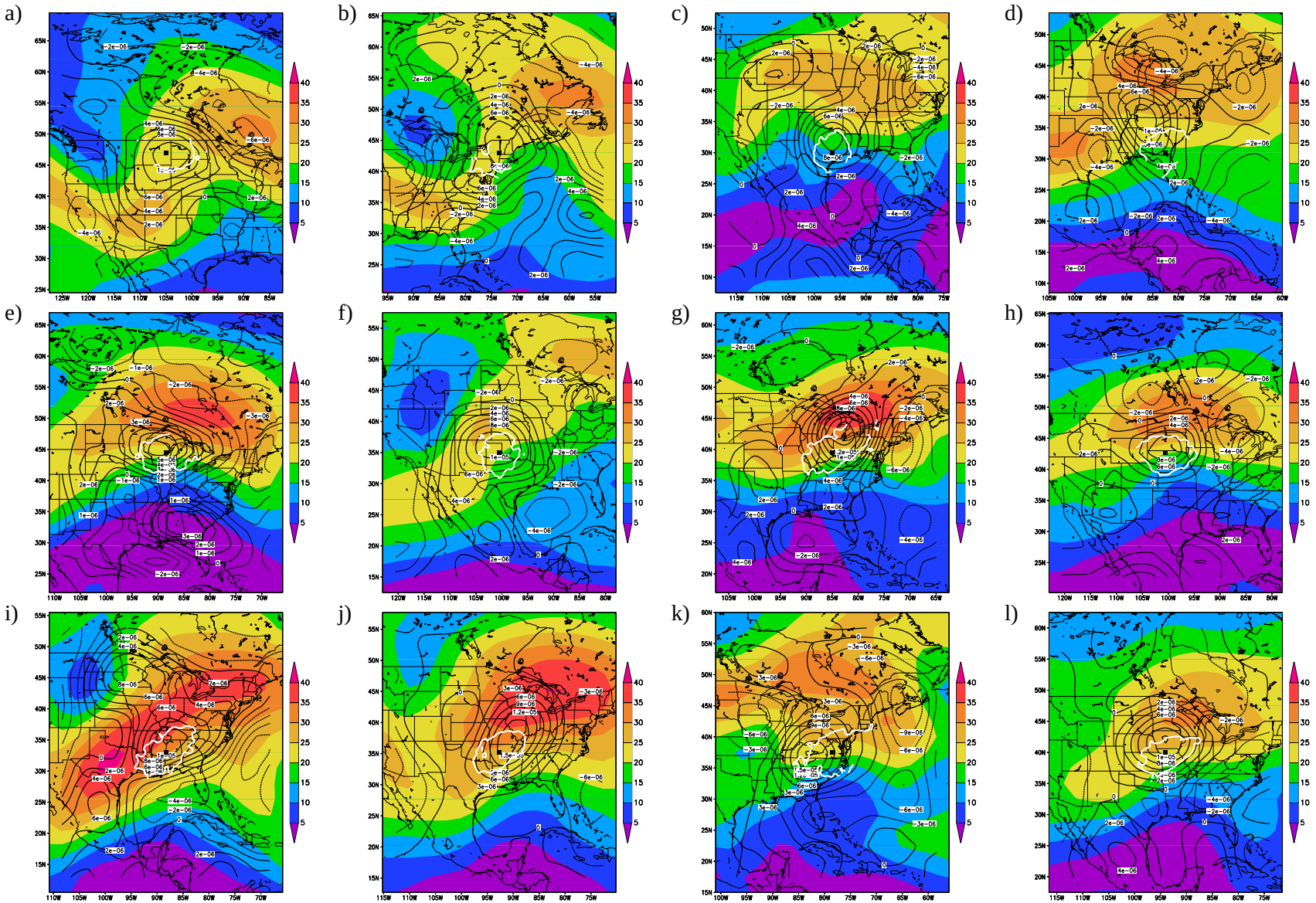

FIG. 6.30: Composite images of 200 hPa divergence (contours, s^{-1}) and isotachs (shaded, m s^{-2}) for non-tropical events in PC Regions a) 1, b) 2, c) 3, d) 4, e) 5, f) 6, g) 7, h) 8, i) 9, j) 10, k) 11, l) 12, and m) 13 and n) the average of all inland PC Regions.

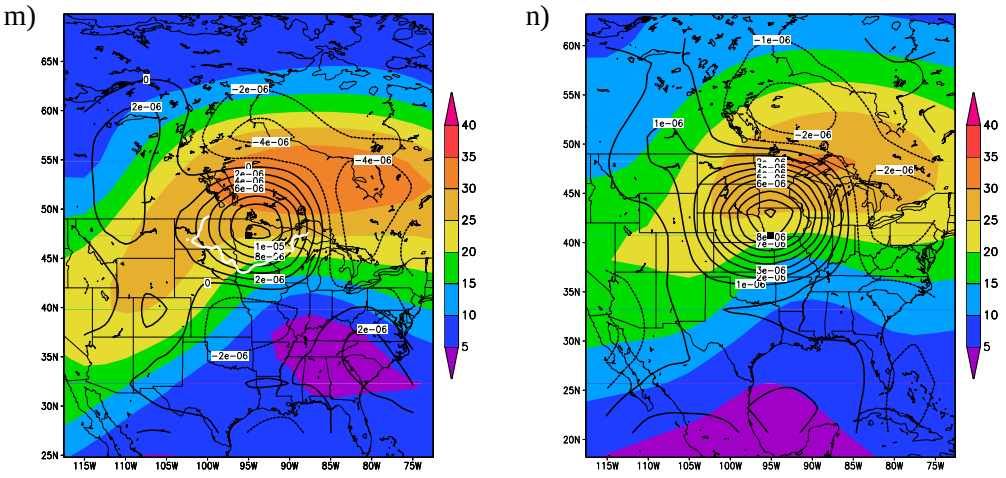

FIG. 6.30: (*Continued*).

Chapter 7

Conclusions

Although a limited number of studies of heavy to extreme rainfall events have been conducted across a few areas of the United States during the past 4 decades, a detailed study of events on a region-by-region basis represents an unfilled need. This study is unique in that no previous work has used the PCA technique to identify statistically stratified regions of coherent precipitation patterns across such large areas and lengthy study periods, nor have they examined the intensity or seasonal distribution of significant but rare precipitation events. Although the NCEP–NCAR Reanalysis data have been available since 1996, this unique, high-quality dataset has not been used to examine upper atmospheric features associated with a large number of significant rainfall events on a regional or national level over a long study period, or used it to quantify the forcing that produces synoptic scale ascent (i.e., the two terms on the right side of the Q-G omega equation).

To identify regions of statistically similar precipitation patterns, a PCA of 576 nearly evenly-spaced precipitation stations uncovered 13 statistically coherent regions across the eastern two-thirds of the Continental United States. The new PC regions reported in this manuscript bore a strong resemblance to those presented in RL85 between the Rocky and Appalachian Mountains, even though different integration periods and precipitation seasons were studied. The similarity of the two results suggest that extremely large summer rainfall events, as studied by RL85, played an important role in determining the PC patterns from annual data. This finding was supported by an examination of the seasonal

distributions of heavy precipitation events across a similar spatial domain. The similarity between the PCA regions in this study and those in RL85 was weakest in southern and western Texas. Heavy summertime precipitation events were less frequent in this area than in other regions of the United States, and consequently, the summertime events played a less important role in the determining the PC patterns from annual data.

The PCA-derived regions had unique characteristics in their precipitation distributions. For example, the distributions of precipitation intensity for heavy and significant events differed considerably from one region to another. The sharpest contrasts existed between those regions in the northern Great Plains versus the PC Regions along the coastlines with the Gulf of Mexico and the Atlantic Ocean. Stations located close to sources of warm, moist air recorded extremely large precipitation events not prevalent in drier parts of the country. The magnitude of the rainfall events classified as significant (the top 20 heaviest unique events in each region) increased from lower maximum values in the northwest to a largest maximum in the south and southeast. These significant events ranged from the lowest observation of 12.07 cm (4.75 inches) in Montana (PC Region 1) to the largest observation of 65.41 cm (25.75 inches) in Texas (PC Region 3).

The likelihood of a heavy or significant precipitation event occurring during a given season varied substantially from region to region. Heavy events in those regions near the Gulf of Mexico and Atlantic Ocean were more evenly distributed throughout the year. In contrast, most heavy events in the northern Plains and near the western Great Lakes occurred during the summer months of June, July, and August. Over half of all heavy events in Regions 1 and 13 occurred during this peak period of the warm-season. Heavy events during the winter months in these regions were extremely rare; only 1% of all heavy events in the far northwest region (Region 1) occurred during the climatological winter (December, January, and February). In contrast, nearly 28% of all heavy events occurred in the Deep South region (Region 9) during the same cool-season period. The vast majority of significant events (84%) occurred during the warm season months of April–September.

This study uncovered decadal differences in the distributions of heavy and significant

rainfall events. Of all precipitation bins of heavy events ranging from 1–23 inches (25–584 mm), the 1990s had the largest number of heavy events in 15 of the 22 bins–larger than any other decade. The early part of the 21st century had the largest number of heavy events in four categories. The number of significant events also revealed an increasing trend throughout the study period; more significant events occurred during the second half of the study period (post-1980) than during the first half (1950–1979), with the most number of significant events recorded during the 1990s.

The classification of 13 coherent patterns of annual rainfall across the United States east of the Rocky Mountains enabled the identification of the top 20 extreme rainfall events in each of the 13 regions. The costly and deadly impacts from these extremely large rainfall events make accurate long-range forecasts a necessity. Out of the two phases of forecasting convective weather described by Rockwood and Maddox (1988), this study focuses on the first step–assessing the synoptic-scale environment to identify the broad areas which have the greatest potential for developing convective storms. The NCEP–NCAR Reanalysis data provided an excellent, high-quality dataset for creating composite maps of the synoptic environment of significant rainfall events on a regional and national level. These 'regionalized' composite maps will provide operational meteorologists with easy-to-identify synoptic-scale patterns associated with significant rainfall events. Using these composite images alongside the best numerical guidance that extends to 3, 4, and 5 days, forecasters will be able to identify regions likely to receive very heavy precipitation.

Although the Reanalysis data set provided sufficient data for acquiring relevant synoptic-scale features, it has limitations. Due to its coarse grid spacing, the NCEP–NCAR 40-year Reanalysis failed to capture important mesoscale features (including outflow boundaries, mesolows and land surface discontinuities) and topographical elements that may have played an important role in the development and evolution of individual storms. Nevertheless, the composite Reanalysis maps used in this manuscript provide the critical synoptic-scale ingredients that are essential for significant rainfall to occur.

Composite maps from significant events, which occurred across regions bordering the

Gulf of Mexico and Atlantic Ocean, had characteristics much different from the composite images calculated for the eight inland regions. The proximity to the Gulf of Mexico or Atlantic Ocean helped create an environment wherein the readily available supply of moisture and unstable air masses led to relatively low lifting condensation levels (LCL). The Deep South region along the Gulf Coast had a bi-modal frequency distribution of significant events. Along the coastal regions, a large number of significant events occurred during the spring and fall months–more so than was observed across most inland PC Regions. For two PC Regions along the Atlantic Ocean, more than half of the significant events occurred during the fall season, primarily due to the increased frequency of tropical systems. Conversely, at least half of the significant events across many inland regions occurred during the summer months of June, July and August. Due to the large percentage of inland significant events (87%) which occurred during the warm season, the composite maps generated in this study predominantly reflect warm season significant precipitation events. A study of cool season events may reveal different features that were not represented in this work.

The environments that characterized significant events over inland regions had stronger, better defined synoptic features than did the environments of non-tropical significant events in coastal regions. When the coastal and inland composite images were calculated separately, the 850 hPa thermal and thickness advection values for the inland composites were approximately 2.5 times stronger than the thermal and thickness advection magnitudes across coastal regions. Not surprisingly, the LLJ was 28% stronger for significant events over inland regions than over coastal regions. At 500 hPa, the vertical velocity was 39% stronger over inland regions than along coastal sections. Near the tropopause, divergence at 200 hPa was 33% stronger in the composite images associated with inland regions compared with those from coastal regions.

Consequently, only the inland PC Regions were used to develop the national composite images of important synoptic-scale features. The national composite of nearly 160 significant events in 8 regions revealed a preferred location for the heaviest rainfall in the northeast quadrant of a surface low along a baroclinic zone. Significant events occurred at

the northern limits of a narrow tongue of copious moisture and a strong LLJ, and in an area of concentrated surface convergence and maximum thermal advection at 850 hPa. At 500 hPa, a concentrated bulls-eye of ascent was located slightly west of the heaviest precipitation, near the inflexion point region of ageostrophic divergence between a trough to the west and ridge to the east. The significant event centroid was located in the right entrance region of an anticyclonically curved Polar jet at 200 hPa and in an area of strong upper-level divergence. These important ingredients, when aligned in a dynamically consistent manner, create an ideal setup for unusually large 24-hour rainfall events.

Regarding forcing terms in the Q-G Omega equation (Appendix A), the 500 hPa differential advection of vorticity (Term B) near the centroid of significant rainfall was near zero for all 13 PC regions (weakly positive at inland locations and slightly negative across coastal regions). Conversely, the thickness advection term at 850 hPa (Term C) was substantially larger (~ 2.5 times larger for events across inland regions than for events across coastal regions). This important result means that, during episodes of significant rainfall, vorticity advection plays little role in initiating or modulating the rainfall event. Instead, thickness advection is by far the most dominant synoptic-scale forcing mechanism to initiate an outbreak of heavy to significant rainfall.

These findings substantiate the work of Maddox and Doswell (1982), who wrote:

> "It is suggested that, for situations in which mid-level vorticity and vorticity advection patterns are weak, the operational forecaster might better subjectively diagnose significant upward motion areas...by placing much less emphasis on the 500 mb height/vorticity analyses and prognoses and examining instead the low-level thermal advection fields. The meteorological logic supporting this approach is that convective development often depends upon lifting within the lowest several kilometers to release conditional instability and that one's attention should therefore be directed to these lower levels."

The low-level jet played a prominent role in the inferred isentropic lifting of warm air from the θ_e ridge impinging upon the baroclinic zone. All regional composite maps (except those in the southeast United States north to the mid-Atlantic Coast) revealed an area of strong warm air advection at 850 hPa located over the heaviest precipitation. These

areas were coincident with high levels of conditional instability (determined using the Total Totals index), which created synoptic-scale environments conducive to strong convection, and consequently, significant precipitation events. Thus, this dissertation documented and described synoptic patterns favorable for the production of significant precipitation on a national and region-by-region basis.

An examination of the composite maps developed for all significant rainfall events across the inland PC Regions from 1950–1979 (the first 30-years of the dissertation data set) and 1980–2009 (the final 30-years of the dissertation data set) revealed no substantial trends based on an inspection of the national composite images of the synoptic environment or the magnitude of the dynamical forcing terms from the Q-G omega equation. Both the early (first 30 years) and late events (last 30 years) reflected strong environments that were remarkably similar to those described for the 60-year composite over all inland regions. Consequently, this dissertation rejects the original hypothesis that trends exist in the synoptic-scale environments associated with the increasing frequency of exceptionally large rainfall events during the latter part of this study period.

In summary, this manuscript adds the following accomplishments to the body of scientific knowledge on the subject of synoptic-scale environments during significant rainfall events:

- Identified 13 coherent patterns of daily precipitation data across the eastern two-thirds of the Continental United States using the principal component analysis technique and the full Richman-Lamb precipitation dataset from 1950-2009;

- Developed a subset of heavy precipitation events and significant precipitation events associated with each of the 13 PCA-derived regions using a high-quality data set that spanned the 60-year period from 1950–2009;

- Determined that regional and seasonal differences were present and trends were not present in the heavy and significant precipitation events; an increasing decadal trend through the 1990s was evident in the heavy events, and significant events in the

Southern-Coastal PC Regions increased throughout the study period;

- Quantitatively recreated the synoptic environments associated with each significant rainfall event using the NCEP-NCAR Reanalysis Dataset;
- Created regional and national composite maps of the environments associated with significant rainfall events by upgrading the qualitative methods used by scientists since the first known data composites produced by Smith and Younkin in 1972;
- Determined the magnitude of the terms on the right-hand side of the quasi-geostrophic omega equation to identify the dominant mechanism which leads to vertical motion and created composite maps of these terms for all 13 PCA-derived regions and for a national set of composite images; and
- Evaluated the national composite maps for trends in the synoptic environment and the magnitude of dynamical forcing terms prior to and after 1980. Because no trends were discovered in the early and late portions of the dissertation data set, the null hypothesis of this dissertation is hereby accepted.

These seven accomplishments listed above are new to the scientific literature and go well beyond the work of Maddox et al. (1979; 1980), Maddox and Doswell (1982), Richman and Lamb (1985), Uccellini and Kocin (1987), and Junker et al. (1999). Each accomplishment contributed unequivocal new results to the field of meteorology. The original work in this dissertation tied together the results of previous research, advanced the scientific understanding through use of novel methodologies, and constructed a new framework for the early identification of significant rainfall based upon the best forecasts possible by today's synoptic scale models to save lives and property.

References

Allen, M. R., and W. J. Ingram, 2002: Constraints on future changes in climate and the hydrologic cycle. *Nature,* **419,** 224–232.

Ashley, S. T., and W. S. Ashley, 2008: Flood fatalities in the United States. *J. Appl. Meteor. Climatol.*, **47,** 805–818.

Aylward, R. P., and J. L. Dyer, 2010: Synoptic environments associated with the training of convective cells. *Wea. Forecasting*, **25,** 446–464.

Barnes, S. L., 1964: A technique for maximizing details in numerical weather map analysis. *J. Appl. Meteor.*, **3,** 396–409.

Barnes, S. L., 1973: Mesoscale objective analysis using weighted time-series observations. NOAA Tech. Memo. ERL NSSL-62, National Severe Storms laboratory, Norman, OK 73069, 60 pp. [NTIS COM-73-10781.]

Barnett, D. N., S. J. Brown, J. M. Murphy, D. M. H. Sexton, and M. J. Webb, 2006: Quantifying uncertainty in changes in extreme event frequency in response to doubled CO_2 using a large ensemble of GCM simulations. *Climate Dyn.*, **26,** 489–511.

Bluestein, H. B., 1992: *Synoptic-Dynamic Meteorology in Midlatitudes, Volume I.* Oxford University Press, 431 pp.

Bolton, D., 1980: The computation of equivalent potential temperature. *Mon. Wea. Rev.*, **108,** 1046–1053.

Bonner, W. D., 1968: Climatology of the low level jet. *Mon. Wea. Rev.*, **96,** 833–850.

Bony, S., J. P. Duvel, and H. Le Treut, 1995: Observed dependence of the water vapor and clear-sky greenhouse effect on sea surface temperature. *Climate Dyn.*, **11,** 307–320.

Boone, K. M., R. A. McPherson, M. B. Richman, and D. J. Karoly, 2010: Spatial coherence of rainfall variations using the Oklahoma Mesonet. Submitted to *Intl J. Clim*.

Bradley, A. A., and J. A. Smith, 1994: The hydrometeorological environment of extreme rainstorms in the southern plains of the United States. *J. Appl. Meteor.*, **33,** 1418–1431.

Brooks, H. A., and D. J. Stensrud, 2000: Climatology of heavy rain events in the United States from hourly precipitation observations. *Mon. Wea. Rev.*, **128,** 1194–1201.

Brunetti, M., M. Colacino, M. Maugeri, and T. Nanni, 2001a: Trends in the daily intensity of precipitation in Italy from 1951 to 1996. *Int. J. Climatol.*, **21,** 299–316.

——, M. Maugeri, and T. Nanni, 2001b: Changes in total precipitation, rainy days and extreme events in northeastern Italy. *Int. J. Climatol.*, **21,** 861–871.

Buell, C. E., 1975: The topography of empirical orthogonal functions. Preprints, *4th Conf. on Probability and Statistics in Atmospheric Sciences*, Tallahassee, FL, Amer. Meteor. Soc., 188–193.

——, 1979: On the physical interpretation of empirical orthogonal functions. Preprints, *6th Conf. on Probability and Statistics in Atmospheric Sciences*, Banff, AB, Canada, Amer. Meteor. Soc., 112–117.

Cao, Z., J. Ma, 2009: Summer severe-rainfall frequency trend and variability over Ontario, Canada. *J. Appl. Meteor. and Clim.*, **48,** 1955–1960.

Carbone, R. E., J. D. Tuttle, D. A. Ahijevych, and S. B. Trier, 2002: Inferences of predictability associated with warm season precipitation episodes. *J. Atmos. Sci.*, **59,** 2033–2056.

Cattell, R. B., 1966: The scree test for the number of factors. *Multivar. Behav. Res.*, **1,** 245–276.

Changnon, S. A., 1985: Secular variations in thunder-day frequencies in the twentieth century. *J. Geophys. Res.*, **90,** 6181–6194.

——, 2001: Thunderstorm rainfall in the conterminous United States. *Bull. Amer. Meteor. Soc.*, **82,** 1925–1940.

——, and K. E. Kunkel, 1995: Climate-related fluctuations in Midwestern floods during 1921–1985. *J. Water Res. Planning Management*, **121,** 326–334.

Chappell, C. F., 1985: Requisite conditions for the generation of stationary thunderstorm systems having attendant excessive rains. *Preprints, 6th Conf. on Hydrometeor.*, Boston, Massachusetts, Amer. Meteor. Soc., 221-225.

COLA, cited 2010: Grid Analysis and Display System (GrADS). [Available online at http://grads.iges.org/grads/.]

Compagnucci, R. H., and M. Richman, 2007: Can principal component analysis provide atmospheric circulation or teleconnection patterns? *Int. J. Climatol.*, **28,** 703–726.

Daley, R., 1991: *Atmospheric Data Analysis*. Cambridge University Press, 457 pp.

Del Genio, A. D., A. A. Lacis, and R. A. Ruedy, 1991: Simulations of the effect of a warmer climate on atmospheric humidity. *Nature,* **351,** 382–385.

Doswell, C. A., III, 1987: The distinction between large-scale and mesoscale contribution to severe convection: A case study example. *Wea. Forecasting*, **2,** 3–16.

——, Brooks, H. E., and R. A. Maddox, 1996: Flash flood forecasting: an ingredients-based methodology. *Wea. Forecasting*, **11,** 560–581.

Duffy, P. B., C. Doutriaux, B. D. Santer, and I. K. Fodor, 2001: Effect of missing data on estimates of near-surface temperature change since 1900. *J. Climate,* **14,** 2809–2814.

Easterling, D. R., 1989: Regionalization of thunderstorm rainfall in the contiguous United States. *Int. J. Climatol.*, **9,** 567–579.

——, 1990: Persistent patterns of thunderstorm activity in the Central United States. *J. Climate*, **3,** 1380–1389.

——, J. L. Evans, P. Ya. Groisman, T. R. Karl, K. E. Kunkel, and P. Ambenje, 2000: Observed variability and trends in extreme climate events: A brief review. *Bull. Amer. Meteor. Soc.*, **81,** 417–425.

Fiebrich, C. A., 2007: Transitioning the historical climate archives to data from newly automated sites: maintaining continuity in the temperature climate record. Ph.D. dissertation, School of Meteorology, The University of Oklahoma, 172 pp.

Fovell, R. G., and M.-Y. C. Fovell, 1993: Climate zones of the conterminous United States defined using cluster analysis. *J. Climate,* **6,** 2103–2135.

Frei, C., C. Schär, D. Lüthi, and H. C. Davies, 1998: Heavy precipitation processes in a warmer climate. *Geophys. Res. Lett.*, **25,** 1431–1434.

Fritsch, J. M., and R. A. Maddox, 1981: Convectively driven mesoscale weather systems aloft. Part I: Observations. *J. Appl. Meteor.,* **20,** 9–19.

——, ——, and A. G. Barnston, 1981: The character of mesoscale convective complex precipitation and its contribution to warm season rainfall in the U.S. Preprints, *4th Conf. on Hydrometeorology*, Reno, NV, Amer. Meteor. Soc., 94–99.

——, R. J. Kane, and C. R. Chelius, 1986: The contribution of mesoscale convective weather systems to the warm-season precipitation in the United States. *J. Climate Appl. Meteor.,* **25,** 1333–1345.

Fukouoka, A. 1951: A study of 10-day forecast (a synthetic report), *Geophys. Mag.*, **22,** 177–208.

Gadgil, S., and R. N. Iyengar, 1980: Cluster analysis of rainfall stations of the Indian peninsula. *Quart. J. Roy. Meteor. Soc.*, **106,** 873–886.

Gaffen, D. J., T. P. Barnett, W. P. Elliott, 1991: Space and time scales of global tropospheric moisture. *J. Climate*, **4,** 989–1008.

——, W. P. Elliott, and A. Robock, 1992: Relationships between tropospheric water vapor and surface temperature as observed by radiosondes. *Geophys. Res. Lett.*, **19,** 1839–1842.

Gallus, W. A., N. A. Snook, and E. V. Johnson, 2008: Spring and summer severe weather reports over the Midwest as a function of convective mode: A preliminary study. *Wea. Forecasting*, **23,** 101–113.

Glass, F. H., and D. L. Ferry, 1995: Characteristics of heavy convective rainfall events across the mid-Mississippi Valley during the warm season: Meteorological conditions and a conceptual model. *Preprints, 14th Conf. on Weather Analysis and Forecasting*, Dallas, TX, Amer. Meteor. Soc., 34–41.

Gong, X., and M. B. Richman, 1995: On the application of cluster analysis to growing season precipitation data in North America east of the Rockies. *J. Climate*, **8,** 917–931.

Grice, G. K., and R. A. Maddox, 1982: Synoptic aspects of heavy rain events in South Texas associated with the westerlies. NOAA Tech. Memo. NWS SR-106, 21 pp.

Groisman, P. Ya., and Coauthors, 1999: Changes in the probability of heavy precipitation: Important indicators of climatic change. *Climatic Change*, **42,** 243–283.

——, R. W. Knight, and T. R. Karl, 2001: Heavy precipitation and high streamflow in the contiguous United States: Trends in the Twentieth Century. *Bull. Amer. Meteor. Soc.*, **82,** 219–246.

——, ——, and ——, 2002: Very heavy precipitation over land: estimates based on a new global daily precipitation data set. *Preprints, 13th Symposium on Global Change Studies*, Orlando, FL, Amer. Meteor. Soc., 88–90.

——, ——, ——, D. R. Easterling, B. Sun, and J. M. Lawrimore, 2004: Contemporary changes of the hydrological cycle over the contiguous United States: Trends derived from in situ observations. *J. Hydrometeor.*, **5,** 64–85.

——, ——, D. R. Easterling, T. R. Karl, G. C. Hegerl, and V. N. Razuvaev, 2005: Trends in intense precipitation in the climate record. *J. Climate*, **18,** 1326–1350.

Haan, C. T., 1977: *Statistical Methods in Hydrology*. The Iowa State University Press, 378 pp.

Heideman, K. F., and J. M. Fritsch, 1988: Forcing mechanisms and other characteristics of significant summertime precipitation. *Wea. Forecasting*, **3,** 115–130.

Henderson, K. G., and P. J. Robinson, 1994: Relationships between the Pacific/North American teleconnection patterns and precipitation events in the south-eastern USA. *Int. J. Climatol.*, **14,** 307–323.

Hennessy, K. J., J. M. Gregory, and J. F. B. Mitchell, 1997: Changes in daily precipitation under enhanced greenhouse conditions. *Climate Dyn.*, **13,** 667–680.

Holton, J. R., 1992: *An Introduction to Dynamic Meteorology*, 3rd Ed. Academic Press, 511 pp.

Hoskins, B. J., I. Draghici, and H. C. Davies, 1978: A new look at the omega-equation. *Quart. J. Roy. Meteor. Soc.*, **104**,31–38.

Hotelling, H., 1933: Analysis of a complex of statistical variables into principal components. *J. Educ. Psych.*, **24,** 417–441.

Houze, R. A., Jr., B. F. Smull, and P. Dodge, 1990: Mesoscale organization of springtime rainstorms in Oklahoma. *Mon. Wea. Rev.*, **118,** 613–654.

Insightful Corporation, 2007: *S-PLUS 8 Guide to Statistics*. Vol. 1. Insightful Corporation, 718 pp. [Available online at http://www.splus.com/support/splus80win/statman1.pdf.]

Iwashima, T., and R. Yamamoto, 1993: A statistical analysis of the extreme events: Long-term trend of heavy daily precipitation. *J. Meteor. Soc. Japan*, **71,** 637–640.

Johns, R. H., 1984: A synoptic climatology of northwest-flow severe weather outbreaks. Part II: Meteorological parameters and synoptic patterns. *Mon. Wea. Rev.*, **112,** 449–464.

Junker, N. W., Schneider, R. S., and S. L. Fauver, 1999: A study of heavy rainfall events during the Great Midwest Flood of 1993. *Wea. Forecasting*, **14,** 701–712.

Juying X., and R. A. Scofield, 1989: Satellite-derived rainfall estimates and propagation characteristics associated with mesoscale convective systems (MCS). NOAA Tech. Memo. NESDIS 25, 49 pp.

Kaiser, H. F., 1958: The Varimax criterion for analytic rotation in factor analysis. *Psychometrika*, **23,** 187–200.

Kalnay, E., and Coauthors, 1996: The NCEP/NCAR 40-year reanalysis project. *Bull. Amer. Meteor. Soc.*, **77,** 437–470.

Karl, T. R., and R. W. Knight, 1998: Secular trends of precipitation amount, frequency, and intensity in the United States. *Bull. Amer. Meteor. Soc.*, **79,** 231–241.

——, A. J. Koscielny, and H. F. Diaz, 1982: Potential errors in the application of principal component (eigenvector) analysis to geophysical data. *J. Appl. Meteor.*, **21,** 1183–1186.

——, R. W. Knight, D. R. Easterling, and R. G. Quayle, 1995a: Trends in U.S. climate during the twentieth century. *Consequences*, **1,** 2–12.

——, ——, and N. Plummer, 1995b: Trends in high-frequency climate variability in the twentieth century. *Nature*, **377,** 217–220.

Kharin, V. V., and F. W. Zwiers, 2005: Estimating extremes in transient climate change simulations. *J. Climate*, **18,** 1156–1173.

Kistler, R., and Coauthors, 2001: The NCEP–NCAR 50–Year Reanalysis: Monthly means CD–ROM and documentation. *Bull. Amer. Meteor. Soc.*, **82,** 247–267.

Konrad, C. E. II, 2001: The most extreme precipitation events over the eastern United States from 1950 to 1996: Considerations of scale. *J. Hydrometeor.*, **2,** 309–325.

Kunkel, K. E., S. A. Changnon, and R. T. Shealy, 1993: Temporal and spatial characteristics of heavy-precipitation events in the Midwest. *Mon. Wea. Rev.*, **121,** 858–866.

——, K. Andsager, and D. R. Easterling, 1999a: Long-term trends in extreme precipitation events over the conterminous United States and Canada. *J. Climate*, **12,** 2515–2527.

——, R. A. Pielke Jr., and S. A. Changnon, 1999b: Temporal fluctuations in weather and climate extremes that cause economic and human health impacts: A review. *Bull. Amer. Meteor. Soc.*, **80,** 1077–1098.

——, D. R. Easterling, K. Redmond, and K. Hubbard, 2003: Temporal variations of extreme precipitation events in the United States: 1895–2000. *Geophys. Res. Lett.*, **30,** 1900, 10.1029/2003GL018052.

Lorenz, E. N., 1956: Empirical orthogonal functions and statistical weather prediction. Science Rep. 1, Statistical Forecasting Project, Dept. of Meteorology, Massachusetts Institute of Technology, 48 pp.

Lupo, A. R., P. J. Smith, and P. Zwack, 1992: A diagnosis of the explosive development of two extratropical cyclones. *Mon. Wea. Rev.*, **120,** 1490–1523.

Maddox, R. A., 1980a: Mesoscale convective complexes. *Bull. Amer. Meteor. Soc.*, **61,** 1374–1387.

——, 1980b: An objective technique for separating macroscale and mesoscale features in meteorological data. *Mon. Wea. Rev.*, **108,** 1108–1121.

——, and C. A., Doswell III, 1982: An examination of jet stream configurations, 500 mb vorticity advection and low-level thermal advection patterns during extended periods of intense convection. *Mon. Wea. Rev.*, **110,** 184–197.

——, L. R. Hoxit, C. F. Chappell, and F. Caracena, 1978: Comparison of meteorological aspects of the Big Thompson and Rapid City flash floods. *Mon. Wea. Rev.*, **106,** 375–389.

——, C. F. Chappell, and L. R. Hoxit, 1979: Synoptic and meso-α aspects of flash flood events. *Bull. Amer. Meteor. Soc.*, **60,** 115–123.

——, F. Canova, and L. R. Hoxit, 1980: Meteorological characteristics of flash flood events over the western United States. *Mon. Wea. Rev.*, **108,** 1866–1877.

——, D. J. Perkey, and J. M. Fritsch, 1981: Evolution of upper tropospheric features during the development of a mesoscale convective complex. *J. Atmos. Sci.*, **38,** 1664–1674.

Madsen, T., and E. Figdor, 2007: When it rains, it pours. Environment America Research and Policy Center Rep., 48 pp.

Means, L. L., 1952: On thunderstorm forecasting in the central United States. *Mon. Wea. Rev.*, **80,** 165–189.

——, 1954: A study of the mean southerly wind-maximum in low levels associated with a period of summer precipitation in the middle west. *Bull. Amer. Meteor. Soc.*, **35,** 166–170.

Meehl, G. A., J. M. Arblaster, and C. Tebaldi, 2005: Understanding future patterns of increased precipitation intensity in climate model simulations. *Geophys. Res. Lett.*, **32,** L18719.

Menne, M., I. Durre, T. Houston, and R. Vose, cited 2009: Global Historical Climatology Network–Daily. [http://www.ncdc.noaa.gov/oa/climate/ghcn-daily/index.php]

Mercer, A. E., 2008: Discrimination of tornadic and non-tornadic severe weather outbreaks. Ph.D. dissertation, School of Meteorology, The University of Oklahoma, 160 pp.

——, and M. B. Richman, 2007: Statistical differences of quasigeostrophic variables, stability, and moisture profiles in North American storm tracks. *Mon. Wea. Rev.*, **135,** 2312–2338.

Mesinger, F., and Coauthors, 2006: North American Regional Reanalysis. *Bull. Amer. Meteor. Soc.*, **87,** 343–360.

Mo, K. C., J. N. Paegle, and R. W. Higgins, 1997: Atmospheric processes associated with summer floods and droughts in the central United States. *J. Climate*, **10,** 3028–3046.

Molteni, F., P. Bonelli, and P. Bacci, 1983: Precipitation over northern Italy: A description by means of principal component analysis. *J. Climate Appl. Meteor.*, **22,** 1738–1752.

Montroy, D. L., 1997: Linear relation of central and eastern North American precipitation to tropical Pacific sea surface temperature anomalies. *J. Climate*, **10,** 541–558.

——, M. B. Richman, and P. J. Lamb, 1998: Observed nonlinearities of monthly teleconnections between tropical Pacific sea surface temperature anomalies and central and eastern North American precipitation. *J. Climate*, **11,** 1812–1835.

Moore, J. T., S. M. Nolan, F. H. Glass, D. L. Ferry, and S. M. Rochette, 1995: Flash flood-producing high-precipitation supercells in Missouri. *Preprints, 14th Conf. Wea. Analysis and Forecasting*, Dallas, TX, Amer. Meteor. Soc., 7–12.

——, F. H. Glass, C. E. Graves, S. M. Rochette, and M. J. Singer, 2003: The environment of warm-season elevated thunderstorms associated with heavy rainfall over the Central United States. *Wea. Forecasting*, **18,** 861–878.

National Research Council, 2010. When weather matters: Science and service to meet critical societal needs. National Academies Press, 208 pp.

North, G. R., T. L. Bell, and R. F. Cahalan, 1982: Sampling errors in the estimation of empirical orthogonal functions. *Mon. Wea. Rev.*, **110,** 699–706.

Osborn, T. J., M. Hulme, P. D. Jones, and T. A. Basnett, 1999: Observed trends in the daily intensity of United Kingdom precipitation. *Int. J. Climatol.*, **20,** 347–364.

Parker, M. D., and R. H. Johnson, 2000: Organizational modes of midlatitude mesoscale convective systems. *Mon. Wea. Rev.*, **128,** 3413–3436.

——, and ——, 2004: Structures and dynamics of quasi-2D mesoscale convective systems. *J. Atmos. Sci.*, **61,** 545–567.

Peppler, R. A., and P. J. Lamb, 1989: Tropospheric static stability and Central North American growing season rainfall. *Mon. Wea. Rev.*, **117,** 1156–1180.

Perry, C., 2000: Significant floods in the United States during the 20th century – USGS measures a century of floods. USGS Fact Sheet 024-00, March 2000.

Petersen, W. A., and Coauthors, 1999: Mesoscale and radar observations of the Fort Collins flash flood of 28 July 1997. *Bull. Amer. Meteor. Soc.*, **80,** 191–216.

Petterssen, S., 1956: *Weather Analysis and Forecasting*. 2d ed. Vol. 1, McGraw-Hill, 422 pp.

Pettet, C. R., and R. H. Johnson, 2003: Airflow and precipitation structure of two leading stratiform mesoscale convective systems determined from operational datasets. *Wea. Forecasting*, **18,** 685–699.

Petty, G. W., 2008: *A First Course in Atmospheric Thermodynamics*, Sundog Publishing, 352 pp.

Pielke, R. A., and M. W. Downton, 2000: Precipitation and damaging floods: Trends in the United States, 1932–1997. *J. Climate*, **13,** 3625–3637.

Pontrelli, M. D., G. Bryan, and J. M. Fritsch, 1999: The Madison County, Virginia, flash flood of 27 June 1995. *Wea. Forecasting*, **14,** 384–404.

Portis, D. H., M. P. Cellitti, W. L. Chapman, and J. E. Walsh, 2006: Low-frequency variability and evolution of North American cold air outbreaks. *Mon. Wea. Rev.*, **134,** 579–597.

Raddatz, R. L., 2000: Summer rainfall recycling for an agricultural region of the Canadian Prairies. *Can. J. Soil Sci.*, **80,** 367–373.

——, 2005: Moisture recycling on the Canadian prairies for summer droughts and pluvials from 1997 to 2003. *Agriculture and Forest Meteor.*, **131,** 13–26.

——, and J. M. Hanesiak, 2008: Significant summer rainfall in the Canadian prairies provinces: Modes and mechanisms 2000–2004. *Int. J. Climatol.*, **28,** 1607–1613.

Richman, M. B., 1986: Rotation of principal components. *J. Climatol.*, **6,** 293–333.

——, 1987: Rotation of principal components: A reply. *J. Climatol.*, **7,** 511–520.

——, and X. Gong, 1999: Relationships between the definition of the hyperplane width to the fidelity of principal component loading patterns. *J. Climate*, **12,** 1557–1576.

——, and P. J. Lamb, 1985: Climatic pattern analysis of three- and seven-day summer rainfall in the Central United States: Some methodological considerations and a regionalization. *J. Climate Appl. Meteor.*, **24,** 1325–1343.

——, and ——, 1987: Pattern analysis of growing season precipitation in southern Canada. *Atmos.-Ocean*, **25,** 137–158.

Rockwood, A. A., and R. A. Maddox, 1988: Mesoscale and synoptic scale interactions leading to intense convection: The case of 7 June 1982. *Wea. Forecasting*, **3,** 51–68.

Rogers, R. R., and M. K. Yau, 1989: *A Short course in cloud physics*, 3rd Ed. Pergammon Press, New York, 304 pp.

Ross, R. J., and W. P. Elliot, 1996: Tropospheric water vapor climatology and trends over North America: 1973–93. *J. Climate*, **9,** 3561–3574.

——, and ——, 2001: Radiosonde-based Northern Hemisphere tropospheric water vapor trends. *J. Climate*, **14,** 1602–1612.

Schumacher, R. S., and R. H. Johnson, 2005: Organization and environmental properties of extreme-rain-producing mesoscale convective systems. *Mon. Wea. Rev.*, **133,** 961–976.

——, and ——, 2006: Characteristics of U.S. extreme rain events during 1999–2003. *Wea. Forecasting*, **21,** 69–85.

Schwartz, B. E., C. F. Chappell, W. E. Togstad, and X-P. Zhong, 1990: The Minneapolis flash flood: Meteorological analysis and operational response. *Wea. Forecasting*, **5,** 3–21.

Shi, J., and R. A. Scofield, 1987: Satellite-observed mesoscale convective systems (MCSs) propagations and a 3-12-hour heavy precipitation index. NOAA/NESDIS Tech. Memo. 20, Washington, DC, 43 pp. [Available from National Environmental Satellite Data and Information Service, Rm. 703, 5200 Auth Rd., Camp Springs, MD 20746.]

Smith, W. and R. J. Younkin, 1972: An operationally useful relationship between the polar jet stream and heavy precipitation. *Mon. Wea. Rev.*, **100,** 434–440.

Smith, J. A., M. L. Baeck, Y. Zhang, and C. A. Doswell III, 2001: Extreme rainfall and flooding from supercell thunderstorms. *J. Hydrometeor.*, **2,** 469–489.

Thurstone, L. L., 1947: *Multiple Factor Analysis*, The University of Chicago Press, 535 pp.

Timmer, R. P., and P. J. Lamb, 2007: Relations between temperature and residential natural gas consumption in the central and eastern United States. *J. Appl. Meteor. Climatol.*, **46,** 1993–2013.

Trenberth, K. E., 1998: Atmospheric moisture residence times and cycling: Implications for rainfall rates with climate change. *Climatic Change*, **39,** 667–694.

——, 1999: Conceptual framework for changes of extremes of the hydrological cycle with climate change. *Climatic Change*, **42,** 327–339.

——, A. Dai, R. M Rasmussen, and D. B. Parsons, 2003: The changing character of precipitation. *Bull. Amer. Meteor. Soc.*, **84,** 1205–1217.

Tuttle, J. D. and C. A. Davis, 2006: Corridors of warm season precipitation in the central United States. *Mon. Wea. Review,* **134,** 2297–2317.

Uccellini, L. W., and P. J. Kocin, 1987: The interaction of jet streak circulations during heavy snow events along the East Coast of the United States. *Wea. Forecasting*, **2,** 289–308.

Vose, R. S., R. Heim, R. L. Schmoyer, T. R. Karl, P. M. Steurer, J. K. Eischeid, and T. C. Peterson, 1992: The Global Historical Climatology Network: Long-term monthly temperature, precipitation, sea level pressure, and station pressure data. ORNL/CDIAC 53, NDP-041. Carbon Dioxide Information Analysis Center, Oak Ridge National Laboratory, Oak Ridge, Tennessee. [Available online at http://cdiac.esd.ornl.gov/ftp/ndp041/ndp041.pdf.]

Walsh, J. E., M. B. Richman, and D. W. Allen, 1982: Spatial coherence of monthly precipitation in the United States. *Mon. Wea. Rev.*, **110,** 272–286.

Wentz, F. J., L. Ricciardulli, K. Hilburn, C. Mears, 2007: How much more rain will global warming bring? *Science*, **317,** 5835, 233–235.

Western Governors' Association, 2010. Climate adaptation priorities for the Western states: Scoping report. Western Governors' Association, 20 pp.

White, D., M. Richman, and B. Yarnal, 1991: Climate regionalization and rotation of principal components. *Int. J. Climatol.*, **11,** 1–25.

White, E. J., and A. H. Perry, 1989: Classification of the climate of England and Wales based on agroclimatic data. *Int. J. Climatol.*, **8,** 27–291.

Wilby, R. L., and T. M. L. Wigley, 2002: Future changes in the distribution of daily precipitation totals across North America. *Geophys. Res. Lett.*, **29,** 1135.

Wilks, D. S., 2006: *Statistical Methods in the Atmospheric Sciences*, 2nd Ed. Academic Press, 467 pp.

Winkler, J. A., 1985: Regionalization of the diurnal distribution of summertime heavy precipitation. Preprints, *6th Conf. on Hydrometeorology*, Indianapolis, IN, Amer. Meteor. Soc., 9–16.

——, 1988: Climatological characteristics of summertime extreme rainstorms in Minnesota. *Annals, Assoc. Amer. Geographers*, **78,** 57–73.

Yan, H., and R. A. Anthes, 1988: The effect of variations in surface moisture on mesoscale circulations. *Mon. Wea. Rev.*, **116,** 192–208.

Yin, Z.-Y., 1994: Moisture condition in the south-eastern USA and teleconnection patterns. *Int. J. Climatol.*, **14,** 947–967.

Zangvil, A., P. J. Lamb, D. H. Portis, F. Jin, and S. Malka, 2010: Comparative study of atmospheric water vapor budget associated with precipitation in Central US and eastern Mediterranean. *Adv. Geosci.*, **23,** 3–9.

Zawadzki, I. I., and C. U. Ro, 1978: Correlations between maximum rate of precipitation and mesoscale parameters. *J. Appl. Meteor.*, **17,** 1327–1334.

Appendix A

Assessing Vertical Motion in the Atmosphere

The ascent of air in the atmosphere is essential for the generation of precipitation and, consequently, heavy precipitation events. When a parcel of rising air reaches its lifting condensation level (LCL), water vapor in that parcel condenses and, given continued ascent, may accumulate and fall as precipitation. To understand the synoptic environment and dynamical parameters associated with heavy precipitation events, the mechanisms and means of assessing vertical motion in the atmosphere are examined.

It is possible to directly and indirectly measure rising and sinking air in the atmosphere using a sonic anemometer, dual-Doppler radar, lidar, and acoustic sounders. However, networks of such instrumentation are sparse and do not extend backward in time to encompass the entire period of study for this research. Many of these instruments cannot measure vertical velocity with sufficient accuracy due to the small magnitudes of vertical motion. Instead, alternative techniques based on mathematical relationships of physical processes are used to diagnose vertical motion in the atmosphere given standard surface and upper-air observations or grid point representations of these data (e.g., in the reanalysis data set). This appendix will outline several important techniques for estimating rising and sinking motion in the atmosphere.

A.1 Quasi-Geostrophic Omega Method

The most common method used to estimate vertical motion in the atmosphere is through application of the quasi-geostrophic (Q-G) ω equation,

$$\left[\nabla_p^2 + \frac{f_0^2}{\sigma}\frac{\partial^2}{\partial p^2}\right]\omega = -\frac{f_0}{\sigma}\frac{\partial}{\partial p}\left[-\vec{v_g}\cdot\nabla_p(\zeta_g + f)\right] - \frac{R}{\sigma p}\nabla_p^2\left[-\vec{v_g}\cdot\nabla_p T\right]. \tag{A.1}$$

This equation has been derived and described in great detail by Holton (1992) and Bluestein (1992). Thus, this appendix will discuss the mathematical and physical interpretation of terms in this widely used equation. The Q-G ω method is valid for assessing vertical motion on the synoptic-scale, where vorticity is nearly geostrophic and temperature is hydrostatic. In other words, the application of this equation is valid only when horizontal motions in the atmosphere are 'quasi-geostrophic'.

Petterssen (1956) provided an excellent summary of the meaning of a quasi-geostrophic atmosphere. In his eloquent synopsis, Petterssen (1956) stated: "The synoptic charts of any large area of the globe, and especially in middle and high latitudes, show well-defined dynamic systems in which the motion is overwhelmingly horizontal and largely determined by the horizontal gradients of pressure and temperature. These motions indicate the existence of a near balance between the horizontal pressure forces and the forces arising from the rotation of the earth. ... The velocity calculated from this balance is called the *geostrophic wind*. Observations show that the deviation of the actual wind from the geostrophic wind usually is so small that it may be neglected in the routine analyses of synoptic charts. Nevertheless, in many problems (e.g., those concerning pressure variations, the formation and intensification of circulation systems), these small deviations and their spatial distribution constitute essential parts of the mechanisms involved. ...

"Within certain limits, therefore, the Rossby number provides a characteristic estimate of the degree of geostrophic balance, such that the smaller the number, the higher the degree of balance. In the experiments, a Rossby number in the vicinity of 0.01 indicates a very strong balance; a number of about 0.1 would correspond to what is commonly called

quasi-geostrophic motion... and a number in the vicinity of unity would be very strongly *a*-geostrophic."

The left-hand side of Equation A.1,

$$\left[\nabla_p^2 + \frac{f_0^2}{\sigma}\frac{\partial^2}{\partial p^2}\right]\omega, \tag{A.2}$$

represents a simple operator on ω, the vertical velocity in pressure coordinates. The quantity ω can be estimated by reversing this operator and solving for the terms on the right-hand side (RHS) of Equation A.1.

For a mathematical description of this equation, the first term on the RHS of Equation A.1 represents the differential vorticity advection of both relative (ζ_g) and planetary (f) vorticity by the geostrophic wind, $\vec{v}_g$. The differential advection of vorticity is scaled by the Coriolis parameter, f_0, and the static stability parameter, σ. When vorticity advection increases with height, this first term can be summarized as the negative of the partial derivative of the vorticity advection with respect to pressure; mathematically, this term is greater than zero, leading the Laplacian of ω to also be greater than zero. Thus, from a mathematical perspective, the vertical derivative with respect to pressure implies that ω is negative, hence *rising motion*. Conversely, vorticity advection decreasing with height leads to sinking motion.

A more meaningful view of this term would be the physical interpretation of this equation. When cyclonic vorticity advection increases with height and the vorticity is assumed to be nearly geostrophic, then large increases in geostrophic relative vorticity at upper levels must create (or be accompanied by) large upper-level height falls based on the definition of geostrophic vorticity. This definition,

$$\zeta_g = \frac{g}{f_0}\nabla_p^2 z, \tag{A.3}$$

establishes the inverse relationship between height tendency and changes in the magnitude of geostrophic vorticity. Concurrently, at lower levels, a small increase in the geostrophic

relative vorticity leads to small upper-level height falls above a given location. When one considers the height changes necessary in the entire column over a given area, it is clear that *the thickness of a given layer* must decrease (i.e., large height falls aloft versus smaller height falls at lower levels). The decrease in layer thicknesses is greatest in areas where vorticity advection increases the most with height (such as above a surface low located east of a 500-mb trough). The hypsometric equation reveals that layer thicknesses are proportional to the mean virtual temperature in that layer. Thus, the column must cool to maintain a hydrostatic temperature field. In the absence of horizontal advection of temperature such as warm or cold air advection, decreases in layer thicknesses must be accomplished by adiabatic cooling through vertical motion. Thus, *rising motion* must occur in the atmosphere when vorticity advection increases with height. Conversely, *sinking motion* results from cyclonic vorticity advection decreasing with height because adiabatic warming is required for the resultant thickness increases (Holton 1992).

The second term on the RHS of Equation A.1 represents the contribution of temperature advection in the atmosphere to vertical motion. The Laplacian of thermal advection is scaled by the specific gas constant (R), the static stability parameter, and pressure (p). When temperature gradients are large or the geostrophic wind is strong, then ω also will be large. In the case of warm air advection, $-\vec{v}_g \cdot \nabla_p T > 0$, by definition; the Laplacian of the temperature advection term is less than zero and the negative of this Laplacian ($\propto \nabla_p^2 \omega$) is greater than zero. Mathematically, this implies that $\omega < 0$ (due to the Laplacian operator on the LHS of Equation A.1), or *rising motion*. Conversely, cold air advection leads to sinking air in the atmosphere.

Physically, warm air advection leads to rising motion because the thickness of an atmospheric layer (e.g., 1000–700 hPa) must increase as the mean temperature in the layer increases. The height tendency equation,

$$\left[\nabla_p^2 + \frac{f_0^2}{\sigma}\frac{\partial^2}{\partial p^2}\right]\chi = f_0\left[-\vec{v}_g \cdot \nabla_p(\zeta_g + f)\right] - \frac{f_0^2}{\sigma}\frac{\partial}{\partial p}\left[\frac{R}{p}\left(-\vec{v}_g \cdot \nabla_p T\right)\right], \qquad \text{(A.4)}$$

reveals that geopotential heights of a given pressure level must increase above the level of maximum advection and decrease below the level of maximum advection. In this situation, and to maintain geostrophic balance, cyclonic vorticity must decrease at the top of the layer and increase at the bottom of the layer. To compensate for the additional anticyclonic vorticity at higher levels, horizontal divergence develops at upper levels. At lower levels, cyclonic vorticity increases and horizontal convergence occurs. Continuity of mass requires that the diverging air at upper levels be replaced by rising air (assuming stratospheric air above is so stable as to defy any vertical motion). Fortunately, the atmosphere has created converging air at lower levels (this scenario also creates rising motion because the surface of the earth is a material surface). Thus, warm air advection at a given geopotential height represents rising motion through that pressure level. Similarly, subsidence occurs in regions of cold air advection, such as beneath a 500-mb trough.

Written in terms of the geopotential field, Φ, the ω equation becomes,

$$\left[\nabla_p^2 + \frac{f_0^2}{\sigma}\frac{\partial^2}{\partial p^2}\right]\omega = \frac{f_0}{\sigma}\frac{\partial}{\partial p}\left[\vec{v_g}\cdot\nabla\left(\frac{1}{f_0}\nabla^2\Phi + f\right)\right] + \frac{1}{\sigma}\nabla^2\left[\vec{v_g}\cdot\nabla\left(-\frac{\partial\Phi}{\partial p}\right)\right]. \qquad \text{(A.5)}$$

This version of the omega equation relates the field of ω to the Φ field at any moment in time. It does not require:

- direct observations of the ageostrophic wind (unlike the continuity equation method discussed below),
- direct wind observations or vorticity tendency (unlike the vorticity equation method described below),
- direct observations of the temperature tendency (unlike the adiabatic method highlighted below).

Based on Equation A.5, the vertical motion field can be derived simply from the geopotential field at a single instant in time. The primary disadvantage to using this version of the omega equation is the required higher-order derivatives on the right-hand side of the equa-

tion, which may prevent the accurate estimation of ω from noisy Φ observations (Holton 1992).

A.2 Kinematic Method

The kinematic method for estimating vertical motion involves the vertical integration of the continuity equation in pressure coordinates,

$$\nabla_p \cdot \vec{v} + \frac{\partial \omega}{\partial p} = 0, \tag{A.6}$$

to obtain an estimate of ω. Here, $\vec{v}$ represents the horizontal velocity vector and p is pressure. Both the geostrophic and ageostrophic components of the wind are included in $\vec{v}$ such that this method links ω with the ageostrophic wind. However, Equation A.6 becomes deficient when the flow is non-divergent (such as when calculations performed using pressure coordinates), leaving the partial derivative of ω with respect to pressure equal to zero. Estimates of ω derived with this method depend heavily upon the horizontal wind field. Unlike surface winds that typically blow at speeds on the order of tens of kilometers per hour under clear conditions and upper-level winds that can reach speeds in excess of one hundred kilometers per hour, vertical motion is on the scale of only a few centimeters per second. Consequently, small errors in the horizontal wind field lead to large errors in the derived vertical motion. As a result, the kinematic method is not recommended to estimate vertical motion for most purposes (Holton 1992).

A.3 Adiabatic Method

Alternatively, the adiabatic form of the thermodynamic energy equation,

$$\omega = \frac{(\frac{\partial T}{\partial t} + \vec{v} \cdot \nabla_p T)}{(\frac{\sigma P}{R})}, \tag{A.7}$$

can be used to estimate ω if the diabatic heating is assumed to be small. The adiabatic method links ω with temperature advection, which is dominated by the geostrophic wind. This method requires the local rate of change of temperature, which rarely (if ever) is measured over large areas with sufficient temporal frequency. This adiabatic method works best near the tropopause, but not in areas with diabatic influences such as near clouds, precipitation, or near the surface. Because of these severe limitations, the adiabatic method cannot be applied near areas of heavy precipitation such as in the present study (Holton 1992).

A.4 Vorticity Method

The vorticity method combines the simplified vorticity equation in an Eulerian framework,

$$\frac{\partial \zeta}{\partial t} = -\vec{v} \cdot \nabla_p \zeta - \beta - \delta f, \tag{A.8}$$

and the continuity equation (Equation A.6) to obtain an estimate of the vertical velocity as a function of pressure,

$$\frac{\partial \omega}{\partial p} = \frac{1}{f} \left(\frac{\partial \zeta}{\partial t} + \vec{v} \cdot \nabla_p \zeta + v\beta \right). \tag{A.9}$$

Here, ζ represents the relative vertical vorticity, f is the Coriolis parameter, $\vec{v} \cdot \nabla_p \zeta$ is the advection of relative vorticity, $\vec{v}$ the y-component of velocity, $\beta = \frac{\partial f}{\partial y}$ the latitudinal variation in the Coriolis parameter, and δ the horizontal divergence of the wind field. When integrated with respect to pressure, the vertical velocity as a function of pressure can be calculated as

$$\omega(p) = \frac{1}{f} \int_0^p \left(\frac{\partial \zeta}{\partial t} + \vec{v} \cdot \nabla_p \zeta + v\beta \right) dp. \tag{A.10}$$

However, $\frac{\partial \zeta}{\partial t}$ and $\vec{v} \cdot \nabla_p \zeta$ have similar orders of magnitude and tend to oppose one another. Thus, these terms must be computed with extreme accuracy to prevent large errors in ω. This method neglects the twisting/tilting and vertical advection terms in the vorticity equation; on occasion, these terms may be significant (Bluestein 1992).

Appendix B

Table of Significant Events

TABLE B.1: Table of 260 significant events from every PC region. Precipitation amounts are in cm, the station ID number is the GHCN-D identification name, and 'N' indicates non-tropical events while 'T' indicates tropical events.

Station ID	State	Region	Prcp	Year	Mon	Day	Lat	Lon	Tropical
USC00240770	MT	1	15.01	1961	5	31	48.13	-110.05	N
USC00244538	MT	1	12.07	1962	5	20	46.67	-109.75	N
USC00329425	ND	1	12.52	1963	7	10	48.18	-103.63	N
USC00392797	SD	1	17.09	1964	6	18	45.78	-99.63	N
USC00323826	ND	1	12.90	1965	6	26	46.03	-100.00	N
USC00320995	ND	1	13.72	1966	7	13	46.18	-103.38	N
USC00328913	ND	1	13.56	1968	8	24	48.62	-100.73	N
USC00328627	ND	1	12.70	1972	5	22	48.33	-101.93	N
USC00243554	MT	1	15.93	1972	6	9	48.38	-106.82	N
USC00240770	MT	1	12.50	1974	5	13	48.13	-110.05	N
USC00242122	MT	1	12.40	1976	6	12	48.15	-104.50	N
USC00243929	MT	1	14.63	1986	9	25	48.55	-108.85	N
USC00395544	SD	1	16.48	1987	7	18	44.52	-101.62	N
USC00325988	ND	1	14.55	1987	8	14	48.27	-101.28	N
USC00246586	MT	1	16.64	1993	7	22	48.77	-104.55	N
USC00245045	MT	1	14.02	1997	7	1	47.22	-105.15	N
USC00394864	SD	1	12.80	1999	8	12	45.93	-102.17	N
USC00246918	MT	1	19.69	2000	5	17	45.20	-109.23	N
USC00327450	ND	1	12.67	2003	9	10	46.10	-102.95	N
USC00246918	MT	1	14.91	2005	5	11	45.20	-109.23	N
USC00307799	NY	2	19.76	1950	11	26	42.02	-74.42	N
USC00170934	ME	2	20.45	1954	9	11	43.90	-69.93	T
USC00193702	MA	2	33.63	1955	8	19	42.20	-72.60	N
USC00307799	NY	2	20.93	1955	10	16	42.02	-74.42	N
USC00276818	NH	2	22.81	1959	10	24	44.27	-71.25	N
USC00063207	CT	2	18.87	1961	9	21	41.35	-72.05	N
USC00194744	MA	2	21.95	1962	10	6	42.60	-71.02	T
USC00368758	PA	2	19.02	1969	8	2	40.78	-75.97	T
USC00283516	NJ	2	18.49	1971	8	28	41.13	-74.32	T
USC00369728	PA	2	22.00	1972	6	22	41.23	-76.92	N
USC00196486	MA	2	18.92	1972	9	4	41.98	-70.70	T
USC00307799	NY	2	18.95	1980	3	22	42.02	-74.42	T
USC00194711	MA	2	20.29	1990	7	25	41.88	-70.92	N
USC00288816	NJ	2	17.96	1991	7	14	39.95	-74.22	N
USC00176905	ME	2	19.69	1991	8	19	43.63	-70.30	T
USC00176905	ME	2	29.82	1996	10	21	43.63	-70.30	N
USC00287587	NJ	2	25.02	1999	9	17	41.08	-74.27	T
USC00309292	NY	2	23.24	2005	10	9	41.38	-73.95	N
USC00194760	MA	2	19.53	2005	10	15	42.17	-71.52	N
USC00198367	MA	2	20.35	2006	5	15	41.90	-71.07	N

TABLE B.1: (*Continued*)

Station ID	State	Region	Prcp	Year	Mon	Day	Lat	Lon	Tropical
USC00415659	TX	3	30.99	1951	5	7	28.68	-95.97	N
USC00414402	TX	3	52.58	1952	9	11	30.25	-98.57	N
USC00412266	TX	3	32.92	1960	6	26	29.05	-96.23	T
USC00414705	TX	3	32.39	1962	7	27	32.55	-96.27	N
USC00163979	LA	3	55.88	1962	8	29	29.88	-93.42	N
USC00416664	TX	3	40.13	1963	9	18	30.12	-93.78	T
USC00415757	TX	3	33.22	1964	6	16	31.43	-97.40	N
USC00417622	TX	3	31.78	1967	9	22	26.38	-98.87	T
USC00410204	TX	3	32.00	1973	6	12	29.37	-95.23	N
USC00410204	TX	3	65.41	1979	7	26	29.37	-95.23	T
USC00413340	TX	3	31.34	1979	9	19	28.98	-95.38	T
USC00414810	TX	3	38.23	1980	8	10	27.50	-97.80	T
USC00410235	TX	3	33.53	1981	6	5	29.78	-94.67	N
USC00413622	TX	3	41.43	1981	8	31	29.53	-97.45	N
USC00416024	TX	3	44.45	1994	10	17	30.38	-95.70	N
USC00416276	TX	3	46.61	1998	10	18	29.73	-98.12	N
USC00414321	TX	3	49.73	2001	6	9	29.78	-95.43	T
USC00413299	TX	3	32.51	2002	9	9	28.48	-98.87	N
USC00419076	TX	3	32.39	2008	9	15	30.10	-95.62	T
USC00414556	TX	3	36.40	2009	9	12	30.82	-97.60	N
USC00085539	FL	4	37.13	1964	9	12	30.05	-83.17	T
USC00091345	GA	4	31.39	1969	8	22	31.15	-81.38	N
USC00085793	FL	4	30.68	1970	6	3	30.77	-87.13	N
USC00010252	AL	4	31.19	1975	4	10	31.30	-86.52	N
USC00085663	FL	4	29.24	1977	5	4	25.82	-80.28	N
USC00083909	FL	4	41.63	1979	4	25	25.83	-80.28	N
USC00088788	FL	4	29.08	1979	5	8	27.97	-82.53	N
USC00086414	FL	4	29.77	1982	4	8	29.20	-82.08	N
USC00088841	FL	4	35.03	1982	6	2	25.00	-80.52	N
USC00010252	AL	4	31.34	1990	3	17	31.30	-86.52	N
USC00095314	GA	4	41.71	1990	10	12	33.00	-82.38	N
USC00089176	FL	4	30.02	1992	6	25	27.10	-82.43	T
USC00090253	GA	4	53.59	1994	7	6	32.05	-84.27	T
USC00084366	FL	4	31.90	1995	8	19	30.28	-81.38	N
USC00010252	AL	4	32.51	1995	10	4	31.30	-86.52	T
USC00010252	AL	4	29.08	1998	3	8	31.30	-86.52	N
USC00085793	FL	4	30.48	1998	9	26	30.77	-87.13	N
USC00010252	AL	4	45.42	1998	9	29	31.30	-86.52	T
USC00085663	FL	4	31.90	2000	10	3	25.82	-80.28	N
USC00083207	FL	4	30.76	2008	8	20	27.47	-80.35	T
USC00478827	WI	5	21.08	1951	7	21	43.53	-90.87	N
USC00110338	IL	5	26.62	1954	10	10	41.77	-88.32	N
USC00116526	IL	5	22.28	1958	7	14	41.32	-88.90	N
USC00135837	IA	5	24.16	1967	6	7	41.40	-91.07	N
USC00132367	IA	5	22.48	1967	9	14	42.38	-90.70	N
USC00132388	IA	5	28.65	1968	7	17	42.75	-92.97	N
USC00217405	MN	5	21.89	1968	8	7	44.30	-93.98	N
USC00218227	MN	5	20.32	1978	7	1	44.30	-92.22	N
USC00203858	MI	5	20.29	1982	7	17	42.78	-86.12	N
USC00205488	MI	5	21.74	1986	9	11	43.23	-83.57	N
USC00215435	MN	5	23.24	1987	7	23	44.87	-93.22	N
USC00470516	WI	5	19.76	1993	7	18	43.45	-89.72	N
USC00476764	WI	5	25.07	1996	6	18	43.38	-87.87	N
USC00114530	IL	5	34.54	1996	7	18	41.50	-88.10	N
USC00477725	WI	5	27.53	1998	8	6	43.75	-87.72	N
USC00477113	WI	5	21.01	2000	7	8	45.62	-89.42	N
USC00473405	WI	5	23.95	2002	6	21	44.10	-89.53	N
USC00113312	IL	5	29.69	2002	8	22	42.42	-90.43	N
USC00219046	MN	5	21.95	2005	9	25	43.77	-94.17	N
USC00478827	WI	5	23.44	2007	8	19	43.53	-90.87	N

TABLE B.1: (*Continued*)

Station ID	State	Region	Prcp	Year	Mon	Day	Lat	Lon	Tropical
USC00416780	TX	6	40.69	1954	6	27	30.20	-101.58	N
USC00342660	OK	6	25.02	1955	5	19	34.50	-97.97	N
USC00414517	TX	6	24.38	1957	4	26	33.23	-98.15	N
USC00344055	OK	6	24.84	1957	5	15	36.10	-97.83	N
USC00415821	TX	6	22.35	1960	6	7	34.72	-100.53	N
USC00413411	TX	6	23.19	1960	10	17	32.77	-101.45	N
USC00054076	CO	6	28.14	1965	6	17	38.05	-102.12	N
USC00346139	OK	6	23.19	1972	7	8	36.23	-99.17	N
USC00344573	OK	6	25.40	1973	10	11	36.72	-97.78	N
USC00413992	TX	6	36.30	1978	8	4	33.15	-99.73	N
USC00348110	OK	6	26.97	1983	10	20	35.35	-96.90	N
USC00413828	TX	6	22.48	1986	7	4	33.62	-100.32	N
USC00415707	TX	6	23.19	1986	10	4	31.13	-102.20	N
USC00349278	OK	6	29.57	1987	5	28	34.35	-98.30	N
USC00410271	TX	6	28.40	1989	5	16	33.43	-98.37	N
USC00347505	OK	6	24.99	1998	10	4	36.47	-97.17	N
USC00412096	TX	6	28.14	2000	6	4	32.53	-97.62	N
USC00340224	OK	6	23.24	2000	10	23	35.05	-98.18	N
USC00411761	TX	6	23.50	2001	5	4	34.95	-100.93	N
USC00343497	OK	6	26.44	2007	8	19	35.62	-98.32	T
USC00111475	IL	7	20.83	1951	7	9	40.73	-88.70	N
USC00238561	MO	7	28.80	1957	6	15	38.55	-90.48	N
USC00116610	IL	7	25.91	1957	6	28	39.63	-87.68	N
USC00116725	IL	7	24.28	1957	7	13	41.32	-87.78	N
USC00110608	IL	7	20.80	1959	8	17	38.03	-88.92	N
USC00153430	KY	7	20.45	1967	8	1	37.25	-85.50	N
USC00155067	KY	7	20.70	1969	6	23	37.35	-87.52	N
USC00339312	OH	7	23.80	1969	7	5	40.78	-81.92	N
USC00116725	IL	7	20.12	1972	6	13	41.32	-87.78	N
USC00127125	IN	7	21.06	1979	7	26	38.37	-87.57	N
USC00200146	MI	7	23.70	1986	9	11	43.38	-84.67	N
USC00127522	IN	7	20.45	1989	5	26	39.77	-87.23	N
USC00127875	IN	7	20.32	1992	8	8	38.70	-85.77	N
USC00336645	OH	7	19.96	1995	8	8	40.15	-84.23	N
USC00110608	IL	7	22.28	1996	4	29	38.03	-88.92	N
USC00155067	KY	7	26.04	1997	3	2	37.35	-87.52	N
USC00366233	PA	7	20.32	2004	9	9	41.02	-80.37	N
USC00338534	OH	7	23.75	2007	8	21	40.83	-83.28	N
USC00113879	IL	7	25.40	2008	3	18	37.75	-88.55	N
USC00120877	IN	7	24.13	2008	6	7	39.42	-86.97	N
USC00133718	IA	8	19.20	1953	6	7	43.00	-96.48	N
USC00130923	IA	8	21.84	1954	6	18	43.10	-93.80	N
USC00130385	IA	8	31.83	1958	7	2	41.70	-94.92	N
USC00130923	IA	8	18.95	1959	5	21	43.10	-93.80	N
USC00257640	NE	8	23.62	1959	8	2	41.45	-97.07	N
USC00134038	IA	8	27.97	1962	8	31	42.35	-95.48	N
USC00255250	NE	8	19.05	1964	6	30	41.22	-99.28	N
USC00250070	NE	8	26.14	1966	8	13	41.67	-98.10	N
USC00136800	IA	8	19.56	1973	8	23	43.08	-95.62	N
USC00259510	NE	8	18.29	1985	7	19	40.87	-97.60	N
USC00134735	IA	8	22.25	1985	8	29	42.77	-96.13	N
USC00132171	IA	8	20.04	1993	7	9	42.03	-95.32	N
USC00251990	NE	8	18.75	1995	8	22	42.45	-97.90	N
USC00131277	IA	8	30.53	1996	7	17	42.05	-95.83	N
USC00257640	NE	8	19.56	1996	8	5	41.45	-97.07	N
USC00258480	NE	8	20.96	1999	8	7	41.77	-96.22	N
USC00397052	SD	8	18.80	2007	5	6	44.88	-98.38	N
USC00142459	KS	8	18.42	2007	5	24	38.72	-98.22	N
USC00132689	IA	8	22.86	2007	8	18	43.10	-94.67	N
USC00256837	NE	8	19.05	2008	6	5	41.07	-97.78	N

TABLE B.1: (*Continued*)

Station ID	State	Region	Prcp	Year	Mon	Day	Lat	Lon	Tropical
USC00166911	LA	9	32.08	1953	5	18	30.75	-90.98	N
USC00015478	AL	9	33.93	1955	4	13	30.68	-88.25	N
USC00086997	FL	9	29.67	1956	9	24	30.47	-87.18	T
USC00167096	LA	9	30.48	1959	5	31	29.78	-90.43	N
USC00162534	LA	9	30.73	1961	11	14	30.12	-90.98	N
USC00160549	LA	9	30.45	1967	4	14	30.53	-91.13	N
USC00016847	AL	9	32.31	1979	4	13	33.37	-88.02	N
USC00166938	LA	9	32.64	1979	9	20	30.60	-92.78	T
USC00406012	TN	9	34.54	1982	9	13	35.90	-88.73	T
USC00221865	MS	9	34.80	1983	4	7	31.23	-89.83	N
USC00166836	LA	9	34.95	1983	8	3	30.82	-92.67	N
USC00164674	LA	9	29.39	1984	10	23	29.95	-91.72	N
USC00169803	LA	9	32.77	1989	6	29	31.93	-92.68	T
USC00166660	LA	9	31.09	1995	5	8	29.98	-90.25	N
USC00010583	AL	9	39.57	1997	7	20	30.92	-87.78	T
USC00010583	AL	9	38.38	1998	9	28	30.92	-87.78	T
USC00166666	LA	9	38.96	2002	9	26	29.93	-90.03	T
USC00016988	AL	9	36.55	2005	4	1	30.62	-87.65	N
USC00162367	LA	9	34.54	2005	9	24	30.83	-93.28	T
USC00169806	LA	9	33.66	2008	9	3	32.10	-91.72	T
USC00032300	AR	10	27.05	1958	4	26	33.22	-92.80	N
USC00341711	OK	10	29.72	1960	7	25	35.47	-95.52	N
USC00415766	TX	10	30.73	1964	9	21	33.17	-96.62	N
USC00349118	OK	10	26.54	1971	12	10	34.00	-95.15	N
USC00032842	AR	10	30.25	1972	9	18	34.32	-93.53	N
USC00034756	AR	10	26.49	1972	10	31	34.57	-94.25	N
USC00238700	MO	10	27.94	1977	3	28	36.92	-90.28	N
USC00031750	AR	10	31.12	1978	9	13	34.70	-92.45	N
USC00034528	AR	10	26.54	1980	7	22	35.02	-90.73	N
USC00419125	TX	10	33.07	1982	5	13	33.38	-96.33	N
USC00030664	AR	10	35.71	1982	12	3	34.50	-93.93	N
USC00414081	TX	10	28.07	1989	3	29	32.17	-94.78	N
USC00168067	LA	10	30.07	1989	5	5	32.52	-92.65	N
USC00033466	AR	10	32.94	1990	5	20	34.52	-93.05	N
USC00034756	AR	10	30.23	1990	10	8	34.57	-94.25	N
USC00166244	LA	10	32.69	1991	4	13	32.60	-93.28	N
USC00034548	AR	10	29.79	1997	4	5	33.32	-93.23	N
USC00035112	AR	10	26.16	1998	5	28	34.00	-93.93	N
USC00236970	MO	10	25.91	2006	9	23	36.58	-90.23	N
USC00345563	OK	10	32.56	2009	4	30	33.87	-97.15	N
USC00440720	VA	11	27.20	1954	10	15	38.52	-78.43	T
USC00316108	NC	11	25.15	1955	9	19	35.07	-77.05	T
USC00310674	NC	11	31.52	1962	6	30	35.48	-76.68	T
USC00314055	NC	11	30.15	1964	9	29	35.05	-83.18	N
USC00314055	NC	11	25.17	1964	10	4	35.05	-83.18	N
USC00445050	VA	11	28.40	1969	8	20	38.03	-78.00	T
USC00317486	NC	11	26.42	1970	10	11	35.13	-82.83	N
USC00284887	NJ	11	25.32	1971	8	28	40.88	-74.23	T
USC00449151	VA	11	25.27	1975	9	1	37.30	-76.70	N
USC00314788	NC	11	25.65	1979	3	4	35.13	-82.93	N
USC00449151	VA	11	28.78	1989	8	18	37.30	-76.70	T
USC00318113	NC	11	29.97	1996	9	6	33.98	-78.00	T
USC00319467	NC	11	36.58	1998	8	27	34.32	-77.92	T
USC00318113	NC	11	46.48	1999	9	16	33.98	-78.00	T
USC00188380	MD	11	36.35	2002	9	1	38.18	-75.38	N
USC00311624	NC	11	37.47	2004	9	8	35.82	-82.17	T
USC00091982	GA	11	32.39	2004	9	17	34.85	-83.40	T
USC00318113	NC	11	25.12	2005	9	14	33.98	-78.00	T
USC00319467	NC	11	25.91	2006	9	1	34.32	-77.92	T
USC00098740	GA	11	30.15	2009	9	21	34.58	-83.32	N

TABLE B.1: (*Continued*)

Station ID	State	Region	Prcp	Year	Mon	Day	Lat	Lon	Tropical
USC00233793	MO	12	22.86	1957	6	29	38.70	-91.42	N
USC00143667	KS	12	24.03	1963	7	11	38.33	-97.18	N
USC00137669	IA	12	22.23	1965	7	19	40.75	-95.65	N
USC00148964	KS	12	23.16	1973	10	11	37.25	-97.00	N
USC00143822	KS	12	28.96	1976	7	3	37.52	-96.18	N
USC00143248	KS	12	27.76	1977	6	22	37.35	-96.43	N
USC00134063	IA	12	22.61	1977	8	26	41.37	-93.55	N
USC00142409	KS	12	24.38	1979	11	21	37.00	-96.27	N
USC00142409	KS	12	23.37	1984	10	13	37.00	-96.27	N
USC00230204	MO	12	23.11	1986	10	3	38.18	-94.02	N
USC00136316	IA	12	22.35	1992	9	15	41.02	-93.82	N
USC00238664	MO	12	27.94	1993	9	25	37.23	-94.55	N
USC00235987	MO	12	27.05	1994	4	11	37.83	-94.37	N
USC00130364	IA	12	33.48	1998	6	14	41.42	-95.00	N
USC00142835	KS	12	31.75	1998	9	15	37.85	-94.70	N
USC00144857	KS	12	23.85	2003	6	23	39.90	-98.02	N
USC00142401	KS	12	22.99	2005	8	25	37.82	-96.83	N
USC00148341	KS	12	22.99	2005	10	2	39.35	-95.45	N
USC00142894	KS	12	29.87	2007	6	30	37.53	-95.80	N
USC00148830	KS	12	26.19	2008	9	12	37.63	-97.42	N
USC00215638	MN	13	17.53	1954	4	26	45.58	-95.88	N
USC00214652	MN	13	17.83	1954	7	10	47.23	-94.22	N
USC00215482	MN	13	22.02	1957	6	17	44.55	-95.98	N
USC00323594	ND	13	18.85	1957	9	2	48.42	-97.42	N
USC00479304	WI	13	17.45	1958	7	1	45.88	-91.07	N
USC00473332	WI	13	16.94	1960	4	23	46.47	-90.50	N
USC00471923	WI	13	16.26	1960	8	28	45.53	-92.02	N
USC00214008	MN	13	16.33	1972	7	20	48.62	-93.88	N
USC00214861	MN	13	22.61	1972	7	22	45.97	-94.87	N
USC00325230	ND	13	20.57	1975	6	29	46.65	-98.22	N
USC00324203	ND	13	16.21	1987	7	21	47.43	-97.05	N
USC00211630	MN	13	21.44	1990	9	6	46.70	-92.52	N
USC00324413	ND	13	16.13	1993	7	15	46.92	-98.68	N
USC00218520	MN	13	17.27	1994	8	10	44.50	-95.45	N
USC00215400	MN	13	24.84	1995	7	4	45.12	-95.92	N
USC00212500	MN	13	16.76	2003	6	25	45.30	-93.58	N
USC00473244	WI	13	19.89	2005	10	5	45.80	-92.67	N
USC00391873	SD	13	19.35	2007	5	6	45.73	-98.30	N
USC00218907	MN	13	17.83	2007	6	2	45.80	-96.48	N
USC00218311	MN	13	22.10	2007	9	7	47.75	-92.28	N

Appendix C

Remaining Regional Composite Map Results

The following is a brief overview of the remaining 8 regions not described in Chapter 6. Many of the features described below can be viewed in Figures 6.28, 6.29, and 6.30 or are quite similar to features in neighboring regions described in Chapter 6.

C.1 Region 1: Eastern MT Through the Western Dakotas

Significant precipitation events in region 1, located in the far northwest corner of the domain encompassing parts of Montana and the Dakotas, had the smallest magnitude of all significant events by region (Table 5.3). Nevertheless, this region displayed very strong synoptic signals in the composite maps. Aside from its geographic location in the western high plains and the fact that 18 out of the 20 significant events occurred from May to August, the composites for PC Region 1 have the classic look of a Uccellini and Kocin (1987) east-coast snowstorm: coupled jets with their high-level divergence (1×10^{-5} sec^{-1}) positioned over the location of significant rainfall and synoptic-scale ascent at 500 hPa (magnitude $> 0.21 Pa$ sec^{-1}) spatially located about midway between the location of 850 convergence and the high-level divergence. In other words, the meteorological features tilted almost south-to-north with increasing height. This "sloped response" is consistent with the work of Uccellini and Kocin (1987) who revealed cold season features that sloped along isentropic surfaces. The implication is that latent heat has been released in large quantities, but only a vertical cross section bisecting the heavy rainfall location would reveal this fact. Furthermore, the composite maps resembled the work of Junker et al. (1999) quite closely

(heaviest precipitation west of and at the nose of the low level jet, in the northeast quadrant of a surface low with the preferred rainfall location underneath the ageostrophic divergence aloft, and downwind from the thermal advection at 850 hPa of 50×10^{-6} K sec^{-1}). A narrow tongue of moisture (precipitable water of 25 mm) from the Gulf of Mexico curved cyclonically around the surface cyclone and pointed toward the region of significant rainfall.

The most surprising fact from Region 1 is the magnitude of cold air advection at 500 hPa located over the lower-level convergence; this contributes to differential thermal advection working to quickly decrease atmospheric stability. Clearly, the events in Region 1 are strongly driven by synoptic-scale forces. This latter statement is supported by the fact that positive vorticity advection in the composite 500 hPa image for Region 1 is nearly centered over the location of significant rainfall (magnitude of 0.004 sec^{-2}). Even differential vorticity advection through 500 hPa (Term B of the Q-G Omega equation) is supportive of ascent over the region of rainfall, though weaker in the composite of 20 cases (magnitude of approximately 0.002 Pa km^{-2} hour^{-1}) that simple advection at 500 hPa. However, the strongest support for ascending air comes from Term C of the Q-G Omega equation, which has warm thickness advection centered over (magnitude near 0.003 Pa km^{-2} hour^{-1}) the region of significant rainfall and stretching southeast toward the low-level jet.

C.2 Region 3: Southeast TX

PC Region 3, located in southeast Texas, did not reveal well-defined dynamical signals in the many non-tropical composite images produced for this discussion. Most meteorological ingredients were supportive for significant rainfall, but all were very weak and rarely aligned favorably compared to the forcing ingredients in other regions described above. Perhaps the strongest clue to support the location and magnitude of significant rainfall in Region 1 was hidden in the isentropic ascent over the adjacent coastal waters off the central Texas coast. Even so, the composite low-level moisture fields and moisture axes (precip-

itable water in excess of 40 mm) were co-located with the low-level jet at 850 hPa, which extended north-northwest from the average location of significant rainfall. The warm thermal advection and mass convergence at 850 hPa were weakly positive over and just west of the average location of significant rainfall (1×10^{-6} K sec^{-1} and 5×10^{-6} sec^{-1}, respectively), and an inflection point center-of-divergence at 200 hPa was located less than 100 km north (1×10^{-5} sec^{-1}). Ascending air at 500 hPa (-1 Pa sec^{-1}) was centered over the location of significant rainfall. The advection of relative vorticity at 500 hPa and the differential vorticity advection (Term B) through 500 hPa were both near zero. The thickness advection through 850 hPa (Term C) was effectively zero as well.

Thus, the scientific explanation for the location and magnitude of significant rainfall across Texas likely lies in the thermodynamic variables (e.g., a close-to-the-ground LCL) and a strong moist LLJ. These results agree with the conclusions of Bradley and Smith (1994) and Moore et al. (1995) that events characterized by weak dynamic forcing tend to be associated with a quasi-stationary front or residual gust front in the presence of low-level southerly winds transporting warm moist air. Storms that did form may have been driven along the frontal boundary and heavy precipitation totals may have resulted from the training of multiple storms. Despite the likely major role of mesoscale boundaries in the evolution of these significant rain events (Maddox and Doswell 1982), an examination of these features were beyond both the capability of the Reanalysis dataset and the scope of this research. Finally, the events in Region 3 most often occurred during June (6) and September (9) and accounted for 75% of the significant rainfall in this region of the United States. Many of these were tropical in nature. Of the twelve non-tropical significant events in Region 3, three occurred in June, three in September, and the rest were spread throughout the warm season months of May through October.

C.3 Region 4: Southeastern U.S.

Like PC Region 3, non-tropical events in the southeast region of the United States did not reveal any well-defined dynamical signals. Perhaps the strongest dynamical clue, albeit several hundred kilometers northwest of the PC Region, was the super-ageostrophic flow into a low-amplitude ridge along the east coast that produced weak divergence at 200 hPa (1×10^{-5}). A broadly defined axis of precipitable water had been transported northwest by the prevailing lower-level flow but maximum values were hardly above normal values (30–40 mm) for the 14 non-tropical significant events spread nearly evenly across the months of March–October. At 850 hPa, the warm thermal advection was maximized in a long corridor to the northwest of the PC Region but thickness advection was zero at the event centroid. In addition, low-level mass convergence was centered far to the northwest while vorticity advection at 500 hPa and differential vorticity advection were both near zero. Thus, a broad scientific explanation for all non-tropical significant rainfall across the southeast USA was not readily apparent, although it could be hidden in the thermodynamic variables (such as the low height of the LCL). In other words, there was no predictable forcing cause for the non-tropical significant rainfall events in the southeast region.

The lack of a coherent pattern in Region 4 likely was due to differences in the environments of each of the 14 non-tropical significant events. When the individual composite members were examined, a large variability occurred from event to event. For example, 6 of the 14 non-tropical events had a bulls-eye of warm thermal advection at 850 hPa over the significant event location, while the remaining 8 had little to no (or negative) thermal advection near the rainfall maxima. Some inland events (such as in Alabama or Georgia) were associated with synoptic-scale low pressure systems, while most events across the Florida Peninsula were unassociated with large synoptic systems. The disparity between individual events in Region 4 makes a composite map impossible unless one first classifies a type of event and makes multiple types of composite map groups. Such groups of composite maps would likely lose the wide-range of applicability and value by compositing the

very small sample size of 14 non-tropical events.

C.4 Region 5: WI Through MI

The features associated with significant rainfall in PC Region 5, near the Great Lakes, blend nicely with the work of Johns (1984) and his study of summertime northwest flow events. In this region, the magnitudes of the thermodynamical features were quite strong. Although the significant events do not fit into the Johns (1984) classification as northwest flow events, the significant events in Region 5 display one of the strongest warm air advection areas of all PC regions (6×10^{-5} K s^{-1}). The significant events in the PC Region are distinctly warm season in nature (19 of the 20 significant events occurred during the months of June–September and the remaining event in early October). Consequently, the forcing mechanisms for large storms may vary by season (cf. Johns 1984). In contrast, the magnitudes of the dynamical features were quite weak. Differential vorticity advection through 500 hPa, vorticity advection at 500 hPa, and the thickness advection at 850 hPa all were barely positive. Furthermore, the composite models from this region mirror the great Chicago flood of October 1998 and are a close fit to the composite models developed by Junker et al. (1999).

However, this PC Region had one distinguishing characteristic compared to the other regions: the major features at multiple levels were just west or northwest of the centroid of significant rainfall: warm thermal advection at 850 hPa (60×10^{-6} K sec^{-1}), ascent at 500 hPa (-0.1 Pa sec^{-1}), and divergence at 200 hPa (6×10^{-6} sec^{-1}). While the synoptic-scale atmosphere tends to work on sloped isentropic surfaces, the composite models from PC Region 5 suggest something was slightly different in this region. Perhaps the thermodynamical variables of region 5 were much stronger than those in other regions (possibly due to evapotranspiration from corn across the upper Midwest; precipitable water was in excess of 39 mm upwind of the favored area for significant rainfall and featured a maximum that had its roots in eastern Iowa through southern Wisconsin).

C.5 Region 7: Ohio River Valley

Synoptic-scale forces that signaled significant rainfall across the Ohio River Valley, primarily during the months of June–August (14 of the 20 events occurred during this 90-day period), were tightly packed across the PC Region 7. In fact, none of the major features discussed in the other PC Regions were located outside of the Ohio River Valley (850 hPa convergence of 8×10^{-6} sec^{-1}; ascent at 500 hPa more negative than -0.25 Pa sec^{-1}; divergence of 1.6×10^{-5} sec^{-1} at 200 hPa). The slight tilt of features with increasing height was toward the northeast in less than 300 km, suggesting that low-level moisture from the Gulf of Mexico increased the convective instability and forced the atmosphere to respond vertically more so than along gently sloped isentropic surfaces. The strongest signal in the composites for this PC Region was the narrow tongue of copious Gulf moisture (precipitable water values of 0.42 mm). As with many of the inland PC Regions, the lower-level maps from Region 7 closely resembled the composite images of Junker et al. (1999). Strong thermal advection and thickness advection (Term C; 0.002 Pa km^{-2} hour^{-1}) were evident across the Region but differential vorticity advection was zero. A low LCL was associated with isentropic lift in the right exit region of a jet at 500 hPa.

C.6 Region 8: NE and SD

Lower level features in PC Region 8, across parts of Nebraska and South Dakota, strongly resembled the Maddox et al. (1979) frontal type of convective event and clearly were confined to the warm season months of May-August (all 20 significant events occurred during this four month period). For example, a rich plume of precipitable water (> 36 mm) from the Gulf of Mexico pointed toward the location of significant rainfall as determined by mass convergence at 850 hPa, which was associated with a quasi-permanent baroclinic zone and at the nose of a strong low level jet. These features appeared strongest southwest of the centroid of significant rainfall and were co-located with strong 850 hPa thermal advection (in excess of 5×10^{-5} K sec^{-1}). Vertical velocities at 500 hPa were

strongest (magnitudes were > -0.15 Pa sec^{-1}) over the low-level mass convergence. The presence of a basic west-to-east high-level jet stream along the Canadian border created ageostrophic divergence (8×10^{-6} sec^{-1}) over the preferred location of significant rainfall. Differential vorticity advection through 500 hPa (Term B) was zero at the event centroid (although high to the northwest), while a maximum of thickness advection at 850 hPa (Term C; > 0.003 Pa km^{-2} hour^{-1}) was positioned above the center of significant rainfall.

C.7 Region 9: LA Through TN

Of the 11 non-tropical events in Region 9, along the central Gulf Coast, the preferred location for significant rainfall was at the nose of the LLJ, in an inferred area of strong isentropic ascent, near the maximum in precipitable water (> 39 mm) that was co-located with a weak convergence zone. At 850 hPa, the southerly jet was aligned with the maximum of warm thermal advection and a zone of strong mass convergence (7×10^{-6} sec^{-1}). The thickness advection (term C) was weakly positive downwind from the nose of the low level jet. Vertical velocities at 500 hPa were very strong (magnitude of ascent exceeded 0.25 Pa sec^{-1} just northwest of the event centroid). Relative vorticity advection and differential vorticity advection through 500 hPa were both near zero at the center of heaviest rainfall. All features were aligned north-to-south but mid- to upper-level features were shifted 50–100 km to the north-northwest relative to the centroid of significant rainfall. By 200 hPa, inflection point divergence over-powered the right exit region of a subtropical jet stream (divergence was still 1.2×10^{-5} sec^{-1}). Thus, isentropic lift associated with the indirect circulation of the exit region, combined with weak topographic lift, was able to tap a low-to-the-ground LCL and a baroclinic zone (apparent in the 1000 hPa wind vectors) to create strong convection by utilizing the moisture plume from the Gulf of Mexico via the strong LLJ. In a final analysis, the composite patterns for PC Region 9 closely resembled the frontal zone composites of Maddox et al. (1979).

The significant rainfall events in this PC Region were very much bi-modal in their

frequency of occurrence: 8 non-tropical events occurred in April–May and 7 tropical events took place in September; no other month recorded more than one significant rainfall event.

C.8 Region 10: Northeast TX Through Southern IL

Significant rainfall events in PC Region 10, covering an area from northeast Texas through southern Illinois, also were bimodal in their frequency of occurrence: ten events occurred in March-May and six events in September–October. However, no events in this region were found to be tropical in origin. The composite images of meteorological features revealed that the centroid of significant rainfall occurred at the nose of a southerly surface jet, in an area of inferred isentropic ascent, and at the north end of a narrow corridor of copious precipitable water (maximum values near 42 mm). At 850 hPa, the preferred location for significant rainfall was located in the center of the low-level jet, in an area of strong thermal advection, and in a narrow zone of substantial mass convergence (6×10^{-6} sec^{-1}). Midway through the troposphere, vertical motions of -0.25 Pa sec^{-1} were centered over the location of maximum rainfall. This general area also was located in the right entrance region of an anticyclonically curved jet stream with 200 hPa divergence peaking at 1.8×10^{-5} sec^{-1} slightly northeast of the event centroid. Relative vorticity advection at 500 hPa along with differential vorticity advection through 500 hPa were both near zero at the event location but peaked further west and northwest, respectively. However, the thickness advection at 850 hPa was positive (> 0.001 Pa km^{-2} hour^{-1}) in a narrow corridor that mirrored the location of the low-level jet.